High-Temperature Oxidation and Fatigue Performance of Alloy 625: Effect of Alloy Manufacturing Process

by

Grace Vanessa de Leon Nope

Chemical Engineering, Universidad Nacional de Colombia, 2015

Masters in Materials Science, CINVESTAV, 2018

Submitted to the Graduate Faculty of the

Swanson School of Engineering in partial fulfillment

of the requirements for the degree of

Doctor of Philosophy

University of Pittsburgh

2023

UNIVERSITY OF PITTSBURGH

SWANSON SCHOOL OF ENGINEERING

This dissertation was presented

by

Grace Vanessa de Leon Nope

It was defended on

October 5, 2023

and approved by

Guofeng Wang, Ph.D., Professor, Department of Mechanical Engineering and Materials Science

Wei Xiong, Ph.D., Professor, Department of Mechanical Engineering and Materials Science

Mostafa Bedewy, Ph.D., Professor, Department of Industrial Engineering

Jonathan Vande Geest, Ph.D., Professor, Department of Bioengineering

Dissertation Director: Brian Gleeson, Harry S. Tack Chair Professor, Department Chairman,

Department of Mechanical Engineering and Materials Science

High-Temperature Oxidation and
Fatigue Performance of Alloy 625: Effect of Alloy Manufacturing Process

Grace Vanessa de Leon Nope, PhD

University of Pittsburgh, 2023

Multiple efforts have been made to fabricate complex parts by additive manufacturing (AM), taking advantage of the freedom of design, sustainability benefits, and the manufacture of hard-to-machine alloys. However, one of the major drawbacks of the AM implementation for components with both high mechanical and chemical requirements is the lack of full understanding of the processing-structure-properties relationships. This study explores the impact of the microstructural variables stemming from laser AM processes on the high-temperature oxidation behavior and fatigue performance of the Ni-based, chromia-scale forming alloy 625. Two laser-assisted AM processes were studied: laser powder bed fusion (LPBF) and direct energy deposition (DED), and wrought and cast alloy were used as references. During the early stages of oxidation, it was observed that the extent of Nb and Mo segregation affects the formation of transient products (refer to section 5.1.3.5). In the steady-state oxidation regime, it was noted that the AM samples show consistently faster oxidation kinetics (refer to section 5.2.3.2.1). Additionally, the AM samples exhibit more damaged subsurface and chromia scale, characterized by a larger oxide scale decohesion, non-planar interface, internal voids, and severe intergranular oxidation (refer to section 5.4.3.1). The excess of void formation in oxidized AM samples is attributed in part to the higher oxygen uptake during the alloy manufacturing processes. The combined effect of these defects (i.e., interfacial voids, delta-precipitates, internal oxidation) enhances the alloy degradation during high cycle fatigue, ultimately resulting in a significant reduction in fatigue life compared to the wrought sample. The most detrimental factor for fatigue performance is severe intergranular oxidation (refer to section 5.4.3.4).

Table of Contents

List of Tables

List of Figures

Nomenclature

Symbol	Description
AM	Additive manufacturing
BSE	Back-scattered Electron Detector
DED	Direct energy deposition
EDS	Energy-dispersive X-ray spectroscopy
EPMA	Electron probe micro-analyzer
GBs	Grain boundaries
HT	Heat treatment
IGO	Intergranular oxidation
LPBF	Laser powder bed fusion
OX	Oxidation
SEM	Scanning electron microscope
STEM	Scanning transmission electron microscopy
TA	Thermal aging
TCP	Topologically close-packed phases
TGA	Thermogravimetric Analysis
XRD	X-ray diffraction analysis

Acknowledgments

My Ph.D. journey has been a roller coaster of emotions. Full of joy when experiments worked out and frustration when they didn’t. Despite being a highly motivated and curious individual pursuing a learning process; my successful completion required suitable conditions in the whole social, personal, and professional environment. Today, I would like to thank everyone who made this thesis completion possible for me.

To start, Dr. Gleeson, my advisor, was a crucial part of my well-being during this journey. He cares for his students in their professional and personal growth. Despite his large list of duties, he has always procured time to attend to questions and guide each of his students. Besides, there is no better way to teach than by example, and in my opinion, he is a role model of what an excellent professor and researcher should be. And I hope that we, as Ph.D. students, can continue to grow in a healthy environment as Dr. Gleeson's group offers.

To my colleagues in Dr. Gleeson's group, thanks for the friendship I found in each of you. I couldn't have asked for better group mates. Patrick, Emily, and Matt have been so welcoming and supportive since the beginning of my process. They have taught me many things, and I am grateful for that. Preston and Isabella, this process would have been boring without you. Laughing and joking is a vital spice for keeping your sanity during this process. To Rafa, thanks for the energy, and new perspective you brought to the group. To all of you, I hope you continue enjoying this journey, as much as I did by your side.

To Ahmed, I am grateful that this journey led me to know you, my partner in life, نو العين. Thanks for cheering me up and supporting me during this process. Thanks for patiently teaching

me better ways to do things and motivating me when I was lacking it. Thanks for always looking to improve my language skills. Above all, thanks for being always there.

Thanks to the NFCF staff, especially Dan and Susheng, who were always available either on-site or online to help solve problems, improve our skills, and teach us better ways to do things. Thanks for your patience, willingness, and good mood.

Thanks to my family and friends, they were a fuel that kept me motivated when things were not going well, and they celebrated my victories as theirs. Thanks to my mom for being caring, and supportive, and filling me with love when I most need it. Thanks for knowing Pittsburgh better than I do, I appreciate every detail you did to make my life easier. Thanks to my grandma, for all the advice, and keeping me connected and updated with the family stories despite being hundreds of miles away. Thanks to my aunt, for always seeing the good side of things, and keeping up with all my processes. You have always had a smile for me, and I am confident that you will have the energy to overcome the current difficulties.

Last but not least, thanks to Pitt, for offering abundant options to improve the students' welfare. Specifically, thanks to the group fitness classes that help me to release stress and keep a healthy lifestyle.

1.0 Introduction

Nickel-based alloys manufactured using additive manufacturing (AM) have advantages such as greater freedom of design, including internal cavities and intricate geometries, less material usage, fewer assemblies, and less machining time [1], [2]. The applications of nickel-based superalloys range from cryogenic to high temperatures (>950°C), requiring high strength, good fatigue resistance, and good oxidation resistance [3]. For use in high-temperature applications, a Ni-based alloy such as 625 relies on the protectiveness of the thermally grown chromia scale [4]–[6].

Alloy 625 is widely used for gas turbine components where the cooling technology is still challenging since the cooling determines the efficiency and operation of the entire system [7]. Innovative cooling systems have been designed based on the capabilities of AM in metallic molds for plastic injection, resulting in a reduction in the production time, and improving the quality of the components [1]. These cutting-edge cooling systems would not have been possible to fabricate using conventional manufacturing processes. Soon, gas turbine blade cooling systems might also benefit from novel designs that can only be fabricated using AM, which will lead to further efficiency gains.

However, the implementation of AM in parts with high mechanical and chemical performance requirements is delayed by the high variability in the reported properties relative to conventional manufacturing counterparts, and the lack of experimental data regarding the impact of this variability on the service life. Variability in the mechanical (i.e., UTS, YS [2], [8]) and oxidation (scaling kinetics) performance has been reported for the same material and AM technique used [9]–[12]. Moreover, some studies report a negative influence of mesostructural

defects such as porosity, roughness, and warping on the mechanical and oxidation properties of AM samples [13], [14]. These observations show the necessity for standardization and qualification of AM processes and products [15]. Therefore, a more complete understanding of the relationships of microstructure-process-performance is essential for the implementation of AM –processed Alloy 625 in high-temperature applications.

Due to the requirements of Alloy 625 in high-temperature applications, relying solely on a rudimentary study process-microstructure-performance may not reflect the complexities of real application conditions. Certain defects that may not seem significant for oxidation performance could actually be critical for fatigue performance, and vice versa. This work aims to achieve the following three objectives in response to this challenge: (1) gain a comprehensive understanding of how the manufacturing process affects the alloy's microstructure; (2) correlate microstructural features inherent from the alloy processing to the oxidation behavior; and (3) evaluate how these oxidation differences ultimately impact fatigue performance.

In the first chapter of this dissertation, the context and research objectives are introduced, with an emphasis being placed on the significance of the research. Moving on to chapter two, a review of the literature and key concepts pertaining to Alloy 625 metallurgy, laser additive manufacturing, and high-temperature oxidation of Ni-based alloys is provided. Chapter three summarizes deficiencies in the existing knowledge base and outlines the research objectives to address these gaps. In chapter four, the experimental procedures used are presented, including AM processes used, associated process parameters, and the raw material characteristics.

The original contribution covering the experimental results and an in-depth analysis of the findings are provided and discussed in chapter five, which has six subchapters. The first subchapter delves into the evolution from transient oxidation to a steady-state regime at an exposure temperature of 800°C. The discussion revolves around the impact of interdendritic segregation on the transient products and establishment of chromia. The second subchapter studies the oxidation kinetics contributions at 800°C in an effort to explain the consistently faster kinetics exhibited by AM samples compared to the wrought counterpart. Additionally, the subsurface oxidation-induced changes were studied, focusing on the higher faction of precipitates beneath the chromia scale in the AM samples. The third subchapter examines the oxidation behavior and kinetics contributions at 950°C, with a focus on chromia scale doping and intergranular oxidation. The potential reasons for the enhanced intergranular oxidation and abundant voids formation in the AM samples relative to the wrought sample are also discussed. In the fourth subchapter, the impact of AM oxidation-induced features at 800°C on room-temperature fatigue performance is discussed. The combined effects of interfacial voids, delta-precipitates, and internal oxidation lead to enhanced degradation, resulting in earlier crack initiation. Subchapter five delves into the effects of minor element content on interfacial defect formation and the role of intergranular oxidation on crack initiation, analyzing the fatigue performance of samples oxidized at 950°C. Finally, subchapter six provides mitigation strategies to improve the fatigue performance of oxidized AM samples. Optimal homogenization heat treatments were developed for each sample, and the impact on oxidation and fatigue performance after oxidation was studied.

It is important to note that although the recommended service temperature of Alloy 625 under mechanical load is limited to about 650°C (due to the δ-precipitates that embrittle the alloy), higher use temperatures are common in service. Moreover, studying the oxidation behavior at higher temperatures allows for extrapolation of performance for extended periods at lower temperatures, assuming that the mechanisms are similar. Additionally, studying oxidation at 800°C and 950°C allows for evaluation of performance under those situations when the alloy is used above recommended service temperatures.

2.0 Background

2.1 Ni-based Superalloys

2.1.1 Overview

A "superalloy" may be defined as a metallic system designed to have high-temperature strength, toughness, and corrosion resistance. The past few decades of extensive alloy and processing development efforts have resulted in alloys that can tolerate average temperatures of 1050˚C with occasional excursions to as high as 1200˚C, which is approximately 90% of the absolute melting point of the alloy [3].

Throughout history, superalloys have been developed for applications where efficiency improves with the temperature increase, including industries such as material processing, petrochemical engineering, and power generation. Some of these applications require not only good mechanical properties at high temperatures but also oxidation and corrosion resistance to operate in harsh environments [16].

In the early 20th century, Fe-based stainless steels emerged to fulfilled both purposes, but their strength was limited at temperatures exceeding about 600˚C. Further alloying, particularly the change to Ni-based systems, led to the development of superalloys, fulfilling the strength needs and oxidation resistance at high temperatures [17]. More recent advances in superalloy capabilities have been largely associated with advances in manufacturing processes (directional solidification, single crystals) and post-processes (heat treatments). The manufacturing process affects the grain size, grain morphology, type, and distribution of secondary phases in the matrix.

The base crystal structure of superalloys is face-centered cubic (FCC), generically referred to as austenite or γ, which can be strengthened by solid-solution hardening and/or precipitation hardening. Among the secondary phases, the most common ones are γ' (Ni_3(Al,Ti)) ,γ" (Ni_3(Nb, Al, Ti)), and metal carbides. The superalloy systems include nickel-, iron-nickel-, and cobalt-based.

The benefits of nickel as a base metal for high-temperature superalloys are numerous. Nickel has a face-centered cubic (FCC) structure providing ductility and toughness to the matrix. The FCC Ni structure also has a low rate of thermally-activated processes as required in creep and diffusion, which contributes to the microstructure stability at high temperatures. Furthermore, Ni also keeps the same FCC structure from room temperature up to the melting point, thus providing stability since contractions and expansions due to allotropic phase transformation are avoided [16]. Alloying elements that complete the nickel-based superalloys system are around a dozen; most of them are transition metals from the d block. The partitioning of alloying elements is influenced strongly by thermodynamic driving forces. Elements like Cr, Mo, Re and Co partition preferentially to the γ structure, which contributes to the solid-solution strengthening. By contrast, elements like Al, Ti, Nb, and Ta promote the formation of order-strengthening phases (γ' and γ")[16]. Other elements, such as W and Ru, do not partition preferentially to γ/γ'.

2.1.2 Alloy 625

The first patent of Alloy 625 was issued in 1962 [18] after research on the basic Ni-Cr-Mo-Nb alloy system under the register named Inconel 625. The target application that drove the development of this alloy was a steam-line for supercritical steam power plants; therefore, the

alloy needed good weldability and high creep resistance [19]. Alloy 625 is essentially a solid solution strengthened alloy; however, under defined conditions, it precipitates γ". Table 2-1 shows the nominal composition of Alloy 625. Additions of Cr, Mo and Nb increase the room-temperature strength by solid-solution strengthening, while mainly Nb improves creep strength. A low level of Al+Ti enhances weldability and brazeability. Limited amounts of C, Si, and N serve to improve intermediate temperature low cycle fatigue. Regarding corrosion resistance, Ni improves the resistance to stress-corrosion cracking in acids (except for nitric acid) and reducing environments, Cr improves resistance to oxidizing conditions, and Mo enhances pitting resistance.

Table 2-1. Chemical composition of alloy 625 [20]

Element	Weight %
Ni	58.0 min.
Cr	20.0-23.0
Fe	5.0 max
Mo	8.0-10.0
Nb + Ta	3.15-4.15
Mn	0.50 max.
Si	0.50 max.
Al	0.40 max.
Ti	0.40 max.
C	0.10 max.

Alloy 625 applications benefit from the combination of high strength, resistance to pitting, stress-corrosion cracking, good fatigue resistance, and outstanding weldability. In addition, Alloy 625 operates over a wide temperature range, from cryogenic to high temperatures (900°C). Alloy 625 usages include steam-lines, aerospace applications (rocket nozzles, aircraft ducting systems, turbine seals), nuclear applications, navy and marine use (submarine

components), chemical processing (reaction vessels, distillation columns, valves), dissimilar welding [19] [21].

2.1.2.1 Physical Metallurgy of Alloy 625

Gamma phase (γ): The FCC structure of nickel provides an alloy matrix with ductility and toughness. As already stated, Nickel keeps the same structure from room temperature up to the melting point, which provides stability since contractions and expansions due to allotropic phase transformation are avoided [2]. Also, the structure presents a low rate of thermally activated processes as required in creep and diffusion, which contributes to the microstructure stability at high temperatures.

Gamma double prime (γ") and delta phase (δ): γ" is a metastable phase with a BCT crystal structure and a base stoichiometry of Ni_3Nb. The morphology of γ" precipitates is disc-shaped or platelet, as characterized using dark-field transmission electron microcopy since the thickness is in the order of tenths of a nanometer. γ" precipitates have at least partial coherency with the matrix, with a coherence strain of ~2.9% [17][17], which means that the particles provide resistance to dislocation slip, but eventually dislocations cuts through them. γ" precipitates are usually uniformly distributed; however, the Nb local supply determines γ" denuded zones. These γ" denuded zones generally surround high Nb-containing phases as NbC, laves phase, or δ phase, where the Nb-content is depleted by the formation of these phases and retards the γ" formation. The impact of γ" denuded zones at grain boundaries has been related to loss of corrosion resistance and reduced mechanical properties [20].

The metastable γ" will eventually transition to stable δ phase formation (see TTT diagram in Figure 2-1). The δ phase has an orthorhombic crystal structure with the same base stoichiometry as γ", Ni_3Nb, but is incoherent with the γ-Ni matrix. As a consequence,

dislocations cannot cut through the δ precipitates, and instead, they bend and loop around the precipitates (Orowan mechanism).

Intergranular δ precipitates usually are plate-like shape, while globular precipitates are primarily intergranular [22]. However, heat treatments and deformation strain lead to morphological evolution. For example, deformation at large strain causes dissolution and fragmentation of needlelike δ precipitates; with the latter spheroidizing, leading to blocky/globular morphologies [23] [24]. In the range 650°C to 700°C (~1200-1300°F), δ precipitates along grain boundaries, where the γ" supplied the Nb. In the range, 840°C to 950°C (~1540-1740°F), needlelike or platelet precipitates form inter and intragranularly at short times directly from the austenite (<24h)[16]. Above about 1100°C (1200°F) for 24 hours, according to the TTT diagram, the δ phase dissolves completely.

Morphology, size, amount, and distribution of δ precipitates determine if it is detrimental or beneficial to mechanical properties. The beneficial effect is reported for a limited amount of intergranular δ spheroidized precipitates, which provide grain size control and grain refinement [25] [26]; δ precipitates prevent grain growth through a pinning effect. Detrimental effects are attributed to excessive amounts of intragranular δ platelets or acicular precipitates, which lead to early cracking, loss of ductility [27], and brittle fracture. Besides, prolonged aging causes coarsening of incoherent precipitates, reducing the strengthening process effectiveness and lowering ductility.

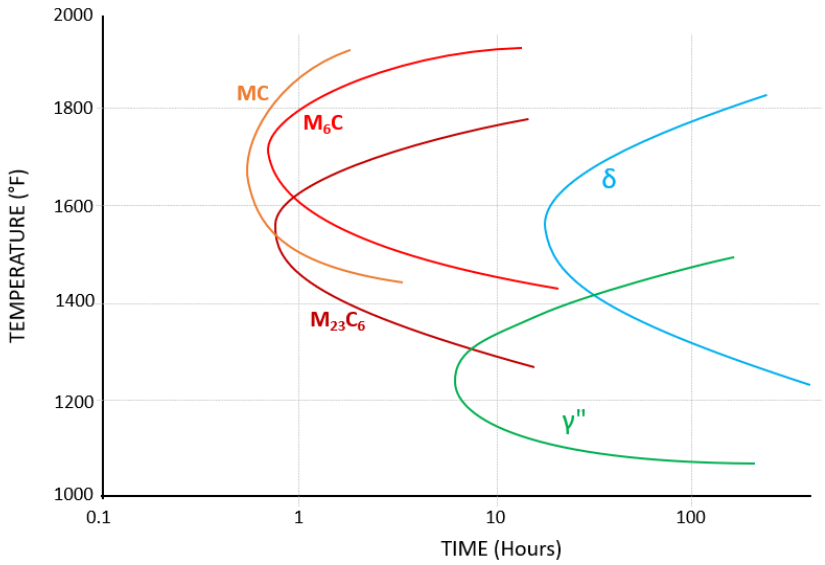

Figure 2-1. Approximate Temperature-Time-Transformation diagram of alloy 625 [20]

Carbides ($M_{23}C_6$, M_6C, MC): Fine carbides in the gamma matrix strengthen it, while carbides at grain boundaries have a grain-pinning effect that restricts grain growth [17][16]. The more beneficial are the $M_{23}C_6$ carbides, where the cell size is three times bigger than the gamma matrix.

A TTT diagram shows the occurrence of carbide precipitation after thermal exposures at times of 0.1 to 100 hours: MC carbides form at high temperature (1038 °C); M_6C formation is favored at intermediate temperature (816 to 982 °C); and $M_{23}C_6$ form at a lower temperature (790°C to 816°C)[16]. MC carbides form in different morphologies that depend on the manufacturing process: large cube-shaped in wrought and small discrete particles at high cooling rates during casting.

Regarding M_6C carbides, they can have Cr, Si, and N in solution. M_6C can be present in different morphologies: discrete particles, platelets/acicular shapes, and a grain-boundary network. Wrought alloys show that M_6C carbides control the grain size during alloy processing. Additionally, the decomposition of M_6C carbides results in the $M_{23}C_6$ formation. $M_{23}C_6$

precipitation from this reaction is favorable along the grain boundaries, enhancing creep resistance [28].

$$M_6C + M' \rightarrow M_{23}C_6 + M'' \quad \textbf{(2-1)}$$

Discrete $M_{23}C_6$ carbides along the grain boundaries are the most suitable, but in less proportion; some locate at twin boundaries and intragranularly. Usually, M is entirely chromium. $M_{23}C_6$ carbides improve creep resistance by preventing grain-boundary sliding [17].

Although carbides strengthen the alloy, some detrimental effects are reported in some instances. For example, Alloy 625 wrought can present bands of carbides [20] and acicular M_6C [17] that contribute to ductility loss. Also, carbides affect the fracture mode, promoting intergranular fracture [29].

Minor phases (TiN, TCP Phases): Minor phases in Ni-based alloys are not intentionally precipitated since they are not beneficial for the strengthening or incrementing temperature capabilities [30]. Topologically close-packed (TCP) phases are complex crystal structures with a high density of atoms. Stoichiometry of TCP is A_xB_y, where A and B are transition metals. Most of the TCP phases have a morphology of plate-like or needlelike. Alloying transition elements with BCC crystal structure (Nb, Cr, Mo) promote TCP formation. They frequently appear when solute segregation increases, where they decrease strength and ductility.

The Laves phase has a stoichiometry of A_2B (e.g., Fe_2Ti, Fe_2Nb, Fe_2Mo). Usually, Laves phase particles are irregular shaped or globular and are enriched in Nb, Mo, and Si contrasted with the nominal composition. The Laves phase is a final solidification product, which is promoted by Nb, Mo, Si, Fe, and Ti. An excessive amount of Laves phase decreases ductility, fatigue, and creep resistance [20].

Additional observed minor phases include carbonitrides, which are spheroidal particles composed of TiN, or a solid solution of TiN and TiC.

Table 2-2. Summary of phases presented in alloy 625

Phase Name	**Phase Symbol**	**Pearson Symbol**	**Struktur bericht symbol** [31]	**Formula**	**Lattice Parameter (nm)** [17]
Gamma	γ	FCC	$A1$	$Ni-Cr-Fe$	$a_0 = 0.3616$
Gamma Double Prime	γ"	Ordered BCT	$D0_{22}$	$Ni_3(Nb, Al, Ti)$	$a_0 = 0.3624$ $c_0 = 0.7406$
Carbides	MC	Cubic	$B1$	$(\mathrm{Ti, Nb, Mo})\mathrm{C}$	$a_0 = 0.430 - 0.470$
	$M_{23}C_6$	FCC	$D8_4$	$(\mathrm{Cr, Fe, Mo})_{23}\mathrm{C}_6$	$a_0 = 1.050 - 1.070$ (varies with composition)
	M_6C	FCC	$E9_3$	$(Ni, Co)_4\,(Mo, W)_2C$	$a_0 = 1.085 - 1.175$
Delta	δ	Orthorhombic	$D0a$	Ni_3Nb	$a_0 = 0.5106 - 0.511$ $b_0 = 0.421 - 0.4251$ $c_0 = 0.4532 - 0.4556$
Laves	-	Hexagonal	C_{14}	$(Fe, Cr, Mn, Si)_2(Nb, Ti, Mo)$	$a_0 = 0.475 - 0.495$ $c_0 = 0.770 - 0.815$

2.1.3 Solidification Behavior of Alloy 625

2.1.3.1 Solidification Mode and Constitutional Supercooling

Alloys solidify in a range of temperatures (from liquidus to solidus). During the solidification, the solute redistribution is quantified by the partition coefficient. The partition or distribution coefficient, k, is defined as the ratio of solidus and liquidus concentration (C_s/C_l). In Alloy 625, the as-solidified values of k coefficients for C, Si, and Nb are 0.21, 0.57, and 0.54,

respectively [32]. Since values are smaller than unity, it means that these elements, as a solute, accommodate preferentially in the liquid than in the solid during the solidification.

Simplified solidification calculus for alloy 615 takes Ni as the matrix and Nb as the solute. Nb traceability is crucial since it is involved in the precipitation of solidification products, strengthening, and detrimental phases. Convenient simplification includes that the solidification process involves no solid diffusion and limited liquid diffusion of the solute. The Nb, as a solute, is rejected by the solid, forming an Nb-rich boundary layer ahead of the growth front [33]. Since the liquid diffusion is limited, Nb distribution in the liquid is not homogeneous. Solute concentration changes the chemical composition locally and consequently the solidus temperature. The solute-concentrated liquid reduces the solidification temperature below the actual temperature, where the liquid at the interface is defined as constitutionally supercooled.

Figure 2-2 illustrates how the rejected solute forms the rich boundary layer. As indicated in this figure, the maximum solute concentration in the liquid is C_0/k, and the maximum depletion in the solid is $k \cdot C_o$, where C_0 is the overall composition. The solute redistribution is slightly different if convection is included; the solute segregation follows the same behavior but is higher- i.e., the liquid enriches higher than C_0 in all the extensions (see orange dashed line in Figure 2-2).

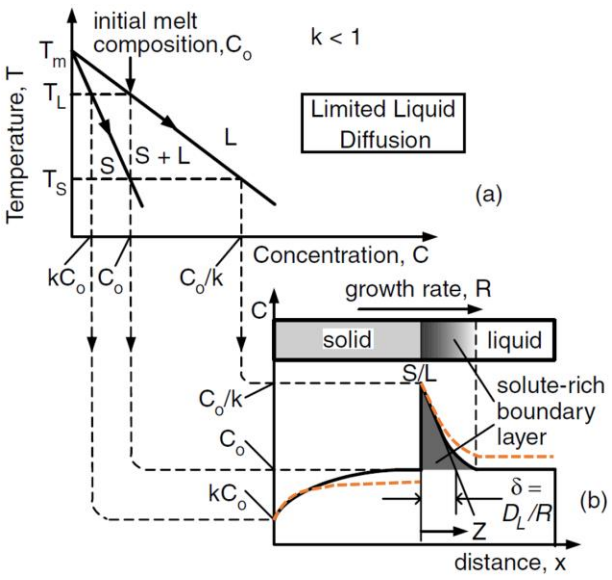

Figure 2-2. Solute redistribution during solidification with limited diffusion in liquid and no diffusion in solid (Dashed orange line makes the case of convection included): (a) phase diagram, (b) composition profile in solid and liquid. [33]

The solute distribution during solidification drives to a geometric instability at the liquid-solid interface. As a result of the liquid stability, the planar interface occurs when the liquid exists above the liquidus temperature (Figure 2-3). When the actual temperature is below the liquidus, solid and liquid coexist. Then, the extent of constitutional supercooling defines the solid-liquid interface or so-called solidification mode: cellular, columnar dendritic, and equiaxed dendritic (Figure 2-3). According to the constitutional supercooling theory, the criterion to stable a planar interface and avoid constitutional supercooling is

$$\frac{G}{R} \geq \frac{\Delta T}{D_L} \qquad \textbf{(2-2)}$$

where G is the temperature variation per longitude throughout the solid/liquid interface, R is solidification rate, D_L is the solute diffusion in the liquid, and ΔT is the thermal gradient in the interface. The planar growth criterion shows that the G/R ratio determines the supercooling extent and consequently the solidification mode. Additionally, the product $G \cdot R$, defined as the

cooling rate, determines the solidification structure size [33]. The higher the cooling rate, the finer the solidification structures.

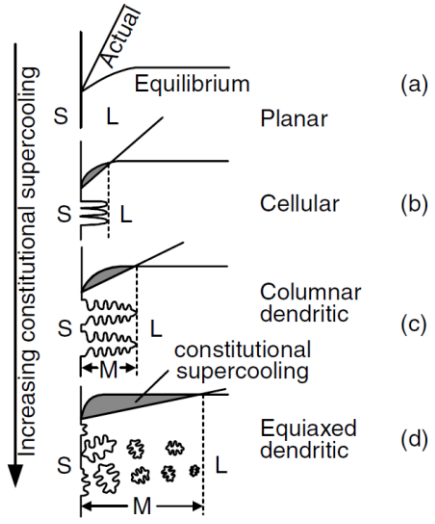

Figure 2-3. Effect of the constitutional supercooling on the solid-liquid interface morphology [33]

2.1.3.2 Solidification Path for Ni-Nb-C Alloys

The alloy chemistry variations affect the solidification rate and final microstructure, with Nb and C having the highest impact for Alloy 625 [34]. The solidification path for 625 is similar to a ternary system Ni-Nb-C; thereby, the liquidus projection of the ternary system is depicted in an Nb-C plane (Figure 2-4).

The solidification path for the intermediate C/Nb ratio will be explained in the following. In the beginning, just above the liquidus temperature, the liquid phase fraction is unity (f_L=1). Then γ forms from the liquid ($L \rightarrow \gamma$), while the liquid changes the composition following the reaction line. Liquid enriches gradually in Nb and C until it reaches the two-fold saturation that separates gamma and NbC. Then, NbC formation occurs from the liquid, while the liquid composition follows the representation line of the first "eutectic-like reaction" ($L \rightarrow \gamma + NbC$). At this point, liquid gets depleted from C, and NbC formation stops. Liquid composition

progresses to the second eutectic-like reaction ($L \rightarrow \gamma + Laves$), resulting in Laves phase formation. The solidification path finishes when the liquid phase fraction is zero (f_L =0). The final microstructure contains spatially separate formation of two products: NbC and laves phase [35].

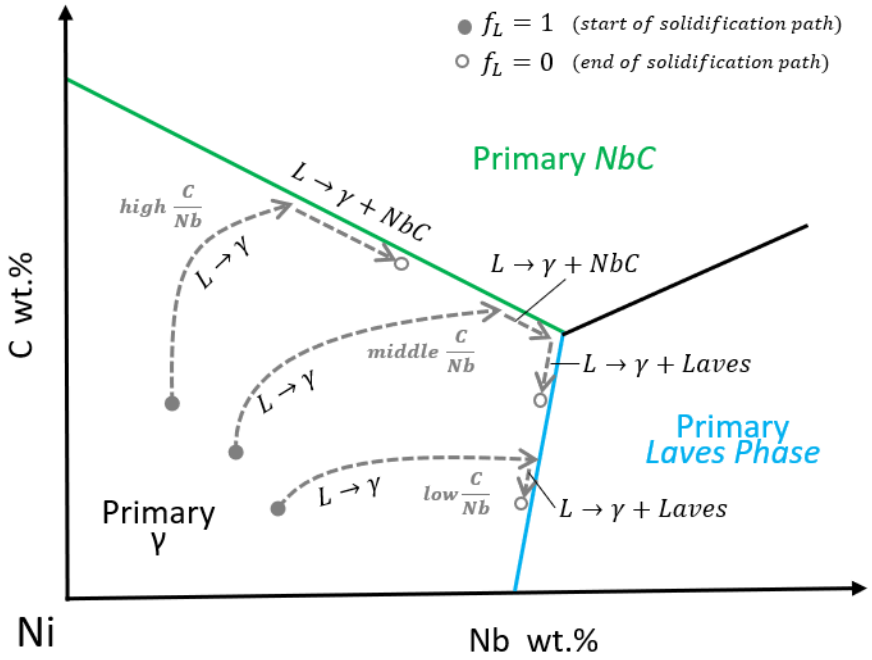

Figure 2-4. Scheme of solidification paths over a liquidus projection for the Ni-Nb-C system (based on [20]**,**[35]**,** [33]**)**

Figure 2-4 also presents the solidification paths at different C/Nb ratios, which defines the final solidification products. At a high C/Nb ratio, carbon content promotes the NbC formation and avoids the Laves phase formation, being γ and NbC the solidification products. In contrast, at a low C/Nb ratio, solidification leads to gamma and Laves phase formation, avoiding NbC formation [20][20].

During welding, reduction of Nb, Mo, Si, Fe, and Ti decreases the solidification range (Nb has the greatest extent), which reduces the segregation during the solidification. In turn,

segregation reduction lowers the Laves phase formation and minimizes hot cracking observed in welding.

2.1.3.3 Effect of the Cooling Rate on Refractories Segregation

Cooling rate affects the liquid → solid transformation rate and hence the segregation. Wang et al. [36] studied the microstructure of IN718, after remelting, using different cooling systems: furnace cooling (1 °C/min), quenching (3 °C/min), and saltwater (6 °C/min). Their results showed that the lower the cooling rate, the lower the transformation rate, leaving time for element diffusion in liquid and crystal growth. The Nb and Mo contents increase in the residual liquid with decreasing cooling rate (Figure 2-5). In agreement with previous studies, local Nb enrichment changes the phase transformation during solidification. According to a thermodynamic simulation using the software package ThermoCalc, the Laves phase, and δ phase precipitate from the liquid enriched in Nb and Mo [36].

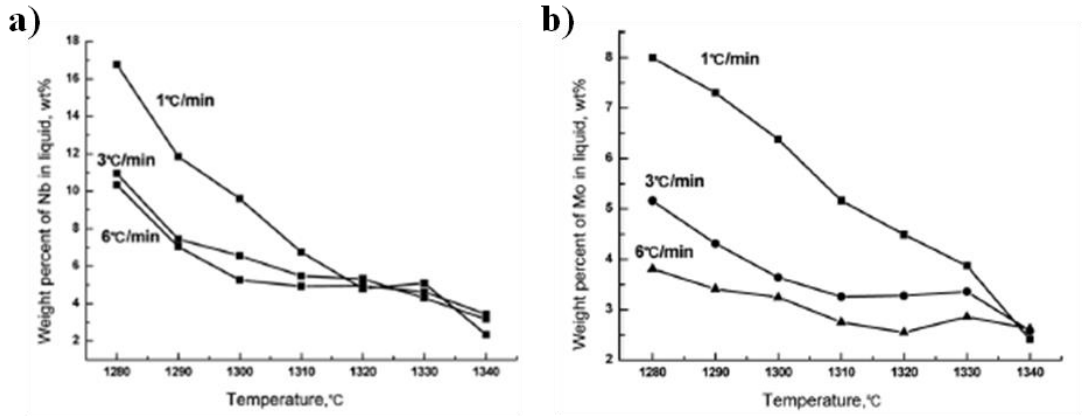

Figure 2-5. a) Nb and b) Mo content in residual liquid as a function of temperature for different cooling rates [36]

2.2 Additive Manufacturing of Ni-based Alloys

2.2.1 Additive Manufacturing Overview

Additive manufacturing (AM) is a set of fabrication techniques where the material structure is built layer-by-layer based on computer-aided design [37]. AM has numerous advantages that distinguishes it from conventional manufacturing, the most important being: 1) freedom of design; 2) sustainability benefits; and 3) manufacture of hard-to-machine materials. Regarding the freedom of design, AM eliminates some of the limitations of conventional manufacturing, allowing high geometric complexity so that designers can focus more on functionality. Freedom of design enables the production of lightweight components with reduced assembly, tooling, etc. One of the successful cases is the fuel nozzle in General Electric's LEAP Engine, which decreases its weight by 25% compared to the original nozzle by only simplifying assembly without changing the design [1]. Another successful example is plastic injection molding redesign, seeking an improvement in a cooling system [38]. Salcomp, a company of electrical plugs and power supplies for mobile phones, redesign the cooling system of the plastic injection molds based on the capabilities of AM processes. This results in a reduction of the time production and improving the quality of the components after making the heat dissipation quicker [1], [38]. AM offers the possibility to design intricate geometries, multiple cooling channels, and thinner walls that are not possible with conventional manufacturing methods. A better cooling system reduces the production time and improves the quality of the plastic components made. Regarding sustainability benefits, AM has the potential to extend the product life through repair and remanufacture. Additionally, AM use reduces the production chain due to the minimization of machining and assemblies.

AM technologies are classified into seven categories, regardless of the material manufactured: direct energy deposition; powder bed fusion; binder jetting; material extrusion; material jetting; sheet lamination; and vat photo-polymerization according to the ASTM F2792 [37]. The first two categories are the most widely used for metals.

2.2.1.1 Direct Energy Deposition

Direct Energy deposition is the process where the focused thermal energy melts the metal while it is deposited [37]. Laser cladding is the commercial name of a DED when the thermal energy source is a laser beam; it could be wire or powder fed. An schematic of the process is shown inFigure 2-6. In a coaxial nozzle, the powder is fed using an inert carrier gas coaxially with respect to the laser beam. These nozzles usually include external shielding gas to avoid oxidation during the process. During the process, a clad track is formed when the laser beam focus point coincides with the fed powder, creating a melt pool in a junction with the substrate. A CNC (Computer Numerical Control) or robot is programmed to move the nozzle and generate the cladding path according to the CAD file of the part.

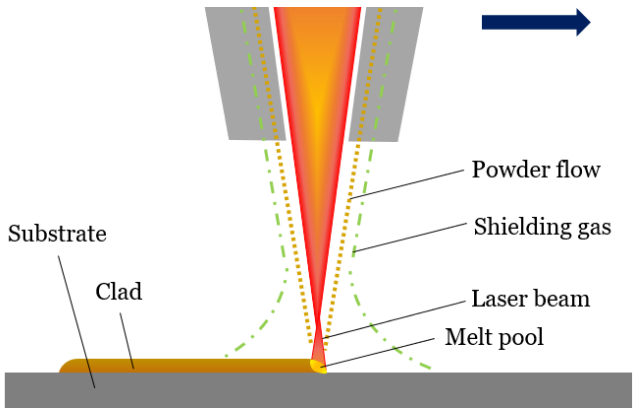

Figure 2-6. Scheme of DED process with a coaxial nozzle

2.2.1.2 Laser Powder Bed Fusion

Laser powder bed fusion (LPBF) equipment has four systems: mechanic; optic; electric; and pneumatic. Figure 2-7 shows an schematic of the LPBF process. The optic system includes the laser beam, a galvanic mirror arrangement, a collimator, and a beam expander. The pneumatic system controls the inert gas flow rate. Finally, the mechanical system includes the recoater blade mechanism and platform movements. LPBF systems have a dispenser platform as a powder reservoir, a building platform where the substrate is located, and a collector platform, which stores the remained powder after raking.

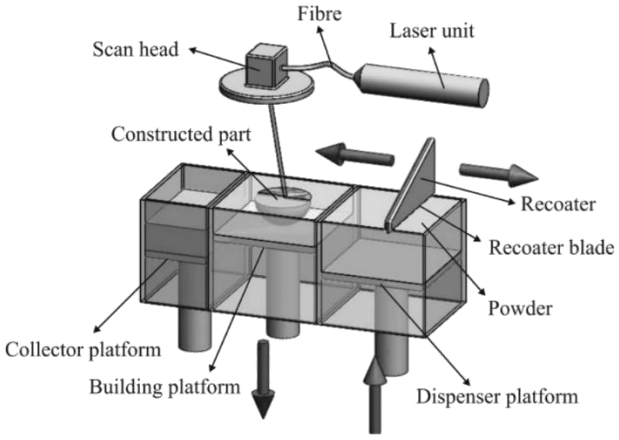

Figure 2-7. Scheme of the LPBF process [39]

The process cycle is described below. First, the dispenser platform rises a layer thickness up. Then the recoater blade spreads the powder from the dispenser platform to the building platform, where the remaining powder falls to the collector platform. After that, the laser selectively melts the powder bed according to the laser pattern programmed. After the laser switch-off, the building platform lowers down, and the dispenser platform rises, while the recoater blade returns to its initial position. Then the new layer is spread, melted, and so on. This process cycle repeats layer-by-layer until the component fabrication had finished.

2.1.1. Laser-material Interactions

2.1.1.1. Laser-assisted AM Solidification in a Single Bead

The energy input by the laser is mainly absorbed by the powder and the substrate forming the melt pool. Melt pool shape depends on the laser parameters, but it is usually elongated. Some energy loss occurs by convection through the shielding gas and radiation, but the main heat extraction is through the substrate; hence, the solidification in a clad occurs mainly from bottom to top. In the beginning, epitaxial growth from the substrate takes place. Then, the crystallographic orientation of the solidified structures depends on the competitive growth among the preferential orientation for cubic structures <001>, the thermal gradient direction (G), and the substrate or previous layer (epitaxial growth)[33].

As previously mentioned, the solidification depends on the G/R ratio, and both G and R change locally along with the melt pool. Concerning the growth rate in the melt pool, an approximation is $R = V \cos \alpha$, where α is the angle between the laser velocity (V) vector and the growth direction of a dendrite. This expression assumes that the difference between the dendrite direction growth and the normal to the molten pool boundary at the same point is negligible. Therefore, the minimum R is at the fusion line, while the maximum R is at the top of the melt pool (Figure 2-8).

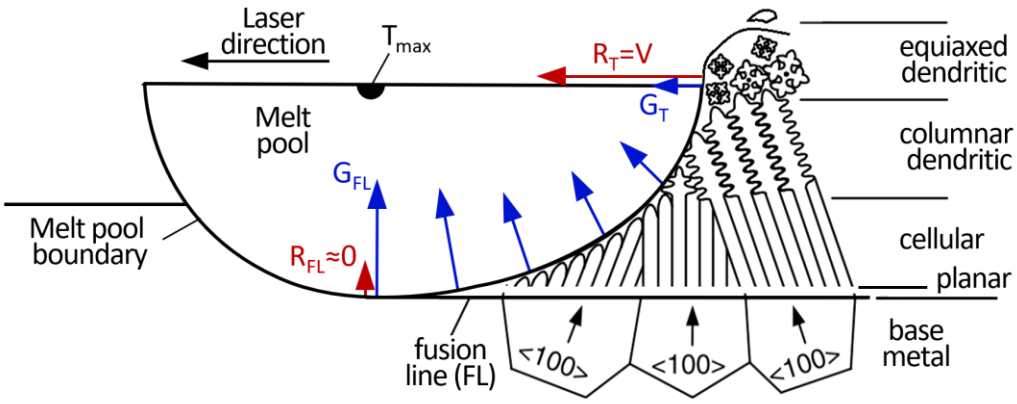

Figure 2-8. Variations in G, R along pool boundary, and a subsequent variation in solidification mode in a bead cross-section (adapted from [33]**).**

On the other hand, G is defined by the thermal difference over the distance of the mushy zone (the region where liquid and solid coexist). Therefore, G becomes smaller with decreasing the distance between the T_{max} point and the melt-pool boundary. Due to the elongated shape of the melt pool, the distance between the bottom fusion line and the T_{max} point is the shortest; consequently, G is the longest at this point. Summarizing, the scheme in Figure 2-8 illustrates the G/R reduction (constitutional supercooling increase) from the bottom to the top of a bead and the consequent morphology evolution as a result of G and R variation throughout the molten pool.

Huang et al. [40] reported the morphology evolution in single beads of Alloy 625 made by DED at different laser speeds. Their results are summarized in Figure 2-9, which shows from bead cross-sections that bigger deposits are obtained at lower laser speed, hence higher energy input. The lowest laser speed sample shows a clear and distinguishable separation between the morphological regions (Figure 2-9c, d). The bottom region is composed predominantly of columnar-dendritic structures without secondary arms. In the middle or transition region, the columnar dendritic structures exhibit secondary arms. Finally, the top region shows finer equiaxed dendrites.

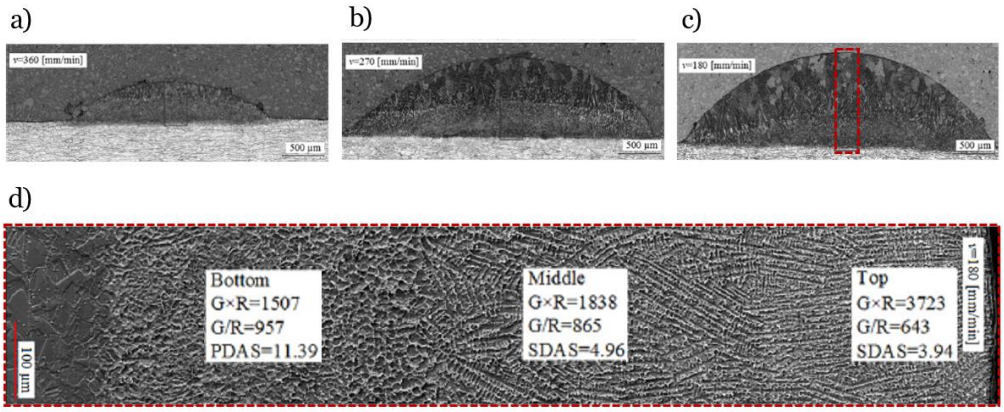

Figure 2-9. Single beads cross-sections at different laser speed: a) 360 mm/min, b) 270 mm/min, c) 180 mm/min, d) high magnification view along the clad height for the red square marked at 180 mm/min [40]**.**

The same regions in other samples exhibited different structure sizes depending on laser speed (i.e., energy input); the higher the energy input, the slower the cooling rate, hence the larger the primary and secondary arm spacings.

Figure 2-10 shows an experimental example of the evolution of the morphology in a wall of Ti6Al4V made by DED [41]. A single bead cross-section shows how the top center of the melt pool is formed by equiaxed grains, and columnar grains constitute the bottom melt pool (Figure 2-10a). Assuming that the laser direction and other laser parameters are kept constant, a wall construction (multi-beads, one build over another) results in two microstructures depending on the dilution (remelting) of the previous layer. The first case comes when the depth of the molten pool is enough to remelt the equiaxed top part; it results in a complete columnar epitaxial grain structure (Figure 2-10d). The schematic in Figure 2-10b shows how the top layer still has the equiaxed region on the surface and how the remelting of the previous layer is nearly half of it. The second microstructure is referred to as a "bamboo-like" grain morphology, in which layers of equiaxed grains are alternate with columnar grains in the building direction (Figure

2-10c). In this case, the dilution is enough to keep good bonding between layers but not enough to remelt the equiaxed grains at the top of the layer.

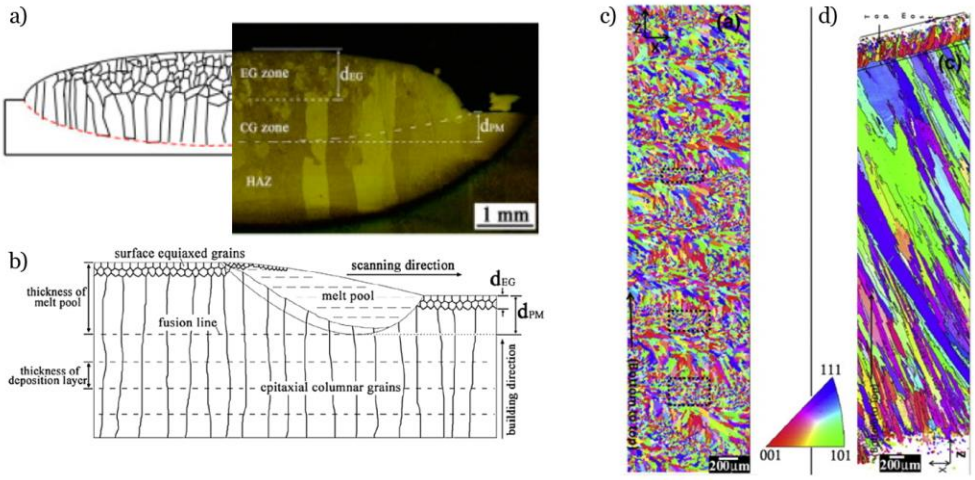

Figure 2-10. a) Cross-section of a Ti6Al4V bead made by DED (deposition rate:25g/min), b) Schematic illustration of large columnar grains [41]**. EBSD of IN718 made by DED: c) "Bamboo-like" morphology, d) columnar grains due to high power scanning** [42]**.**

2.1.1.2. Processing Thermocycles on AM Microstructure

The thermal condition for an AM component during its building is continuously changing. For an LPBF process, the temperature increases when the laser exposes the powder bed (melting). Then, the temperature decreases while the recoater blade spreads the powder for a new layer (solidification and cooling of the system). This thermocycle repeats when a new layer is built, but the new initial temperature is higher than the previous layer's initial temperature. Dunbar et al. [43] reported the temperature increment of the substrate (underside) during the building process (Figure 2-11a). The temperature variations in the same conditions are attributed to excess build height due to the geometrical distortion. According to the authors, during the melting, the layer suffers an expansion causing a bowing up in the center of the sample (Figure 2-11b-ii); then, during the cooling in the solidification, the contraction causes a bowing down

(Figure 2-11b-iii). At the end of each cycle, the distortion is not compensated, leaving a contraction distortion. During the powder spreading, the bowing down region has a greater mass than normal, which causes an excess of deposit and subsequent excess of building height. Mass excess affects the dimensional accuracy of the final part but also can disrupt the process suddenly due to a crush of a building part with the recoater. Moreover, distortion and stress concentration on the final part may end up with other mesostructural defects as warping and delamination [44].

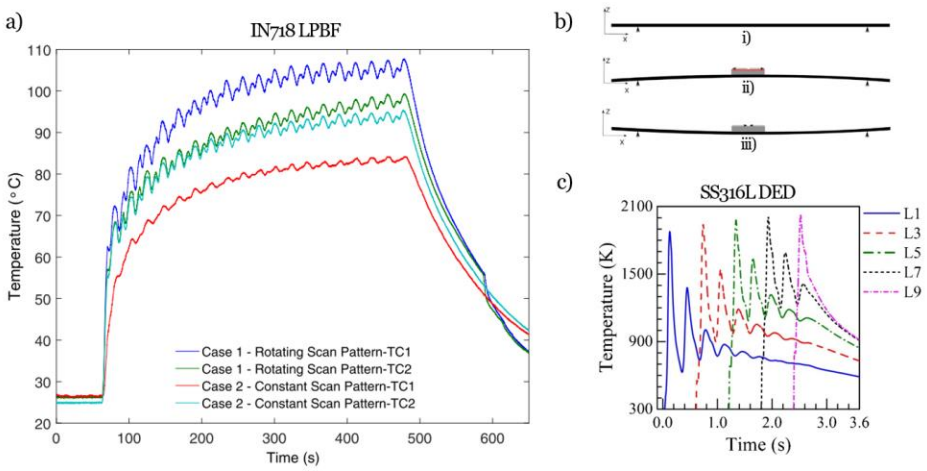

Figure 2-11. a) In situ temperature during the building process of IN718 made by LPBF [43]**, b) Scheme of the distortion during LPBF: i) powder spread, ii) expansion in laser melting, iii) compression during the solidification and cooling of the system** [43]**. c) Thermocycles monitoring at mid-length and mid-height of each layer in SS316L made by DED** [45]**.**

Manvatkar et al. [45] reported the thermal profile variation in a wall of SS316L made by DED. A continuous increase in size and the overall temperature of the melt pool with continued layer-by-layer build was reported Figure 2-11c shows the thermal cycles of the alternate layers. The first peak corresponds to when the laser locates above the monitoring location, and the consecutive peaks correspond to the upper layer depositions. According to this, the top layer (L9) involves just the first peak since no upper layers exist, and the first layer involves the highest

number of peaks. Furthermore, the temperature of the first peak in a layer increases with the height increase as the heat dissipation is reduced through the substrate. Thus, each layer exhibits a different thermal history throughout the building, which results in heterogeneous microstructure and subsequent heterogeneous mechanical properties in the final part.

Tian et al. [46] reported a heterogeneous microstructure and hardness throughout an Inconel 718 wall fabricated by DED. Highlights of their results are shown in Figure 2-12. Since the first deposited layers keep at a high temperature for longer than the top ones, it indicates that the first layers suffer a heat treatment during the building process that the top ones are not experiencing. As a result, top layers show a primary solidification of Inconel 718, high refractory segregation, and a formation of Laves phase (Figure 2-12ii-a); in the middle layers, the Nb diffusion toward the matrix takes place; while finally, the first deposited layers show nucleation and growth of γ" precipitates starting in the Nb enrichment regions. The heterogeneous microstructure throughout the sample impacted the hardness; the higher the amount and size of γ" precipitates, the higher the strengthening of the alloy. Thus, a hardness map shows a gradient increasing from bottom to top where the bottom has the higher exposure time to nucleate and grow the maximum γ" precipitates throughout the part.

Summarizing, multiple thermocycles, typical of the AM process, promote a different microstructural evolution throughout the sample during the process.

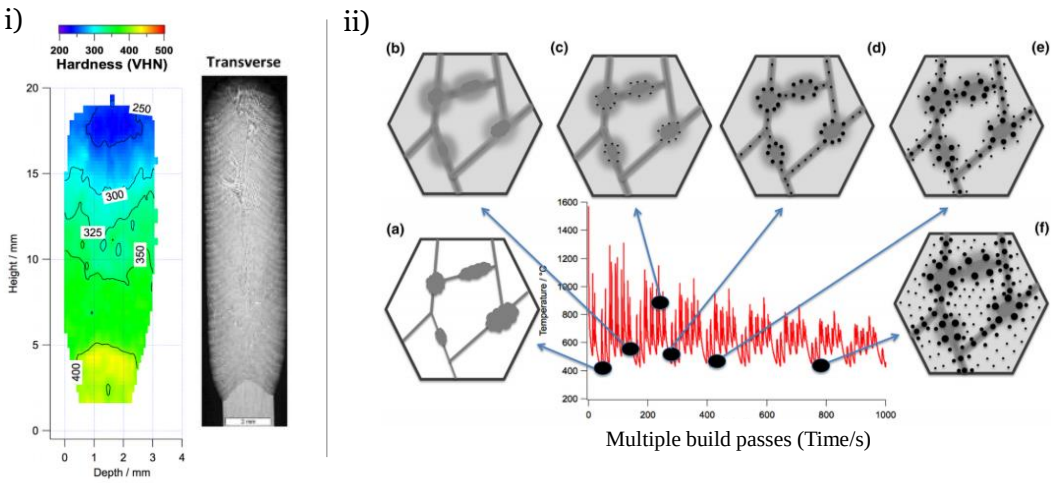

Figure 2-12. Inconel 718 wall fabricated by DED. i) Hardness map and optical micrograph of the wall cross-section. ii) Microstructure evolution during the DED process as a function of multiple build passes: a.) Primary solidification, b.) Remelting of eutectic products and diffusion of Nb, c. & d.) γ'' precipitation during subsequent cycles, e.) Growth of existing precipitates and more γ'' precipitation after more thermal cycles, f.) The onset of nanoscale precipitation within the dendrite core after many thermal cycles [46]**.**

2.3 High-temperature Oxidation of Ni-based Alloys

2.1.2. Fundamentals of High-temperature Oxidation of Metals

Oxidation takes place when a metal reacts with oxygen in the atmosphere to form an oxide. In the majority of cases, the oxide is a solid, and it develops on the metal surface as a scale. The oxide scale properties determine its protectiveness; the ideal scale is slow-growing, continuous, dense (non-porous), highly stable, and shows a good adherence with the metallic substrate. Alumina and chromia are the most used oxides scales in industrial applications at high temperatures.

From the fundamental aspects, thermodynamics dictate if the oxidation reaction is feasible, while kinetics dictate the rate at which it will be.

2.1.2.1. Thermodynamics

Reviewing the oxidation of pure metals helps to understand more complex systems. General oxidation of a metal reaction is written as follows:

$$\frac{2x}{y}M + O_2 \rightarrow \frac{2}{y}M_xO_y \qquad \textbf{(2-3)}$$

At equilibrium, the law of mass action for the oxidation reaction (1) given above is described below,

$$K_2 = \frac{a_{M_xO_y}^{2/y}}{a_M^{2x/y}a_{O_2}} = \frac{1}{P_{O_2}} \qquad \textbf{(2-4)}$$

where K_2 is the temperature-dependent equilibrium constant, and a_i is the thermodynamic activity of the species i. The activity for the solid species (i.e., metal and its oxide) is assumed to

be one, while activity for the oxygen is approximated as its partial pressure. Thermodynamically, the Gibbs free energy (ΔG) determines the favorability of a given reaction. The following equation describes the Gibbs free energy under constant pressure,

$$\Delta G = \Delta G° + RT \ln K_1 \quad \textbf{(2-5)}$$

where $\Delta G°$ is the standard Gibbs free energy of formation of the oxide, R is the ideal gas constant, and T is the temperature. If ΔG is negative, the reaction is spontaneous; if ΔG is positive, the reaction is non-spontaneous; if $\Delta G = 0$, the reaction is at equilibrium where the forward and reverse reaction rates are the same. Thus, at equilibrium:

$$\Delta G° = -RT \ln K_1 = -RT \ln P_{O_2} \quad \textbf{(2-6)}$$

$$P_{O_2}^{diss} = \exp\left(\frac{\Delta G°}{RT}\right) \quad ; \quad \Delta G° = \Delta H° - T\Delta S° \quad \textbf{(2-7)}$$

The oxygen partial pressure at equilibrium is called the dissociation pressure of the oxide ($P_{O_2}^{diss}$); when the partial pressure is higher than $P_{O_2}^{diss}$, the metal oxide M_xO_y is likely to form. $\Delta G°$ can be calculated with tabulated data of the standard enthalpy of reaction ($\Delta H°$) and standard entropy change ($\Delta S°$), where $\Delta G°$ has a linear behavior as a function of temperature. The Ellingham diagram summarizes the $\Delta G°$ as a function of temperature (T) for several oxidation reactions, allowing a comparison of metal thermodynamic stabilities. The lower the position of the line on the diagram (see Figure 2-13), the more negative $\Delta G°$, the higher the stability of the oxide.

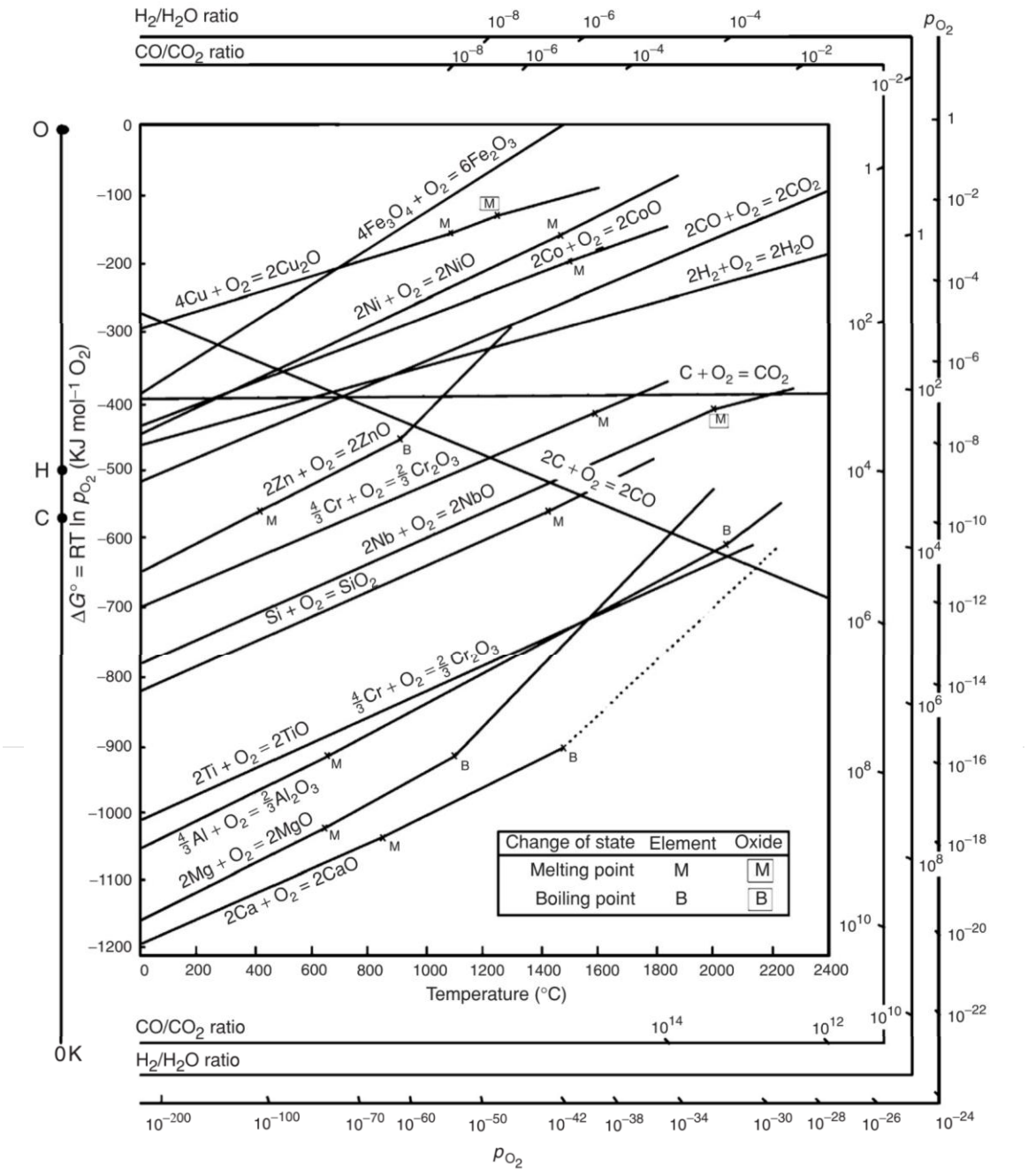

Figure 2-13. Ellingham diagram: standard free energy of formation of selected oxides as a function of temperature [47].

2.1.2.2. Oxidation Kinetics and Mechanisms

Kinetics determines the rate of oxide-scale thickening during oxidation and hence the weight gain due to oxygen uptake and the extent of metal consumption. Weight gain can be quantified directly $\Delta W(mg\ cm^{-2})$ or it can be calculated from the oxide scale thickness $x(cm)$, both measurements are related by

$$x = \frac{V_{ox}}{yM_o}\Delta W \qquad \textbf{(2-8)}$$

where V_{ox} is the molar volume of the oxide, y is dictated by the stoichiometry of M_xO_y, and M_o is the atomic weight of oxygen. On the other hand, the metal consumption can be estimated using the weight gain with the following expression

$$X = \frac{V_m}{\gamma M_o}\Delta W\ ;\ \ \gamma = \frac{x}{y}\ for\ M_xO_y \qquad \textbf{(2-9)}$$

Oxidation rates of metals may follow linear, logarithmic, and parabolic kinetics laws.

Parabolic rate law: Parabolic rate stems from a diffusion-controlled process. At the beginning of the oxidation at a high temperature, the reaction is surface-reaction controlled. Then, after forming a continuous oxide scale, the oxidation rate may be controlled by the diffusion of reactants through the scale. The thicker the scale, the longer the diffusion distance, the slower the oxidation rate; which means that the instantaneous oxidation rate (dx/dt) is inversely proportional to the scale thickness, as shown in equation 2-10. Integration of this equation results in the parabolic rate equation, where $k_p{}'$ is a proportionality constant.

$$\frac{dx}{dt} = \frac{1}{x}k_p{}' \qquad \textbf{(2-10)}$$

$$x^2 = k_p t + C\ \ ;\ \ \ k_p = 2\,k_p{}' \qquad \textbf{(2-11)}$$

The diffusion through the oxide scale is a thermally activated process, such that the dependence of the oxidation rate constant with temperature is in accordance with the Arrhenius equation:

$$k_p = k_0 \exp\left(-\frac{Q}{RT}\right) \qquad \textbf{(2-12)}$$

where k_0 is a constant of that depends on the oxide composition, and Q is the activation energy corresponding to the oxide scale formed. The Arrhenius plot shown in Figure 2-14 illustrates the temperature dependence of k_p for several oxide scales. Cr_2O_3 and Al_2O_3 show a range of k_p values at the same temperature owing to their sensitivity to impurities.

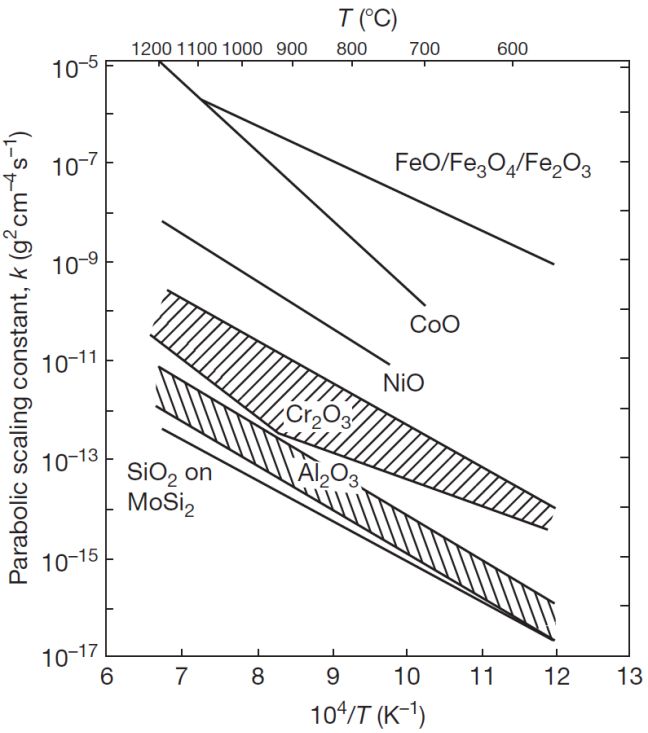

Figure 2-14. Arrhenius plot: parabolic oxidation rate constant for various oxide scales as a function of temperature [48].

Linear rate law ($x = k_1 t$): Unlike parabolic kinetics, in linear kinetics the oxidation is fixed with time, which results in faster metal consumption. Therefore, linear rate law generally reflects a nonprotective scale; volatilization, melting, spallation, or cracking in a protective oxide

scale, e.g., Nb and Ta oxides form according to linear kinetics due to continuous scale cracking [49]. If during the oxidation, the oxide scale continuously heals after spalling or cracking, the overall kinetics are called 'paralinear'.

Short-circuit diffusion: Figure 2-15 shows how transport paths through a scale have different diffusion values at the same temperature. For the NiO, it has been reported that the oxidation is controlled by Ni ions diffusing outward along the grain boundaries at temperatures below 1100°C; while lattice diffusion dominates above 1100°C. The contribution of the lattice and GB diffusion depends on the oxide grain size, temperature, and pO_2. Other is the case for alumina and chromia formation, where diffusion through the scale occurs predominantly along grain boundaries. In the case of chromia, chromium ions diffuse outward through the scale, while O ions move inward for the alumina scale formation.

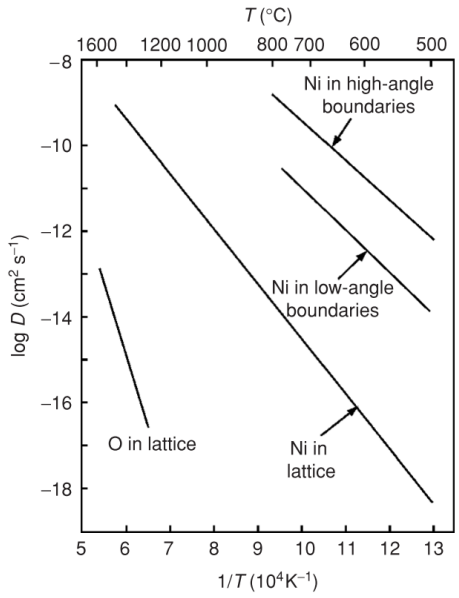

Figure 2-15. Diffusion parameters modes for NiO [47]

2.1.2.3. Mechanisms of Oxidation

Oxidation takes place when oxygen, metal ions, or both transport through the oxide scale. The transport mechanism depends on if the crystal is stoichiometric or nonstoichiometric. Schottky and Frenkel defects are predominant in highly stoichiometric ionic compounds. Schottky explains ionic mobility by the presence of ionic vacancies; identical cationic and anionic vacancies should exist to keep the ionic charge balance. Frenkel explains the transport by the existence of interstitial defects and vacancies; if a cation is mobile and migrates occupying interstitial sites, then a cationic vacancy should exist to maintain electroneutrality.

However, metallic oxides are seldom stochiometric, which means that the metal-to-oxygen ratio dictated by the oxide's stoichiometry is not exactly fulfilled. Usually, it is more likely to find variable valency in the cation (metallic) than in the anion sublattice. Regardless, in order to keep electroneutrality, electron and electron holes are present in non-stochiometric oxides. Besides, since nonstoichiometric oxides consist of these defects, they exhibit electronic and ionic conductivities.

Nonstoichiometric compounds can show positive or negative behavior; therefore, they can be classified as semiconductors: n-type (excess of electrons) and p-type (excess of electron holes). Negative semiconductors get the negative carriers by an excess of metal (cation interstitials, $M_{1+\delta}O$) or deficit of non-metal (oxygen vacancies, MO_{1-x}); some examples of n-type include ZnO, TiO_2, Fe_2O_3, $NiFe_2O_4$, Al_2O_3, and SiO_2 [50]. On the other hand, in positive semiconductors, positive carriers come from a metal deficit (cation vacancies, $M_{1-\delta}O$) or an excess of non-metal (oxygen interstitials, MO_{1+x}). Some examples of p-type are NiO, CoO, FeO, and $NiAl_2O_4$ [50]. Amphoteric oxides can show either positive or negative behavior, where chromia is an example ($Cr_{2\pm y}O_3$). It is an n-type oxide at very low oxygen activity, whereas a

higher oxygen activity a duplex structure of n- and p-type chromia form. The major point defect reported in the n- and p- chromia is oxygen vacancy and chromium vacancy, respectively [51].

During oxidation at high temperatures, Figure 2-16 illustrates the distinction between cation and anion migration. When the cation migrates outward, oxidation occurs at the scale/gas interface; if the anion migrates inward, the scale growth takes place at the metal/oxide interface. Although the two reactions can happen simultaneously, it is more common to find one predominant mechanism. Duplex structures can develop under certain circumstances, e.g., a duplex chromia scale, where an equiaxed structure is present internally corresponding to the n-type, while the p-type chromia is present externally, exhibiting a columnar grain structure [51].

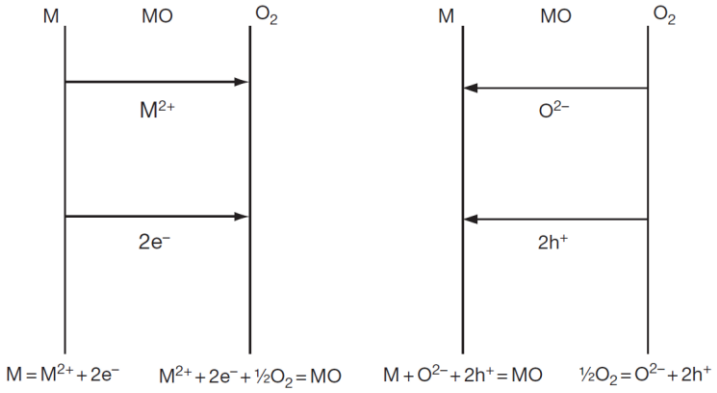

Figure 2-16. Interfacial reactions for high-temperature oxidation mechanism: (left) cation migration and (right) anion migration.

On the other hand, nonstoichiometric oxides can exhibit impurities, or the so-called ‘doping effect’, affecting ionic transport. For example, suppose a p-type, metal-deficient oxide, is doped with a cation of lower valence. In that case, it will increase the concentration of electron holes and decrease the concentration of cation vacancies. Alternatively, if the same oxide is doped with higher valence cations, the concentration of electron holes will fall, and the concentration of cation vacancies will increase. In the last scenario, the cation diffusivity will increase, deriving in an oxidation rate increase and a faster scale growth.

The ionic defect concentration has a proportional relation with the oxygen partial pressure: for n-type $C \propto (P_{O_2})^{-1/n}$, for p-type $C \propto (P_{O_2})^{1/n}$.

2.1.2.4. Wagner's Theory of Metal Oxidation

The primary assumption of Wagner's theory is that the lattice diffusion of the reacting species is rate controlling. The scale assumed by the model is continuous, dense, single-phase, and perfectly adhered to the metal surface. Thermodynamically, it is assumed that the metal/oxide and oxide/metal interface are at equilibrium and a local equilibrium throughout the scale exists.

Compositions at both interfaces are fixed by the thermodynamic equilibrium established; it originates chemical potential gradients across the scale. These chemical potential gradients are a driving force for metal and oxygen ions to migrate across the scale in opposite directions. Afterward, the ionic fluxes will derive in an electric field set up across the scale, a driving force for electronic and ionic fluxes. Ionic and electronic migrations keep the electroneutrality, so no charge builds up within the scale. Figure 2-17 shows the diagram of the Wagner's model, following the mentioned assumptions.

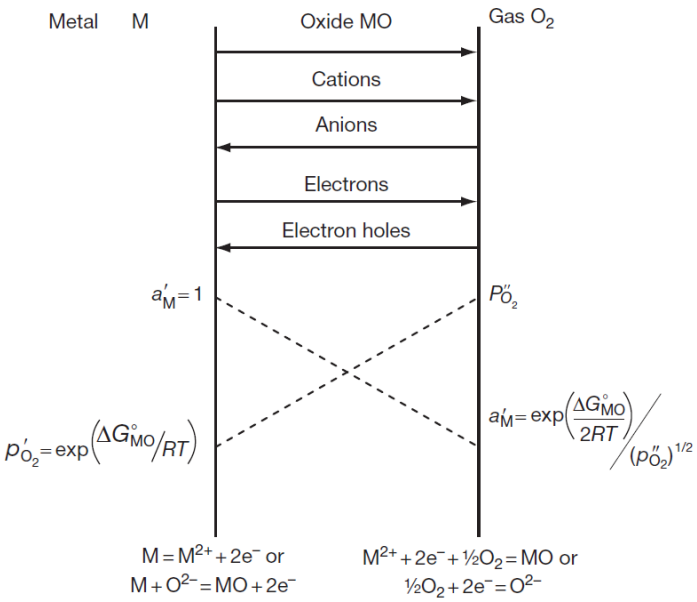

Figure 2-17. Diagram of scale formation according to Wagner's model [47]**.**

Wagner [52] derived expressions to describe the parabolic rate constant in terms of self-diffusion coefficient for metal (D_M) and non-metal (D_O), and the chemical potential of metal (μ_M) and non-metal (μ_O). When cation diffusion predominates, the following expression is valid

$$k' = \frac{1}{RT} \int_{\mu''_M}^{\mu'_M} D_M \, d\mu_M \qquad \textbf{(2-13)}$$

when anion diffusion predominates, the valid expression is:

$$k' = \frac{1}{RT} \int_{\mu''_X}^{\mu'_X} D_X \, d\mu_X \qquad \textbf{(2-14)}$$

On the other hand, a correlation of the oxidation rate in terms of the partial pressure can be derived since diffusion flux across the oxide is proportional to the defect concentration, and the defect concentration is correlated with the partial pressure. Resulting in the following expression for a p-type and n-type, where $P^o_{O_2}$ and $P^i_{O_2}$ are the oxygen partial pressures at the

scale/gas interface and metal/scale interface, respectively. Simplifications apply since usually $P_{O_2}^{o} \gg P_{O_2}^{i}$.

$$p-type \qquad k' \propto \left[(P_{O_2}^{o})^{1/n} - (P_{O_2}^{i})^{1/n}\right] \propto (P_{O_2}^{o})^{1/n} \qquad \textbf{(2-15)}$$

$$n-type \qquad k' \propto \left[(P_{O_2}^{i})^{-1/n} - \left(P_{O_2}^{o}\right)^{-1/n}\right] \propto (P_{O_2}^{i})^{-1/n} \qquad \textbf{(2-16)}$$

These expressions show that p-type oxides' growth rate depends on the oxygen partial pressure in the atmosphere, while the growth rate for n-type oxides is independent of the partial pressure in the atmosphere.

Wagner's theory has been validated experimentally (e.g., FeO, CoO, FeS, CuI); its importance relies on showing a mechanistic understanding of the high-temperature oxidation process. Even so, some deviations have been reported when the experiments have a significant difference from the assumptions giving place to a modifications case based [53] [54]. For example, the rate constant of NiO above 1000°C is factor of two with the Wagner's predicted value, but below 1000°C the differences is much greater. An agreement is reached if short circuit diffusion by the grain boundaries is considering in the prediction[53]. Other deviations from the ideal oxide growth predicted by Wagner include impurities, pores, voids and fissures [49].

2.1.2.5. Stress Generation in Oxide Scales

Stress in oxide scales might trigger cracking, rupture, spallation, and eventually, loss of scale protectiveness. Scale stresses arise from different contributions, including growth mechanism, oxide to metal volume ratio, and surface geometry.

Intrinsic growth stresses: These stresses come from the nature of the oxidation process. Experimental observations of the morphology of some oxides show evidence of repeated formation and detachment processes, which result from the stress relaxation due to the additional

volume from new oxide formed. The first attempt of modeling the intrinsic growth stresses is associated with the Pilling–Bedworth ratio (ratio of the molar volume of the oxide formed to the metal consumed) [55]. The main assumption is that the oxide grows inwardly. If PBR>1, the oxide scale would be in compression, but if PBR<1, the oxide scale would be in tension. However, outwardly grown oxides are not considered in this model. Rhines and Wolf [56] were the first ones to consider a model with counter diffusion between inward oxygen (intergranular) and outward cations (intragranular) for pure nickel oxidation. Initially, nickel oxide columnar grain grows following a parabolic behavior. Then, the new oxide forms in the grain boundaries resulting in volume increase and subsequent lateral compressive strain. The bigger the grain size and the slower the oxide scale growth, the slower the lateral growth strain rate [57]. Additionally, growth stresses can develop during oxidation due to different contributions:

- Phase transformations in the oxide or the subsurface metal in contact with the oxide (e.g. , transformation of $(Cr, Fe)_2O_3$ to $(Fe, Cr)_3O_4$ during the initial stages of Fe-Cr alloys oxidation)[58].
- Impurities at the scale metal interface (e.g., Pt markers in oxidation of pure Nickel reduces cohesion between the outer and inner oxide layer)[59].
- Local heterogeneities (e.g., grain boundaries; enhanced diffusion promotes a faster and ticker oxide that results in oxide ridges)[60].
- Epitaxial growth of the first oxide layer from the metal substrate due to the different lattice parameters between the oxide and the metal [61].

Geometrically induced growth stresses: Surface geometry also contributes to the growth stresses during the oxide formation. The geometrically induced stress is determined by the surface profile (i.e., concave or convex) and the interface of oxide growth (i.e., gas/oxide or

oxide/metal). Figure 2-18 illustrates two of the possible scenarios for the case of compressive intrinsic growth stress (PBR>1). For example, the square edge (convex curvature) of a cation diffusion sample will show an outward growth of the oxide above the existing oxide. In that case, the oxide/metal interface will have the highest compressive circumferential stresses and tensile stresses perpendicular to the interface.

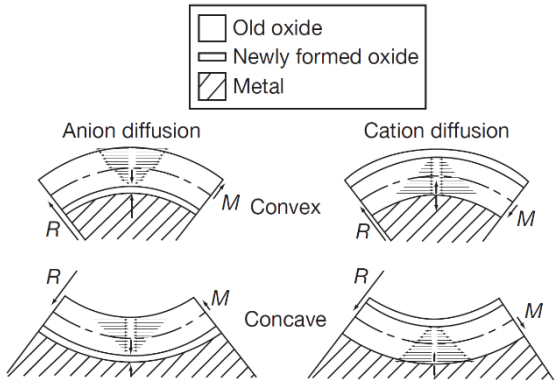

Figure 2-18. Growth stresses during the oxidation of curved surfaces with PBR>1 [61]**.**

Geometrically induced growth stresses are more noticeable as surface curvature radius decreases and the oxide growth rate increases.

Thermally-induced stresses: Differences in the coefficient of thermal expansion (CTE) between the metallic substrate and the oxide formed result in stress formation; the oxide CTE is usually lower than the metal CTE [61]. After oxidation, intrinsic growth, geometrical, and thermal stresses are superimposed, leaving residual stress in the scale. This residual stress can be measured by, for example, Raman spectroscopy and XRD at room temperature. Some Raman results have shown that the sample center has more compressive stresses than the sample corners, showing an effect of the geometry in the thermal stresses developed. For example, the sample corners (convex curvatures) present circumferential compressive stresses and tensile stress perpendicular to the interface when $CTE_{metal} > CTE_{oxide}$, as it is illustrated in Figure 2-19.

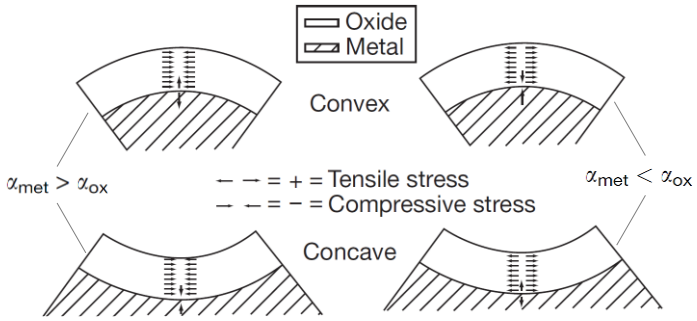

Figure 2-19. Direction of thermal stresses in curved geometries [61].

Oxide scale failure: Oxide failure models based on fracture mechanics assume that physical defects (e.g., pores, cracks, etc.) trigger failure. Critical stress (σ_c), assuming linear elastic behavior, can be calculated with the following equations:

$$\sigma_c = \left(\frac{E^* G_c}{\pi c}\right)^{1/2} \quad \textbf{(2-17)}$$

$$K_c = (E^*_{ox} G_c)^{1/2} \quad \textbf{(2-18)}$$

where c is the size of the defect, and K_c is the fracture toughness, which reflects the resistance to crack growth. On the other hand, the critical strain (ε_c) is calculated depending on the damage situation.

Nonetheless, healing potential exists since oxide scale growth continues during applications at high-temperature exposure. The different modes of scales failure under tensile and compressive stresses are summarized in Table 2-3, showing schematics and equations corresponding to each scenario.

Table 2-3. Potential failure mechanisms of oxide scales [62] [63] [64]

Tensile Stresses		
Through scale cracking	$\varepsilon_c^t = \frac{K_{Ic}}{f E_{ox}\sqrt{\pi c}}$ f: geometrical factor (1 for embedded defects)	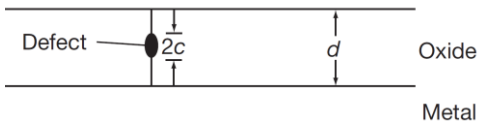

Compressive Stresses		
Beginning of interfacial crack growth/ delamination	$-\varepsilon_c^i = \frac{K_{Ic}}{f\sqrt{\pi c}} \frac{\left(1+\frac{r}{d}\right)(1+\nu_{ox})}{2E_{ox}}$ r: interfacial roughness amplitude ν_{ox}: Poisson ratio	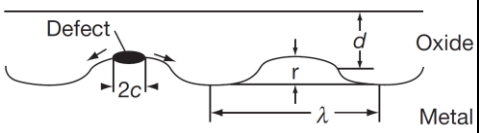
Buckling	$-\varepsilon_c^b = \frac{1.22}{1-\nu_{ox}^2}\left(\frac{d}{R}\right)^2$ R: radius of existing delamination	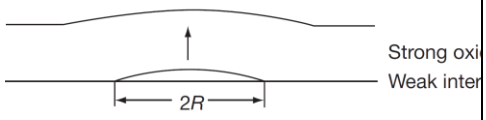
Crack deflection at scale buckles toward the surface	$-\varepsilon_c^{bf} = 3.6\left(\frac{d}{R}\right)^2$	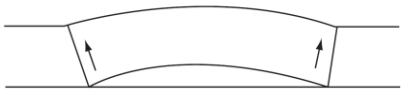
Spalling	$-\varepsilon_c^s = \sqrt{\frac{2\gamma_o}{dE_{ox}(1-\nu)}}$ γ_0: surface energy needed to create two new surfaces by cracking or detachment	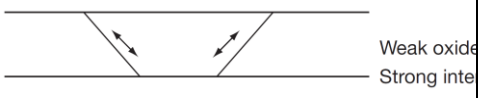
Shear failure		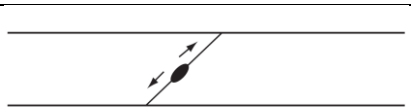

2.1.3. High-temperature Oxidation of Ni-Cr Alloys

High-temperature applications of binary Ni-Cr-based alloys rely on chromia scale formation for protection against corrosion. Figure 2-20 illustrates the oxidation rate as a function of the chromium content in the alloy. At low Cr content, the formation of doped NiO controls the oxidation rate, together with Ni-Cr spinel and little doped Cr_2O_3 as internal oxide [65]. The slight decline in the oxidation rate in Figure 2-20 occurs due to the Ni-Cr spinel increase and the

growth of a partial layer of Cr_2O_3. At high Cr content around 10-15%, the steeper decline of k_p occurs because the internal oxide particles coalesce and form a complete and continuous chromia layer, which determines the mode of oxidation [66][66][65].

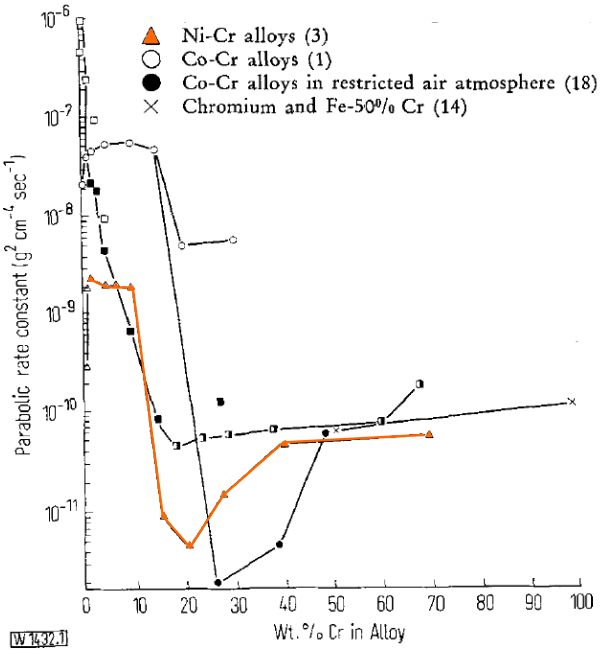

Figure 2-20. Variation of kp with Cr composition for Ni-Cr alloys oxidized at 1000°C in 1 atm [65]**.**

2.1.3.1. Internal Oxidation

Internal oxidation takes place when subsurface oxides precipitate due to inward oxygen diffusion to the alloy; it is an undesired process since it ensues in internal stress and grain boundary weakening. Rapp [67] presents the requirements necessary for internal oxidation in a binary alloy (A-B), where A is the base metal and B the solute metal:

1. B should have a higher affinity with the oxygen than A; i.e., $\Delta G^{\circ}_{BO_\nu} < \Delta G^{\circ}_{AO_\nu}$
2. The base metal should have solubility and diffusivity of oxygen enough to dissolve oxygen at the reaction front, faster than B diffusion toward the surface.

3. B concentration must not surpass a critical value where a continuous layer of BO_ν can form.
4. No surface layer impedes the oxygen dissolution at the beginning

After the dissolution of oxygen, the formation of BO_ν takes place ($B + \nu O_{diss} \longrightarrow BO_\nu$). If the activity product $[a_O^\nu][a_B]$ from the formation reaction is higher than the solubility product (K_{sp}), then the precipitates start to nucleate, and internal oxidation occurs.

Kinetics of internal oxidation generally follow a parabolic time dependence, which is predicted by the following equation for the case with no external scale formed [47]:

$$X = \left[\frac{2\, N_O^{(sol)} D_O}{\nu N_B^{(O)}} t\right]^{1/2} \quad \textbf{(2-19)}$$

where $N_B^{(O)}$ is the initial B concentration (bulk) and the dissolved oxygen solubility-diffusivity product ($N_O^{(sol)} D_O$) describes the oxygen permeability in the alloy. Moreover, the internal oxidation depth goes down to the oxygen dissolved give the critical oxygen activity to precipitate BO_ν.

2.1.3.2. Transition from Internal to External Oxidation

Internal or external BO_ν formation is determined by the flux balance between inward oxygen (N_O) and outward solute (N_B). There is a critical solute concentration ($N_B^{(O)}$), where the solute can reach the surface and sustain the formation BO_ν in the surface up to form a continuous layer; if this condition is not fulfilled, BO_ν will precipitate as internal oxidation.

Wagner [68] predicted a criterium where the transition from internal to external BO_ν scale formation should occur, for the case of external chromia establishment it will be:

$$N_{Cr}^{I} > \left[\frac{\pi g^{*}}{3} N_{O}^{sol} \frac{D_O V_{all}}{D_{Cr} V_{ox}}\right]^{1/2} \quad \textbf{(2-20)}$$

where D_O is the oxygen diffusivity in the alloy, D_{Cr} is chromium interdifussion coefficient in the alloy, V_{ox} is the molar volume of the oxide and g^{*} is a critical volume fraction of oxide [69]. Wagner's criterion shows that transition from internal to external can occur at lower solute concentrations with decreasing the inward oxygen flux and increasing the outward solute flux, e.g., cold work and small grain size assist chromia development due to the D_{Cr} enhancement by short-circuit diffusion role.

2.1.3.3. Chromium Depletion:

The interfacial concentration of chromium is essential to determine if the alloy can sustain chromia-scale growth or establish a new chromia layer in case of spallation. Wagner's analysis [52] of one-dimensional diffusion processes can be used for the chromium subsurface depletion as a consequence of the chromia-scale growth process. Assuming that the scale formed is pure chromia, the steady-state equation is given by:

$$\frac{N_{Cr}^{0} - N_{Cr}^{i}}{1 - N_{Cr}^{i}} = F\left(\frac{2\,V_{all}}{V_{ox}}\sqrt{\frac{k_{p,ox}}{D_{Cr}}}\right) \quad \textbf{(2-21)}$$

where F is an auxiliary function

$$F(u) = \sqrt{\pi} u (1 - \operatorname{erf} u) \exp(u^2) \quad \textbf{(2-22)}$$

N_{Cr}^{0} is the initial chromium mole fraction, V_{all} is the molar volume of the alloy, V_{ox} is the molar volume of the oxide (29 cm^3/mol for Cr_2O_3), D_{Cr} is the chromium difussion coefficient. Knowing the oxidation constant rate ($k_{p,ox}$), the chromium concentration at the metal/oxide interface can be determined.

Breakaway oxidation occurs when an oxide scale goes from a protective to a nonprotective period. After a critical chromium depletion, the reaction rate can be limited by the Cr supplied from the alloy to the surface, more than the diffusion rate of Cr cation through the chromia scale. In other words, the alloy cannot maintain the growth of the scale oxide once it is formed; Wagner predicted the chromium flux necessary to sustain the growth:

$$N_{Cr}^{II} > \frac{V_{all}}{32\,\nu}\left(\frac{\pi\,k_p}{D_{Cr}}\right)^{1/2} \qquad \textbf{(2-23)}$$

where k_p is the parabolic rate of the chromia-scale formation.

If after spallation the critical chromium depletion is reached, it means that the interfacial Cr concentration is smaller than the solubility product of chromia and the chromium activity is too low to maintain the Cr_2O_3/alloy equilibrium. Thus, the reformation of a protective scale would not be formed.

Without a protective scale, the increase in oxygen activity at the interface will promote the oxidation of other alloying elements that might not be as protective as chromia, e.g., $FeCr_2O_4$ [70]. This phenomenon is called intrinsic chemical failure, which can occur instantaneously when the initial interfacial value is below the critical one ($C_I < C_{Cr}^*$), or it can by time-delayed, when the critical chromium depletion is reached after a critical exposure time. The critical exposure time depends on the thickness and temperature; the thicker the section, the longer the exposure time needed to deplete the Cr reservoir.

Breakway oxidation can also be mechanically induced chemical failure; it occurs when a former scale suffers a mechanical failure, and rehealing is impossible since the Cr flux is insufficient to reform a protective chromia, leading to the formation of nonprotective oxides [70].

Summarizing, Figure 2-21 classified alloys into four groups according to the k_c/D and the critical interface mole fraction (N_{Cr}^0) [71], where the four regions correspond to:

1. $N_{Cr}^0 < N_{Cr}^I$: Insufficient Cr to form a continuous and protective oxide layer.
2. $N_{Cr}^I < N_{Cr}^0 < N_{Cr}^{II}$: Sufficient Cr to establish a protective oxide initially, but not sufficient to re-form a new layer in case of spallation.
3. $N_{Cr}^{II} < N_{Cr}^0 < 1 - (1 - N_{Cr}^I)^3$: Sufficient Cr to re-form a new oxide layer, but not sufficient to reheal at high frequency.
4. $N_{Cr}^0 > 1 - (1 - N_{Cr}^I)^3$: Sufficient Cr to reheal at rapid spallation

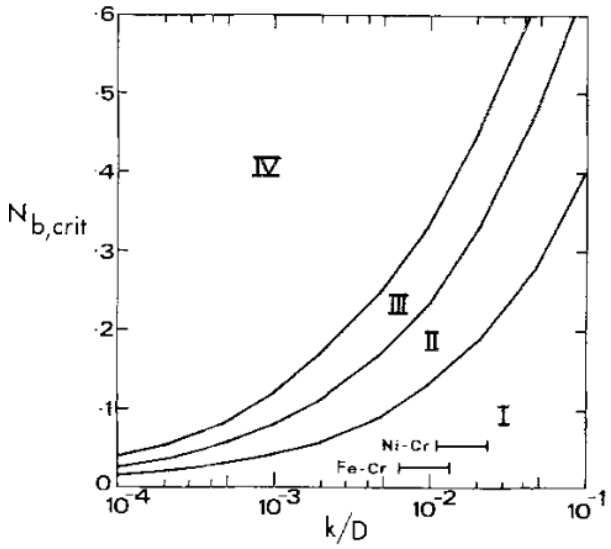

Figure 2-21. Critical interfacial mole fractions to resist repeated spallation of the protective oxide as a function of k_c/D.

2.1.3.4. High-temperature Oxidation of Alloy 625

The nominal composition of alloy 625 is given in Table 2-4 with the oxygen potential, and equilibrium partial pressure for the two-phase oxides of each element; this is informative to understand the oxides formed and their distribution.

Initially, non-steady/transient oxidation takes place where less-stable oxides form. For example, Ti, Al, Nb, and Si may oxidize, increasing the degradation rate [72]. During the transient oxidation, the kinetics follow a linear behavior. Then, the scale formation depends on the competition of these fast-diffusing oxides growth and the replacement for more thermodynamically stable but slow-growing oxides. Once the continuous chromia forms, transient oxides stop growing, and the kinetics follow a parabolic behavior. Some of the transient products remain, form spinels, then spall, leaving the chromia scale roughly intact. Furthermore, a high chromium concentration allows an external and stable chromia layer formation [47].

Table 2-4. Oxygen potential and dissociation pressure at 1000°C for possible two-phase during oxidation of Alloy 625 [4]**.**

Elements	**Composition**		**Two-phase mixture**	**$\Delta G°$ (kJ mol^{-1} O_2)**	**P_{O2} (Pa)**
	at.%	**wt.%**			
Ni	62.8	61.9	Ni-NiO	-60.2	4.7×10^{-6}
Cr	24.3	21.2	Cr-Cr_2O_3	-139.6	1.1×10^{-19}
Mo	5.6	9.0	Mo-MoO_2	-86.4	1.5×10^{-10}
Fe	3.7	3.5	Fe-FeO	-86.8	1.2×10^{-10}
Nb	2.4	3.7	Nb-NbO	-146.2	8.1×10^{-21}
			NbO-NbO_2	-129.3	6.2×10^{-18}
			NbO_2-Nb_2O_5	-107.4	3.6×10^{-14}
A1	0.4	0.2	Al-Al_2O_3	-203.3	1.2×10^{-30}
Si	0.4	0.2	Si-SiO_2	-162.8	1.1×10^{-23}
Ti	0.3	0.2	Ti-TiO	-190.3	2.1×10^{-28}
			TiO-Ti_2O_3	-179.8	1.3×10^{-26}
			Ti_2O_3-Ti_3O_5	-126.8	1.7×10^{-17}
			Ti_3O_2-TiO_2	-87.4	9.7×10^{-11}
Co	0.1	0.1	Co-CoO	-68.8	1.6×10^{-7}

Alloy 625 oxidized in air typically exhibits a formation of nearly exclusive continuous chromia as a protective oxide up to 1000°C, where the oxidation kinetics have been reported to obey a parabolic time dependence [4][5][6]. When the scale is not entirely chromia, conspicuous additions of Nb_2O_5 in the oxide scale at elevated temperatures have been reported [4]. Also, the

extent of Nb enrichment of the oxide scale rises with increasing temperature [4]. Additionally, Buscail [6] reported a stratified oxide structure of inner $CrNbO_4$ and external chromia at 1100°C. The outer oxide surface comprises the chromium-manganese spinel [73].

Ideally, the chromia scale should be continuous, homogeneous, dense, and adherent to maintain its protectiveness; however, reported defects include pores in the scale and oxide/metal interfacial pores [6][74]. Pores in the interface are attributed to the vacancy annihilations due to the increased concentration of cation vacancies during the outward chromium diffusion. On the other hand, porous scales have been attributed to chromia volatilization loss via CrO_3 formation [73]; it has been reported to be significant at temperatures above 1000°C in high oxygen pressures [75], where the dominant gas specie is CrO_3(g).

$$\frac{1}{2}Cr_2O_3 + \frac{3}{4}O_2 \rightarrow CrO_{3(g)} \qquad \textbf{(2-24)}$$

Furthermore, the subsurface suffers several changes during high-temperature oxidation. For example, Nb enrichment and discontinuous δ-phase precipitates are reported from 800°C up to 1000°C at the scale/alloy interface. Figure 2-22a also shows a minor amount of internal alumina, reported from 900°C [5], and located mainly at the alloy grain boundaries being followed by a precipitates free zone.

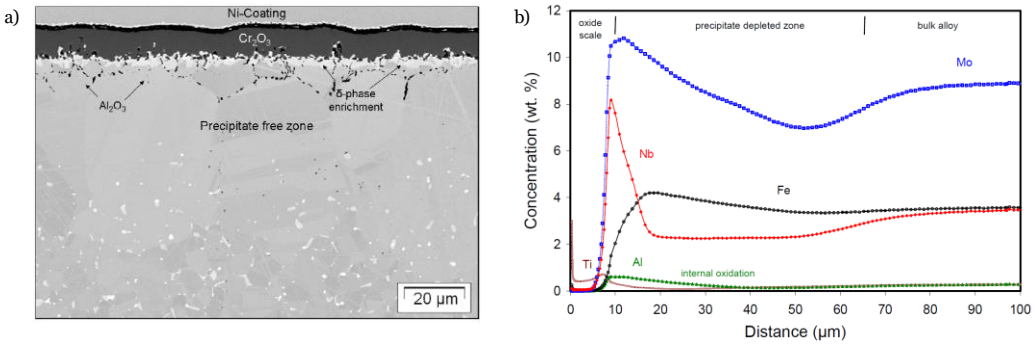

Figure 2-22. Oxidized alloy 625 after 1000h at 900°C in Ar-4%H2-2%H2O a) Cross-section and b) compositional depth profiles [5]

The composition profile depicted in Figure 2-22 helps understand the oxidation mechanism of Alloy 625. First, there is a chromium subscale depletion toward the surface due to the outward diffusion promoted by the selective oxidation of chromium. The chromium depletion naturally should increase the remaining elements' concentration in a similar proportion to the nominal composition, which will enrich Nb up to 4.5 wt%. However, the Nb concentration doubles the bulk composition, implying an additional Nb diffusion towards the scale/alloy interface. Diffusion is possible when a chemical potential gradient exists. For that reason, Chyrkin et al. [5] simulated the alloying elements' chemical potential as a function of chromium content, showing that the Nb and Si activity decreases with the Cr depletion, as seen in Figure 2-23. Since Nb diffusion occurs from the high to the low activity, the Nb flux occurs from the inner part toward the surface. This phenomenon, where the solute diffusion flux is against its concentration gradient, is called uphill diffusion. In this case, the Nb uphill diffusion results in an Nb enrichment just beneath the oxide/alloy interface, favoring the δ-phase precipitation. Successively, the δ-phase formation depletes the Nb in the vicinity, which decreases the Nb activity more and helps to sustain the Nb uphill diffusion from the bulk.

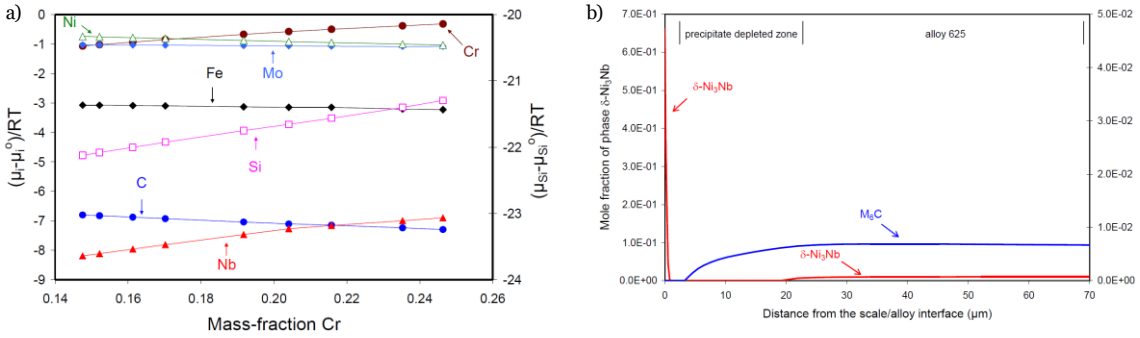

Figure 2-23 The chemical potential of alloying elements at 900°C (Thermocalc-TTNI7), b) Phase distribution in the subscale region of alloy 625 after 100 h oxidation at 900°C in Ar-4%H_2-2%H_2O [76]

In addition, according to equilibrium simulations, the alloy 625 is expected to have δ-phase precipitates and M_6C at 900°C. However, the phases formed in the subsurface are affected

by the compositional changes triggered by the oxidation process. The chromium depletion and its induced uphill diffusion resulted in an Nb depletion region, where the δ-phase formation is not favored. In a similar manner, the carbon is diffusing backward (toward the inner bulk) since the activity of carbon increases with chromium depletion, resulting in carbides destabilization and dissolution.

The role of the subsurface changes induced by the oxidation process needs to be studied in depth. For example, in the case of the δ-phase precipitation beneath the chromia, it is unclear if it acts as a diffusion obstacle for the chromium cations and affects the oxidation kinetics.

2.1.3.5. High-temperature Oxidation of Ni-base Alloys Made by Additive Manufacturing.

Oxidation of AMed samples in comparison with conventional methods has shown slight differences regarding the oxide composition, oxidation kinetics, transient oxidation products, and subsurface changes induced by the oxidation (e.g., discrete pores) [14][74]. These differences are attributed to inherent characteristics of the AM processed alloys, such as crystallographic texture, refractory segregation, surface finishing, and porosity.

2.1.3.5.1. Effect of the Manufacturing Process on the Oxidation Behavior of Ni-base Alloys

Chromia-forming alloys fabricated by laser and electron beam have reported parabolic kinetics, indicating that the solid-state transport through the scale formed dictates the oxidation rate, e.g., Inconel 718 by LPBF and EPBF [38] [39], Alloy 625 by LPBF [9], Hastelloy X by LPBF and EPBF [11], and alloy K648 by DED [78]. However, some oxidation kinetics show deviations from parabolic behavior; for example, Alloy 625 fabricated by LPBF oxidized at 1050°C. Conventional manufactured (CM) Alloy 625 forms a duplex scale structure, with an inner discontinuous layer of $Nb_{1.5}Cr_{0.5}O_4$ and an external chromia layer [9]. The LPBF sample

exhibits a larger amount of $Nb_{1.5}Cr_{0.5}O_4$ than a conventional manufactured sample since a high Nb segregation in the as-built LPBF sample resulted in a higher Nb availability. Thus, the excess of $Nb_{1.5}Cr_{0.5}O_4$ in the LPBF sample affects the oxidation kinetics until it deviates from pure parabolic behavior. At 1050°C, the measured k_p was 3 -4 times higher for the LPBF than CM.

Slight oxide composition differences existed depending on the manufacturing process in the oxidation of Alloy 625 at 1050°C. The external oxide consists of chromia with additions of TiO_2 and $Ni(Fe, Cr)_2O_4$ spinel [6][79]; Mn-Cr spinels($MnCr_2O_4$) was found in the conventional manufactured sampled while Nb-Cr spinel ($NbCrO_4$) was located at LPBF sample [9]. Oxidation at 750°C of Inconel 718 made by EPBF showed the formation of Fe-rich nodules that the wrought sample does not present [80].

Regarding the internal oxidation, the conventional sample forms TiO_2 and Al_2O_3, while LPBF shows an abundant amount of discrete voids correlated with the internal oxidation.

2.1.3.5.2. Effect of AM Process Parameters on Oxidation Behavior

Building direction: Parts fabricated by AM processes that involve laser and electron beams typically have crystallographic texture in the <001> direction, resulting in columnar grains formed along the building direction [81]. Therefore, the building direction affects the grain-boundary density in a sample cross-section (see Figure 2-24). Grain boundaries act as short-circuit paths for chromium diffusion and enhance the chromium supply from the alloy; therefore, the higher the grain-boundary density, the faster the chromia establishment. Consequently, the oxidation of different building directions can lead to faster chromia establishment with increasing grain boundaries density. Li et al. [82] reported this phenomenon in the oxidation of Inconel 718 fabricated by EPBF (electron powder bed fusion) at low temperatures where grain boundary diffusion was dominant over lattice diffusion.

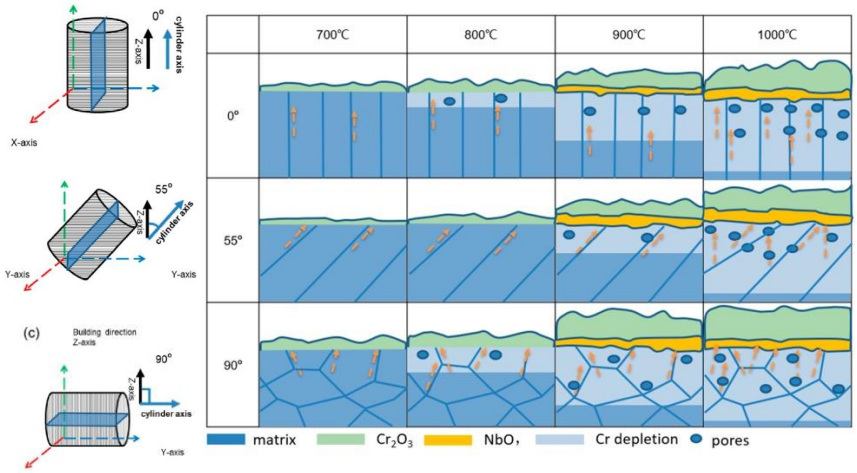

Figure 2-24. Influence of building direction on the oxidation behavior of Inconel 718 fabricated by EPBF [82]**.**

Porosity: In the LPBF process, the optimization of the volumetric energy density (VED) decreases the porosity, reduces the surface roughness, increases the grain refinement, etc. Regarding the oxidation of chromia-forming alloys fabricated by LPBF, it has been reported that the higher the VED, the better the oxidation resistance [10] [83]. Sun et al. [83] attributed the higher mass gain at the lowest VED to abundant chromia-scale spallation, and subsequent Ni(Fe, $Cr)_2O_4$ spinel formed for Alloy 625 oxidized at 900°C in air for 100h. Meanwhile, Jia et al. [84] attribute the oxidation resistance enhancement at high VED to a more refined and homogeneous microstructure in comparison with low VED, for Inconel 718 at 850°C in air for 100h.

Heat treatment: Since Alloy 625 is solution strengthened, heat treatments of AMed samples look for homogenization of interdendritic Nb, Mo, Ti segregation. Marchese et al. [85] reported a solution annealing heat treatment for Alloy 625 fabricated by LPBF, where dendritic structures were eliminated together with refractory segregation leaving isotropic equiaxed grains recrystallized. The described heat treatment consisted of 2h at 1150°C in air followed by water quenching. Afterward, the oxidation behavior of the solution annealed and the as-built Alloy 625

were studied at 900°C in air up to 100h by Parizia et al. [74]. The heat-treated sample shows a higher mass gain than the as-built one due to $NiCr_2O_4$ and Nb_2O_5 clusters formation inside the scale product. The suggested mechanism for the cluster formation assumes oxide spallation due to chromia scale defects as cracks.

3.0 Research Objectives

3.1 Deficiencies in the Current Body of Knowledge

The overview provided in the previous chapter revealed the complexity of AM processes and the associated rapid solidification of alloy 625. Such complexity manifests as residual stresses, high-angle grain boundaries, variable composition within the built part, and mesostructural defects like pores, warping, and rough surface finishing. Previous studies have examined the impact of some of these meso- and microstructural features on the oxidation behavior, either for the alloy 625 [9] or other systems [12], [14], [86]

So far, aside from the mesostructural features, most of the differences observed between the oxidation of AM and wrought systems are attributed to basic and direct factors in the processing variables. For example, some oxidation differences have been attributed to the powder composition [11], [12], [14], [87]. This implies that comparable differences in oxidation behavior should be observed when a conventional method is used to fabricate the same AM powder. Nevertheless, there are reports of slight composition changes in the AM processes due to the long residence time. Compositional differences in trace elements are significant in proportion, which could impact the oxidation behavior.

Certain characteristics resulting from AM processing have been observed in traditionally manufactured alloys, albeit through different means. These traits have been found to impact oxidation behavior in some cases. For example, residual stresses have been identified in AM components due to the melting-cooling cycle during the process. Meanwhile, Bertali et al. [88]

induced different residual stress levels in conventionally manufactured alloy 600 by bending it, and reported that residual stresses enhance intergranular oxidation. It is, therefore, expected that a similar effect can be observed in AM samples; however, no studies have systematically compared the impact of residual stress resulting from the AM process on intergranular oxidation.

Likewise, other factors that need to be considered include the role of segregation in oxide scale formation, the impact of grain boundaries on intergranular oxidation, the limit of chromium supply of thin walls over long oxidation exposures, the influence of intricate geometries on surface reactivity, and how surface geometry (e.g., concave, convex) may affect stress on a small scale.

Additionally, most alloy 625 applications at high temperatures require good mechanical properties combined with good oxidation and corrosion resistance. Certain oxidation features in Ni-based alloys have been reported to be detrimental for fatigue life [89]–[93]. The subsurface precipitate-free zone development, and internal and intergranular oxidation have been correlated with fatigue life shortening in oxidized IN100 [92]. Despite similarities in the alloy systems, oxidation of alloy 625 shows enrichment of delta precipitates beneath the scale and differences in the composition profiles in the subsurface that could impact the degradation during fatigue in different ways. Further research needs to be done to have a better understanding of the impact of these differences on fatigue performance. Besides, in the best of this author's knowledge, the impact of differences in the oxidation behavior caused by manufacturing process on the fatigue life of oxidized alloys has not yest been carefully explored.

3.2 Research Goals

Based on the gap of knowledge highlighted in the previous section, the main research goals of this dissertation are:

1. Better understand the role of the microstructural features inherent from the alloy 625 AM processing on the oxidation behavior at 800°C and 950°C during the transient and steady-state regime, including oxidation kinetics, oxide products, scale properties, and subsurface changes. The main focus will be to evaluate the contributions of the Nb and Mo segregation and variations in minor element composition in the alloys (i.e., Ti, Al, S, and O).

2. Determine the failure mechanism of high cycle fatigue of alloy 625 oxidized specimens at 800°C and assess the impact of the oxidation differences stemming from the manufacturing process in the failure mode. To evaluate and compare the impact of the oxidation-induced features, it is necessary to isolate the contributions from thermal aging and oxidation for each tested condition.

3. Propose mitigation strategies to enhance the oxidation behavior and fatigue performance of oxidized AM samples and evaluate at least one. The objective is to reduce intergranular oxidation and decrease the voids formation at the oxide/alloy interface and subsurface, which are associated with the crack initiation during fatigue.

4.0 Materials Studied

In this study, Alloy 625 manufactured by four different processes was investigated: laser powder bed fusion (LPBF), direct energy deposition (DED), casting, and wrought. Wrought alloy is VDM® Alloy 625 (UN06625) in soft annealed condition, while LBPF and DED samples used prealloyed gas atomized powder from the same provider. Figure 4-1 shows the powder particle distribution and a micrograph of it. The powder size distribution is normal and unimodal, with d_{10} = 21.3 µm, d_{50} = 37.6 µm, and d_{90} = 60.7 µm. In general, the powder exhibits high circularity. Some particles show elongation, agglomeration, and satellites.

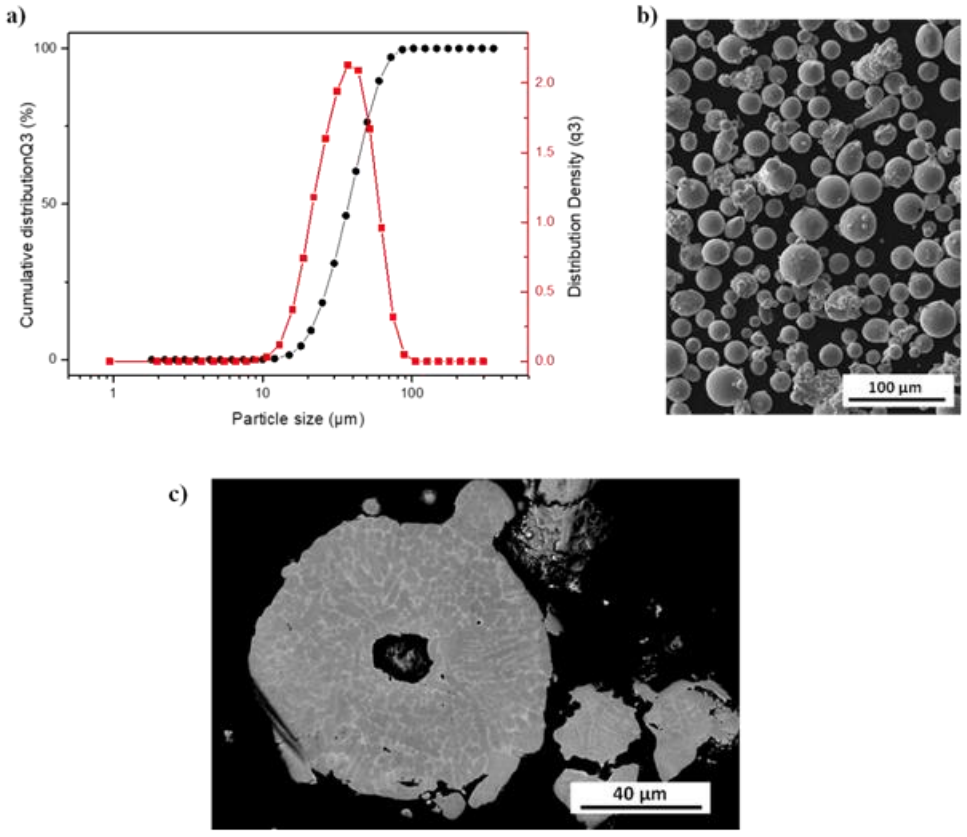

Figure 4-1. Alloy 625 powder characterization: a) particle size distribution, b) representative SEM micrograph of powder particles, c) BSE micrograph of a powder cross-section.

Based on the powder cross-section BSE micrograph, there is evidence of dendritic growth, with partition of Nb and Mo in the brighter areas. Additionally, some powder particles exhibit trapped gas porosity of considerable size, as well as smaller pores that are primarily situated in the interdendritic regions. These smaller pores are likely a result of shrinkage during the cooling process.

Figure 4-2c shows the LPBF cubic samples (10 mm x 10 mm x 20 mm (height) fabricated. The LPBF equipment used was a EOSINT M 290 system (EOS GmbH-Electro Optical Systems, Germany), which is shown in Figure 4-2a. Default optimal laser parameters for alloy 625 were used (layer thickness: 40 µm, scan speed: 960 mm/s, hatch distance: 100 µm, rotation between layers: 67°, laser pattern: stripes).

Figure 4-2e shows the DED cubic samples (80 mm x 50 mm x 20 mm (height)). The DED system used was custom-built, consisting of a three-port coaxial head BEO D70, with a laser source TruDisk6002 (Trumpf, Saalfeld, Germany), and a robotic arm IRB6620-120 (ABB Ltd., Zürich, Switzerland), as shown in Figure 4-2b. Previously optimized parameters to decrease porosity were used (laser power: 850 W, robotic arm speed: 4 mm/s of, hatch distance: 3 mm, powder feed rate: 5 g/min, layer thickness: 1 mm. Laser pattern used was back and forth, with no rotation between the layers. Alloy 625 wrought plates were used as a substrate to avoid CTE differences and diminished warping.

Regard the atmosphere, the LPBF process is performed under Ar, into a closed chamber with control of the oxygen level. In the case of the DED process high purity argon gas was used as shielding gas injected directly in the nozzle, as shown in Figure 4-2f.

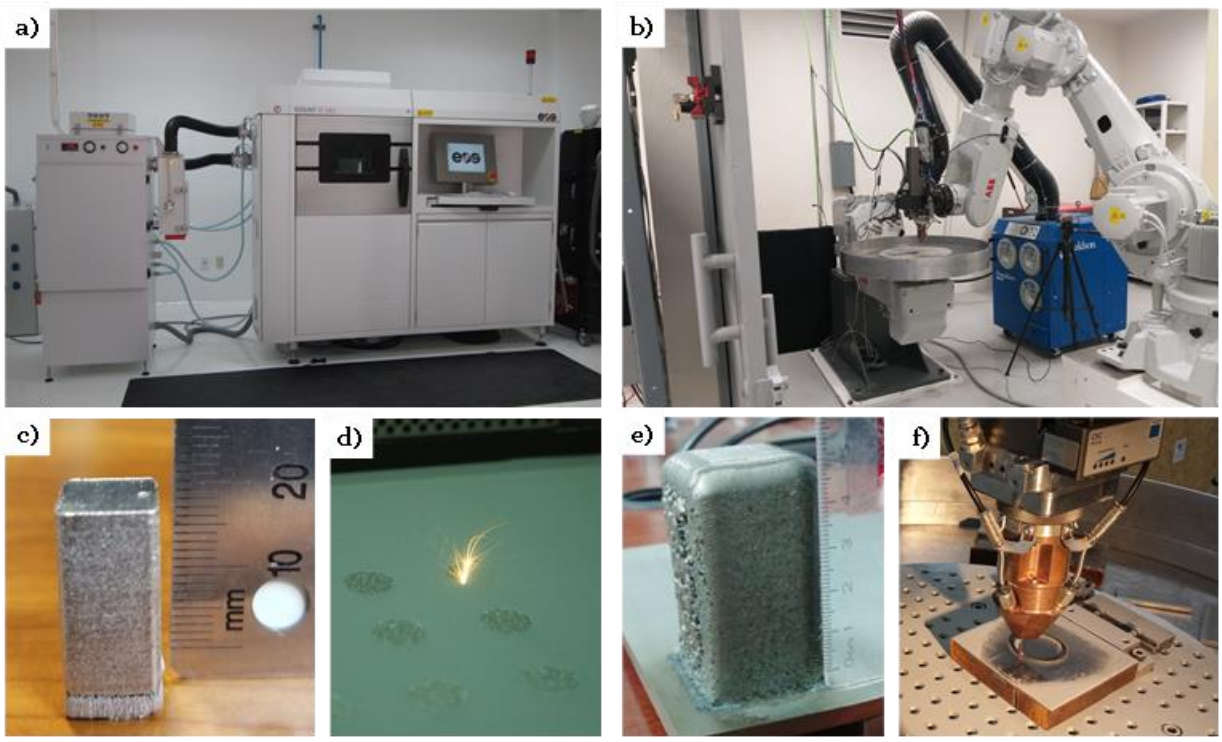

Figure 4-2. AM processes to fabricate samples: LPBF (a,c, and d) and DED (b, e, and f). Equipment used for the processes: a) LPBF (EOSINT M280) and b) DED (Trumpf laser). During process pictures for d) LPBF and f) DED. Obtained square samples for each process: c) LPBF and e) DED.

5.0 Results and Discussion

5.1 Transient Oxidation Behavior of Alloy 625

5.1.1 Introduction

Alloy 625 is a nickel-based superalloy strengthened mainly by solid-solution hardening; however, under defined conditions, it can also be strengthened by γ" coherent precipitates [20]. As a result, it shows high strength, good fatigue resistance, and good weldability. It is widely used in high-temperature applications at where it relies on the protectiveness of a slow-growing chromia scale [3]. Recently, multiple efforts have been made to fabricate complex parts by additive manufacturing (AM), by leveraging the freedom of design, sustainability benefits, and the manufacture of hard-to-machine alloys. One of the major drawbacks to the application of AM to components that require mechanical performance and oxidation resistance has been the lack of a full understanding of the influence of the manufacturing process on the oxidation behavior.

AM processes are challenging since they are multifactorial systems which include several parameters that impact the mesostructural and microstructural features of the printed parts, which in turn affects the mechanical performance and corrosion resistance [44]. Concerning the oxidation behavior of AM nickel-based alloys, prior studies have reported the influence of mesostructural defects of as-built samples. Specifically, high surface roughness and open porosity increase the reactive surface area during thermal oxidation, resulting in an increase in the mass gain in comparison to a grounded counterpart (i.e., control roughness)[14][10].

Microstructural features such as crystallographic texture and grain-boundary character affect the oxidation kinetics as well [82][14]. Laser-assisted microstructures typically exhibit columnar grains preferentially orientated along the build direction. Thereby, the grain-boundary density will vary according to the orientation of the cross-section taken to oxidize [82]. Concerning the grain-boundary character, as-built samples lack special grain-boundaries, which generally have better oxidation resistance [14]. The effect of other typical microstructural AM features on oxidation, such as residual stresses, post-treatment conditions, heterogeneous microstructure, and microsegregation, have been considered in [86].

Specifically for the alloy 625, microsegregation of the refractory-metal constituent is a typical microstructure feature with a potential effect on the oxidation behavior [94]. The typical microstructure after primary solidification consists of a refined cellular-dendritic structure of γ-Ni with Nb and Mo segregation in the interdendritic regions, where NbC and Laves phases can appear [9][94]. Studies on oxidation of AM-alloy 625 reported the formation of an external chromia that followed parabolic oxidation kinetics. The effect of the AM method on the oxidation kinetics is either null or detrimental, where faster kinetics are reported for the AM samples [79][9][94]. At 1050°C the kinetics differences are associated to a larger amount of $Nb_{1.5}Cr_{0.5}O_4$ in the as-built AM samples due to the higher Nb availability from the original segregation [9]. Other differences reported in the oxidation behavior are differences in the oxidation products formed [9][80] and decohesion of the scale in the case of the AM [74][83].

Effects of the manufacturing process on the steady-state oxidation have been explored; however, there is a lack of experimental data regarding the transient oxidation stage of AM samples. Complex microstructure driven by the continuing cooling and melting in the AM processes may affect the transient oxidation behavior. One of the more significant differences in

the microstructure of as-built AM samples and the wrought is the Nb and Mo segregation in the former. The refractories segregation could potentially affect the formation of transient products and thereby impact the oxidation kinetics and the properties of the formed scale.

To have a better understanding of the effect of the manufacturing process on the oxidation behavior, this study seeks to better understand the role of Nb and Mo segregation in the early-stage oxidation behavior of alloy 625 AM-samples and its comparison with the wrought and cast alloy.

5.1.2 Experimental Procedures

Gas atomized alloy 625 powder was used to fabricate the AM samples by two different processes: direct energy deposition (DED) and laser powder bed fusion (LPBF). These alloys were compared to cast and wrought 625. Table 5-1 shows the measured composition of the four samples (DED, LPBF, cast, and wrought) obtained by ICP spectroscopy conducted by Eurofins EAG Laboratories (https://www.eag.com/). Microstructural characterization of the four samples was carried out by optical microscopy (OM) (Zeiss Smart Zooms 5, Carl Zeiss AG, Oberkochen, Germany) and by field-emission scanning electron microscopy Apreo (FE-SEM) (ThermoFisher Scientific, USA) in backscattered electron (BSE) mode. A cross-section of each sample was prepared using standard metallographic procedures. Electron probe microanalysis (EPMA) (JXA-8100, JEOL, Japan) was specifically used to quantify the refractories segregation at 20kV acceleration voltage, 100nA beam current, 20-30 s of peak dwell time, and a 0.1 µm of beam diameter. A solid solution wrought sample of alloy 625 was used as a standard for the same analysis conditions used for the test specimens.

Prior to oxidation, coupons of approximate dimensions 1x1x0.3 cm^3 were cut and ground to a 1200-grit finish with SiC paper. Oxidation tests were conducted in an open furnace at 800°C for 24 min, 3h and 24 h. The oxidation kinetics were measured using a thermogravimetric analyzer (TGA). Heating and cooling rates were 99 and 50 °C/min, respectively for the TGA. Kinetic measurements for each sample were taken three times, and the values reported are the average of those measurements. After oxidation, surface topography analysis was performed using SEM and energy-dispersive spectroscopy (EDS). To examine the microstructure of the oxide scale and the subsurface changes, TEM cross-sections from the oxidized coupons were obtained using focused ion beam (FIB) milling. Resulting lamellae were analyzed in a scanning transmission electron microscope (STEM).

Table 5-1. Chemical composition (wt.%) comparison of Alloy 625 measured by ICP spectroscopy: wrought, cast, LPBF and DED

	Cr	Mo	Fe	Nb	Mn	Ti	Al	Si	Co	Ni
Wrought	22	8.79	4.16	3.93	0.08	0.33	0.19	0.22	< 0.05	Bal.
Cast	20.9	8.67	4.46	3.84	0.28	0.25	0.21	0.17	0.14	Bal.
LPBF	20.4	8.93	0.74	4.29	0.04	0.34	0.27	0.11	0.16	Bal.
DED	20.6	8.78	0.74	4.19	0.04	0.33	0.27	0.11	0.17	Bal.

5.1.3 Results and Discussion

5.1.3.1 Initial Microstructure Characterization

Figure 5-1 shows representative as-processed microstructures of the four samples: wrought, cast, LPBF and, DED. The wrought sample shows a homogeneous equiaxed grain structure with annealing twins. Some primary and secondary carbides can be found, with the latter being predominantly located at the grain boundaries. On the other hand, the cast and as-built AM samples exhibit a cellular dendritic morphology. The dendritic regions correspond to

gamma-Ni(Fe,Cr) and the interdendritic regions show segregation of Nb, Mo, Si, and Ti. The interdendritic regions of the cast alloy exhibit two kinds of precipitates: NbC and Laves phase; whereas the DED sample shows exclusively Laves phase, and the LPBF sample does not exhibit distinguishably discrete phases. The NbC precipitates are characterized by a blocky shape, whereas the Laves phase displays a script-like shape. Despite showing the same dendritic morphology, the structure size and segregation extent varies among the processing methods. The interdendritic spacing within the LPBF structures is 0.40±0.08 μm, for DED it is 2.30±0.65 μm, and for cast it is 42.19±11.50 μm.

Regarding segregation, the cast alloy shows significant Ti and Si contents of 3.7 wt.% (in the NbC) 2.7 wt. % (in Laves precipitates), respectively, in the dendritic regions. However, although the measured Si and Ti interdendritic contents in the LPBF and DED samples were generally higher than those in the dendritic regions, their variability is in the margin of error of the EPMA measurements (± 0.1 wt.%). As a result, it is not possible to reach a quantitative conclusion about the partitioning of Ti and Si during the AM solidification processes.

On the other hand, the significant Nb and Mo interdendritic contents compared to those measured in the dendritic regions in the four samples allows for confidently calculating the segregation ratio (i.e., the ratio between the maximum and minimum concentration). Figure 5-2 displays the Nb and Mo segregation ratios as a function of the processing method. The cast shows the highest Nb and Mo segregation ratios, followed by DED and LPBF. Besides, the Nb segregation ratio is systematically higher than the Mo. The segregation is the result of non-equilibrium solidification. The dendrites solidify first, and the last liquid remains in the interdendritic region. In accordance with the results, Nb and Mo partitioning to the liquid during solidification has been widely reported in nickel-based alloys [32], [33], [95].

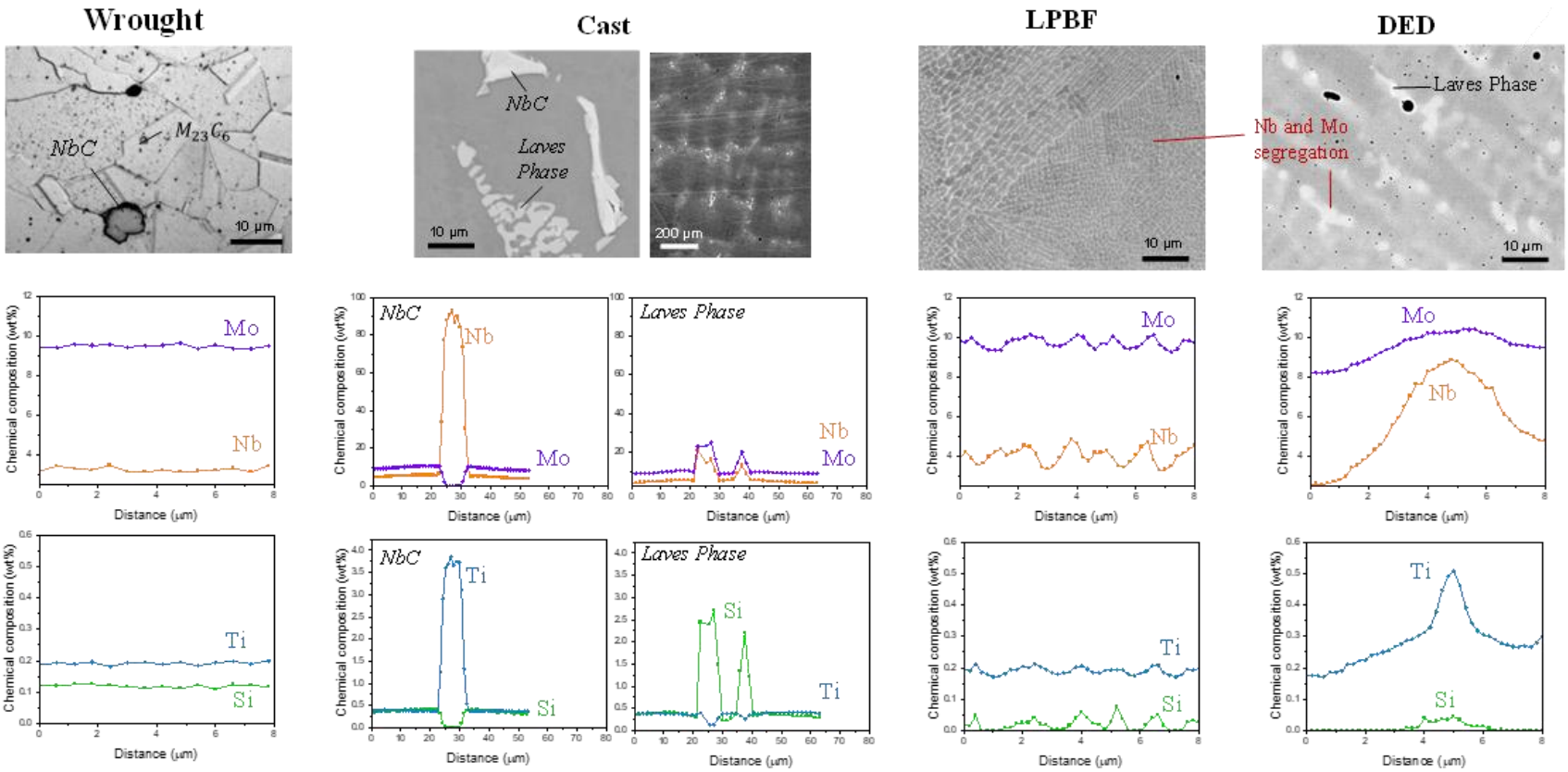

Figure 5-1. SEM micrographs of cross-sections and composition profiles measured by EPMA of wrought, cast, LPBF and DED alloy 625.

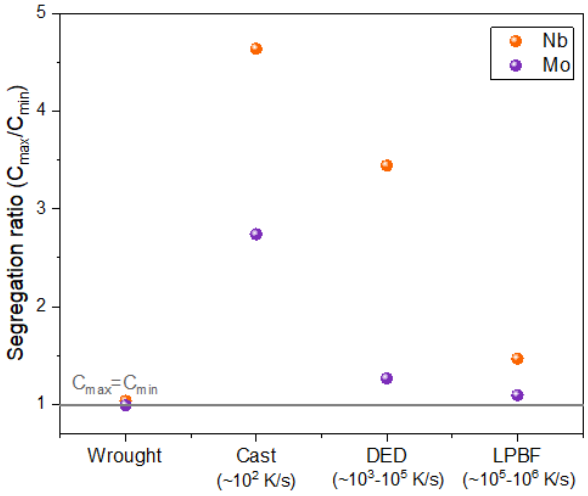

Figure 5-2. Nb and Mo segregation ratio as a function of the Alloy 625 manufaturing process. A reference for no segregation is indicated by a horizontal grey line when the segregation ratio equals 1. The concentrations used were obtained by using EPMA.

The segregation variation among the samples results from differences in the cooling rate among manufacturing processes. The typical cooling rate of the cast alloy is on the order of 10^2 K/s, DED is on the order of $10^3 – 10^5$ K/s, whereas LPBF is on the order of $10^5 – 10^6$ K/s. Figure 2 shows that the Nb and Mo segregation decreases as the cooling rates increases. At a slow cooling rate, Nb, Mo, Si and Ti have more time to partition preferentially to the liquid, leading to increased segregation in terms of concentration and spread area. High segregation during solidification leads to a higher fraction of the final solidification products (i.e., NbC and Laves phase). To summarize, the segregation of elements and the fraction of final solidification products both decrease as the cooling rate increases in both laser-assisted additive manufacturing processes and casting.

5.1.3.2 Isothermal Oxidation Kinetics

Oxidation tests were conducted at 800°C for 24h. No spallation was observed for any of the coupons tested. Figure 5-3 shows the mass gain per surface area as a function of the exposure time. The mass gains were confirmed to follow parabolic behavior for the four samples, suggesting that the oxidation kinetics were diffusion controlled. In accordance with literature, the LPBF and DED samples show higher final mass gain than the wrought [9], [94]. Higher mass gains in the LPBF and DED samples than in the wrought are correlated with a more convoluted scale (rougher) and a smaller chromia grain size (in width) [94]. The impact of changes in the scale composition and transient products in affecting the oxidation kinetics will be discussed later in this chapter.

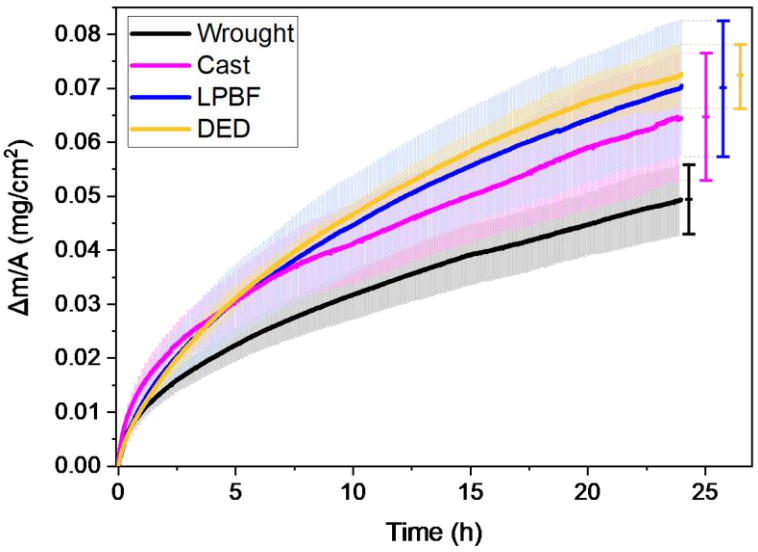

Figure 5-3. Isothermal oxidation kinetics at 800°C for 24h in dry air of alloy 625: wrought, cast, LPBF and DED. Measurements were conducted using the TGA.

In the case of the cast alloy, its initial mass gain is the highest up to approximately four hours. However, the final mass gain of the cast alloy is higher than the wrought but lower than the LPBF and DED samples. Additionally, the error bars for the final mass gain are significantly

higher in the LPBF and cast alloy samples, indicating a high variability in oxidation behavior within the same sample type.

Table 5-2 presents the parabolic rate constants calculated using linear and parabolic fitting methods. The differences that are found using the two approached can be summarized as follows:

- **Linear fitting ($\Delta m/A$ vs. $t^{1/2}$ plot)**, where $\Delta m/A = \sqrt{k_p}\sqrt{t}$. This equation correlates the constant rate (k_p [g^2 $cm^{-4}s^{-1}$]), with the mass gain per surface area ($\Delta m/A$ [g cm^{-2}]), and the exposure time (t [s]). This method is reliable for calculating the steady state constant rate [96], and allows to evaluate secondary effects on the oxidation constant rate (e.g., oxide grain growth).

  In this study, constant rates were calculated using linear fitting based on experimental data collected between 9 and 24 hours (ensuring to be in the steady-state oxidation regime). Calculations that considered shorter times were imprecise due to a poor linear fitting. Oxidation behavior in early stages typically leads to non-parabolic kinetics.

- **Complete parabola fitting (t vs. $\Delta m/A$ plot),** where $t = A + B\left(\frac{\Delta m}{A}\right) + C\left(\frac{\Delta m}{A}\right)^2$ and $k_p = 1/C$. A linear fitting typically confirms that the oxidation rate is controlled by the diffusion of the reactive species through the scale [97] However, protectiveness of initial transient oxides, and additional interfaces formed by additional reactions could affect the oxidation rate as well. This method of fitting accounts for mixed (diffusion/reaction) control and a transient regime [98].

Table 5-2. Parabolic rate constant comparison for alloy 625 oxidation in air at 800°C for 24h

	k_p [$mg^2\,cm^{-4}h^{-1}$] **Linear fitting (Δm vs. $t^{1/2}$ plot)**	k_p [$mg^2\,cm^{-4}h^{-1}$] **Complete parabola fitting (t vs. Δm plot)**	**Difference between fitting methods** $\left\|1-\frac{k_{p\ (lin.\ fitt.)}}{k_{p\ (Com.\ Par.\ fitt.)}}\right\|$
Wrought	1.0 ± 0.3 E-4	1.0 ± 0.4 E-4	0 %
Cast	1.6 ± 0.6 E-4	1.9 ± 0.8 E-4	16 %
LPBF	2.3 ± 0.8 E-4	2.1 ± 0.7 E-4	10 %
DED	2.7 ± 0.7 E-4	1.6 ± 0.5 E-4	69 %

When comparing the calculated oxidation rates, it was found using both methods that the wrought specimen formed the slowest growth oxide. The trend for the linear fitting follows in the order k_p (wrought) < k_p (cast) <k_p (LPBF) < k_p (DED). The trend for the complete parabolic fitting is in the order k_p (wrought) < k_p (DED) <k_p (cast) < k_p (LPBF). The purpose of the third column of Table 5-2 is to compare the oxidation rates for the same sample using different methods. It shows that irrespective of the fitting method used, the k_p (wrought) value was the same. However, the calculated oxidation rate for the DED differed ~70% between them, followed by the one calculated for the cast alloy with a difference of 16%. Differences between the rates calculated by different methods come from secondary effects including additional reactions, products, and interfaces involved in the transient oxidation. Therefore, the transient oxidation has a significant impact on the DED and cast alloys, but none on the wrought.

Instantaneous rate constants (k_p^i) were calculated to have a better understanding of the measured kinetics. We obtain the instantaneous rate constant from differentiating the simplified parabolic law ($(\Delta m/A)^2=k_p t$), as follows:

$$\frac{d\left(\left(\frac{\Delta m}{A}\right)^2\right)}{dt}=\frac{d\left(k_p t\right)}{dt} \qquad \textbf{(5-1)}$$

$$2\left(\frac{\Delta m}{A}\right)\frac{d\left(\frac{\Delta m}{A}\right)}{dt} = k_p^i \quad \textbf{(5-2)}$$

In Figure 5-4, we can see how the oxidation rate changes over time. Ideally, if the oxide scale properties and boundary conditions stay the same, the oxidation rate should remain constant. However, the trend shows a high initial rate that gradually stabilizes and reaches a steady state. It took around 5 hours for both the wrought and DED samples to reach this point, while the LPBF and cast samples took longer (approximately 20 and 22 hours, respectively).

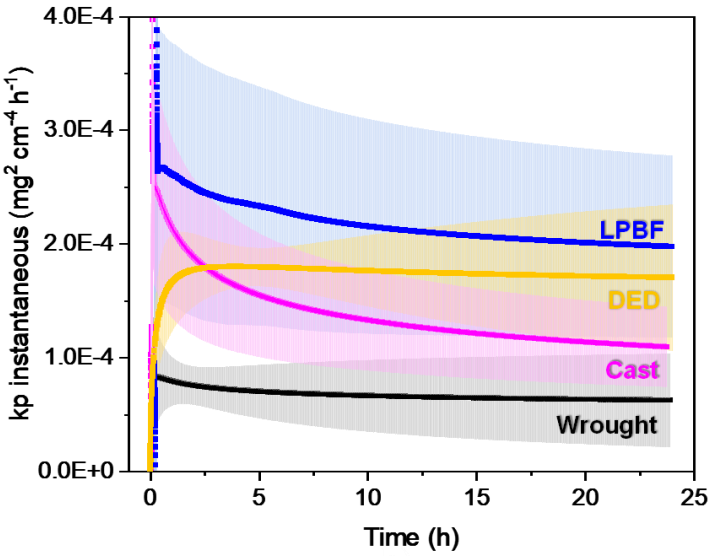

Figure 5-4. Instantaneous oxidation rate constant as a fucntion of oxidation time at 800°C.

5.1.3.3 Oxide Scale Topography

Figure 5-5, the surface morphologies of the oxidized coupons after 24 min and three hours of oxidation at 800°C are shown. The resulting oxide scale formed under these conditions is thin enough to display distinct colors under optical microscope-reflected light. The vertical lines correspond to the grinding lines. Regarding the color, the wrought specimen appears homogeneous, while the other samples show some heterogeneity. These color differences can be

attributed to variations in oxide composition and/or thickness due to different initial microstructure and crystallographic orientation.

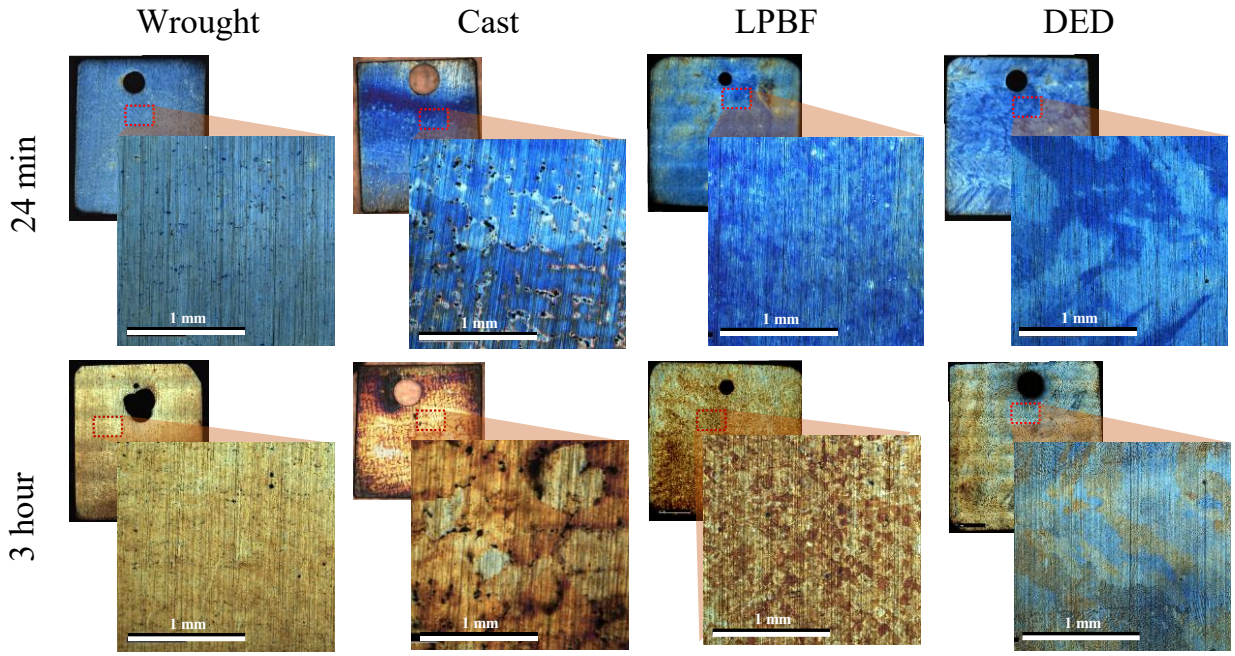

Figure 5-5. Low magnification optical micrographs of oxide surface of Alloy 625 at different manufacturing conditions and oxidation time exposures at 800°C. Differences in color are attributed to different interactions with light due to the variability in oxide thickness, oxide composition, and crystallographic structure.

For example, the dendritic microstructure from the as-built conditions can still be distinguished for the DED and cast alloy, showing a different oxidation behavior between interdendritic and intradendritic regions. To illustrate this, Figure 5-6 displays high magnification surface images of a DED sample after oxidation for 3 hours. Both oxidized (Figure 5-6a,b,c) and non-oxidized (Figure 5-6d) DED samples exhibit morphological and size similarities in their microstructures. The dark spots seen in the OM correspond to oxidized interdendritic regions. The absence of a color due to light reflection indicates the formation of a thicker product. The EDS composition in Figure 5-7d also confirms the thicker product on the

interdendritic region since it has a composition closer to chromia than the intradendritic region, which has similar values to the alloy composition.

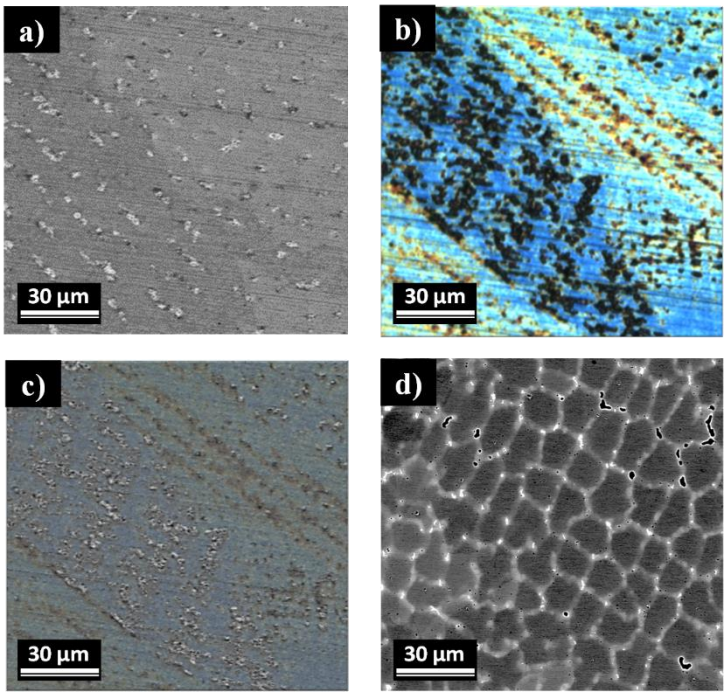

Figure 5-6. Topography of DED sample oxidized after 3h at 800°C: a) SE-SEM image, b) OM image, c) overlay of BSE-SEM and OM image. d). BSE-SEM image of DED as-built, as a reference of the microstrcuture scale. Dark sports in the OM image correspond to thicker oxide nodules formed on interdendritic regions.

Another contribution to the color intensity difference is the oxide thickness among alloy grains. It is observed that the regions with different color intensities correspond to the grains in both LPBF and DED samples. First, it is distinguishable that dendrite orientation is the same in the limits of those regions for the DED sample. Second, the size of these regions is similar to the grain size of each sample. There are also differences in measured composition between these regions. Figure 5-7c shows the EDS compositions in distinct color intensity regions for the LPBF sample. The darker region has a composition closer to that of chromia than the brighter region. The brighter regions still reflect the alloy composition, which is due to the thinner oxide.

Furthermore, it has been reported that the oxidation rate and scale composition are affected by grain orientation, particularly during transient oxidation [99], [100].

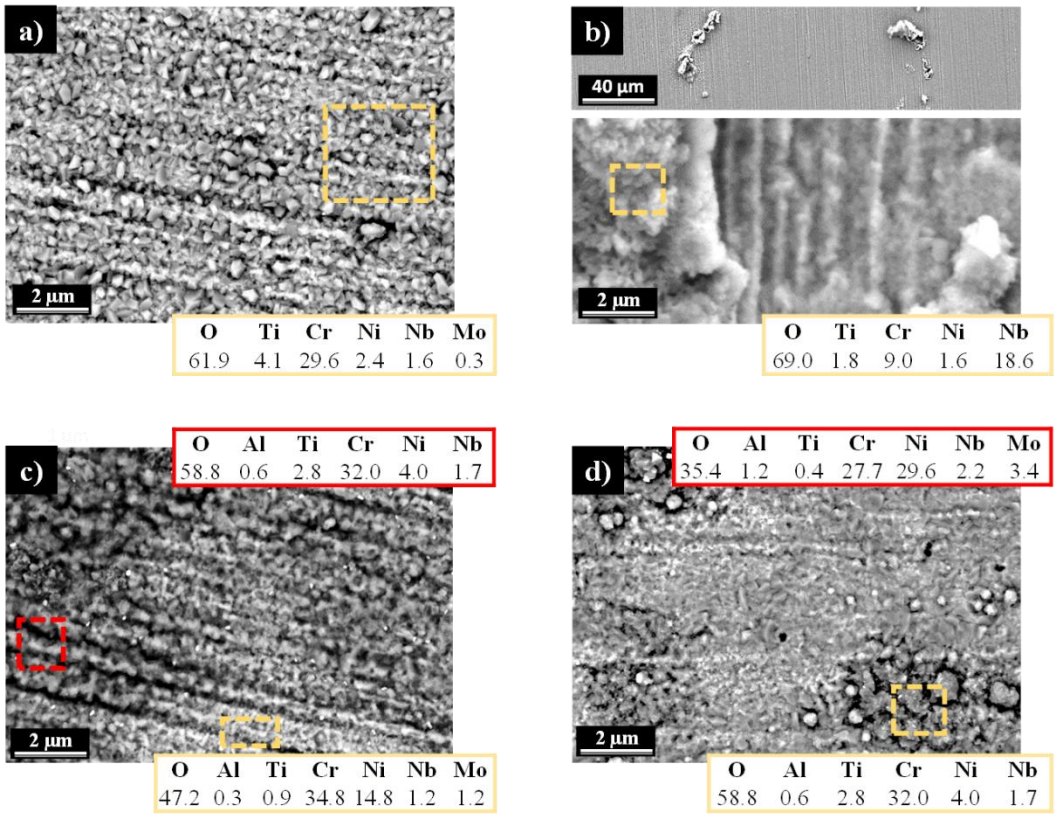

Figure 5-7. Surface SEM images of oxidized samples after 3h at 800°C: a) wrought, b) cast, c) LPBF, and d) DED. Elemental composition were measured by EDS and given in at.%.

5.1.3.4 Oxide Scale Morphology: Variability within the Sample

Cross-sectional micrographs of coupons after 24 min, 3h, and 24h oxidation at 800°C for the four samples are shown in Figure 5-8. Upon examining the scale formation, the wrought alloy forms a homogeneous and continuous chromia scale within the first 24 min, with slight variation in thickness after 3 hours and 24 hours. The LPBF sample also exhibits a continuous chromia scale at 24 min but with significant thickness variation, which is consistent with the color intensity variability observed from the surface images. Furthermore, voids at the alloy/scale

interface start to appear at 3h. The cast alloy shows a continuous chromia scale, but it is disrupted by the fast oxidation of the (Nb, Ti)C primary carbides and Laves phase located in the interdendritic regions. The resulting eruptions from the oxidation of these phases correspond to the dark spots in the surface micrographs. After 24h, a substantial volume expansion from the oxidation of these phases is observed, leading to noticeable localized deformation. The volume expansion associated with the oxidation of NbC to Nb_2O_5 can be 1.96 or 2.38, depending on the Nb_2O_5 crystal structure [101]. Similarly, the DED sample shows discontinuous chromia scale formation due to some oxide nodule formation coinciding with the interdendritic regions. The chromia scale becomes fully continuous after 3 hours, and the nodules spall before 24h. Additionally, multiple voids at the scale/alloy interface are observed at 24h.

In the very early stages of oxidation, oxygen molecules adsorb and dissociate on the alloy surface. Subsequently, oxide nuclei form and grow laterally to form a continuous oxide scale. The formation and growth of oxide nuclei are influenced by various factors, such as composition, surface deformation, heating procedure, alloy grain size, and crystallographic orientation [102]–[104]. In this study, the surface images and cross-sectional findings reveal different oxidation behaviors between the interdendritic and intradendritic regions for the DED and cast alloy samples.

.

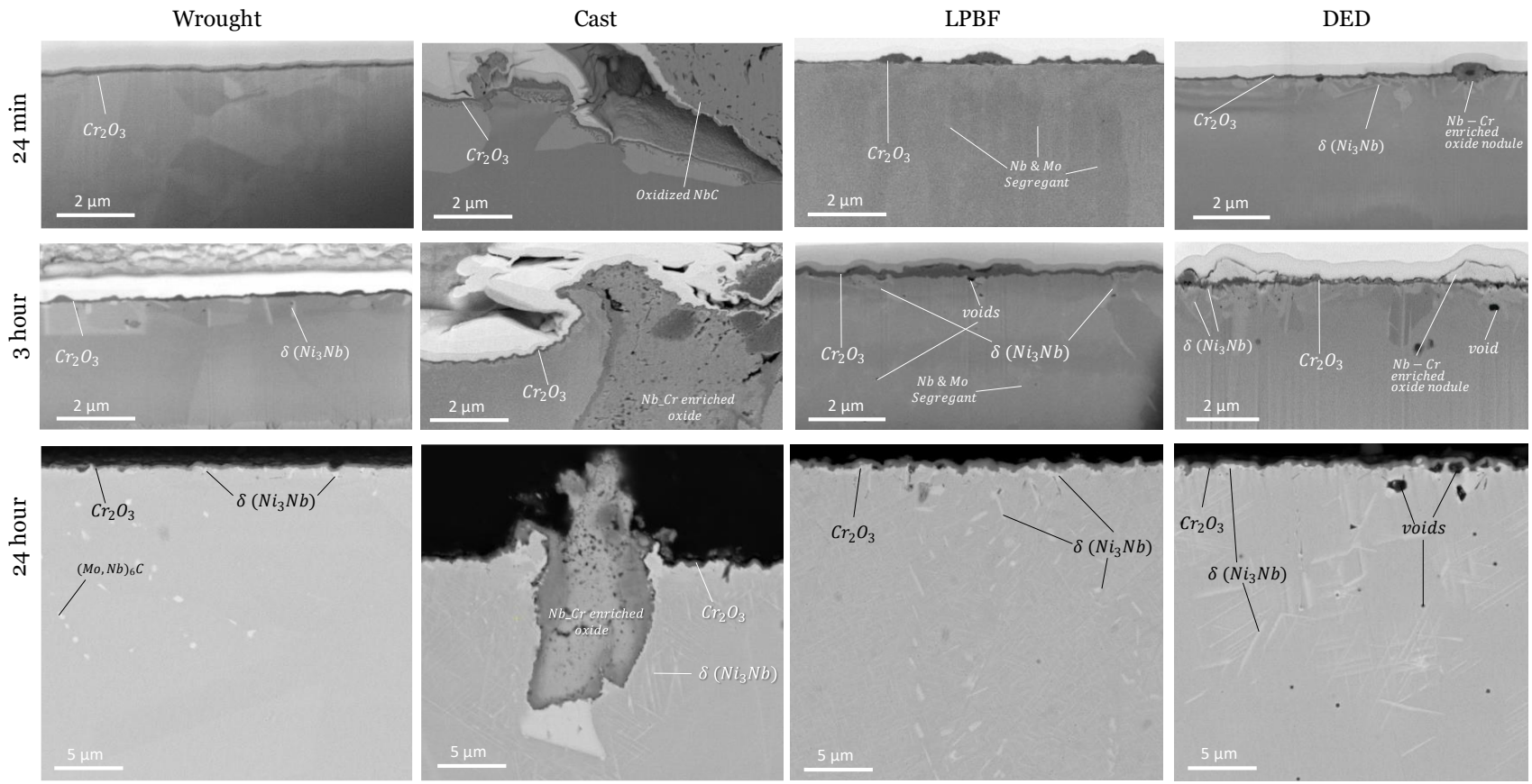

Figure 5-8. Cross-sectional BSE-SEM images of Alloy 625 (wrought, cast, LPBF, and DED) oxidized in air at 800°C for 24 min, 3h, and 24h. The wrought sample exhibits a continuous, uniform chromia scale, whereas LPBF establishes a variable thickness chromia at 24min. The cast and DED samples show a disrupted chromia by Nb-Ti-Cr oxide nodules formed on the interdendritic regions. After 24h, most of these nodules spall in the DED sample while most remain in the cast alloy.

Figure 5-9 shows STEM-BF cross-sectional images of the oxide scales formed after three hours at 800°C. The wrought sample shows a dense and continuous oxide layer formation. Similarly, the oxide scale formed in the intradendritic regions of the cast, LPBF, and DED samples is continuous and dense. However, the oxide scale formed in the interdendritic region of the cast, LPBF, and DED samples is thicker, porous, and finer grained. The finer oxide grains shown in the oxide nodules contribute to their relatively fast growth. The ratio between thicknesses of oxide grown on the intradendritic and interdendritic regions is approximately 2, 4, and 5 for the LPBF, DED, and cast, respectively. These numbers correspond to oxide scales measured from the surface down to the averaged location of the oxide/alloy interface. Oxidation of the Laves phase and carbides in the cast goes deeper into the alloy. Figure 5-8 shows the borderline of the NbC oxidation around ~12μm below the oxide/alloy interface. The higher the as-processed segregation (as it relates to either elemental quantity or spread), the larger the difference in thickness between the oxide formed on the interdendritic and the oxide formed on the intradendritic region.

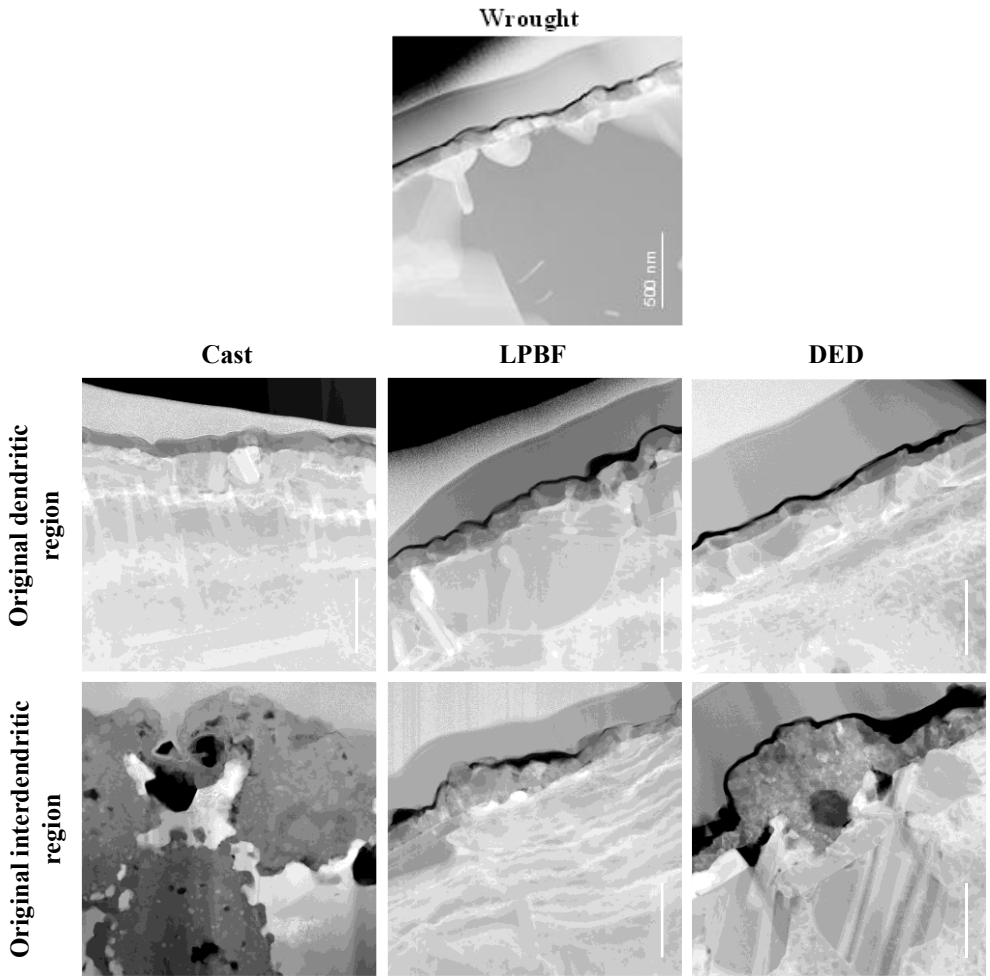

Figure 5-9. STEM-BF micrographs of the oxide scale formed at 800°C for 3h. Cast, LPBF, and DED samples present different oxidation behavior in the dendritic and interdendritic regions. The intradendritic regions, similar to the wrought alloy, show exclusively chromia. The interdendritic regions in the cast and DED show Nb-Ti-Cr oxide nodule formation.

Although the LPBF sample initially has a dendritic microstructure, there is no oxide-nodule formation as observed on the oxidized interdendritic regions of the DED and cast samples. This occurs because of the finer microstructure and lower segregation (in comparison); diffusion distance is short enough to form a continuous chromia scale, avoiding nodules formation.

The as-built AM samples have a pronounced crystallographic texture and a grain distribution that is widely spread compared to their wrought counterpart [105], [106]. This is due to a different thermal history along the builds and thermal fluctuations. The variability in

the grain-size distribution and crystallographic texture affects the initial stage of oxidation. Firstly, grain size and orientation determine affect the supply of chromium, thereby affecting the chromia establishment [82]. Secondly, depending on the cellular-dendritic orientation (crystallographic texture), a more abundant region with high segregation can be exposed, resulting in differences in the amount of nodules formed during the early-stage oxidation. These sources of variability account for the error bars observed in the measured kinetics for samples of the same type.

5.1.3.5 Oxide Scale Composition: Interdendritic Regions vs. Intradendritic Regions

Figure 5-10 presents the EDS composition maps of the oxides formed on the intradendritic region after three hours. The oxide scale that formed on the wrought alloy is composed of chromia and a discontinuous inner layer of aluminum and titanium oxide. The nominal chromium content of alloy 625 is enough to have selective oxidation of chromium [5]. Once the chromia layer forms, the partial pressure of oxygen at the scale/alloy interface drops, but above a level that allows for the formation of more stable oxides. In accordance with thermodynamic stability, aluminum and titanium could oxidize below the chromia scale. However, the concentration in the alloy is insufficient to form continuous layers of their oxides. As a result, the alumina and titania form as discontinuous products beneath the chromia in the wrought sample.

Similar to the wrought alloy, the oxide scale on the cast, LPBF and DED samples is chromia with a discontinuous inner layer of titania. However, these samples show a titanium enrichment in the chromia scale that the wrought alloy did not (as shown in Table 5-3). The titanium solubility in the chromia can be up to 18 at.% at 1000°C [107]. The chromia growth kinetics is affected by the Ti-doping in the Cr lattice since titanium (IV) has a different

valence state than chromium (III). Replacement of Cr^{+3} by Ti^{+4} creates cation vacancies in the chromia scale via the defect reaction [108],

$$3TiO_2 \rightarrow 3Ti_{Cr}^{\cdot} + V_{Cr}^{'''} + 6O_o^x \quad \textbf{(5-3)}$$

Where, $Ti_{Cr}^{\cdot}$ is a Ti^{+4} in a Cr site in the chromia lattice with a positive charge, and the $V_{Cr}^{'''}$ is a vacancy in a Cr site with a triple negative charge, and O_o^x is the oxygen ion in the oxygen sub-lattice. This assumes that the formed chromia is p-type. The cationic vacancies that result from the Ti^{+4} doping will enhance the chromium diffusion and in turn, lead to faster Cr_2O_3-growth kinetics. The observation of enhanced chromia-scale growth kinetics due to Ti^{+4} doping has been widely reported [109]–[112].

Table 5-3. Chemical composition (% at.) of external scale formed in the wrought, and on the intradendritic region of cast, LPBF and DED, measured by STEM-EDS.

	Wrought	Cast	LPBF	DED
O	67.5 ± 1.1	71.4 ± 1.4	68.0 ± 1.8	65.5 ± 5.0
Ti	0.6 ± 0.1	0.7 ± 0.3	3.0 ± 3.8	1.2 ± 0.4
Cr	31.1 ± 2.1	27.6 ± 1.4	28.2 ± 3.1	31.4 ± 6.7

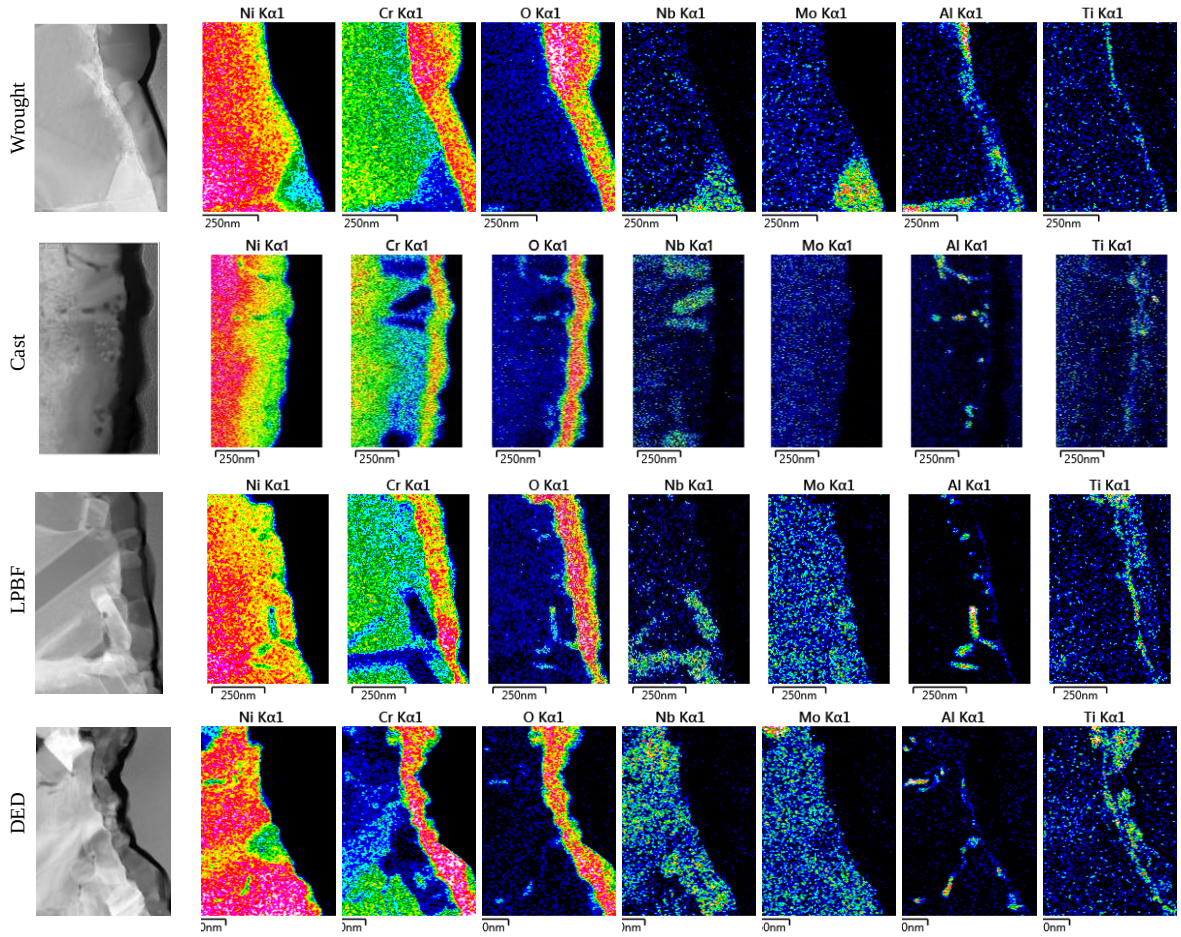

Figure 5-10. STEM-EDS maps for oxidized alloy 625 samples at 800°C for 3h. Cast, LPBF, and DED analyzed regions correspond to their respective intradendritic region. The scale corresponds to chromia with additions of Ti in the LPBF, DED, and cast alloys. The depletion of Cr in the subsurface and precipitates beneath the chromia scale (δ,σ-phase) can be observed in the four samples.

Figure 5-11 and Figure 5-12 show the composition distribution within the oxide nodules formed on the interdendritic regions of the DED and cast samples, respectively. The DED nodule consists of a Nb-Cr-Ti complex oxide, with a center of alumina. The nodule that is shown on the cast alloy is inferred to correspond to the oxidation of an initial Laves phase precipitate, where it is also composed of a complex oxide enriched in Cr, Ti, and Nb. A comparison of the composition of the oxide products grown on the interdendritic regions are presented in Table 5-4.

Table 5-4. Chemical composition (at. %) of oxide nodules grown on the interdendritic regions of cast and DED samples, measured by STEM-EDS.

	Cast	DED	
	Main body	Main body	Core
O	36.9 ± 3.2	71.2	69.9
Ti	1.5 ± 0.4	3.1	0.6
Cr	17.8 ± 6.6	16.5	0.4
Nb	43.8 ± 9.2	6.5	-
Al	-	2.5	28.7

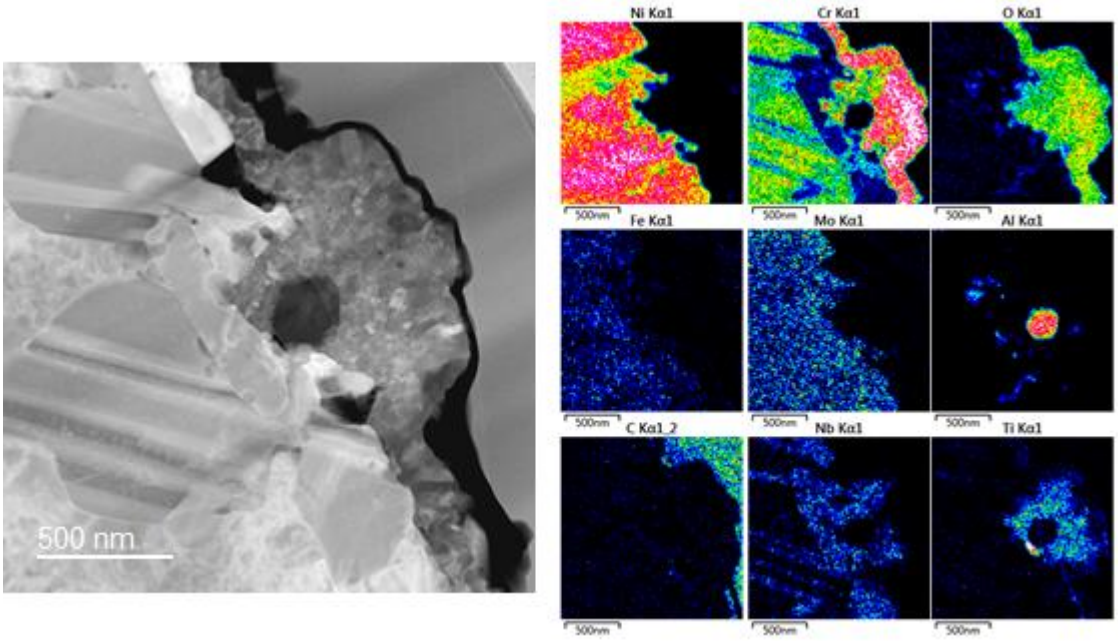

Figure 5-11. STEM micrograph and EDS of a representative Cr-Ti-Nb rich oxide nodule located at the interdendritic region of the DED sample oxidized after three hours at 800°C. The fast formation of the oxide nodule is consistent with a finer grain compared to the adjacent chromia scale. The nodule consists of a core of alumina enveloped in Ti-Cr oxide.

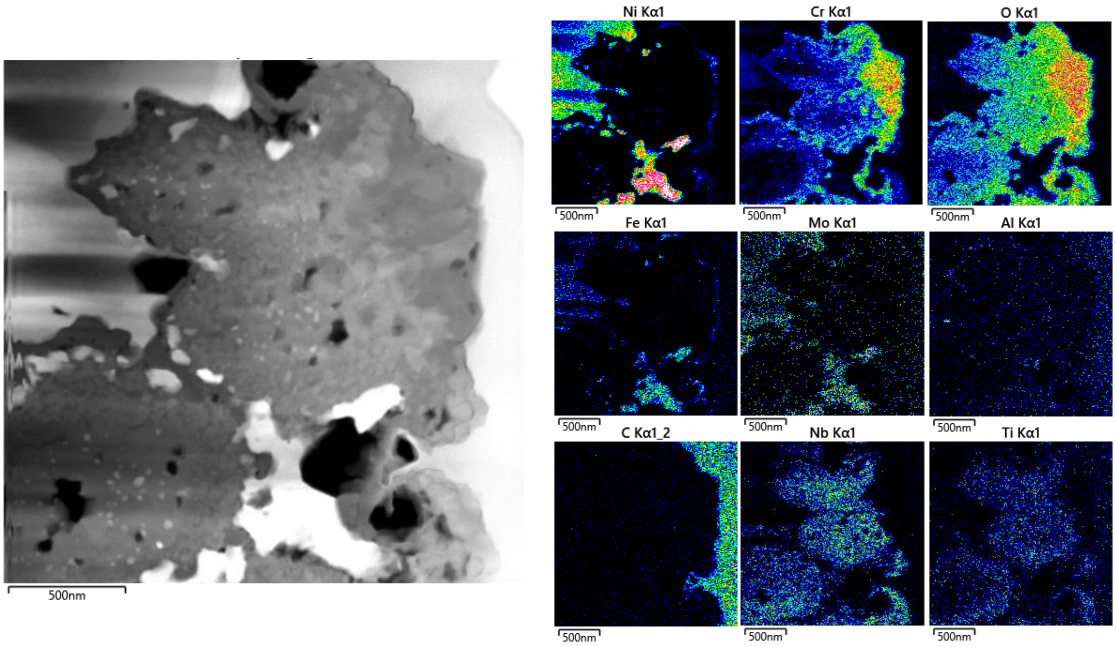

Figure 5-12. STEM micrograph and EDS of a Cr-Ti-Nb rich oxide nodule located at the interdendritic region of the cast alloy oxidized after three hours at 800°C. This specific oxide nodule corresponds to an oxidized Laves precipitate. The nodule shows a higher porosity and finer grain oxide consistent with the fast formation.

The interdendritic regions have a higher reservoir of the segregated elements (Nb, Mo, Ti, and Si) available to oxidize. From a thermodynamic point of view, all the segregated elements are susceptible to oxidizing at 800°C. In general, oxides with lower thermodynamic stability have a faster growth rate [104], [113]. Based on this generalization, it is anticipated that there will be Nb content present in the oxide nodules, but the absence of Mo is unexpected. However, at 800 °C MoO_3 is highly volatile [114], [115]. MoO_3 volatilization can cause porosity formation in the oxide nodules, compromising the integrity of the oxide nodules. Indeed, it has been reported that oxidation in flowing oxygen of Mo-containing Ni-15%Cr alloys reduces integrity of the chromia scale and hinders the chromia establishment [116].

It was observed that most nodules detached from the DED sample after 24h of oxidation, but the cast sample still had significant oxide nodules remaining after that same

time. Since the oxide nodules of the cast sample are associated with oxidation of Laves phase and carbide precipitates, the nodule spallation is dependent on the exposed precipitate depth. Shallow precipitates will detach faster than deeper ones. It is expected that the oxidation of deep precipitates continues as the oxygen ingress increases, as the one shown in Figure 5-8. Eventually, the chromia will continue forming at the oxidized precipitate/alloy interface and passivate the alloy.

5.1.3.6 Oxidation-induced Changes to the Alloy Subsurface

Although alloy 625 is primarily solid-solution strengthened, under certain heat treatment δ-phase [$(Ni, Cr)_3(Nb, Mo)$] and σ-phase [Mo-Ni-Si-Cr-Nb] precipitates may form. (σ+δ)-phase precipitates were observed both beneath the chromia scale (referred to as alloy subsurface) and throughout the bulk (either inter- and/or intergranular). Differences between the alloy subsurface and bulk are visible among the samples after 24 minutes and 3 hours of oxidation, respectively.

At 24 min, the DED exhibited significant δ-phase formation in the subsurface, localized preferentially at the interdendritic regions. Most of the precipitates are plate-like and blocky shaped. However, in other samples, no precipitate formation was observed beneath the chromia at this time.

After 3h, the wrought and LPBF samples exhibit plate-like δ-phase precipitates uniformly distributed in the subsurface. Additionally, the bulk of the LPBF sample shows δ-phase formation along its grain-boundaries. On the other hand, the DED sample shows coarsening of the δ-precipitates in the subsurface, keeping the highest phase fraction at the intradendritic regions.

After 24h of exposure the trend of (σ+δ)-phase fraction in the subsurface (beneath the chromia) follows the order DED > LPBF > wrought. The LPBF bulk shows intragranular

needle-like δ-precipitates with coarser intergranular δ-precipitates. The bulk of the cast and DED samples show needle-like δ-precipitates along the interdendritic regions and globular clusters at Laves phase locations.

The δ-phase precipitates in the bulk, cast, LPBF and DED samples formed earlier than in the wrought alloy, localized preferentially on the interdendritic regions and grain boundaries. As-built AM samples have mainly high-angle grain boundaries [85] which exhibit a terrace structure with dislocations, leading to a higher driving force for nucleation compared to low-angle boundaries in wrought samples [117], [118]. Additionally, an earlier δ-precipitation has been predicted using the interdendritic composition (high segregation) for alloy 625 fabricated by LPBF, than the one shown by the wrought alloy [20], [119]. The transformation diagram in Figure 5-13 confirms this behavior. The earlier δ-precipitation is explained by the positive impact of Nb and Mo segregation in the driving force for δ-precipitates to nucleate from the γ-matrix. Following the same argument, an even earlier precipitation is expected for the DED sample. There are three marks on the TTT diagram for the three studied times, i.e., 24min, 3h, 24h. According to this, there is no expected δ-precipitation at 24 min for the LPBF and wrought alloys. At 3h, it is expected to observe δ-precipitates in the LPBF sample but not in the wrought alloy. However, δ-precipitates beneath the chromia are observed at 3h in the wrought alloy. This is explained by Nb enrichment induced by the selective oxidation of Cr. There is a positive chemical relation between the Nb and Cr; in other words, the activity of Nb decreases with Cr depletion. This results in a chemical potential gradient in the subsurface, which is a driving force for Nb uphill diffusion [5].

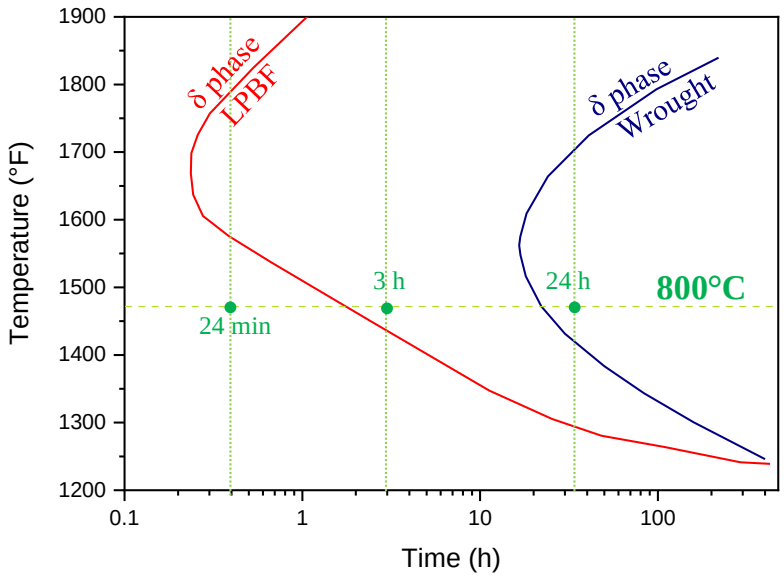

Figure 5-13. TTT Diagram for alloy 625: differences influenced by segregation [20], [119] **The LPBF prediction is based on the interdendritic composition. The earlier precipitation in the LPBF compared to the wrought is correlated with Nb enrichment.**

On the other hand, δ-phase not only shows earlier precipitation but also a greater phase fraction in the interdendritic segregation. The positive effect of Nb segregation on δ-precipitates growth kinetics has been reported [119], where this effect is stronger at 800°C than other tested temperatures (870°C). Figure 5-14 shows a δ-phase equilibrium map at 800°C as a function of Cr and Nb composition, which was predicted using ThermoCalc-TCNI8. This map illustrates what will be the δ-phase fraction predicted at equilibrium at determined Cr and Nb composition. The composition ranges were determined by EPMA data taken from the as-built AM samples and from the subsurfaces of oxidized wrought, LPBF, and DED samples. The triangle and circle marks overlapping the map correspond to spot measurements indicated in the micrographs of LPBF and DED as-built samples. The red marks correspond to the highest segregation of each sample, and the blue diamond corresponds to the nominal composition of the alloy. On these bases, the highest segregation composition given by the LPBF and DED samples will precipitate 3.2 and 7.7 times the δ-

phase fraction predicted for the nominal composition. This indicates the positive impact on Nb segregation and Cr depletion in the δ-phase fraction predicted at equilibrium at 800°C.

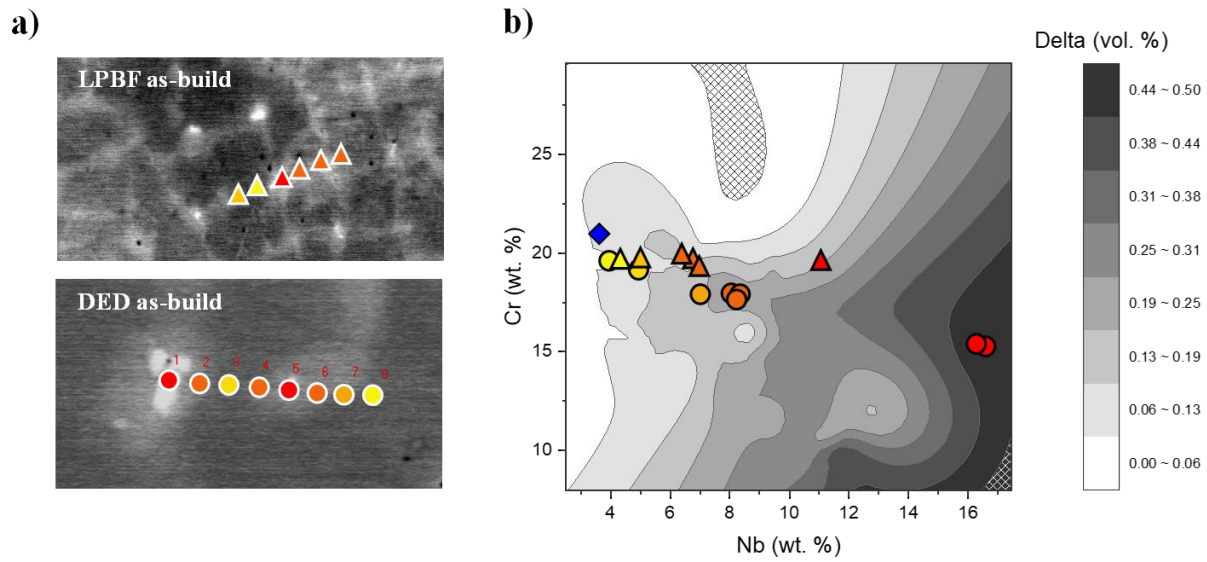

Figure 5-14. Compositional spots overlap in the map of the δ-phase fraction at equilibrium: a) DED and LPBF as-built compositional spots measured by EPMA. This map shows the predicted equilibrium δ-phase fraction at 800°C as a function of the Cr and Nb compositions. Grid pattern regions are outside the calculated range. The blue diamond correponds to the nominal composition of alloy 625.

When using the δ-phase equilibrium map in a wrought oxidized sample, the mentioned Nb enrichment toward the chromia/alloy interface can be observed (see Figure 5-15). Similar to the interdendritic segregation, the highest segregation right in the interface will precipitate 7.2 times the δ-phase fraction predicted for the nominal composition. This explains the greater δ-phase fraction beneath the chromia scale compared to the bulk in alloy 625 samples, regardless of the manufacturing process.

An interesting observation comes after examining the cast sample. Since the NbC is thermodynamically more stable than δ-phase [119], less "interdendritic" Nb is available for δ precipitation. However, there is still evidence of earlier precipitation and greater δ-phase fraction in the segregated areas compared to the intradendritic regions.

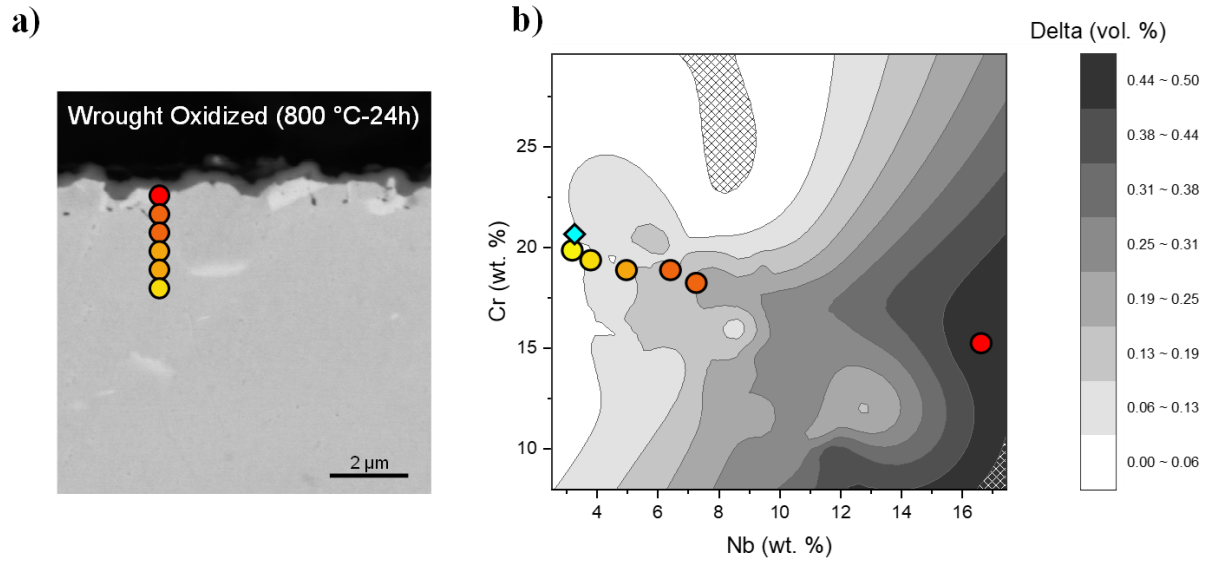

Figure 5-15. Compositional spots overlap in the map of the δ-phase fraction at equilibrium: a) oxidized wrought subsurface compositional spots measured by EPMA. This map shows the predicted equilibrium δ-phase fraction at 800°C as a function of the Cr and Nb compositions. Grid pattern regions are outside the calculated range. The blue diamond correponds to the nominal composition of alloy 625.

Summarizing, the earlier δ-phase formation preferentially located at the interdendritic regions is attributed to both Nb enrichment from the oxidation-induced up-hill diffusion and the segregation from the manufacturing process. As mentioned previously, the higher Nb segregation increases the nucleation driving force, growth kinetics of δ-phase [119], and δ-phase fraction predicted at equilibrium.

5.1.3.7 Effect of Refractories Segregation on the Surface and Subsurface Evolution During Early Stages of Oxidation at 800°C

The following deductions apply to coarse dendritic microstructures where the diffusion distance between dendrites does not allow the initial chromia formation, as the DED and cast alloy. Figure 5-16a illustrates the microstructure before thermal exposure, with high Nb and Mo segregation levels found in interdendritic spaces. When exposed to air at 800°C, the initial oxidation products of the inter- and intradendritic regions vary due to their differences in composition (Figure 5-16b). Intradendritic regions show Nb depletion/Cr

enrichment, resulting in the establishment of chromia without any indication of transient products or changes in the subsurface. On the other hand, interdendritic regions exhibit complex oxide nodules formation (Nb-Cr-Ti-oxides) due to the fast-growth oxides that overtake the slow-growing and more protective chromia. Since the oxide nodules still have approximately 18at.% of Cr, the depletion of Cr leads to even higher levels of Nb segregation than in the interdendritic regions in the bulk, resulting in earlier δ-precipitation in the interdendritic regions below the nodule.

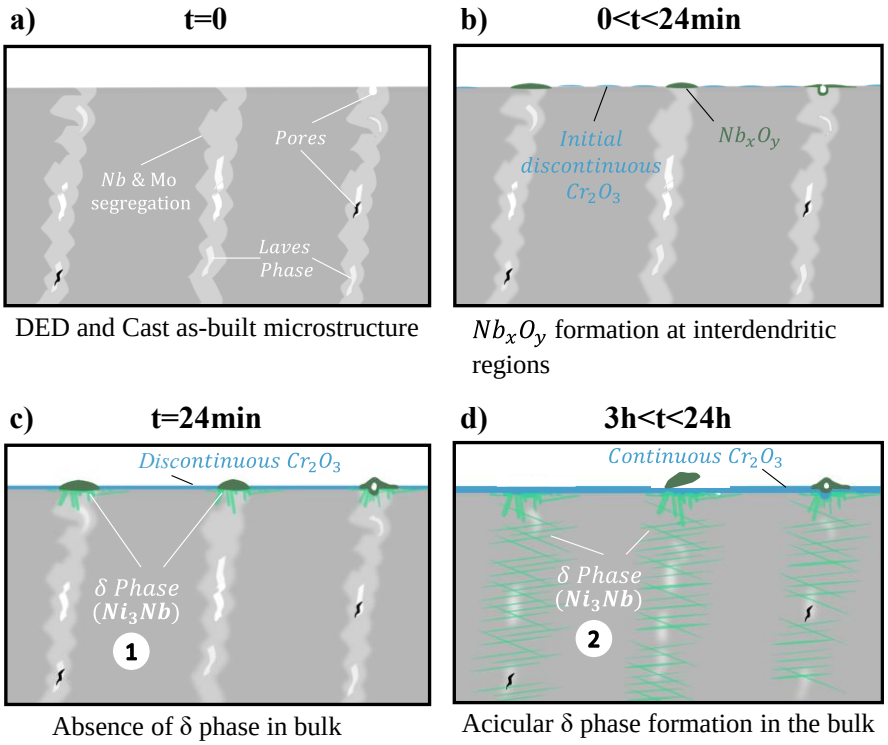

DED and Cast as-built microstructure

Nb_xO_y formation at interdendritic regions

Absence of δ phase in bulk

Acicular δ phase formation in the bulk

Figure 5-16. Schematic of alloy and subsurface phase evolution with oxidation time at 800°C for DED and Cast alloy. Intradendritic regions exhibit chromia formation, while interdendritic regions show Nb-Ti-Cr oxide nodules formation. After 3h, the chromia establish beneath the chromia along the entire sample, and the oxide nodules stop growing and spall at longer exposure times. The delta phase beneath the chromia precipitates earlier beneath the chromia (1) than in the interdendritic bulk (2).

The Nb-Cr-Ti oxide nodules formed lower the oxygen potential at the oxide scale/alloy interface, resulting in reduced oxygen permeability into the alloy. This promotes the outward diffusion of chromium, leading to the formation of chromia below the Nb-Cr-Ti

oxide nodules. Figure 5-16d illustrates that once the chromia is established, the Nb-Cr-Ti oxide nodules tend to have limited growth due to the low solubilities and diffusion through the chromia scale of the nodule components (Nb, Ti). As the chromia grows, nodules detach and spall because of the pores in their structure and poor adhesion.

The formation of Nb-Cr-Ti oxide nodules on the interdendritic regions has a significant impact on oxidation kinetics. The impact is greater when there is a higher Nb and Mo segregation. This is clear in the cast alloy, which has the coarsest microstructure and highest refractories segregation. The measured oxidation kinetics in Figure 5-4 showed that the cast sample exhibited the highest initial oxidation rate in the first three hours and took the longest to reach a steady state. In contrast, the wrought sample, which did not show Nb and Mo segregation, formed the chromia scale directly and was the first to reach steady-state kinetics.

5.1.4 Conclusions

Transient oxide products at 800°C: Wrought alloy 625 forms a more homogeneous and continuous chromia layer than AM samples at 800°C in air. The oxidation kinetics were lowest for the wrought alloy, with relatively fast establishment of a continuous chromia scale due to the lack of disruption caused by the formation of less-stable oxide products.

High variability of oxidation behavior amongst the LPBF, DED and cast samples is due to their initial microstructure differences, stemming from the manufacturing processes. Coarse structures and high segregation of Nb, Mo, Ti in the interdendritic regions promote the formation of Ni-Cr-Ti oxide nodules that disrupt the chromia scale. The transient products increase the initial oxidation rates for the DED and cast alloys. After a continuous chromia scale is established, the nodules stop growing and eventually spall due to poor adhesion (refer to Figure 5-8).

The LPBF sample's finer microstructure and lower segregation, in comparison with the DED and cast samples, led to a notable reduction in the transient products formed.

Subsurface evolution during oxidation at 800°C: The formation of abundant and coarse δ-phase (Ni_3Nb) occurs beneath the Cr_2O_3 scale in the interdendritic regions. Enrichment of Nb in these regions leads to a higher driving force for precipitation and faster growth kinetics of the resulting δ precipitates. The Nb enrichment arises from both the as-built microstructure of the manufacturing process and the Nb up-hill diffusion induced by chromium depletion during oxidation (refer to Figure 5-14 and Figure 5-15).

5.2 Oxidation Behavior at 800°C of Alloy 625: Role of Elemental Segregation

This chapter is modified from the published paper: G. de Leon Nope, G. Wang, J. M. Alvarado-Orozco, and B. Gleeson, JOM 74, 1698 (2022).

5.2.1 Introduction

Oxidation of wrought 625 in air at high temperature generally results in the formation of a dense and continuous Cr_2O_3 (chromia) scale and consequential subsurface chromium depletion [4]. In turn, the chromium depletion causes uphill diffusion of the niobium from within the alloy, leading to niobium enrichment beneath the chromia scale. This niobium enrichment can lead to the discreet formation of δ-phase up to 1000°C [5].

The as-built AM microstructure of Alloy 625 typically has a dendritic morphology with high segregation of Nb and Mo in the interdentric regions [9]. Although Alloy 625 is primarily a solution-strengthened alloy, metastable γ″-Ni_3Nb and stable δ-Ni_3Nb precipitates may form during heat treatment. AM samples show precipitation of both phases earlier than the wrought alloy due to a relatively a high extent of segregation in the interdendritic regions [120]. In relation to this, Ramenatte et al. [7] reported many subsurface voids after high-temperature oxidation of LPBF 625 and attributed the observation to more extensive uphill diffusion of Nb within the interdendritic regions. Apart from this, there has been no direct correlation reported between the microstructural differences of the AM samples and their oxidation behavior.

This chapter aims to understand the effects of microstructural variables stemming from AM processing on the oxidation behavior at 800°C of Alloy 625, with particular focus placed on the effect of Nb segregation.

5.2.2 Experimental Procedures

Three differently processed samples of Alloy 625 were studied. As a reference, a wrought Haynes 625 plate (AMS 5599) was used. The two AM 625 samples were fabricated by either direct energy deposition (DED) or laser powder bed fusion (LPBF). Table 5-5 presents the IN625 nominal composition obtained experimentally using a Varian SpectrAA 220 Atomic Absorption Spectrometer (Varian, USA) and combustion tests with the Leco CNS-2000 equipment for carbon (Leco Corp., USA). The only notable difference is that the wrought has 4 wt% more iron than the AM powder feedstock.

Table 5-5. Chemical composition (wt.%) comparison of Alloy 625: nominal AMS 5599, and experimentally measured Haynes wrought and AM powder.

	Ni	Cr	Fe	Mo	Nb	Co	Ti	Al	Mn	Si	C*
Nominal AMS 5599	58.0 min	20.0-23.0	5.0 max.	8.0-10.0	3.15-4.15	1.0 max.	0.40 max.	0.40 max.	0.50 max.	0.50 max.	0.10 max.
Haynes wrought	61.6	20.7	4.90	8.40	3.45	0.10	0.22	0.20	0.20	0.11	0.03
AM powder	65.3	20.7	0.80	8.50	3.81	0.20	0.33	0.26	0.07	0.06	0.02

The as-processed microstructures of each samplewere characterized by field-emission scanning electron microscopy Apreo (SEM) (ThermoFisher Scientific, USA) in backscattered electron (BSE) mode. Cross-sectional cuts of the AM samples were made parallel to the build direction and then prepared using standard metallographic techniques. Quantification of the refractory-metals segregation in the DED and LPBF samples was conducted using electron probe microanalysis (EPMA) (JXA-8100, JEOL, Japan).

Oxidation tests were conducted using coupons of approximate dimensions 1x1x0.3 cm^3. Coupons of AM samples were cut normal to the built direction. Prior to oxidation, the samples were grounded with P600-SiC paper (20 μm grit size). The test coupons were then

cleaned in an ultrasonic bath in ethanol and acetone. Oxidation kinetics were measured in a symmetrical thermogravimetric analyzer (TGA) (S60/58629, Setaram, France) at 800 °C in air for 24 h. Heating and cooling rates were 99 and 50 °C/min, respectively.

Metallographic cross-sections of the oxidized samples were prepared. Additional sections of the thermally-formed oxide scales were obtained by using a Scios focused ion beam (FIB) (ThermoFisher Scientific, USA). Microstructural analysis of the oxide scale and associated subsurface was done using SEM and scanning transmission electron microscope (STEM) (JEM-2100F, JEOL, Japan). An image analysis of 12 SEM micrographs per sample was conducted to quantify the δ-phase fraction in the subsurface. An algorithm in Matlab was developed to binarize, apply a threshold, and quantify the subsurface δ-phase precipitates (that are exclusively in the immediate vicinity of the chromia scale, up to 1.5 μm below the oxide/alloy interface). Finally, compositional profiles throughout the cross-sections were measured by EPMA.

5.2.3 Results and Discussion

5.2.3.1 Meso and Microstructural Characterization

Figure 5-17 compares the microstructures of the wrought, LPBF, and DED as built. The Alloy 625 wrought was given conventional heat treatment (high solution annealing, low solution annealing, and stress-relieving). The wrought microstructure is characterized by equiaxed grains and globular carbides, where some of the grains exhibit twin boundaries. The AM samples had similar features and also distinctly different microstructures compared to the wrought. Both AM samples show molten pool marks wherein grains can be identified; some grains are elongated and cross more than one layer.

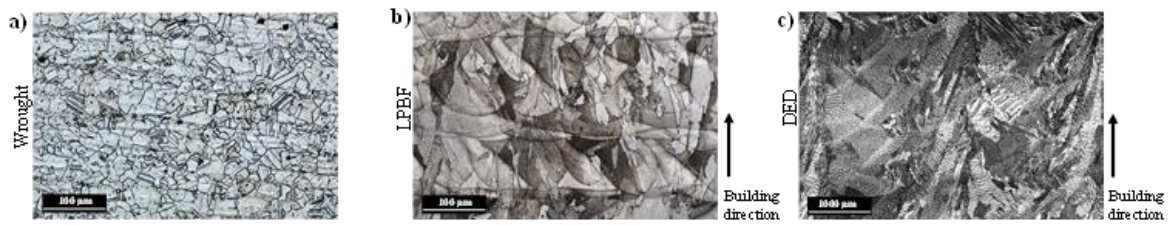

Figure 5-17.Optical micrographs of cross-sections of a) wrought b) LPBF as-built, and c) DED as-built.

Inside the grain, cellular-dendritic structures are revealed. Despite similarities, LPBF and DED structures differ in size; the cell size in the DED alloy was 12.1±1.3 µm, while the LPBF was 1.1±0.1 µm. Primary solidification features in the laser-assisted processes were determined by the temperature gradient in the liquid/solid interface (G) and the solidification growth rate (R) [121]. G/R determines the morphology structure, and GR (cooling rate) defines the structure size, i.e., grain size and cell size. The G/R ratio is in the same range for DED and LPBF, resulting in cellular-dendritic morphology. However, the cooling rate of DED (10^2 – 10^3 K/s) is much lower than that of the LPBF (10^5 – 10^6 K/s), resulting in a smaller cell size for the LPBF by one order of magnitude than DED.

Regarding the chemical composition, the AM samples exhibited refractory segregation in the interdendritic regions (brighter in the SEM micrographs). This Nb and Mo segregation during the primary solidification is expected by its low partition coefficients of 0.48 and 0.82, respectively [95]. The EPMA analysis (Figure 5-187) of the wrought sample shows a constant Nb and Mo content of 3.7 wt.% and 8.2 wt.%, respectively. In contrast, DED shows the highest Nb segregation at 16 wt.% and Mo segregation at 12.7%, while LPBF shows 8 wt.% for Nb and 9.2% of Mo. Differences in refractory segregation levels between AM processes are attributed to the differences in cooling rate. The lower the cooling rate, the lower the transformation rate, facilitating segregation. Manikandan et al.[122] reported that a decreasing cooling rate results in a minimization of Nb segregation and reduction of laves phase in an Alloy 718 welding.

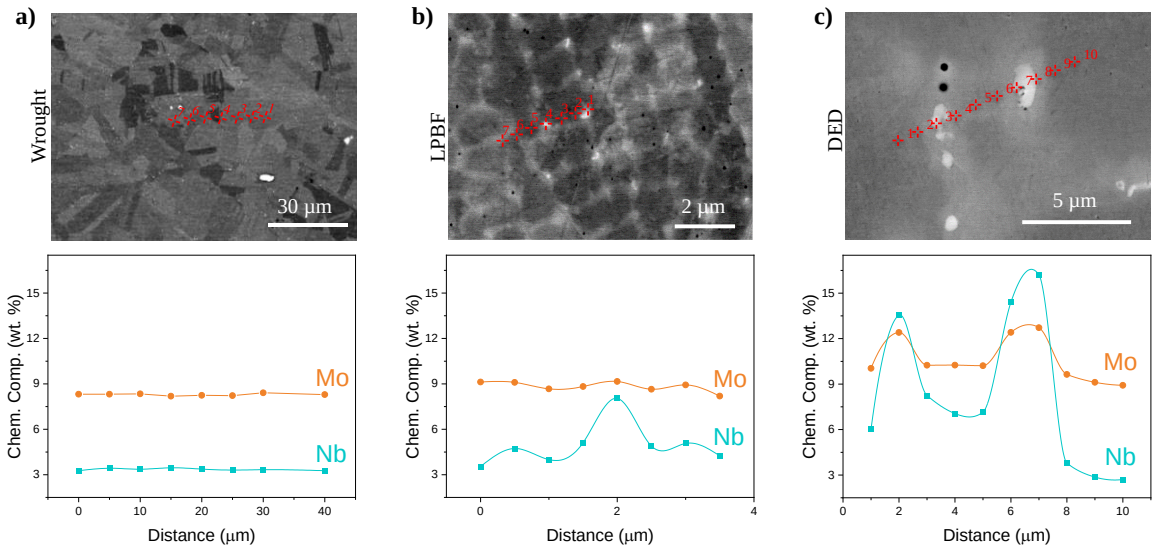

Figure 5-18. EPMA analysis results for Nb and Mo of a) wrought b) LPBF as-built and c) DED as-built.

Calculating the refractory ratio of the highest segregation in the interdendritic regions over the original powder composition, the Nb ratio is 4.0 for DED and 2.1 for LPBF; while the Mo ratio is 1.5 for DED and 1.1 for LPBF. For both AM processes, the Mo segregation was smaller than that of Nb. This may be ascribed to Mo having a lower diffusivity and a higher density than Nb [123].

Summarizing microstructural findings, a faster cooling rate reduces the localized refractory segregation in the interdendritic regions and decreases the resultant cell size.

5.2.3.2 Oxidation Behavior

5.2.3.2.1 Oxidation Kinetics

Figure 5-19 compares the mass gain per unit area as a function of time of the wrought, LPBF and DED for oxidation at 800°C in air for up to 24 h. Every exposure was repeated three times; wherein the experimental errors bars come from. Consistently, the AM samples show higher mass gain than the wrought. As Figure 5-19b illustrates, all the samples follow a parabolic rate law, wherein the oxidation rate constants k_p were calculated. The wrought

sample k_p was $2.8 \pm 0.6\ x\ 10^{-14}\ g^2\ cm^{-4}s^{-1}$, whereas LPBF was $6.1 \pm 0.2\ x\ 10^{-14}\ g^2\ cm^{-4}s^{-1}$ and DED was $6.7 \pm 0.9\ x\ 10^{-14}\ g^2\ cm^{-4}s^{-1}$.

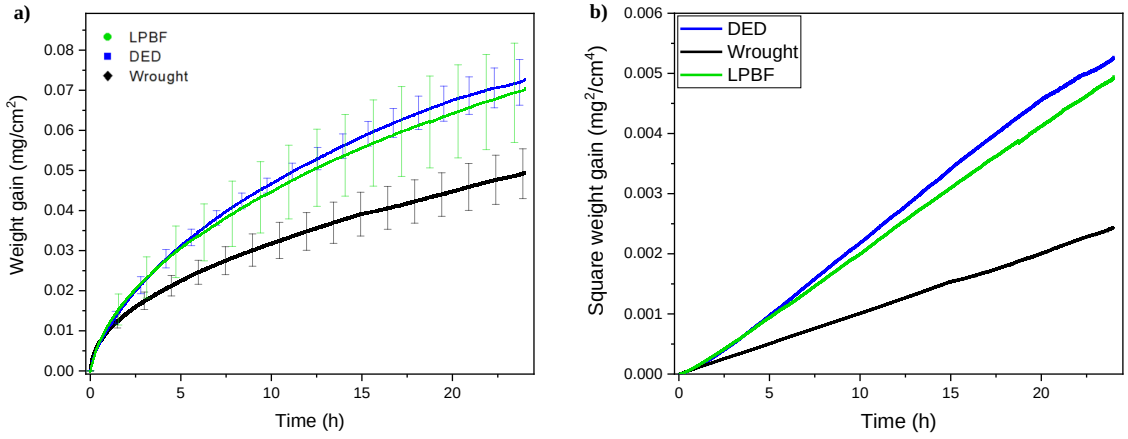

Figure 5-19. Isothermal oxidation kinetics of Alloy 625 studied alloys (wrought, LPBF, and DED) a) Plot of weight change against time at 800°C obtained by TGA b) Plot of square mass gain against time showing that the kinetics can be approximated to parabolic behavior.

In accordance with kinetics results, the oxide scale is thicker for the AM samples than the wrought. The average scale thicknesses after 24 h oxidation were measured to be 0.33±0.08 µm, 0.42±0.04 µm, and 0.45±0.12 µm for the wrought, LPBF and DED samples, respectively. These thicknesses can be used to calculate k_p values, assuming the scales to be pure chromia (density = 5.22 g/cm^3) and the absence of a transient stage. The wrought sample k_p from thickness is calculated to be $1.7 \pm 0.1\ x\ 10^{-14}\ g^2\ cm^{-4}s^{-1}$, whereas that of the LPBF sample is $2.8 \pm 0.3\ x\ 10^{-14}\ g^2\ cm^{-4}s^{-1}$ and the DED is $3.2 \pm 0.4\ x\ 10^{-14}\ g^2\ cm^{-4}s^{-1}$. Thus, the k_p values based on thickness measurements are consistently lower than the k_p values from TGA data, with DED having the biggest difference, followed by LPBF and wrought.

The oxidation rate constants calculated from the TGA results were consistently lower than those determined from the measured scale thicknesses. The greatest difference was for the DED sample, which had developed a scale/alloy interface with the largest nonplanarity.

This suggests that the planarity of the scale/alloy interface plays an important role. Specifically, the development of a nonplanar scale/alloy interface corresponds an increase in alloy surface area being oxidized relative to a planar interface. Given that the k_p determined from TGA data is based on the initial (i.e., planar) surface area of the sample, the more nonplanar the interface, the larger the effective k_p and the larger the difference between the k_p calculated from TGA versus the k_p estimated from scale thickness for the same sample. Adding to this difference is that fact that the latter k_p disregarded weight gain associated with the initial stage of oxidation. Future analysis will quantify the factors contributing to the differences in the two types of k_p measurements.

5.2.3.2.2 Oxide scale/alloy Interface Structure:

Figure 5-20 shows STEM-BF cross-sectional images of the scales formed on the wrought, LPBF and DED samples after 24 h oxidation in air at 800°C. The three samples formed a continuous and dense Cr_2O_3 scale. The AM samples have a more convoluted scale/alloy interface, with interfacial voids; DED interfacial defects sometimes manifest as scale buckling. On the contrary, the oxide scale in the wrought sample exhibits good adherence and a more planar interface with the alloy. The possible sources of such defects are numerous and can operate in tandem. These sources include vacancy condensation (i.e., Kirkendall effect), local volume changes associated with phase changes (e.g., δ precipitation), and strain-energy release from scale-growth stresses and/or stresses induced by cooling due to different thermal expansion coefficients between the oxide and the metal [61]. The δ-precipitates appear to be disruptive to the integrity and planarity of the scale/alloy interface. This is particularly true for the δ-precipitates that became partially or fully occluded in the chromia scale. The LPBF cross-section in Figure 5-20 shows how the oxide scale surrounds δ and consequently increases the oxide/alloy interfacial convolution. When the scale decohesion reaches a critical size, the stresses in the scale may be relieved by buckling [64],

as found with the DED sample. The size and higher amount of subsurface δ-phase in the AM samples compared to the wrought sample caused the former to have more convoluted scale/alloy interfaces. A more convoluted scale/alloy may increase susceptibility to scale spallation. In support of this, the TGA-tested AM samples were found to have the most weight loss (i.e., scale spallation) after cooling from the oxidation exposure.

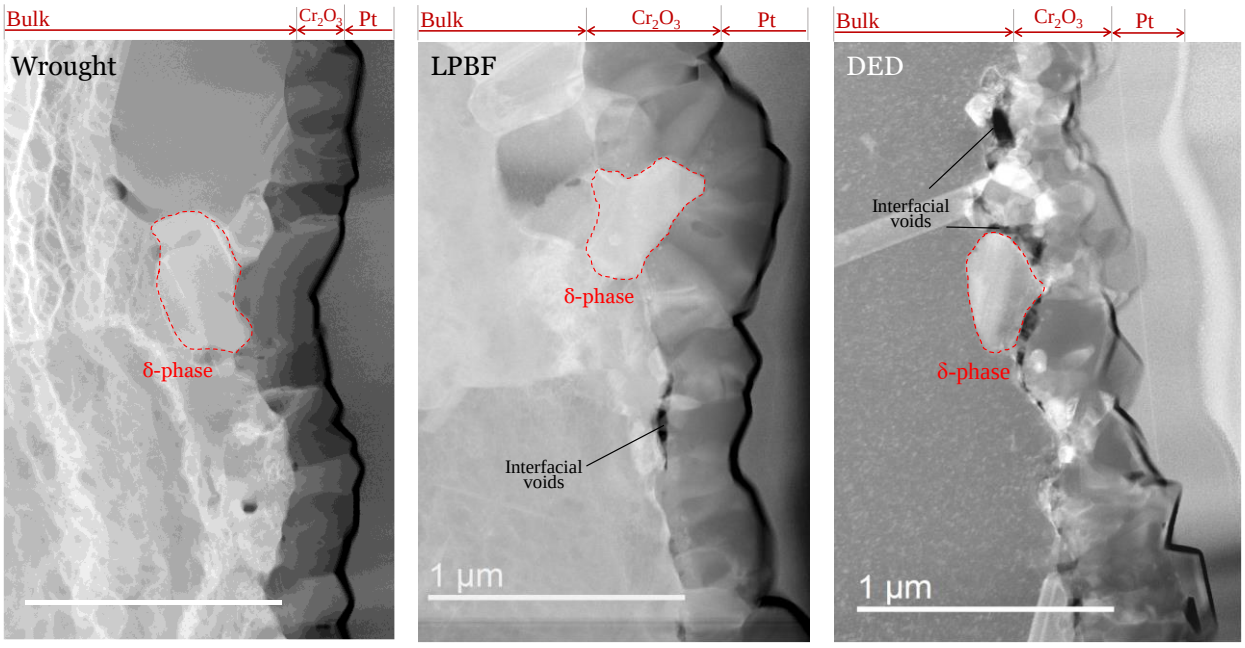

Figure 5-20. STEM-BF micrographs of the scales formed on the three 625 samples after 24 h oxidation in air at 800°C. δ-phase pecipitates can be obsevrved beneath the chromia in the three samples.

5.2.3.2.3 Subsurface Changes During Oxidation: δ-Phase Precipitation

Similar to other studies on Alloy 625 oxidation [5], [74], [124], δ-phase precipitates formed beneath the oxide scale. STEM EDS compositions for the subsurface precipitates are shown in Table 5-6. These precipitates were assessed by STEM EDS to have an approximate stoichiometry of $(Ni, Cr)_3(Nb, Mo)$. The amount and distribution of these precipitates varied amongst the samples. The analysis images in Figure 5-21 show that the interfacial δ-phase precipitates in the wrought and LPBF samples are blocky, while those in the DED sample are more globular. Quantitatively, DED formed the highest amount of subsurface δ-phase, while

the wrought formed the least. The error bars in Figure 5-21 indicate the variation in δ fraction along a given alloy/scale interface; DED has the highest variation, which corresponds to a high heterogeneity in local composition. To that end, δ precipitates are located preferentially in the original interdendritic regions, where Nb segregation occurs, including the subsurface beneath the chromia. Concerning the bulk transformation after the exposure, AM original segregation trigger abundant δ-phase formation. LPBF and DED dendritic structures transitioned to needle-like δ-phase precipitation. The LPBF sample shows a relatively uniform distribution of thin needle-like δ-precipitates, whereas DED shows the presence of thicker precipitates in the original interdendritic regions.

Table 5-6. Chemical composition (at. %) of subsurface δ-phase (in the immediate vicinity of the external oxide layer), measured by EDS.

	Cr	Fe	Ni	Nb	Mo
Wrought	4.5	0.6	74.2	11.2	9.5
LPBF	5.2	0	77.1	8.7	9
DED	5.3	0	77.1	9.2	8.4

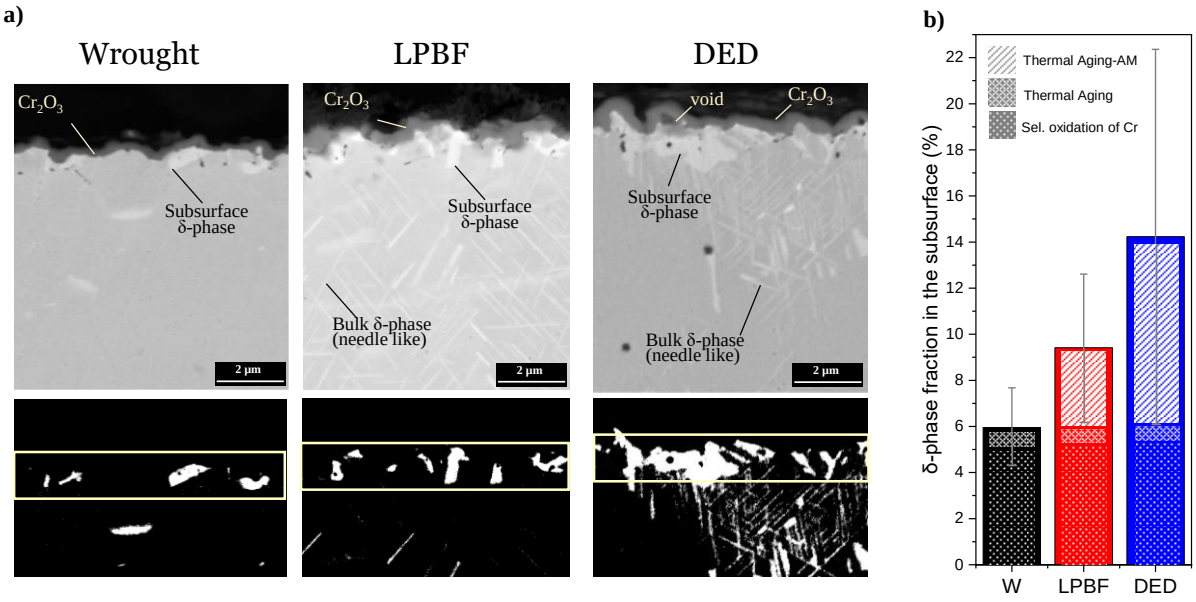

Figure 5-21. a) SEM cross-sections of the wrought, LPBF and DED samples after 24 h oxidation at 800°C in air. The corresponding threshold images are shown directly below (δ-phase is white). The yellow lines delineate the subsurface region, where the δ-phase was measured. b) Summary of

measured δ-phase fractions for each sample. δ-phase fraction formed varies with the alloy composition, being promoted by the Nb increase and Cr depletion. Patterns in the bar chart illustrate the contributions that promote the δ-phase formation: thermal aging, selective oxidation, and refractories segregation in AM processes.

5.2.3.2.3.1 δ-phase Precipitation Source: Oxidation Induced and Thermal Aging

The 625 samples formed a chromium-rich oxide layer due to the selective oxidation of chromium. The concurrent subsurface chromium depletion affects the chemical potential of the other alloying elements, e.g., the lower the chromium content, the lower the niobium chemical potential. This so-called cross-term effect caused the development of a chemical potential gradient of Nb in the alloy subsurface which, in turn, acts as a driving force for Nb uphill diffusion (i.e., up its concentration gradient)[5]. The resulting Nb enrichment is eventually sufficient to cause δ-phase precipitation beneath the scale/alloy interface.

On the other hand, the exposure to high temperature during the oxidation process can promote phase evolution in the alloy independent from the oxidation process. According to the TTT diagram for Alloy 625 [20], δ-phase precipitation starts after 20 h at 800°C. Therefore, delta-phase precipitation is expected in all samples after 24 h exposure due to thermal aging, The rate and extent of this precipitation are enhanced in the AM samples due to greater segregation compared to the wrought. The maximum possible amount of phase formation in a given alloy can be estimated by assuming thermodynamic equilibrium. Using the nominal composition of Alloy 625 and ThermoCalc in combination with the TCNI8 database, the δ-phase fraction at equilibrium is determined to be 10 v/v% at 800°C. Niobium segregation and Cr depletion can cause an increase above this value. At the highest segregation region based on EPMA analysis for DED (17.5%Nb, 14.2%Cr), 50% of δ-phase

is predicted at equilibrium; while the highest measured segregation for LPBF (8.4%Nb, 17.9%Cr) gives 21% δ-phase at equilibrium. This trend is consistent with what was found experimentally in this study.

Summarizing, the δ-phase formation beneath the chromia scale is the result of two separate and interrelated contributions: thermal aging and selective oxidation of chromium. The δ-phase precipitation induced by the oxidation is related to the formation of chromia. Therefore, the greater the amount of Cr oxidation, the greater the amount of δ-phase precipitation for a given oxidation time. From this perspective, and considering the TGA data (Figure 5-19), the DED should have the highest formation of δ-phase, followed closely by LPBF, and then the wrought. This is consistent with what was observed. Concerning the thermal aging, as the thermodynamic predictions for the segregated regions illustrate, the higher the initial Nb segregation, the higher the δ-phase fraction. This is consistent with the observation that the bulk of the DED sample had the highest precipitation and the wrought had the least.

5.2.3.2.4 Subsurface Depletion Behavior

5.2.3.2.4.1 Effect of Nb and Mo Segregation on the Average Effective Interdiffusion Coefficient of Cr

Figure 5-22 shows the EPMA measured compositional changes in the subsurface of the samples after 24 h oxidation in air at 800°C. For each sample a composition profile was measured in regions with and without δ-phase beneath the chromia scale, i.e., profiles through the oxide scale/alloy structure versus through the oxide scale/δ-phase/alloy structure.

For both kind of profiles, the zero distance corresponds to the first measurement in the alloy, and the distance increases as measurements go deeper in the alloy.

For the three samples, the Cr depletion profiles are steeper in the absence of δ-phase, and the depletion is deeper into the alloy when δ-phase is present. All the cases present a very steep chromium profile near the interface and an Nb-enriched region. Additionally, for the three samples studied, the lowest interfacial Cr content occurs in the absence of δ-phase beneath the chromia; the DED has the lowest values, followed by LPBF and wrought.

The average effective interdiffusion coefficient of chromium was calculated by fitting the measured EPMA points into the expression from Wagner's model for scaling of single-phase binary-alloys [52]. The calculated $\widetilde{D}_{Cr}^{eff}$ values are presented in Figure 5-22. Despite the simplification, the minimum R-square was 0.94, demonstrating a good agreement with the model. Furthermore, the results show that the average effective interdiffusion coefficient of chromium in the presence of δ-phase is consistently higher than when it is not present.

Taking the DED sample as the case of highest segregation, the composition profile in the presence of δ-phase was found to be Nb enriched, and the one measured along the oxide scale/alloy was Nb depleted. The presence of Nb in Ni-Cr-Fe alloys has been reported to promote the Cr activity [125], indicating that less Cr is required to keep the same activity. In agreement with this, when δ-phase is present $\widetilde{D}_{Cr}^{eff}$ and interfacial Cr contents are higher. These factors contribute to promoting a faster chromia establishment and a better state for a localized rehealing process in the event of scale spallation or damage. Thus, the presence of δ-phase at the scale/alloy interface may not be detrimental to the scale-rehealing process. However, the heterogeneous microstructure in DED results in a greater variation in $\widetilde{D}_{Cr}^{eff}$ throughout the sample and hence a greater variability in interfacial Cr contents in comparison with the LPBF and wrought.

To summarize, the refractory-metal segregation stemming from the additive process affects the subsurface evolution during the oxidation. In particular, the segregation of Nb and Mo can influence scale healing ability, increase the oxide/alloy interfacial defects, and may increase susceptibility to scale failure during service. Therefore, the oxidation performance of the much more homogeneous wrought alloy is deemed superior to that of the as-processed AM samples; in the case of the AM, LPBF is preferred over DED.

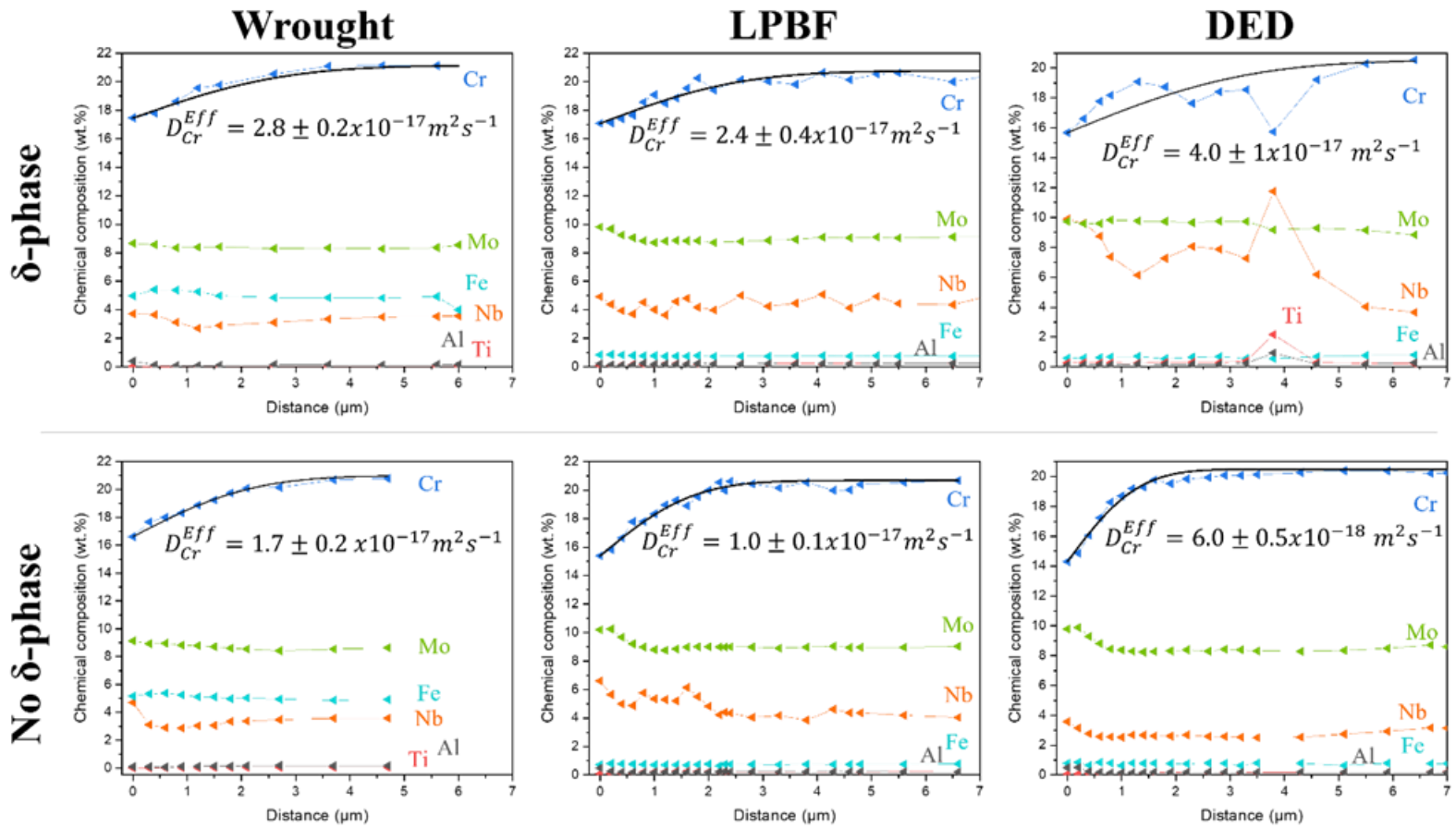

Figure 5-22. Subsurface concentration profiles measured by EPMA in Alloy 625 wrought (left column), LPFB (center column), and DED (right column) after 24 h isothermal oxidation in air at 800°C. Concentration profiles in a region comprised of oxide scale/δ-phase precipitate/alloy correspond to the first row, while the second row corresponds to a δ -free region.

5.2.3.2.4.2 Nb Diffusional Cross-effect

Regarding oxidation-induced changes, a subsurface Nb concentration gradient had developed in all the samples, as discussed earlier. The flux of any component depends on the chemical potential gradients of all components in the alloy [54]. In this case, a pronounced diffusional cross-effect arises between Nb and Cr. Since the local contents of these two constituents are affected by the AM process used, the subsurface composition profiles and the effective interdiffusion coefficient of Cr are consequently varied.

5.2.4 Conclusions

- There is significant microsegregation of Nb and Mo in the interdendritic regions of laser-assisted AM Alloy 625 due to local rapid solidification conditions stemming from the nature of the AM processes. DED exhibited the highest degree of segregation, followed by LPBF (refer to Figure 5-18).
- The level of Nb segregation influenced the extent of subsurface changes induced by oxidation. The amount of δ-phase precipitation beneath the chromia scale increases with the original Nb segregation since it is promoted by both thermal aging and oxidation contributions (refer to Figure 5-21). Additionally, the heterogeneous microstructure evolution promoted by the segregation decreases the interfacial Cr content, reducing the alloy's ability to reheal in the event of scale spallation or damage.

- The amount of δ-phase beneath the chromia scale in AM samples was found to be neutral or detrimental. In the first case, δ-phase does not affect the Cr consumption in a given sample (refer to Figure 5-22). In the second case, some precipitates embedded into the chromia scale and promoted local decohesion at the alloy/scale.
- Variability in the subsurface evolution during oxidation can decrease the local healing ability of the scale and increases the likelihood of decohesion at the alloy/scale. Since AM samples present a higher variability than the wrought, the wrought is preferred over the as-processed AM samples. In the case of the AM, LPBF is preferred over DED.

5.3 Severity of Intergranular Oxidation in AM-alloy 625 Oxidized at 950°C

5.3.1 Introduction

Alloy 625 is widely used due to its excellent mechanical properties, oxidation resistance, corrosion resistance, and weldability [19]. Initially, Alloy 625 in the annealed condition was designed for use up to 600°C, with the risk of delta-phase precipitation-induced embrittlement above this temperature [20]. Nevertheless, its outstanding high-temperature properties make it attractive for applications demanding elevated temperatures, e.g., boilers for services up to 982°C and welding materials for usage up to 1093°C [126].

In terms of oxidation behavior at elevated temperatures (>900°C), the oxidation kinetics are faster, and the intergranular oxidation starts to be noticeable [9], [12], [86], [127]. Recent studies have shown that additive manufacturing (AM) results in more severe intergranular oxidation than conventional manufacturing methods [12], [77]. Consequently, the grain boundaries of the AM alloy are prone to become brittle and vulnerable to cracking, leading to reduced performance and a shorter lifespan [92]. This chapter aims to examine the kinetics contribution at 950°C and understand the factors that exacerbate intergranular oxidation in AM samples.

5.3.2 Results

5.3.2.1 Oxidation Kinetics

Isothermal oxidation tests of alloy 625 coupons were carried out in air at 950°C. As in previous chapters, the alloys, were processed via: wrought, cast, LPBF, and DED. The kinetics

results based on recorded mass gain up to 100h are shown in Figure 5-23. All four samples exhibit a decrease in the rate of mass gain with increasing time. Considering the deviations shown (base on up to four separate tests), it is conclusive to say that the mass gain follows the trend wrought < DED < LPBF. The cast alloy is an exception where the mass gain can be compared to any of the samples within the measurement errors. Results show that the LPBF, cast, and DED mean mass gains are 23±11%, 7±10%, and 5±5% greater relative to the wrought after 100h. In addition to having the lowest mass gain, the wrought also shows the smallest deviation.

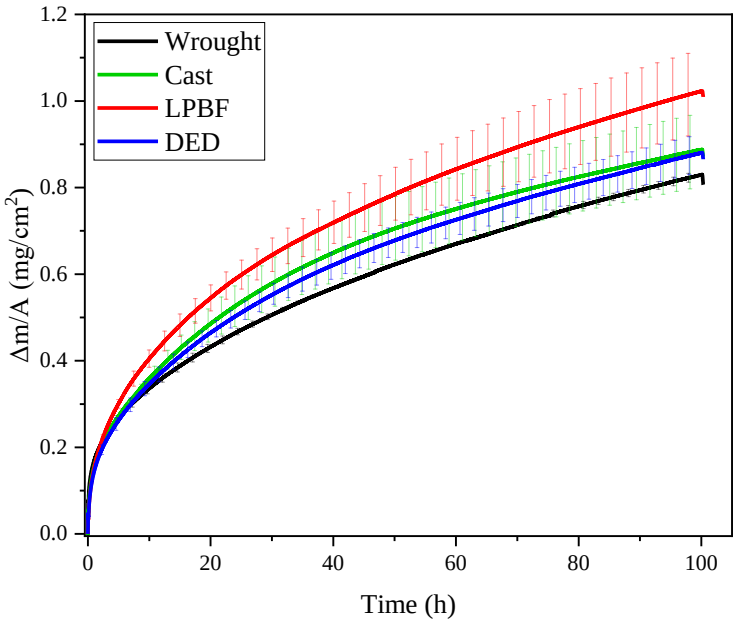

Figure 5-23. Mass gain as a function of time during isothermal oxidation at 950°C of alloy 625: wrought, cast, LPBF, and DED

Parabolic rate constants (k_p) were calculated by plotting the mass gain ($\Delta m/A\ [g/cm^2]$) against the square root of the exposure time over 100h, and fitting a line from 20h to 100h (to be in the steady-stage and hence beyond the transient stage of oxidation). The slope of a given plot corresponds to the square root of the k_p following the equation $\Delta m/A = \sqrt{k_p}\sqrt{t}$. Table 5-7

compares the measured k_p values together, and with literature data for wrought 625 alloys under the same conditions. The agreement is good and the rates correspond to chromia scale growth [48]. The calculated k_p values range from 1.3±0.2 $x10^{-12}$ to 2.1±0.7$x10^{-12}$ $g^2cm^{-4}s^{-1}$. As shown in Figure 5-24, these values fall within the deviation. Comparing mean estimated k_p values, the wrought, LPBF, and cast are similar, whereas the LPBF is 62% higher than the wrought.

Summarizing, kinetic results show that all tested samples exhibit an oxidation rate within the range of chromia formers, with LPBF showing a slightly faster rate than the others.

Table 5-7. Parabolic rate constants of air oxidation at 950°C

Manufacturing method	Oxidation rate (k_p) [$g^2cm^{-4}s^{-1}$]
Wrought	1.3 ± 0.2 x 10^{-12} (this study) 3.86 x 10^{-12} [6] 2.95 ± 0.12 x 10^{-12} [9] 1.58 x 10^{-12} [128] 2.97 x 10^{-12} [129]
Cast	1.4 ± 0.1 x 10^{-12} (this study)
LPBF	2.1 ± 0.7 x 10^{-12} (this study) 2.94 x 10^{-12} [128] 9.22 ± 4.02 x 10^{-12} [9]
DED	1.4 ± 0.2 x 10^{-12} (this study)

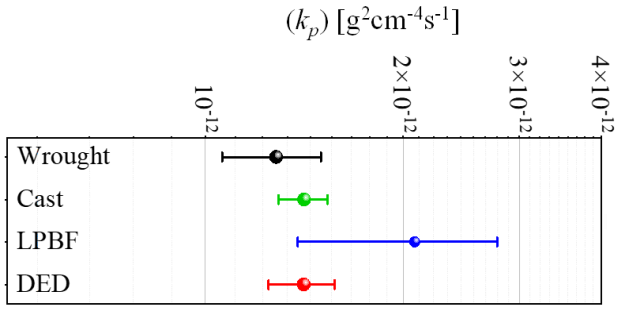

Figure 5-24. Comparison of parabolic rate mean and deviation values

5.3.2.2 Characterization of Oxide Scale and Oxidation Induced Subsurface Changes

After air oxidation at 950°C for 100h, the surface and cross-section of the samples were characterized by SEM and EDS. Additionally, X-ray diffraction was carried out for phase identification.

Figure 5-25 shows the surface of alloy 625 samples oxidized after 100h in air. SEM-EDS on the surface of all samples indicate that the oxide scale is mostly composed of chromia except for protrusions present in each sample, in agreement with the X-ray diffraction (XRD) results shown in Figure 5-26. There is a noticeable difference in the oxide flatness/planarity among the samples. The wrought shows more homogeneous oxide topography, and the occasional protrusions show Mn and Ni together with the chromia components. The surface of the LPBF and DED samples show a protrusion network, or so-called oxide ridge network [128]. The EDS results indicate that they are composed of Ti-Cr-oxides with traces of Mn in the LPBF sample and Nb+Ni in the DED sample. From the XRD, a small amount of TiO_2 can be identified in both DED and LPBF samples. The presence of TiO_2 and $MnCr_2O_4$ has been reported at the outer surface of chromia-rich scales [14], [130], [131]. Because Ti and Mn have faster diffusion through the chromia layer compared to Cr [130], [132], ions of these metals migrate towards the outer surface, forming rutile TiO_2 and $MnCr_2O_4$ over the chromia layer. Additionally, cross-sectional SEM images of the oxidized samples shown in Figure 5-25c,d indicate that the oxide ridge protrusions in the LPBF and DED samples coincide with the grain boundaries in the alloy. Finally, the oxidized cast alloy has coarse discrete protrusions which corresponds to the oxidized Laves phase and NbC. The EDS composition is close to Nb_2O_5, with traces of Cr and Ni. The oxidation of NbC at the surface of alloy 718 has been reported to erupt the chromia scale due to a volumetric expansion of a factor of 2.28 [101].

Cross-sectional BSE images in Figure 5-27, and EDS maps in Figure 5-28 confirm that all samples formed a continuous and dense chromia scale. There is a noticeable variation in the oxide/alloy interfacial defects. The LPBF and DED samples exhibit a higher tendency towards decohesion and the formation of pores in the oxide/alloy interface when compared to the wrought and cast alloys. These pores are preferentially located below the oxide ridges.

An enrichment of Nb beneath the chromia scale can be observed in the EDS maps of all samples and corresponds to discrete δ-phase precipitates (Ni_3(Nb, Mo)). The chromium depletion in the subsurface arising from the external chromia formation leads to Nb uphill diffusion, which in turn, promotes δ-phase precipitation beneath the chromia [5]. Besides, small amounts of δ-phase and γ-phase (Ni-Fe-Cr matrix) were identified in the XRD of all samples, indicating that the X-rays fully penetrated the external oxide scale and reached the δ-precipitates and the matrix.

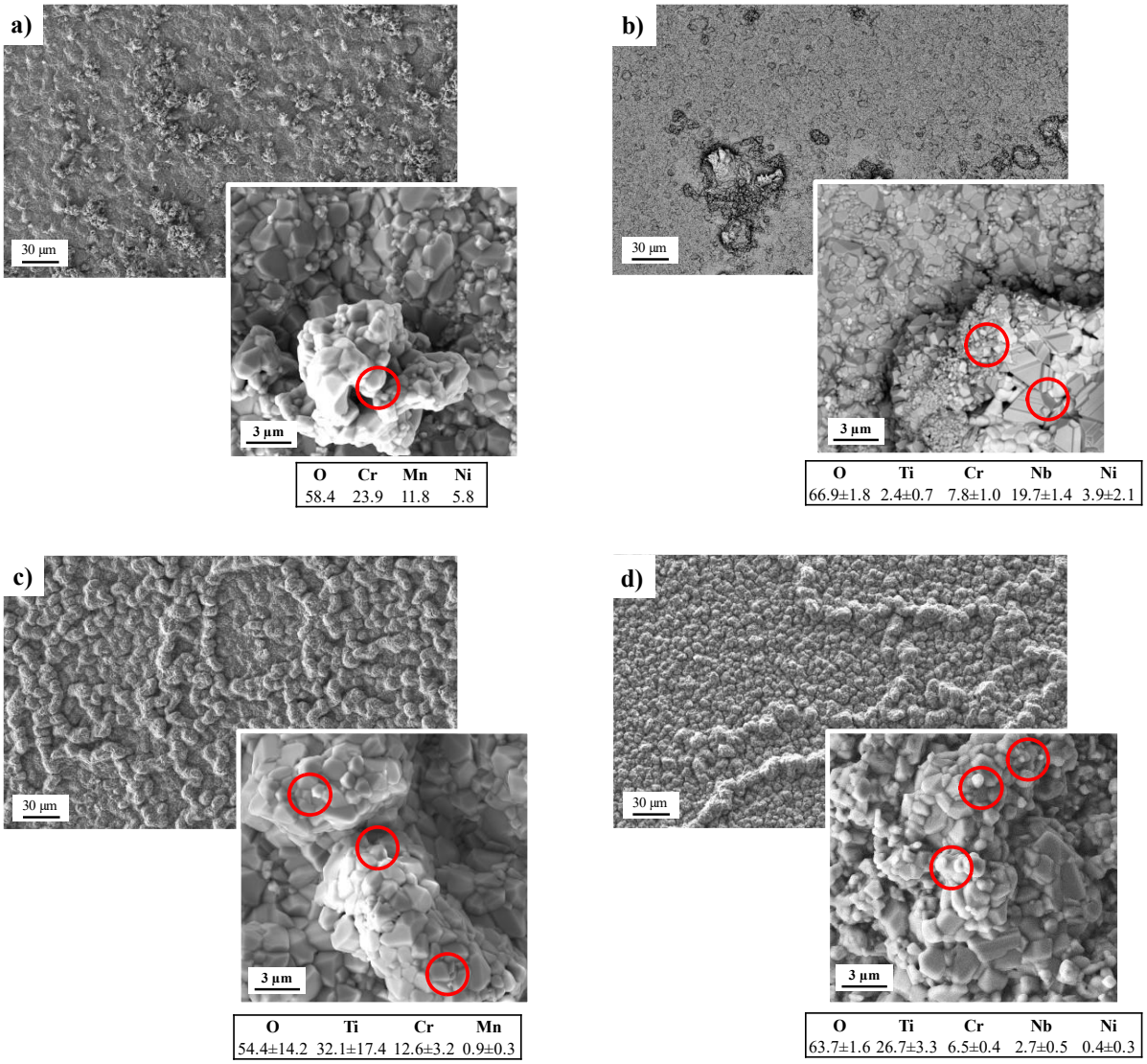

Figure 5-25. Surface BSE-SEM images of alloy 625 oxidized in air at 950°C for 100h: a) wrought, b) cast, c) LPBF, and d) DED. Each sample is zoomed in on to view its protrusions, where its atomic percent composition is obtained using EDS.

As a result of the chromium depletion and the Nb uphill diffusion, changes in the subsurface composition cause dissolution of the δ-precipitates, resulting in a so-called precipitates free zone [47]. This zone can be clearly seen in Figure 5-29, where samples were oxidized for a longer time (1000h at 950°C). The bright precipitates (refractories enriched) in the high contrast images are distributed in the alloy at the chromia/alloy interface, and below the

precipitates free zone. Most of the precipitates below the zone correspond to δ-phase, and a small amount of σ-phase (Mo-Ni-Si-Cr-Nb), and NbC carbides according to their composition.

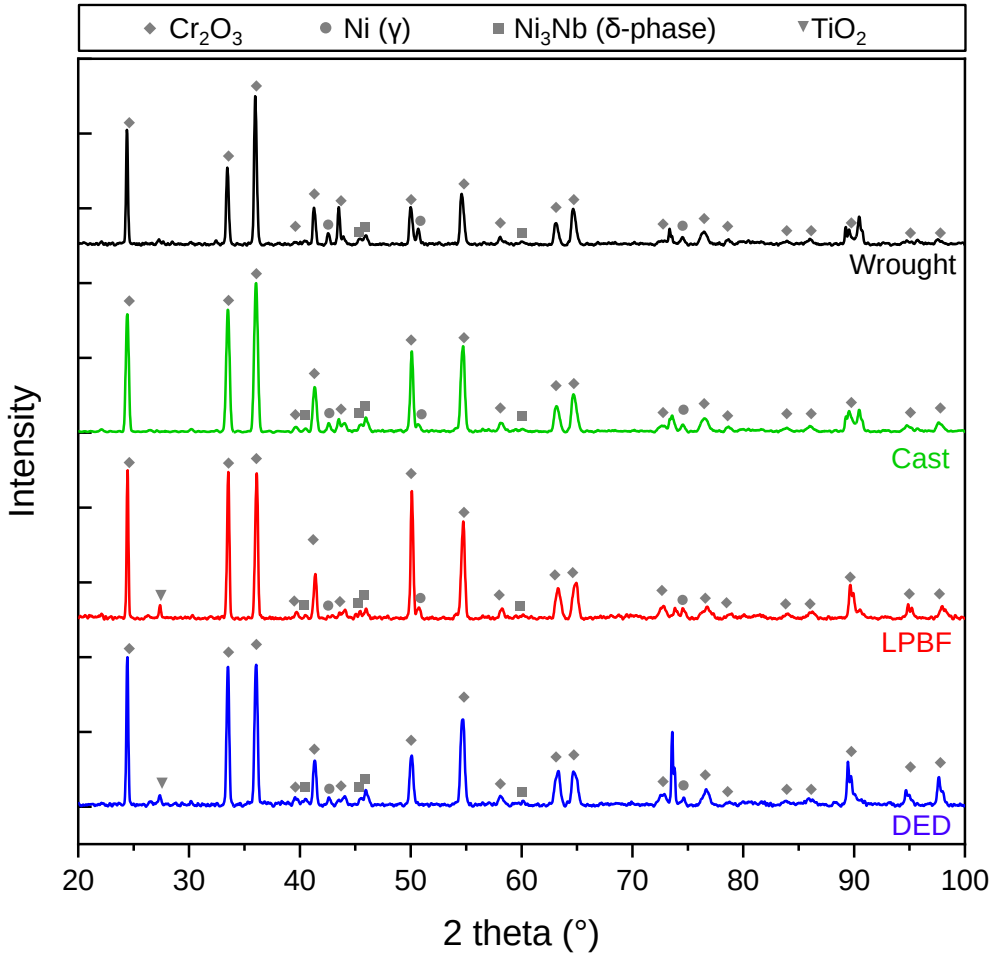

Figure 5-26. Bragg brentano X-ray diffraction diagram of alloy 625 samples after air oxidation at 950°C for 100h.

An additional observation from cross-sectional images was the variations in the extent, morphology, and composition of internal attack among the samples. The term internal attack in this study refers to any subsurface degradation induced during oxidation (internal oxidation, intergranular oxidation, and voids). The internal oxidation in the cast sample is primarily formed by the oxidation of exposed NbC and laves precipitates, it barely shows Al_2O_3 and TiO_2. The wrought exhibits internal oxidation mainly composed of Al_2O_3 after 100h, and TiO_2 was also

identified at longer exposure times. For the LPBF and DED samples, the internal oxidation is composed of Al_2O_3 and TiO_2 at even early exposure times. The BSE- high contrast images allow to see that the internal oxidation is preferentially located along the grain boundaries for the wrought, LPBF and DED samples, thereby it should be called intergranular oxidation (IGO). It is also clear that the depth and volumetric fraction of the IGO vary significantly among samples. The maximum IGO depth measurements are shown in Figure 5-30. The median is ~10µm for the cast and wrought, 24µm for the DED, and 35µm for the LPBF. Regarding the IGO volumetric fraction, the area of the violins plots in Figure 5-30 is directly correlated with the IGO extent (frequency). Consequently, the LPBF exhibits not only the deepest but the higher extent of IGO. Morphologically, the IGO in the wrought alloy is dense, whereas the IGO in the LPBF alloy shows empty spaces along with the Al_2O_3 and TiO_2. The DED sample shows discrete and high circular intergranular voids, which occasionally exhibit Al_2O_3. These intergranular voids are abundant in the DED and less frequent in the LPBF.

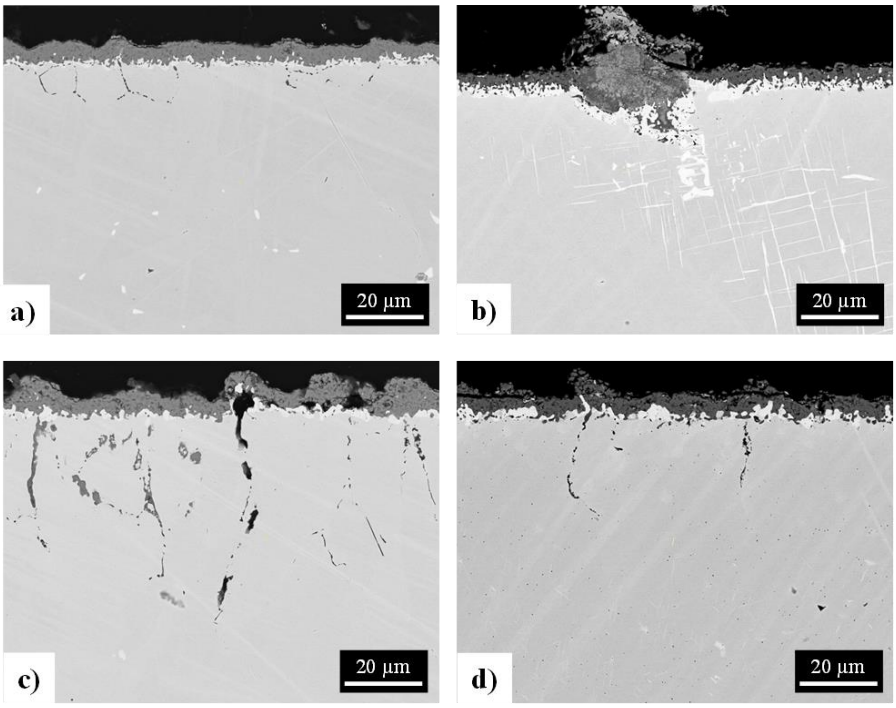

Figure 5-27. Cross-sectional BSE-SEM images of alloy 625 oxidized in air at 950°C for 100h: a) wrought, b) cast, c) LPBF, and d) DED.

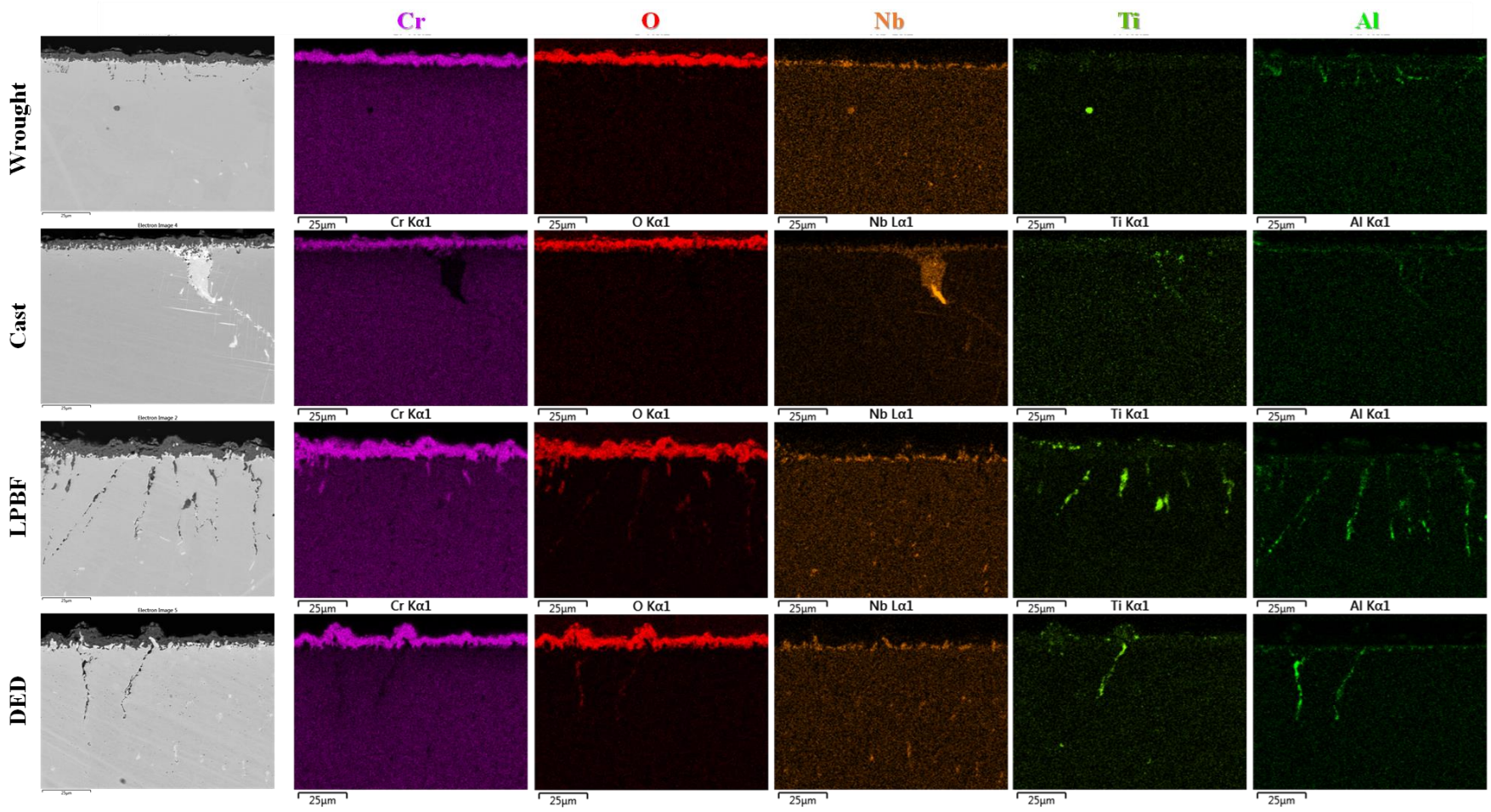

Figure 5-28. SEM-EDS map analysis of alloy 625 samples after air oxidation at 950°C for 100h. Regarding composition, all samples exhibit a continuous external scale enriched in chromia, discrete δ-precipitates in the alloy at the scale/alloy interface, and IGO mainly constitued by alumina and titania.

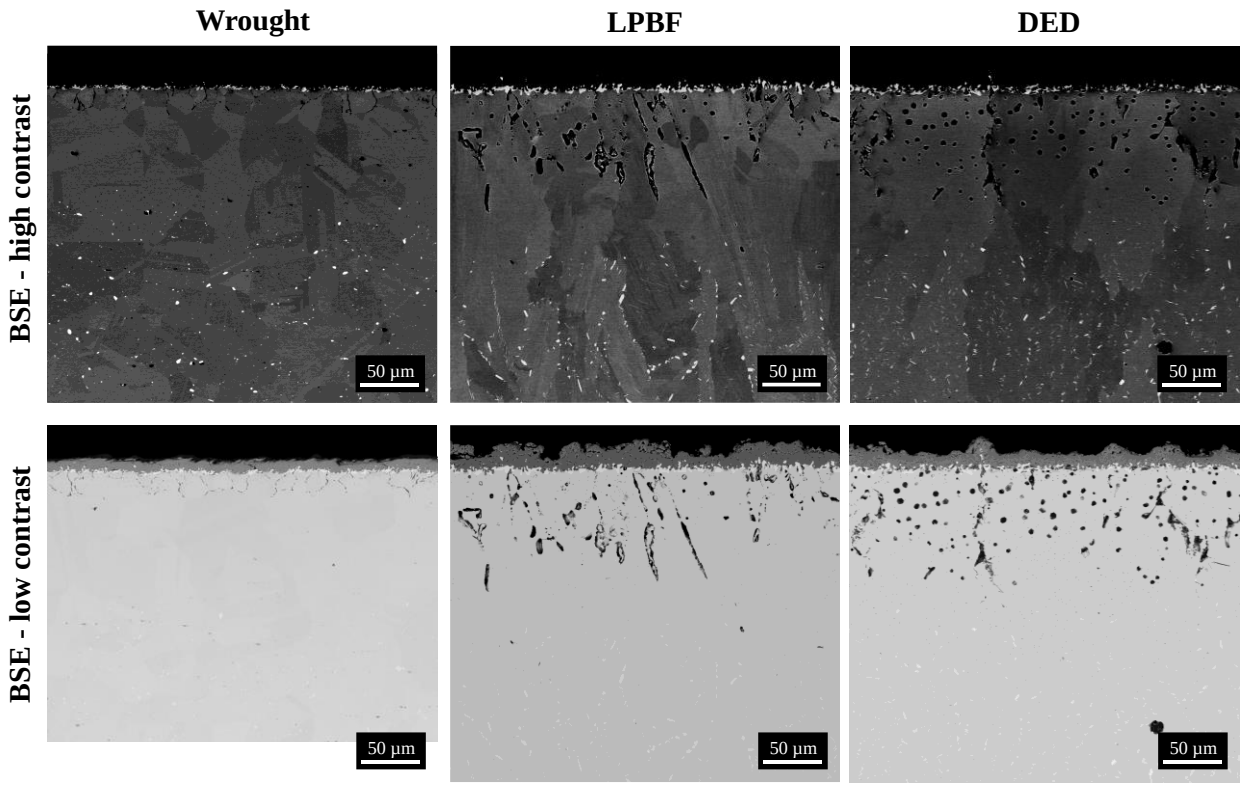

Figure 5-29. BSE-SEM cross-sectional images of alloy 625 after air oxidation at 950°C for 1000h. High and low contrast pictures were taken to appreciate preferentially location of precipitates nucleation and IGO.

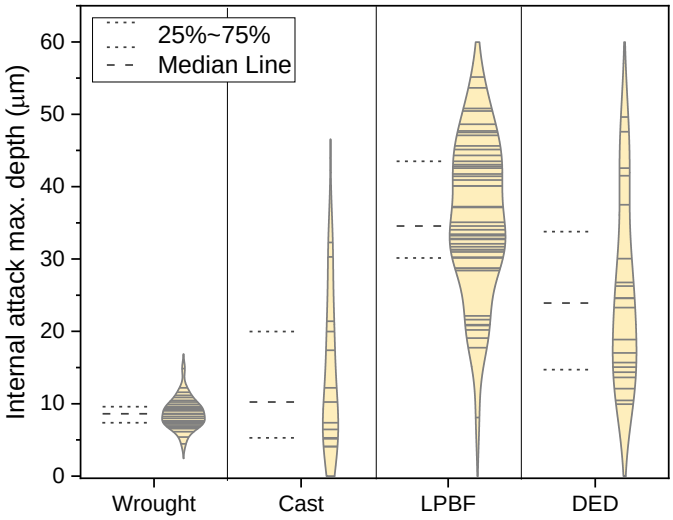

Figure 5-30. Maximum depth of internal attack after air oxidation at 950°C for 100h. Measurements were taken in 5 micrographs (for a 1mm of length per sample).

The size of the oxide grains and the interface between the oxide and alloy play a crucial role in determining the transport through the scale, which ultimately impacts the oxidation kinetics. To study these factors, a STEM characterization of the scales formed on the wrought, LPBF, and DED samples was conducted. Figure 5-31 shows the STEM-DF cross-sectional images of the scales formed, whereas Figure 5-33 shows the STEM-EDS composition maps of the oxide/alloy interface. The chromia scale is generally dense, although some pores are present in all samples. The chromia scale in the wrought exhibits good adherence, unlike the LPBF and DED samples, where interfacial voids are noticeable. Larger debond areas are more commonly found in the LPBF samples than in the DED samples, even in some regions where the oxide has buckled. In the LPBF micrograph, the dashed outline circle highlights a region with smaller chromia grains than the scale inside a buckle formation.

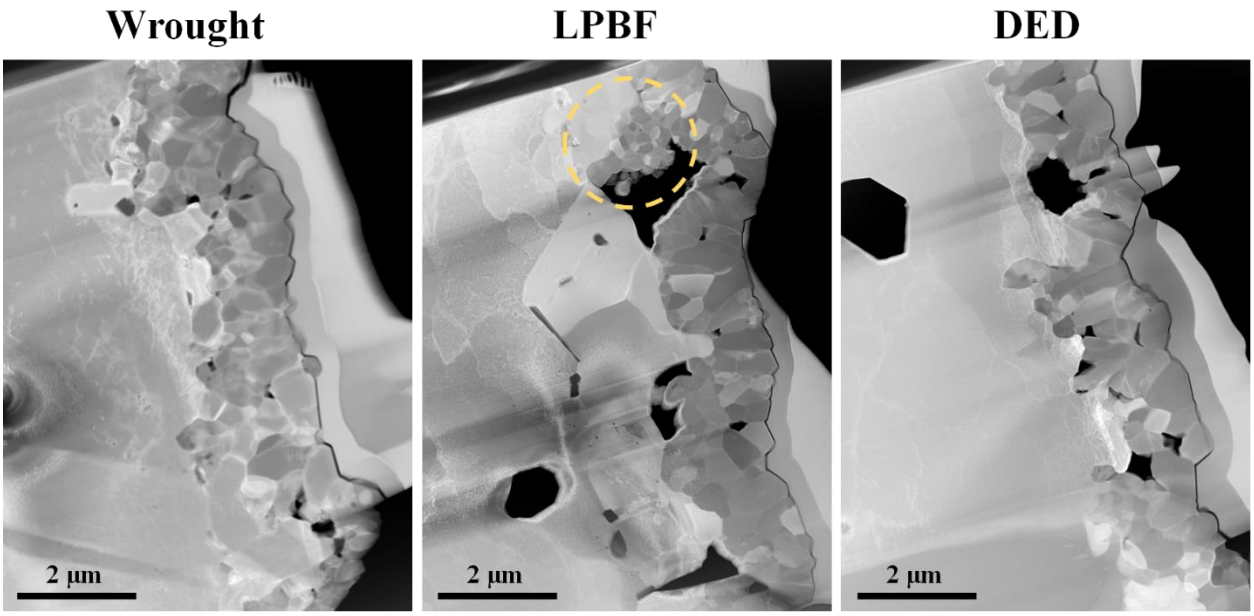

Figure 5-31. STEM-DF cross-sectional images of the oxide scale formed on alloy 625 after air oxidation at 950°C (wrought/14h, LPBF/6h, DED/6h).

Chromia grain sizes in the oxide at the oxide/alloy interface were measured for three sections per sample, results are show in Figure 5-32. Measurements were taken parallel to the

scale and were fitted to a normal distribution. Table 5-8 summarized the normal distribution values for the chromia grain size. On average, the DED has a chromia grain 4% wider than the wrought, whereas the chromia grain width of the LPBF sample is 11% narrower than in the wrought. In addition, the LPBF exhibits a broader grain width distribution than the wrought and DED samples. The more uniform oxide grain width distribution in the wrought and DED samples implies a more homogeneous oxidation behavior along the sample than the LPBF. One example of the heterogeneous behavior in the LPBF is the mentioned area in the buckling zone where the grain size is smaller.

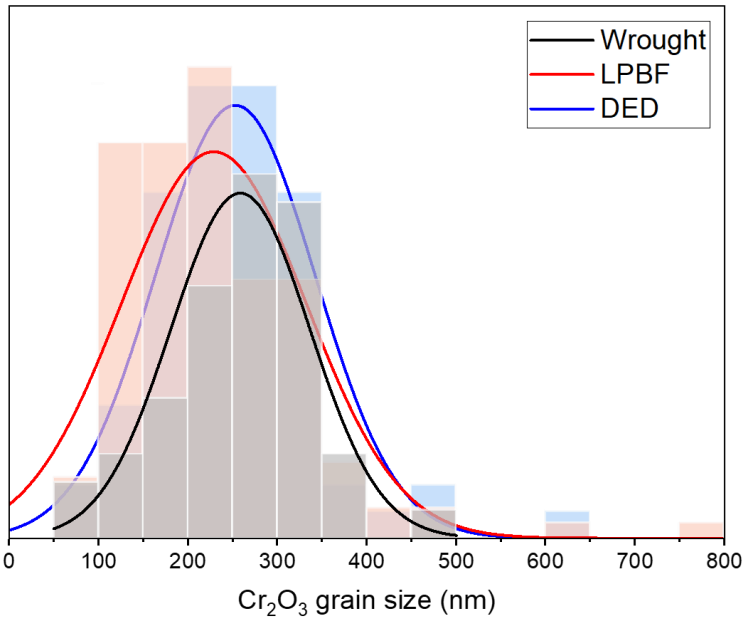

Figure 5-32. Cr_2O_3 grain size distribution measured based on STEM images.

Table 5-8. Summary of Cr_2O_3 grain size distribution values in nm: mean, 1st, 2nd (median) and 3rd quartile.

	Mean	1st Quartile (25%)	Median	3rd Quartile (75%)
Wrought	258.4	219.9	263.6	315.7
LPBF	229.5	161.1	212.9	280.0
DED	268.8	211.93	269.8	314.8

Regarding the analysis of the scale composition, the STEM-EDS maps in Figure 5-33 reveal Ti enrichment in the chromia scales. This enrichment was preferentially located along the grain boundaries. Enrichment of Al along the chromia grain boundaries was also found after EDS spot analysis. In an effort to quantitatively compare the Ti enrichment among the samples, Table 5-9 shows the result of measured Ti and Al atomic composition for the chromia lattice and grain boundaries using STEM-EDS. It was found that the Ti composition in the chromia lattice was consistently 0.15% for all three samples. By contrast, the Ti composition in the chromia grain boundaries varied among the samples; it was higher in the LPBF and DED samples than in the wrought samples by 49% and 86%, respectively. For the chromia grain boundaries, the difference in Al enrichment among the samples is even higher than the Ti enrichment. The chromia grain boundaries exhibit an Al enrichment in the LPBF and DED samples of 2.9 and 1.8 more than in the wrought, respectively. Certainly, the variation of chromia composition (in lattice and grain boundaries) among the samples may cause different mass-transport properties.

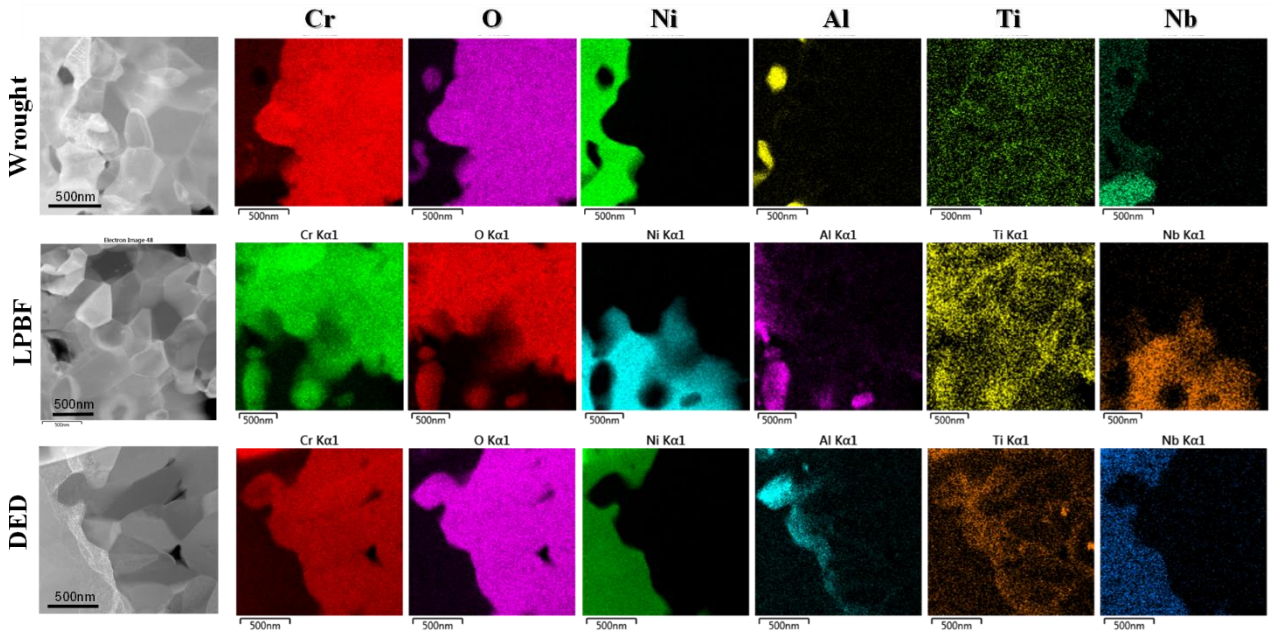

Figure 5-33. STEM-EDS maps oxide/alloy interface on alloy 625 after air oxidation at 950°C (wrought/14h, LPBF/6h, DED/6h). Ti doping is observed at chromia grain boundaries.

Table 5-9. Al and Ti composition in the chromia lattice and grain boundaries measured by STEM-EDS.

	Ti. at.% in Cr_2O_3 Lattice	Ti. at.% in Cr_2O_3 grain boundaries	Al. at.% in Cr_2O_3 grain boundaries
Wrought	0.15 ± 0.08	0.35 ± 0.12	0.16 ± 0.06
LPBF	0.16 ± 0.08	0.52 ± 0.19	0.47 ± 0.34
DED	0.15 ± 0.09	0.65 ± 0.20	0.28 ± 0.17

5.3.3 Discussion

5.3.3.1 Factors that Affect Oxidation Kinetics

5.3.3.1.1 Variability in Kinetic Measurements: Influence of Dendrites Orientation and Thermal Variability in AM Processes

Out of all the samples tested, the wrought sample has the lowest deviations in the mass gain oxidation kinetics (as shown in Figure 5-23). This can be attributed to its distinct microstructure that does not possess dendrites.

Berthod et al. [99] reported that the orientation of dendrites is an important contributor to local variations in kinetics, especially during the transient regime. Perpendicular dendrite orientation seems to favor exposure of emerging subsurface carbides, that subsequently oxidize. By contrast, diagonal and parallel dendrites promote Cr flux, and generally, lead to a faster chromia establishment, as well as hindering the carbides in secondary arms from being exposed and oxidized [82], [99]. Furthermore, the larger dendritic morphology results in a greater mass gain from the oxidation of precipitates in the interdendritic regions during the transient oxidation (see section 5.1.3.5), making the effect of dendrite orientation more pronounced.

In case of AM samples, the microstructure throughout the building part shows variability. This is due to a continuous melting-cooling process that occurs bead-by-bead and layer-by-layer [45]. As a result, variations in the cooling/heating rate and layer temperature induce stresses [43] and the observed microstructural differences. The same building part may exhibit differences in chemical segregation, phase distribution [46], solidification morphology, and wide grain size distribution [133], [134]. In addition, occasional laser-matter interaction fluctuations during the

process can cause keyhole porosities and spatter [121], [135], [136]. These microstructural differences could lead to high margin errors when measuring kinetics of the same type of sample.

5.3.3.1.2 Chromia Scale Properties: Grain Boundary Segregation and Grain Width

Since there are other contributions to the oxidation kinetics aside from the chromia-scale growth, a measure of the kinetics based on the chromia-scale thickness is informative. Additional isothermal tests were carried out up to 1000h, and Figure 5-34 displays the measured kinetics based on scale thickness using the conversion in equations 5-4 and 5-5, where $V_{Cr_2O_3}$ is the molar volume of chromia (29.117 cm^3/mol), $\frac{\Delta m}{A}$ is the mass gain per area, and x is the chromia scale thickness.

$$\frac{\Delta \boldsymbol{m}}{\boldsymbol{A}} = \frac{\mathbf{1}}{\sqrt{\mathbf{2}}} * \frac{\mathbf{16} * \boldsymbol{b}}{\boldsymbol{V_{M_a O_b}}} * \boldsymbol{x} \qquad (5\text{-}4)$$

For chromia the expression will be

$$\frac{\Delta m}{A} = \frac{1}{\sqrt{2}} * \frac{16 * 3}{29.117} * x \qquad \textbf{(5-5)}$$

The estimated k_p for the wrought alloy is 5.9 ± 0.1 x 10^{-13} $g^2cm^{-4}s^{-1}$, whereas for the LPBF it is 11.0 ± 0.5 x 10^{-13} $g^2cm^{-4}s^{-1}$, and for the DED it is 6.5 ± 0.4 x 10^{-13} $g^2cm^{-4}s^{-1}$. The trend is consistent with what was found based on weight change, i.e., $k_{p\ (wrought)} < k_{p\ (DED)} < k_{p\ (LPBF)}$. However, the k_p values based on scale thickness are generally slower in comparison to the measured ones based on weight change after 100h tests, confirming that additional factors are contributing to the mass gained.

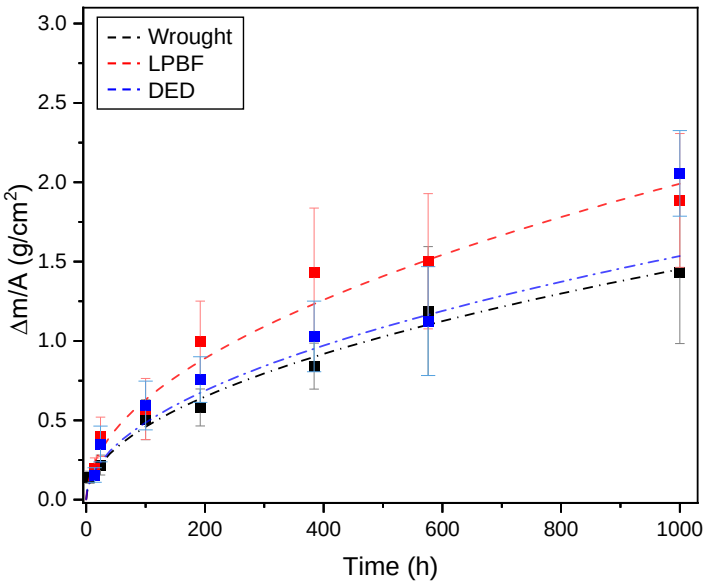

Figure 5-34. Oxidation kinetics based on chromia scale thickness for alloy 625 air oxidation at 950°C: wrought, LPBF, and DED

The oxidation kinetics are controlled by the ionic diffusion of metal or oxygen through the scale [47]. Regarding the chromia scale, the ionic transport predominantly takes place along grain boundaries since the lattice diffusion is negligible compared to the grain boundary diffusion [53], [137]. Therefore, the faster chromia growth in the LPBF sample compared to the DED sample and wrought alloy, solely evaluating the chromia scale thickness, indicates that the ionic transport rates differ among them. The factors that affect the ionic transport through the scale can be evaluated using the basic relation [53].

$$\boldsymbol{k_p = \int_I^{II} D^*_{eff}\, d(\ln a_{O_2})} \tag{5-6}$$

This expression describes the k_p as a function of the effective diffusion coefficient (D^*_{eff}) and oxygen activity (a_{O_2}) gradient across the oxide scale.

Since the diffusion coefficient through the chromia lattice is much smaller than that through grain boundaries, the effective diffusion coefficient can be described by $D^*_{eff} \approx 2\frac{(D_g\delta)^*}{g}$

where D_g is the grain boundary diffusion coefficient, δ is the grain-boundary width, and g is the grain size of the chromia scale at the scale/alloy interface. Assuming that the boundary conditions among the tested sample are the same, the following relation is found,

$$\frac{\boldsymbol{k_{p\,(x)}}}{\boldsymbol{k_{p\,(y)}}} = \frac{\boldsymbol{g_{(y)}}}{\boldsymbol{g_{(x)}}} * \frac{\boldsymbol{D_{g(x)}\delta_{(x)}}}{\boldsymbol{D_{g(y)}\delta_{(y)}}} \quad (5\text{-}7)$$

where *x* and *y* correspond to different samples. This relation shows that differences in the oxidation rates depend on the proportional relationship of the chromia grain-size ratio and the grain-boundary diffusion ratio among the samples.

Table 5-10 presents a comparison of the k_p ratios based on thickness and chromia grain size ratio. The DED/wrought are quite similar, with values close to one. This implies that the k_p similarities based on thickness can be primarily attributed to the grain size. However, considering the LPBF/wrought ratios, 35% of the k_p ratio cannot be explained by differences in grain size. This leads to the deduction that the mismatch is due to the second factor corresponding to the grain boundary diffusion.

Table 5-10. Comparison of oxidation rates ratio with chromia grain size ratio

x/y	$\frac{\boldsymbol{k_{p\,(x)}}}{\boldsymbol{k_{p\,(y)}}}$ [range]	$\frac{\boldsymbol{g_{(y)}}}{\boldsymbol{g_{(x)}}}$ [range]	$\frac{\boldsymbol{D_{g(x)}\delta_{(x)}}}{\boldsymbol{D_{g(y)}\delta_{(y)}}}$
LPBF/Wrought	1.89 [1.84-1.98]	1.23 [1.01-1.43]	>1
DED/Wrought	1.11 [1.07-1.19]	0.98 [0.93-1.10]	>1

Further studies have shown segregation of Ti^{4+}, Nb^{4+}/Nb^{5+}, Mn^{2+}, and Al^{3+} along the chromia grain boundaries [110], [138]–[140]. In the case of aluminum, it is likely to get incorporated into the scale as the alloy is consumed during the oxidation process. However, Al^{3+} ions are not expected to affect the oxidation rate since they have the same valence as Cr^{3+} ions in the chromia. The differences among samples in the measured Al segregation in the grain

boundaries shown in Table 5-9 is attributed to differences on the alloy composition. The LPBF and DED Al content is 0.27 wt.%, whereas the wrought is 0.19 wt.%.

On the other hand, since chromia grows primarily through cationic diffusion at ambient pressure [141], aliovalent doping will affect the defect structure and the transport to the scale. In the case of titanium, the difference in the valence between Ti^{4+} and Cr^{3+} impacts the transport through the oxide scale. As shown when a Ti^{4+} ion substitutes a Cr^{3+} in the chromia lattice ($Ti_{Cr}^{\cdot}$), a cation vacancy in the chromia lattice is created ($V_{Cr}^{\prime}$), following the reaction.

$$\boldsymbol{TiO_2 + \frac{1}{2}O_2 \xrightarrow{Cr_2O_3} Ti_{Cr}^{\cdot} + V_{Cr}^{\prime} + 3O_o} \quad (5\text{-}8)$$

Additional vacancies lead to an increase in oxidation rates by enhancing the diffusion rates of Cr^{3+} across the oxide layer. Even small amounts of dopants might have a significant impact since pure chromia has a low intrinsic vacancy defect population [112].

The Ti-measured values in the chromia lattice are consistent among the samples, but the one measured in the chromia grain-boundaries varies. Unlike Al, the measured Ti segregation differences do not correspond to differences in alloy Ti composition, as all three samples contain 0.33 wt.%. The LPBF and DED samples show similar values (within the error margin), with both being higher than the wrought sample. In addition to the previously discussed enhancement of diffusion via defect increase, it has been suggested that the segregation of Ti at the grain boundaries may affect the width of the grain boundaries (i.e., δ value) [140]. Vayala et al. [140] reported that Ti segregation in chromia grain boundaries is in the range of a monolayer of Ti ions between grains, width coarsening is expected considering that the ionic radius of Ti^{4+} is 0.68Å while that of Cr^{3+} is 0.63Å. Though a quantitative value cannot be estimated for δ in equation 5-7, it is inferred that $(D_g\delta)_{LPBF} > (D_g\delta)_{Wrought}$ and $(D_g\delta)_{DED} > (D_g\delta)_{Wrought}$. These values account in part for the accelerated kinetics compared to the expected ones based on the grain size

ratio previously discussed and summarize in Table 5-10. The contribution of the $D_g\delta$ ratio in the kinetics is stronger for the LPBF sample since it has the highest Ti segregation in the chromia grain-boundaries.

5.3.3.1.3 Intergranular Oxidation

Based on the oxide microstructural analysis, aside from the chromia scale, other oxide products must contribute to the measured oxygen uptake. These include TiO_2 and $MnCr_2O_4$ at the top of the scale and intergranular oxidation, where the latter is more abundant. The extent and frequency of intergranular oxidation vary greatly between samples, with the LPBF and DED samples exhibiting more frequent and deeper intergranular oxidation (IGO) than wrought and cast alloys. In order to calculate the contribution of IGO, image analysis was performed on the cross-sectional micrographs from isothermally tested samples exposed from 14h up to 1000h. An image thresholding was applied to isolate and calculate the IGO area in three micrographs per condition; then, the area was divided by the length of the micrograph to obtain the equivalent of this area in thickness. The thickness is assumed to be 35% TiO_2 and 65% Al_2O_3 for the DED and LPBF samples and entirely Al_2O_3 for the wrought alloy, where these values come from EDS maps analysis. Similar to the kinetics based on chromia thickness, the mass gained was calculated from equation 5-4.

Figure 5-35 shows the oxidation kinetics breakdown for the wrought, LPBF, and DED samples. Each plot contains three lines: the dashed green line corresponds to the weight gain based on chromia scale thickness, the dashed orange line represents the sum of the weight gains based on chromia scale thickness and IGO, and the thicker dashed line represents the recorded mass gain.

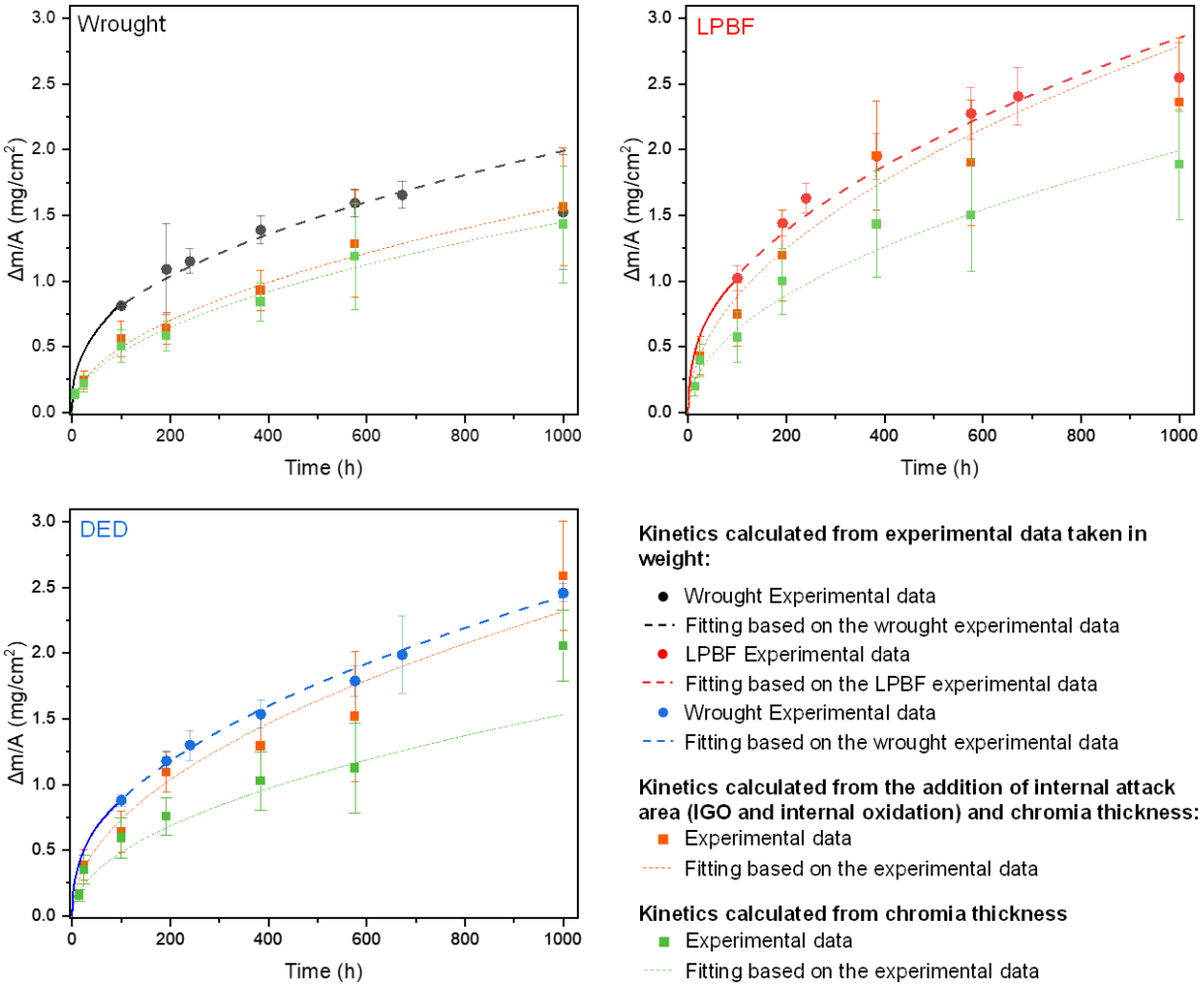

Figure 5-35. Mass gain oxidation kinetics breakdown: chromia scale, IGO.

As an example to evaluate contributions, the data from the fittings at 500h will be compared. The results indicate that the chromia scale was responsible for most of the mass gain for the wrought, LPBF, and DED samples, accounting for 69%, 68%, and 61%, respectively. Additionally, the IGO contributed to a proportional increase in mass gain of 4%, 27%, and 32% for the wrought, LPBF, and DED samples, respectively. As a result, combining the chromia scale and IGO accounted for 74%, 95%, and 93% of the total mass gain for the wrought, LPBF, and DED samples, respectively. Based on these findings, the chromia scale and IGO are the primary

factors that explain the majority of the mass gain kinetics for the LPBF and DED. However, there is still a significant amount of unexplained mass gain in the wrought alloy, which may be attributed to other factors, such as oxide products at the top of the scale. Upon examining the oxide surface, it was found that the wrought alloy had more discrete Cr-Mn-spinel than any other sample as shown in the oxide topography characterization in section 5.3.2.2. This indicates that further analysis is necessary to account for the spinel contribution in the wrought kinetics.

5.3.3.2 Factors that Enhance Degradation During Oxidation in AM Samples

5.3.3.2.1 Intergranular Oxidation Formation Mechanism

According to the classic model of internal oxidation, alloy 625 has the possibility to show internal oxidation of Al and Ti [67]. First, Al and Ti can form more stable oxides than chromia. Second, oxygen is soluble in the Ni-Cr matrix [142]. Furthermore, alloy grain boundaries are a preferential site for internal oxide nucleation due to the greater penetration of oxygen inward and the lower degree of supersaturation needed [143]. As a consequence, IGO is expected to be deeper than internal oxidation. What is noteworthy is that AM samples exhibit a more severe IGO than th cast or wrought alloys, which aligns with prior research findings [9], [12], [77]. Several proposed hypotheses to explain this phenomenon includes (1) grain boundary misorientation, (2) minor elements composition, and (3) subsurface void formation.

(1) Grain boundary misorientation: In terms of grain character, grain boundaries with Σ3 coincident site lattice or twin boundaries display better resistance to corrosion, cracking, and sliding (creep) than grain boundaries with other misorientations [144]. These properties have been correlated to the lowest grain-boundary energy. Other orientations with low grain-boundary energy (such as Σ11, Σ19, and Σ27) have also exhibited similar properties, but not as consistently

as Σ3 [145]. In the case of high-temperature oxidation, the lower oxygen diffusion through Σ3 grain boundaries contributes to their intergranular oxidation resistance [146]–[148].

Upon examining the misorientation of grain boundaries in wrought and AM samples, the former presents a much higher proportion of Σ3 grain boundaries (refer to section 5.6.3.1) Therefore, the less severe IGO of the wrought compared to the AM may be expected. Annealing heat treatments have been reported to successfully increase the amount of Σ3 grain boundaries in the AM samples [85], [149]. However, it was found in this study that the depth of IGO remained similar in heat-treated AM samples compared to as-built AM samples (refer to section 5.6.3.2). Other studies also reported significant IGO after HT [12], [74]. Therefore, further research is needed to understand the differences between the nature of the wrought and AM grain boundaries beyond the misorientation that makes the AM grain boundaries more susceptible to oxidation.

(2) Minor elements contents: Regarding alloy compositional differences, Chyrkin et al. [12] reported that low Si content in AM (0.08 wt.% in the AM to 0.27 wt.% in the forge) impedes the formation of a protective SiO_2 beneath the chromia, thus increasing the oxygen diffusion into the alloy and the IGO. The protective benefit of Si has been observed in other types of alloys as well [113]. In this study, the Si content is 0.22 wt.%, 0.17wt.%, 0.11 wt.%, and 0.11 wt.% for the wrought, cast, LPBF, and DED samples, respectively. So, AM Si content is consistently lower than the wrought and cast, but the difference is one-third of the one reported in Chyrkin et al. study [12], and the IGO severity is as strong. It will be informative to compare alloys additively manufactured with different Si content to evaluate the Si effect on IGO, since the nature of AM processing and its impact on the microstructure may affect the protectiveness level given by the SiO_2.

(3) Subsurface voids formation: Another distinctive characteristic of the oxidized AM sample subsurfaces is the presence of voids. These voids can either be discrete or surrounding the IGO.

In the case of the DED, it is more common to find discrete voids in the subsurface. Similar findings have been found in other studies, where these voids have been described as Kirkendall voids [9], [77], [87]. During the chromia-scale formation, the outward flux of chromium from the subsurface is compensated by an inward flux of vacancies. However, the back diffusion of the remaining elements is slower than the vacancy flux, leading to a saturation of vacancies in the subsurface. Over time, these vacancies annihilate, resulting in void formation. The LPBF sample does not exhibit too many Kirkendall voids because vacancies prefer to annihilate in the incoherent oxide/matrix interface along the grain boundaries [142]. This explains the voids that are associated with the IGO in the LPBF samples.

Another source for voids formation comes from the initial porosity and interstitial oxygen in the as-built part. These pores may arise from trapped gas during atomization of the metal powder, or as a mesostructural defect during the additive manufacturing process (refer to section 4). An analysis of the as-built parts shows that the porosity is $0.12 \pm 0.04\%$ and $0.82 \pm 0.11\%$ for the LPBF and DED samples, respectively. Although gas atomization and additive manufacturing processes were conducted in an argon atmosphere, oxygen traces may be present in the pores. The oxygen control level allowed during the LPBF process is 200ppm, while the DED process didn't have oxygen control. The overall oxygen content in the alloy, encompassing both interstitial oxygen and oxygen within the pores, was determined by the inert gas fusion analysis technique, and the findings are presented in Table 5-11.

Table 5-11. Oxygen and sulfur content in the alloy 625 manufactured by wrought, cast, LPBF and DED. Measurements were acquired by IGF technique.

	Oxygen (ppm)	Sulfur (ppm)
Wrought	16	< 5
Cast	20	< 5
LPBF	120	9.8
DED	240	8.1

The oxygen content in the LPBF and DED samples is significantly higher than in wrought and cast alloy. This aligns with previous research that has reported interstitial oxygen in Ti alloys [150]–[152], Al alloys, and stainless steel additively manufactured. It has been proven that oxygen content increases during the AM process by comparing the powder composition with the built part (increasing up to 43%) [151], [152]. The higher oxygen is likely due to a longer processing time and a higher surface area exposed to the atmosphere at melting temperature during the AM processes. In fact, a positive correlation was found between the oxygen concentration and the building rate, which is mainly attributed to the metal liquid residence time [152]. Besides, it is important to consider that Ti and Al alloys have a higher interstitial oxygen concentration than nickel-based alloys due to their higher oxygen affinity, but the phenomenon remains the same.

Figure 5-36 shows how the pores in the DED matrix are transformed after an isothermal oxidation test. The particle size is within the range from 0.1 um to 1um, and a given particle is comprised of an Al_2O_3 core enveloped by TiO_2. The oxygen used to form these distinct oxide particles is inferred to be sourced from the original porosity and the interstitial oxygen trapped during the DED process. According to Trumble and Ruhle [153], the oxygen in the Ni matrix

required to precipitate alumina is 60 ppm at 950°C. Both conventional methods, wrought and cast, show oxygen contents below this value. The AM processes result oxygen contents that surpasses the limit for alumina precipitation in the matrix. This explains the discrete oxide particles in the DED matrix; however, no oxide particles were detected in the LPBF matrix. There are some caveats to consider: 1) it is difficult to distinguish how much oxygen corresponds to the pores; 2) the interstitial oxygen may not be uniformly distributed in the matrix; 3) the oxygen content necessary to precipitate alumina is based on the Ni-Al-O ternary [153]; and the oxygen required to precipitate increases with the Cr content in the alloy [142]. Additionally, interstitial oxygen near to grain-boundaries may migrate to coarsen the IGO. This phenomenon might be more significant for the LPBF samples since the alloy has higher grain boundary density than the DED sample.

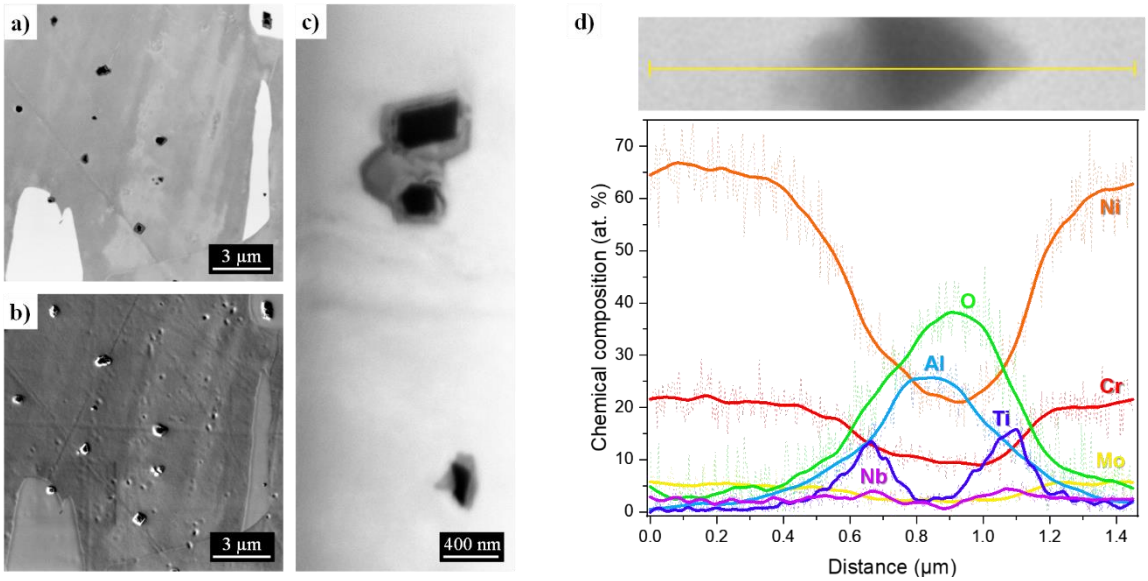

Figure 5-36. Oxidized pores in the DED matrix after 1000h at 950°C: a) BSE-low mag. b) SE-low mag c) BSE- high mag. d) EDS line composition. Resulted oxide particles consist of an alumina core enveloped in titania.

In addition, it is important to note that voids that account for higher oxygen content in LPBF and DED samples may coarsen during oxidation. The voids coarsening can be caused by

vacancies or relief surface energy. Coarsening by vacancies includes Cr (from the chromia scale formation) and Al (from the Al_2O_3 in the IGO). Generally, the Al is negligible, but the contribution of the IGO is significant for the LPBF and DED samples, which partially explains the abundant voids in the IGO of the LPBF sample. On the other hand, surface energy decreases when the number of small voids decreases, and the size of the larger voids increases. Therefore, pre-existing big voids and decohesion regions coarse more easily into bigger voids. Kirkendall's voids in the DED sample commonly nucleate at the incoherent d-phase/matrix interface and might coarsen due to the vacancies injection and relief of surface energy.

5.3.3.2.2 Compressive Residual Stresses in the Chromia Scale

The residual stresses in the scale can be a driving force for scale failure, depending on the scale adhesion. The hypothesis is that factors that increase the oxide-scale non-planarity of the LPBF and DED samples cause an increase in the compressive stresses of the scale as well. The convoluted interface is a result of additional chromia formation in the oxide ridges coupled with δ-phase precipitates, which continue growing in conjunction with the chromia growth, eventually becoming embedded in the growing scale. The mode of relaxation of these compressive stresses can be local scale decohesion, contributing to the pores in the oxide/scale interface.

A basic estimate of residual stresses in the surface of the oxide scale can be estimated from XRD technique [154]. It is worth noting that the large beam size diameter (2 mm) of XRD lens and beam penetration could be deeper than the oxide scale thickness and therefore include the alloy. Thereby, measurements will give only a first approximation for residual stresses of the oxide scale (i.e., including flat oxide, and oxide ridges).

The plane-stress elastic model or so called $\sin^2\psi$ method calculates the residual stress parallel to the surface, assuming no stress perpendicular to the surface and no crystallographic

texture in the scale [155]. After mathematical simplifications, the scale stress is given as [154], [156],

$$\boldsymbol{\sigma_{\phi}} = \left(\frac{\boldsymbol{E_{(hkl)}}}{\mathbf{1}+\boldsymbol{\nu_{(hkl)}}}\right)\frac{\mathbf{1}}{\boldsymbol{d_{\phi 0}}}\left(\frac{\boldsymbol{\partial d_{\phi\psi}}}{\boldsymbol{\partial \sin^2\psi}}\right) \quad (5\text{-}9)$$

where ψ corresponds to the axis normal to the surface, and ϕ axis lies on the surface plane. $E_{(hkl)}$ is the modulus of elasticity in the (hkl) plane, $\nu_{(hkl)}$ the Poisson's ratio in the (hkl) plane , $d_{\phi 0}$ is the interplanar spacing at ϕ equal to zero, and $\left(\frac{\partial d_{\phi\psi}}{\partial \sin^2\psi}\right)$ is the slope of the plot $d_{(hkl)}$ (interplanar distance of the *hkl* plane) against $\sin^2\psi$.

In order to calculate the scale residual stress, XRD measurements were carried out for the (116) diffracting plane of the chromia. Cu Kα was the radiation source, the angular step size was 0.025° and the scan speed was 13 s/step. The sample was tilted to achieve five ψ values (i.e., 0°, 30°, 40°, 50°, and 70°). Measured samples were oxidized at 950°C for 1000h in no visible spalled area, to ensure a thicker scale and avoid alloy interference in the measurements. An example of the measurements taken for the LPBF oxidized samples is given in Figure 5-37a, where each peak was fitted to a Gaussian distribution to calculate the interplanar spacing. Figure 5-37b shows the plot of $d_{(116)}$ vs $\sin^2\psi$. The slopes for all samples are negative indicating compressive residual stress in the scales [154], [156].

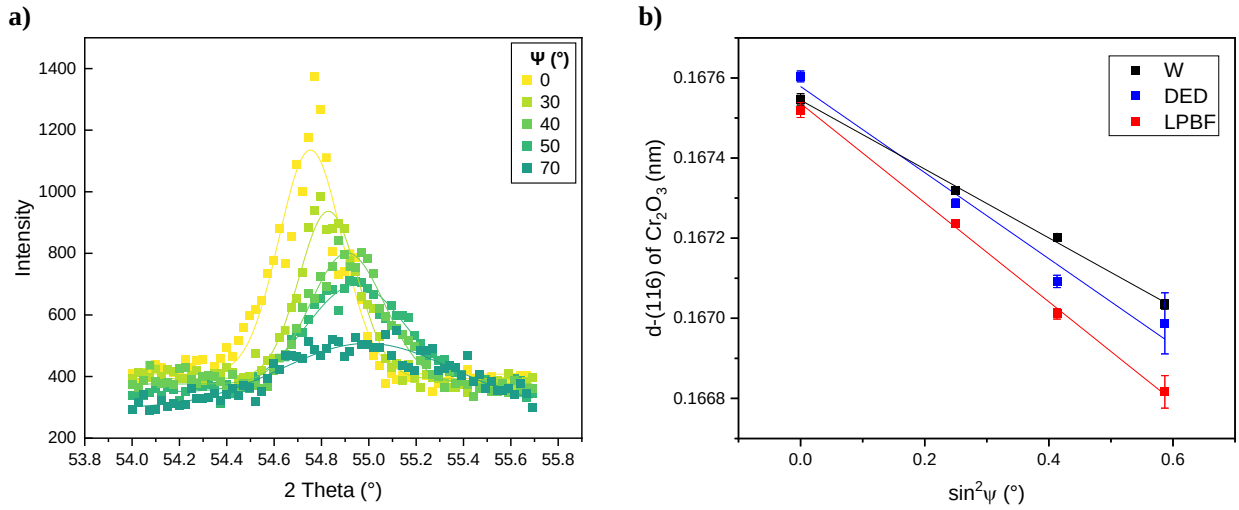

Figure 5-37. Example of data processing for residual stress measurements for Cr_2O_3 scale: a) XRD scans and fitting for LPBF oxdized samples at 950°C for 1000h. b) linear regresion

Table 5-12 shows the slopes and calculated residual stresses, where the elastic constants used were: $E_{(116)}$=334.5 GPa and $\nu_{(116)}$=0.264 [157]. The calculated stresses are comparable to what has been reported in literature for other chromia scales formed in similar systems. The LPBF chromia shows a stepper slope in Figure 5-37b, followed by the DED and the wrought. Therefore, the chromia grown on the LPBF sample has the highest compressive stress, and the chromia on the wrought alloy has the smallest stress. This suggests that chromia formed on the LPBF and DED samples have the greater potential to locally debond than the chromia formed on the wrought alloy. This is in agreement with reported literature, which found that chromia scale grown on LPBF sample has less adherence compared to chromia-scale grown on wrought samples [9].

Table 5-12. Residual stresses in Cr_2O_3 scale grown on alloy 625 measured by XRD tilting method, compared with literature values for Cr_2O_3 grown on other alloy systems.

	$\left(\frac{\partial d_{\phi\psi}}{\partial \sin^2\psi}\right)$	**Residual stress (GPa)**
Alloy 625-Wrought	-8.6E-4	-1.36±0.11
Alloy 625-LPBF	-12.4E-4	-1.96±0.13
Alloy 625-DED	-10.7E-4	-1.69±0.17
Ni-30Cr (900°C-18h) [157]		-2.05, -2.40
Fe-47Cr (900°C-18h) [157]		-1.10, -1.40
Ni-25Cr (1000°C-27h) [158]		-1.25

An interesting example of the buckling formation during oxidation in the LPBF sample is shown in Figure 5-31. There is a buckling region where newer grains nucleate to fill the space created by the scale decohesion. Although buckling is typically associated with cooling due to variations in the thermal coefficient between the alloy and oxide [55], there are instances where compressive stresses trigger it during oxidation. For instance, Lillerud and Kofstad [159] reported scale buckling on the alloy grain boundaries during the oxidation of pure Cr, and Golightly et al. [160] showed it for alumina formed on Fe-Cr-Al alloys.

On the other hand, interfacial defects are also attributed to the sulfur and oxygen contents. Regarding the sulfur content, Sanviemvongsak et al. [87] reported that the sulfur content in AM alloy 718 increases oxide scale spallation compared to the 718 wrought alloy during cyclic oxidation. Table 5-11 shows a higher sulfur content in the AM samples than in the wrought, which may contribute to the more frequent decohesion regions in the AM samples. Regarding oxygen, similar to the formation of the voids in the IGO, the oxide/alloy interface presents a degree of incoherence that makes it a preferential nucleation site for formation of voids.

5.3.3.2.3 Variability of Surface Finishing Effect on Chromia Scale Integrity and IGO

Studies indicate that surface finish significantly influences the oxidation behavior of alumina- and chromia-forming alloys [161]–[165]. This is due to the level of subsurface deformation, which impacts the Al and Cr ionic transport in the alloy. Specifically, deformation increases the dislocation density in the alloy subsurface, which is the driving force for recrystallization during the heating process [161], [162]. The smaller grain size promoted by the recrystallization provides a higher density of grain boundaries, which act as short-circuit diffusion paths for the outward Cr supply. In turn, a higher Cr supply promotes an earlier establishment of a protective chromia scale.

It is still unknown to what extent the alloy manufacturing process could change the surface finishing effect on the oxidation behavior. In order to evaluate this, an oxidation test was performed on ground wrought, LPBF, and DED samples. Coupons were ground with four kinds of SiC paper (grit size): P500 (30 µm), P800 (22 µm), P1200 (15 µm), and P2000 (10 µm). The oxidation exposures were carried out at 950°C for 24h in air. Figure 5-38 shows the resulting cross-sectional images, revealing that the chromia integrity is affected by surface finish. Samples prepared with coarser SiC-paper grit sizes have more scale damage to the scale. Additionally, there is a slight difference in the IGO depth when using different grits of SiC paper for all samples. This is illustrated in Figure 5-38, which depicts the IGO depth measured in relation to the SiC paper grit for each sample. Indeed, IGO depth increases as the SiC grit paper becomes coarser for the three samples. However, the LPBF and DED show steeper slopes than the wrought, indicating a higher susceptibility to the surface finishing effect on the IGO depth in the former samples.

Based on literature findings, the deformation by grinding with greater SiC grit promotes deeper deformation [161]. This explains the correlation of IGO depth with the SiC grit size. Furthermore, the increased susceptibility of the AM samples results from a more damaged chromia scale and an exacerbated attack due in part to the high level of interstitial oxygen.

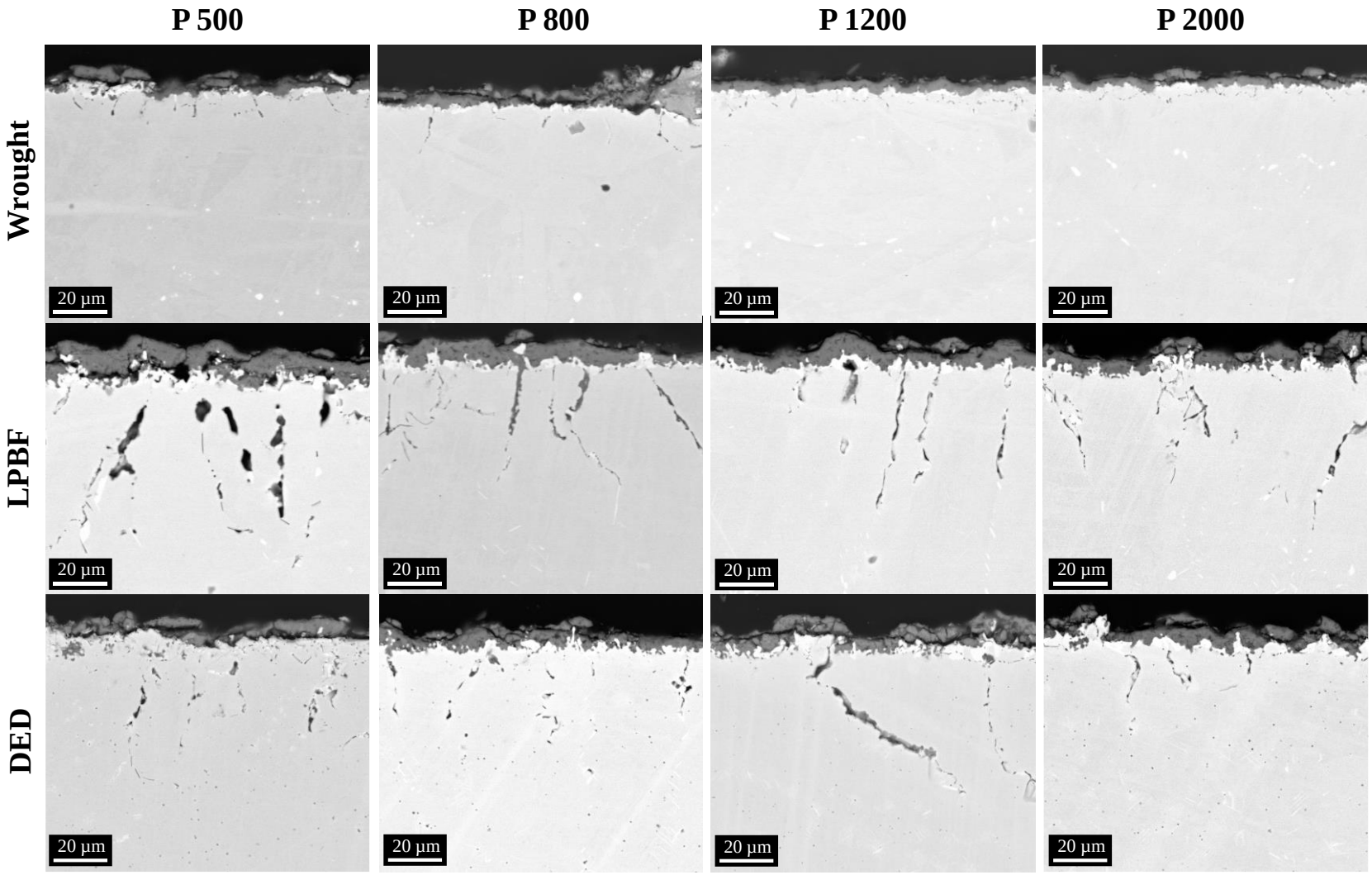

Figure 5-38. Cross-sectional BSE-SEM images of alloy 625 oxidized in air at 950°C for 24h using different surface finishing. Columns corresponds to different SiC paper grit size used. Scale damage and IGO depth are affected by the alloy surface finish.

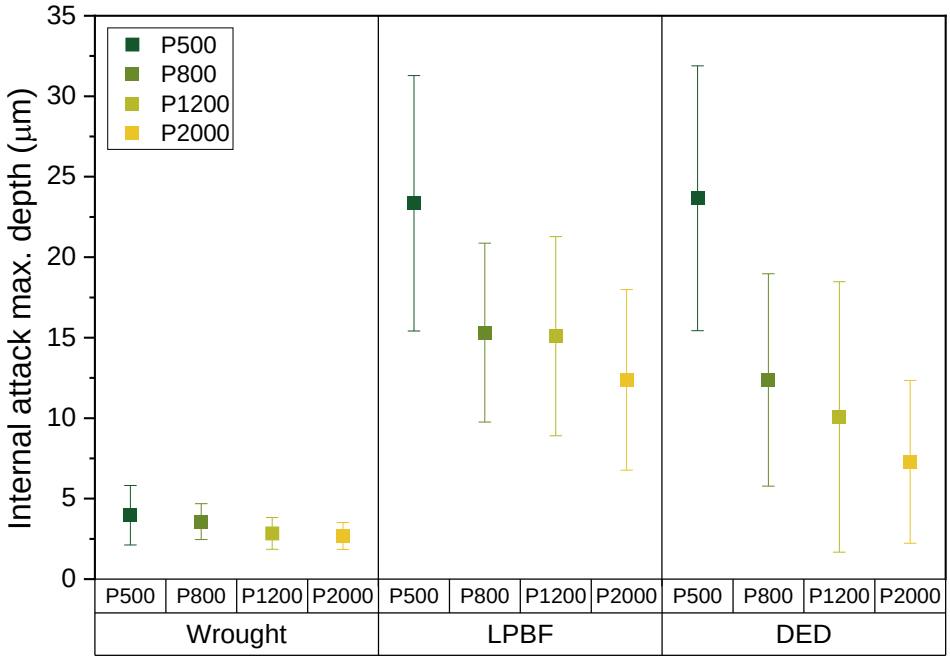

Figure 5-39. Effect of the SiC paper grit size on the maximum internal attack depth in alloy 625 oxidized in air at 950°C for 24h. LPBF and DED samples are more suceptible to the effect of the alloy surface finish on the IGO depth than the wrought alloy.

5.3.4 Conclusions

- The main difference in oxidation behavior at 950°C among wrought, cast, LPBF, and DED samples is the enhanced intergranular oxidation in the LPBF and DED samples. The four samples form a chromia scale with δ-precipitates in the alloy at the scale/alloy interface and intergranular oxidation (IGO) which is mainly composed of Al_2O_3 and TiO_2 (refer to Figure 5-28).

- Based on weight gain, the kinetics are mainly influenced by chromia scale formation and intergranular oxidation. In the case of the wrought alloy,

chromia formation primarily dictates the oxidation kinetics. In the LPBF and DED samples, although chromia formation is the main contributor, intergranular oxidation accounts for 30% of the kinetics based on weight (refer to Figure 5-35).

- Based on the thickness of the chromia scale, it has been observed that the LPBF sample exhibits a higher rate of oxidation than the DED and wrought alloys. This can be attributed to the differences in the size of chromia grains (refer to Figure 5-32) and Ti doping (refer to Figure 5-33). The chromia formed on the LPBF samples has the highest Ti segregation, which enhances diffusion kinetics and chromia thickening.

- The enhanced IGO in AM samples is potentially attributed to the higher oxygen content distributed in voids and interstitially. Interstitial oxygen coarse the IGO by increasing oxygen availability near grain boundaries. Voids coarse during oxidation due to relief of interfacial energy and vacancy injections.

5.4 High Cycle Fatigue of Alloy 625 oxidized at 800°C

This chapter is modified from the published paper: G. de Leon Nope, G. Wang, J.M. Alvarado-Orozco and B. Gleeson, in *Proceedings of the 10th International Symposium on Superalloy 718 and Derivatives 2023*, edited by E. A. Ott et al. (The Minerals, Metals & Materials Society, Pittsburgh, Pennsylvania, USA, 2023).

5.4.1 Introduction

Oxidation of Alloy 625 typically involves the formation of a continuous chromia (Cr_2O_3) scale along with internal oxidation. Even though a chromia scale can provide good oxidation and corrosion resistance, the internal attack has the potential to reduce fatigue life [90].

Several studies have assessed the effect of prior oxidation on fatigue performance, showing a potential for internal oxides to act as preferred crack-initiation sites in Ni-based alloys used in rotor disc applications [90]–[93]. A study of ME3 alloy, also known as Rene 104, showed that notch fatigue life reduction is proportional to the oxide scale thickness and the internal oxidation depth, where the testing was performed in air at 704°C [92]. Specifically, life reduction was attributed to carbide dissolution in the depleted region and internal oxidation. Gabb *et al.* [93] also reported a reduction in the low-cycle fatigue life reduction of alloy U720 at 650°C and ME3 alloy at 704°C due to internal oxidation. Cracks in non-oxidized samples were shown to initiate at the subsurface (~50 μm below the surface), whereas oxidized samples showed initiation at the surface. To the best of the authors' knowledge, no reports have been published regarding the effects of oxidation on the fatigue behavior of Alloy 625.

Prior studies on the oxidation behavior of additively-manufactured (AM) chromia-forming Ni-based alloys have shown differences in comparison to counterpart conventionally-processed alloys that have a potential to affect fatigue performance. For example, oxidized LPBF(laser powder bed fusion)-Alloy 718 was found to exhibit deeper internal attack and a faster internal oxidation rate [77]; whereas studies on oxidized LPBF-Alloy 625 reported higher spallation [9], abundant subsurface voids [128], and an increase of subsurface δ-precipitates [94]. The current study compares the oxidation of as-printed LPBF, as-printed DED (directed energy deposition), and fully heat-treated wrought Alloy 625 and evaluates the impact of the oxidation-driven features on the subsequent fatigue performances.

5.4.2 Experimental Procedures

Alloy 625 fabricated by three different manufacturing methods was investigated. The two laser-assisted AM processes selected were LPBF and DED. Commercially available wrought Alloy 625 was used as a conventional manufacturing method for comparison.

5.4.2.1 Static Oxidation of Flat Coupons

Oxidation of flat coupons was investigated as a reference to characterize the oxide-induced microstructure in the absence of loading. Coupons of approximate dimensions 10 mm x 10 mm x 2 mm were obtained using a low-speed saw from the LPBF and DED cubes, *both* in as-built conditions. The surface was prepared to a P600-SiC finish and then ultrasonically cleaned in ethanol. The flat coupons were oxidized in lab air at 800°C for 24, 300, and 1000 hours in an open furnace. After testing, cross-sections of the coupons were prepared metallographically, and the microstructure was characterized using scanning electron microscopy (Apreo system, ThermoFisher Scientific, Waltham, MA, USA) at 15 keV.

5.4.2.2 Fatigue Test Bars Preparation

For the fatigue tests, thermal aging (TA) and oxidation (OX) treatments were done for samples processed by each manufacturing method to independently evaluate the contributions from oxidation and the concurrent evolution of microstructure due to high-temperature exposure (*i.e.*, phase transformation, grain growth, recrystallization). Both these exposures were conducted on as-printed test bars for 24h, 300h, and 1000h at 800°C in a horizontal furnace. Laboratory air was the atmosphere for the OX exposures, whereas argon was used for the TA exposures.

Cylinders were cut from the bulk AM samples by wire electrical discharge machining (EDM) and then machined by computer numerical control (CNC) milling to obtain the final geometry illustrated in Figure 5-40. The standard hourglass-shaped test bar used for the fatigue testing is in accordance with ASTM E466-07. Each fatigue test bar had a gauge length of 31.4 mm and a minimum gauge diameter of 5.08 mm.

For the OX conditions, the test bar surface finishing was prepared using 320-grit SiC paper and the results of internal attack depth and oxide thickness were compared to previous work [94]. On the other hand, the TA test bars were polished to a mirror finish with a very fine non-woven alumina polishing pad to avoid detrimental interference of a high surface roughness on the fatigue life.

5.4.2.3 High Cycle Fatigue Testing

Uniaxial fatigue testing was conducted at room temperature using an MTS servo-hydraulic universal test machine (MTS 880 landmark, MTS, Eden Prairie, Minnesota, USA) under load control mode. A stress ratio R = -1 was used ($R = \sigma_{min}/\sigma_{max}$), following a sinusoidal waveform at frequency of 36-38 Hz. All experiments used a maximum stress level

of 440 MPa and the fatigue run-out condition was set to 10^7 cycles. Every condition was performed in duplicate, except for the DED at 300h in OX and TA conditions.

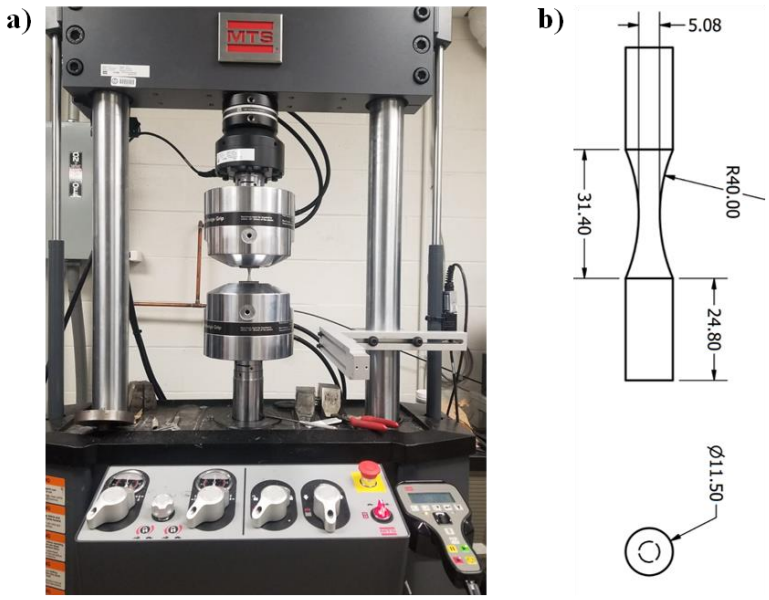

Figure 5-40. a) MTS 880 landmark machine, b) Fatigue test bar dimensions following ASTM E466-07 (measurements shown are in mm).

After testing, fractographic analysis was done using an optical microscope Smart-zoom 5 (Carl Zeiss, Jena, Germany) to identify crack-initiation sites. A cross-section of the fractured sample, parallel to the load axis, was then cut from the main crack initiation and prepared metallographically to characterize secondary cracking and degradation. Eight micrographs at 5000× magnification per sample were examined via SEM at 15 keV. Microstructural features after fatigue testing, including oxide thickness and maximum depth of internal oxidation, were quantitively measured using Gwydion software (Czech Metrology Institute, Brno, Czech Republic). Subsurface precipitates area and average precipitate aspect ratio were measured using Particleanalyzer_HD software [166] (University Hospital Heidelberg, Heidelberg, Germany), where precipitates consisted of δ-phase and σ-phase. Finally, the linear detachment fraction, the non-planar oxide/metal interface index and the interfacial defects area were calculated based on metrics acquired using ImageJ software (National Institutes of Health, Bethesda, MD, USA). The term “interfacial defect” is used in

this study to refer to the formation of free space at the oxide/alloy interface. The linear detachment fraction was calculated as the ratio between the interfacial length without oxide divided by the total interfacial length at the external oxide/metal interface. The non-planar interface index, a measurement related to roughness, was estimated as the ratio between the total interfacial length at the external oxide/metal interface divided by the length if that interface is perfectly flat.

5.4.3 Results and Discussion

5.4.3.1 Oxidation Behavior of Flat Coupons

In this study, oxidation exposures were extended from 24h to 300h and 1000h at 800°C. Figure 5-41 shows cross-sectional images of the flat coupons after oxidation at 800°C for 1000h. At longer exposures, the chromia scales formed on LPBF and DED samples were slightly thicker than those formed on the wrought, in accordance with the kinetics trend reported at shorter times [94]. Main differences in the oxidation behavior between wrought and AM samples occur in the subsurface. Beneath the chromia scale, the composition of the bright precipitates corresponds to δ-phase [$(Ni, Cr)_3(Nb, Mo)$] and σ-phase [Mo-Ni-Si-Cr-Nb]. LPBF and DED showed a higher fraction of these subsurface precipitates than the wrought due to a higher Nb availability from the original segregation in the as-built state [9].

Internal oxidation and bulk transformation represented the most significant differences among the samples. The wrought alloy exhibited internal oxidation preferentially located at grain boundaries and consisting mainly of compact alumina. Internal oxidation in *both* AM alloys was deeper, coarser and more abundant than that in the wrought alloy. As postulated by Sanviemvongsak *et al.* [127], this difference can been attributed to the improved oxidation resistance of twin boundaries present in the wrought. After oxidation, grain boundaries in the AM samples were found to be decorated by coarser δ-precipitates,

internal oxidation, and a noticeable amount of free space among them. The exacerbation of voids in AM samples' grain boundaries has been reported previously and attributed to a faster local Cr consumption [128]. Additionally, internal oxides and voids form preferentially among the precipitate clusters located in the interdendritic regions of the DED-processed alloy, where the highest Nb-Mo-segregation was in the as-built condition. Void formation in oxidized Ni-Cr alloys has been attributed to the Kirkendall effect [127], [167].

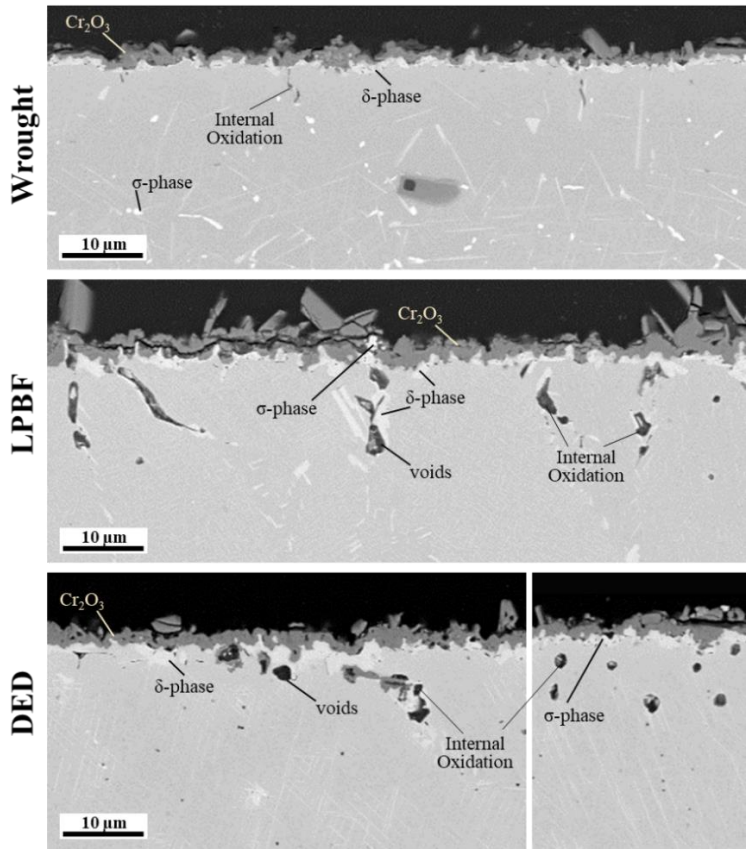

Figure 5-41. SEM backscattered electron image of Alloy 625 oxidized at 800°C for 1000h in air for the wrought, LPBF, and DED fabrication conditions.

On the other hand, the bulk transformation after the oxidation differs for the three conditions (*e.g.*, distribution, morphology, and precipitates' size). Since the original microstructure varies among them (*i.e.*, grain size, refractory segregation, residual stress), different evolution after the heat treatment is expected. Therefore, to solely evaluate the influence of the oxidation behavior on fatigue performance, a counterpart thermal aging

under a non-oxidizing atmosphere of argon was done for the same time as each oxidized sample.

Prior studies on oxidized samples have shown that internal oxidation along grain boundaries [90], [91], [168] and the precipitates-free region [92] are critical factors in accelerating crack initiation during fatigue testing, showing that subsurface evolution during oxidation plays a vital role in fatigue performance. Therefore, since the main differences in the oxidation behavior of the additive samples occur in the subsurface, differences in the fatigue life may be expected. Other possible contributions to initiate and propagate cracks are localized interfacial defects (local detachment of the scale/alloy). Although pores in the scale may also be considered, crack propagation throughout the oxide layer is generally resisted by its compressive stresses. The molar volume difference between the oxide and the alloy, and the mismatch between the thermal expansion coefficients of the oxide and the alloy contribute to the compressive stresses of the external oxide layer [54].

Finally, the long horizontal cracks in the scale are inferred to be artifacts caused during the cutting and polishing of the oxidized coupon. Thus, the integrity of the scale is expected to be intact before starting the fatigue testing.

5.4.3.2 Fatigue Results

Figure 5-42 shows the mean fatigue life as a function of thermal exposure conditions. The wrought test bars did not fail, reaching run-out (10^7 cycles), regardless of the exposure condition. In contrast, both the LPBF and DED test bars failed before 10^7 cycles with the exception of the as-built LPBF samples that were thermally aged for 24h and 300h. Apparently, the differences in the oxidation and thermal aging behaviors associated with the two additive processes are significant enough to affect fatigue performance.

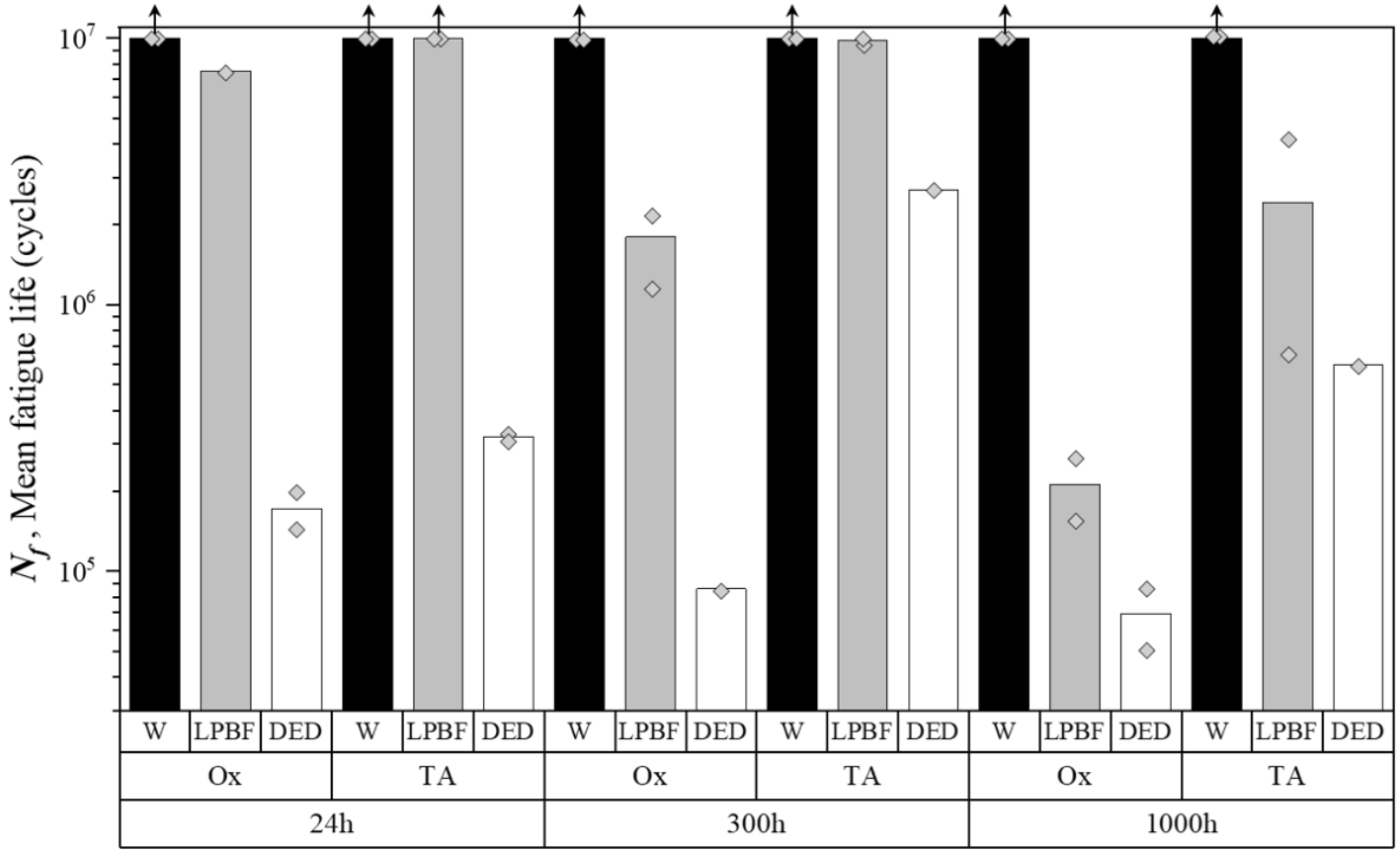

Figure 5-42. Mean room temperature fatigue life of the wrought (W), LPBF, and DED Alloy 625 test bars that were oxidized (Ox) and thermal aged (TA) for 24h, 300h, and 1000h at 800°C prior to testing.

The results in Figure 5-42 indicate that both LPBF and DED consistently exhibit a higher fatigue life after thermal aging than oxidation for the same exposure times. The oxidation reduces the mean fatigue life in the LPBF test bars by 25%, 82%, and 91% for 24h, 300h, and 1000h, respectively. For the DED test bars, the fatigue life reduction by oxidation was 46%, 96.8%, and 88% for 24h, 300h, and 1000h, respectively. Therefore, since oxidized samples show the same bulk evolution as thermal aging, the fatigue life reduction between TA and OX is attributed to the surface and subsurface evolution processes associated with oxidation. Several studies on Ni-based alloys have shown a reduction in fatigue life on exposure to high temperatures in air atmosphere, either during (e.g., N18 alloy [169]) or before the fatigue test (e.g., ME3 alloy [92], [93], IN100 [89]). In this study, the general trend shows that life reduction increases with increasing oxidation time. It is relevant to note that previous studies have shown that life reduction also increases with higher temperature exposures [92], [169]. Additionally, the DED-processed test bars exhibited a shorter fatigue life than those processed by LPBF when comparing oxidation at the same exposure times.

5.4.3.3 Microstructural Degradation Assessment of Oxidized Samples after Fatigue Test

Analyzing the microstructure evolution after testing can lead to a better understanding of the differences in fatigue performance. Figure 5-43 shows representative micrographs of the cross-sections after fatigue testing. The wrought microstructures do not show appreciable degradation after 10^7 cycles; the scales keep their integrity, and non-appreciable cracks are identified after the testing. By contrast, both the LPBF and DED test bars show increased subsurface degradation and breaches of the scale integrity. Quantitative measurements of the degradation state at the failure moment were therefore acquired to better correlate degradation with the fatigue performance. The degradation variables were roughly classified into the

following three main types: (1) oxide products; (2) subsurface precipitates (δ- and σ-phase); and (3) oxide/metal interfacial detachment. Oxide products included maximum depth of internal oxidation and external oxide thickness. Subsurface precipitate measurements consisted of their total area and aspect ratio. Finally, the interfacial detachment included the detachment linear fraction, non-planar interface index, and interfacial defects area (empty space between the oxide scale and the alloy). Figure 5-44 summarizes the results for the wrought, LPBF, and DED alloys for various exposure conditions using spider diagrams, where all values are normalized relative to the maximum value of each variable; the complete data can be found in Appendix A.

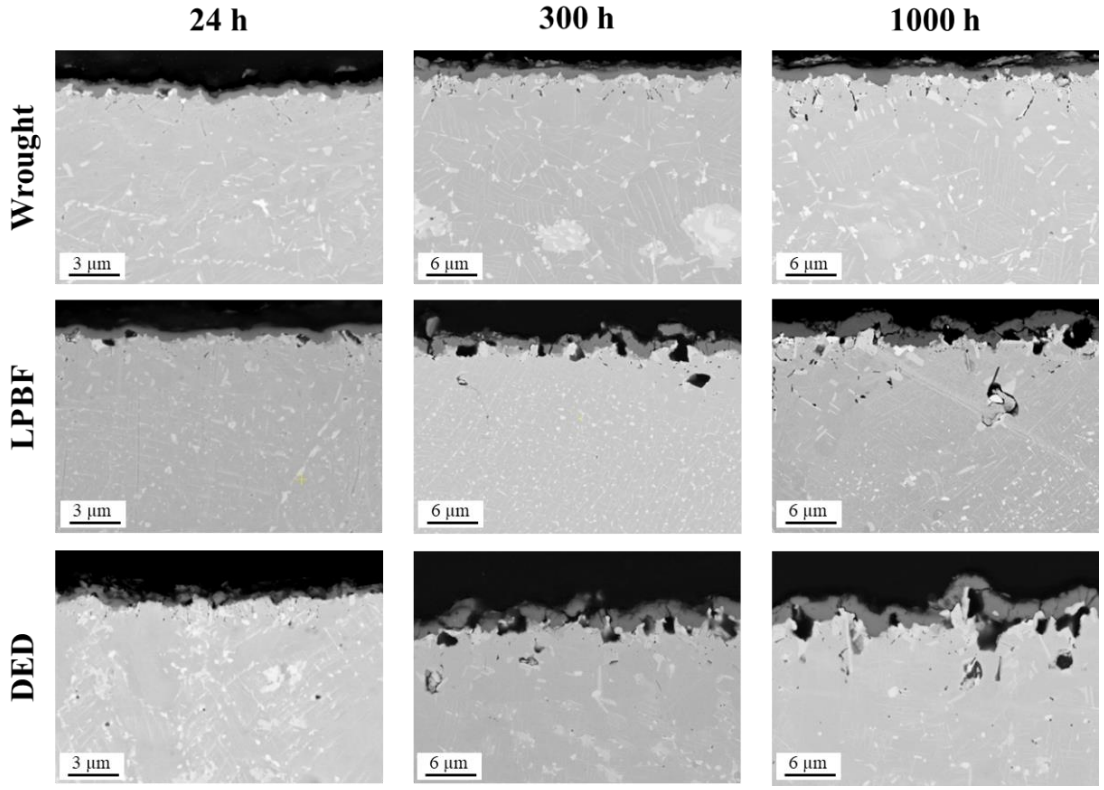

Figure 5-43. SEM images of cross-sections of the oxidized test bars (OX) after fatigue testing. The oxide layer shown is parallel to the load axis. Analized wrought test bars did not fail during the fatigue testing. LPBF and DED micrograpahs were taken near to the failure region.

The first general observation is that the bigger the area for a given variable, the smaller the mean fatigue life, hence those variables that most affect the area play an important role in determining fatigue life. The second observation is the increase in degradation with the oxidation time for the LPBF and DED test bars; the lesser the degradation, the higher the fatigue life. A more detailed analysis is presented in the following.

Since wrought test bars withstand 10^7 cycles, neither the load nor the oxidation induced any critical size crack. Therefore, the wrought values can be considered not detrimental, as a degradation state where failure is not likely. Accordingly, if the variables of an unknown sample are within the wrought range, failure by fatigue is not expected. For example, at 24h the most significant difference between the wrought and the AM samples is the detachment linear fraction followed by the area of the interfacial defect. The detachment linear fraction of LPBF and DED is more than twice that of the wrought. This trend continues at 100 and 300h, where the value of wrought keeps constant while the LPBF and DED values continue to increase with time. Thus, a linear fraction below 0.20 corresponds to non-failure and above 0.28 corresponds to failure. Additionally, the linear fraction increment is inversely proportional to the fatigue life for the LPBF and DED test bars, being the measured variable that best describes the fatigue life.

At the 300h and 1000h oxidation times, the area of the interfacial defects together with the detachment linear fraction show the biggest difference between the non-failure region demarcated by the wrought and the AM test bars, showing that the exacerbation of interfacial defects is a key precursor to imminent failure. The maximum depth of internal oxidation, non-planar interface index, and subsurface precipitates area follow these in relevance.

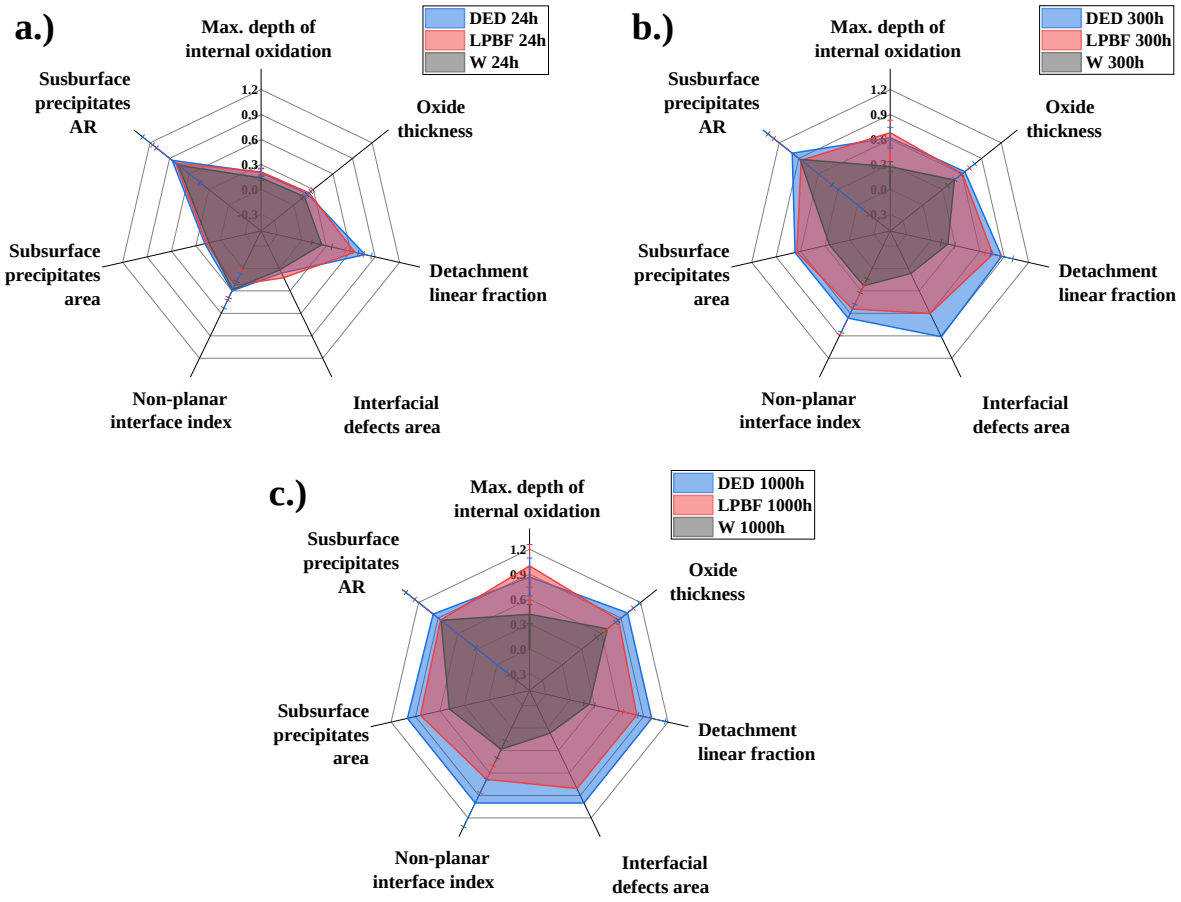

Figure 5-44. Graphical representation of microstructural evolution and degradation measurements after fatigue testing of oxidized test bars. Comparison of wrought, LPBF, and DED alloys after different oxidation times: a) 24h, b) 300h, and c) 1000h.

In contrast, the oxide thickness and the precipitate aspect ratio do not directly correlate with the fatigue life. Regarding the aspect ratio (AR) of the subsurface precipitates, no substantial changes were observed, regardless of the exposure condition. Since the influence of the precipitates' AR will be in the same range in all studied samples, it is not directly contributing to differences in the reported fatigue life. The main difference in the subsurface precipitates among the samples was in the phase fraction, precipitate size, and spatial distribution. Regarding the oxide thickness, the standard deviation of the measurement can be interpreted as a scale homogeneity, showing that AM samples (high deviation) have a high

variability in the oxide scale thickness compared with the wrought (low deviation) for the same exposure times. A highly variable oxide thickness can affect the compressive stress distribution throughout the scale, promoting local stress concentrators that lead to interfacial defects [170].

An additional fatigue test until failure was conducted for a wrought test bar oxidized after 1000h. The sample failed at $5x10^7$ cycles, and Figure 5-45 shows the cross-section of microstructure near the fracture region. The interfacial and subsurface degradations show similarities with the microstructures of the AM test bars (both LPBF and DED) oxidized at 1000h after failure (Figure 5-45). These similarities include the exacerbation of interfacial defects, an increase of linear fraction detachment, and external oxide scale cracking. As such, it indicates that the degradation prior to failure is similarly independent of the manufacturing process, but both LPBF and DED test bars underwent a higher degradation rate than the wrought, causing earlier failure in the former. The reasons behind the acceleration in the degradation during the fatigue testing in the AM test bars (both LPBF and DED) will be discussed in the next section.

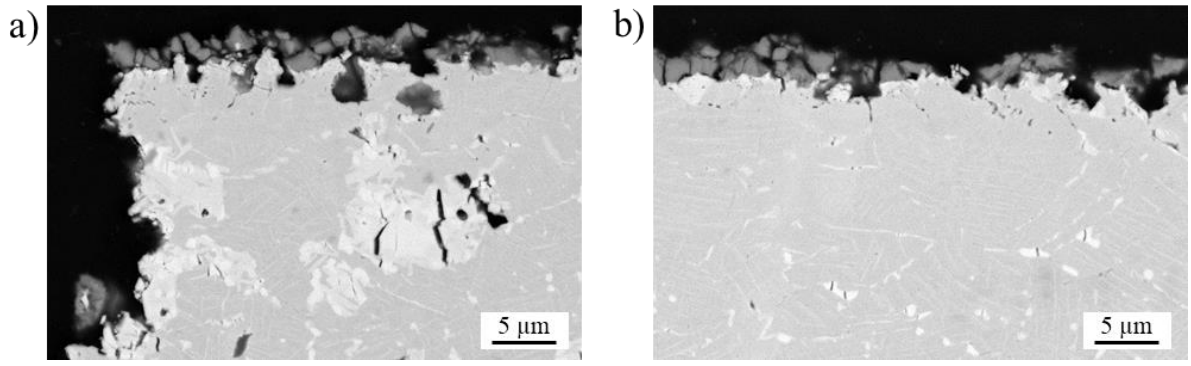

Figure 5-45. SEM backscattered electron images of a cross-section of a failed wrought test bar oxidized after 1000h. A fatigue test was stopped until failure ($5x10^7$ cycles) at different gauge lengths: a) at the fracture (cross-sectional area ~20.2 mm^2), b) 5 mm from the fracture in the load axis (cross-sectional area ~25.6 mm^2)

5.4.3.4 Fatigue Crack Initiation Mechanism of Oxidized Samples

The microstructural variables that best describe the degradation state at failure were discussed in the previous section. Since the characterization of the subsurface degradation in this study requires destructive techniques, it is difficult to assess the degradation evolution. This study proposes an alternative way to evaluate the degradation evolution by analyzing the cross-sections after testing at different distances from the center. Given that the cross-sectional area varies along the gauge length, the stress level also varies along the gauge. The bigger the cross-sectional area, the lower the stress and as such it will result in degradation decrease. Therefore, the degradation evolution with the applied stress can be analyzed. To that end, it is assumed that during fatigue at the same test time, a bigger cross-sectional area experiences an equivalent degradation to a smaller cross-sectional area at shorter times and higher stress.

Figure 5-46 shows representative cross-sections along the gauge of the oxidized LPBF sample after testing. Figure 5-46a shows the largest sample cross-section and in turn, the area of lowest applied stress during fatigue testing. The microstructure is similar to the one shown for the oxidized flat coupons (Figure 5-41). The external oxide scale is still intact, there is a development of a more pronounced non-planar scale/alloy interface and an increase of interfacial local decohesion. Figure 5-46b corresponds to a higher stressed region than that shown in Figure 5-46a and shows how interfacial defects grow and subsurface voids start to appear along the grain boundaries, located among internal oxides and δ-precipitates. As stress increases (Figure 5-46c), interfacial defects continue to grow to the extent that the oxide scale cracks and eventually spalls, while a more pronounced development of subsurface voids also takes place. Finally, Figure 5-46d shows deep and broad void formation in the vicinity of the fracture because of subsurface and surface defects coalescence. It is plausible that such void formation could

serve to initiate crack development during fatigue loading. The subsurface voids associated with the internal oxidation process and the δ-precipitation could thus act as preferential crack initiation sites. Despite that interfacial defects accelerate the degradation, observed microstructures after failure indicate that the sample can withstand abundant subsurface defects formation before failure. However, the same assumptions are no longer valid for subsurface voids since less of them are necessary to generate a critical-size defect that triggers crack propagation and failure.

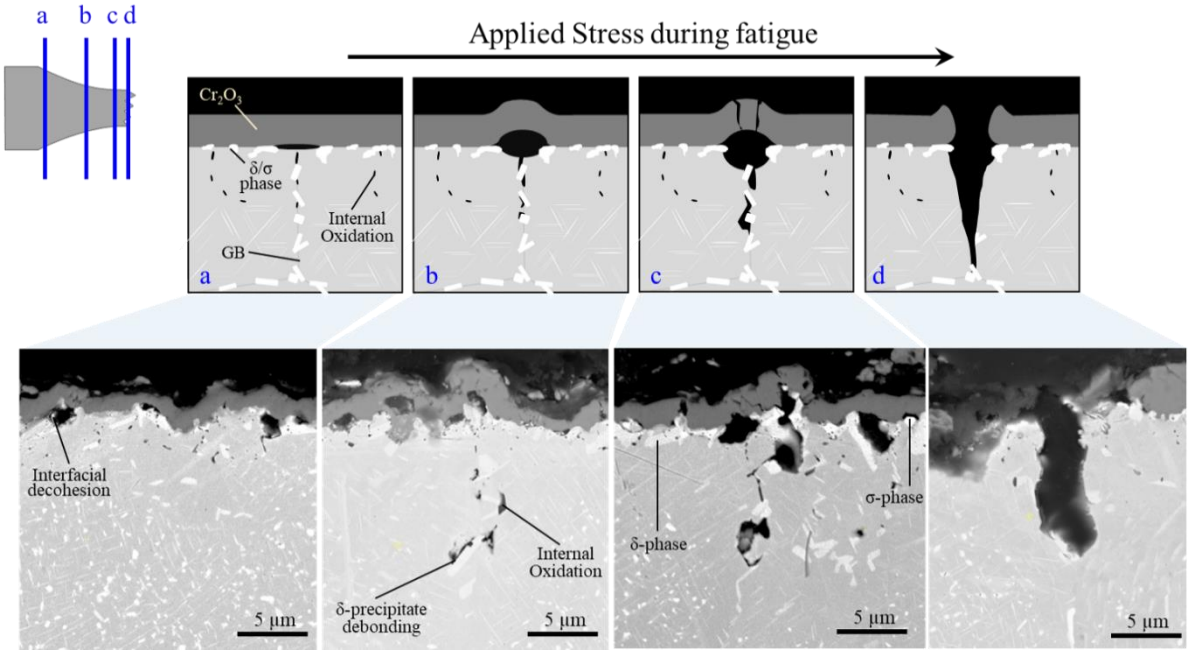

Figure 5-46. Oxidized sample degradation evolution with applied stress. Bottom micrographs correspond to the cross-section of OX-LPBF for 300h after fatigue testing.

5.4.3.4.1 Formation of Interfacial Defects

Interfacial defects formation starts as oxide buckling, but their growth continues toward the alloy as stress increases. The initial scale buckling is presumed to be in response to a compressive stress buildup in the scale during the oxidation in combination with relatively weak

oxide/alloy adhesion. Specifically, if the oxide/alloy interface has a poor adhesion relative to the cohesive strength of the oxide, decohesion that leads to buckling will be favored before the oxide cracking (*i.e.*, failure by shear) [171], [172]. Since the LPBF and DED test bars consistently exhibited buckling formation before oxide cracking, this indicates low adhesive interfacial forces in these systems. Secondly, the interfacial defects growth toward the alloy during the fatigue testing is promoted by the strength loss of the depletion region. The oxidation process promoted Cr and Nb depletion, making the subsurface alloy weaker than the bulk alloy. Moreover, the alloy subsurface is under tensile stresses as a compensation of compressive stresses in the oxide [61], which contributes to enhance the defect growth.

Several reported contributions that favor poor interfacial adhesion and accelerate scale spallation in the AM systems are as follows:

Convoluted scale/alloy interface: Local heterogeneities that influence the diffusion through the oxide promote a non-planar interface (e.g., composition changes in oxide, subsurface precipitates, grain boundaries) [60]. Composition changes in the oxide of the AM samples occur mainly during the first stages of oxidation before the establishment of the chromia layer. The as-built microstructure of the AM samples have regions with significant segregation of Nb, Mo and Ti [94] that likely impact the local transient products due to the different oxygen affinity and different diffusion rates through the alloy and the oxide [60]. Another source of local heterogeneity comes from the grain boundaries. Enhanced diffusion promotes a faster chromia formation, resulting in oxides ridges above grain boundaries [128]. Additionally, the coarsening of subsurface precipitates and phase fraction increase contribute to convolute the interface.

Scale/alloy bond strengths: Interfacial segregation of elements such as sulfur and phosphorus weaken the scale/metal bond strength [170]. Sulfur decreases the surface energy

required to form a metal surface, favoring void nucleation [173]. Despite no measurements of sulfur segregation being acquired in this study, higher content of sulfur in alloys produced by LPBF in comparison with conventional methods has been reported. Son *et al.* [174] reported that the sulfur content of LPBF 625 powder (17 ppm) is twice the value in the wrought counterpart (34 ppm). Sanviemvongsak *et al.* [87] reported that the sulfur content in alloy 718 fabricated by LPBF (23 ppm) was more than one order magnitude higher than the wrought alloy (1 ppm), with greater scale spallation reported for the AM-718 samples in comparison with the wrought.

Furthermore, in the case of Alloy 625, the interface consists of oxide/δ-precipitate/alloy in several regions. Such a multiphase interface would necessarily have a greater amount of interphase boundaries in comparison to a stable scale/alloy interface. The degree of coherency at an interface depends on crystallographic differences between the phases (*e.g.*, lattice misorientation, the ratio of molar volumes), with an incoherent interface providing a potent sink site for vacancies [175]. The formation of interfacial defects in the oxide/δ-precipitate due to the injection of vacancies stemming from the scale-growth process is likely. Although these defects may not be appreciable, they are prone to expand during the fatigue testing and compromise the adherence of oxide/δ-precipitate. Two experimental observations support this. First, there is a correlation between the precipitates fraction area and the detachment linear fraction. Second, most of the δ-precipitates remain within the alloy when there is a scale decohesion.

5.4.3.4.2 Formation of Subsurface Voids

Abundant voids form in the bulk and grain-boundaries of the LPBF and DED alloys during oxidation in comparison to the wrought alloy (Figure 5-41). The interaction of internal oxidation, voids, and large precipitates promoted localized deformation during fatigue (see Figure 5-46). The inferred process for this is as follows. Nb and Mo segregation in the LPBF and

DED alloys promotes a faster nucleation and favors the precipitates growth. The precipitate coarsening process resulted in relatively large precipitates surrounded by denuded FCC matrix [176]. Subsurface voids were able to form and grow due, in part, to strength loss in these denuded zones.

This precipitate-associated subsurface void-formation process was most pronounced on grain boundaries, which in turn were associated with the deepest internal oxidation. The coalescence of subsurface voids along the grain boundaries likely triggered crack formation at least as deep as the internal oxidation. Furthermore, since AM grain boundaries were deeper, the crack propagation reached a critical size sooner in these alloys than in the wrought (see Appendix A).

5.4.3.5 Fatigue Crack Initiation Mechanism of Thermally Aged Samples

Since the fatigue life generally increases as the grain size decreases [177], [178], the DED-processed alloy is expected to have a shorter fatigue life than the LPBF and wrought alloys. However, there is barely a difference in the LPBF and wrought grain size to explain the difference in their fatigue lives. Figure 5-47 shows representative cross-sections of the 1000h TA-LPBF fractured test bar to evaluate the microstructural degradation evolution with the stress applied, given that the cross-sectional area varies along the gauge length. Unlike the oxidized samples, no appreciable surface degradation occurred since thermal aging treatments were performed under back-filled argon. The degradation of the TA samples correlates mainly with the debonding and fracture of σ and δ- precipitates, where the fractures are mainly perpendicular to the loading axis. As the applied stress increases, the number of fractured precipitates increases. These fractured precipitates are more abundant closer to the surface.

During fatigue, in the absence of induced surface/subsurface degradation, fatigue life is mainly determined by the interactions of dislocations and precipitates. Phases predicted at equilibrium at 800°C for the nominal composition of alloy 625 are mainly δ-[$(Ni,Cr)_3(Nb,Mo)$] and σ-[Mo-Ni-Si-Cr-Nb] [119]. The beneficial effect of δ-phase is reported in moderate amounts, where it provides grain-size control and grain refinement through a pinning effect below 990°C [25], [26]. In coexistence with γ", δ-phase increases mechanical properties below 426 °C for IN718 and Super Waspalloy [26]. This may explain the LPBF fatigue results after thermal aging for 24h and 300h. However, the coarsening of incoherent δ precipitates at longer times reduces the strengthening process effectiveness and lowers the ductility [27]. Since δ and σ precipitates act as stress and strain concentrators, they fracture once the stress concentration overcomes the precipitate strength. Then, these fractured precipitates can induce crack nucleation [179]–[181].

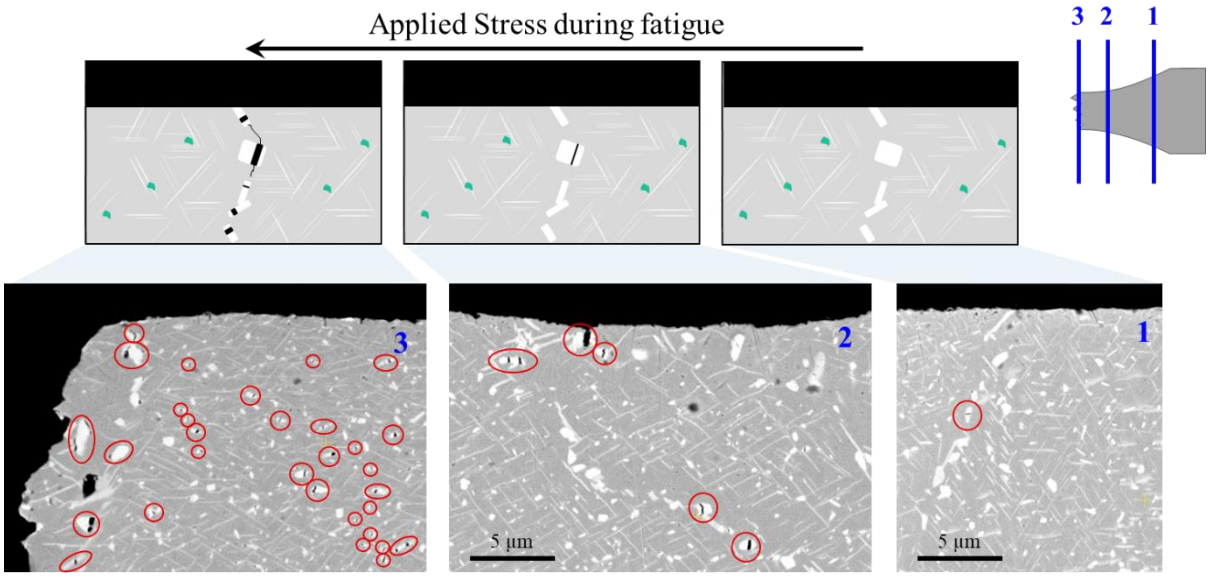

Figure 5-47. Thermal aged sample degradation evolution with applied stress. Bottom micrographs correspond to the cross-section of TA-LPBF for 1000h after fatigue testing.

These precipitates/dislocation interactions depend on the precipitate's size [182], morphology, distribution [183], orientation to the tensile stress, location relative to the surface [184], [185], and the

strength characteristics of the matrix [180], [181]. The heterogeneities from the initial microstructures (*i.e.*, as-built condition) influence these factors.

The different Nb and Mo segregation levels in AM samples affect the phase fraction predicted at equilibrium. As an illustrative exercise, the phase fractions at equilibrium assuming an alloy with the measured composition of depleted (dendritic) and segregated (interdendritic) regions were calculated using ThermoCalc in combination with the TCNI8 database (Table 5-13). In agreement with reported literature [119], the higher the Nb and Mo segregation, the bigger the difference between the (δ+σ)-phase fraction in the depleted and segregated regions.

Table 5-13. Predicted phase fractions at equilibrium at different segregated and depleted compositions.

Sample		Nb (wt.%)	Mo (wt.%)	δ Ni_3(Nb,Mo)	σ (Mo-Ni-Si-Cr)	γ (Ni-Fe-Cr)
Wrought	-	3.45	8.40	0.06	0.10	0.83
LPBF	Depleted	3.14	8.19	0.03	0.08	0.89
	Segregated	6.44	10.05	0.17	0.12	0.71
DED	Depleted	2.70	8.91	0.04	0.04	0.92
	Segregated	16.20	12.72	0.48	0.32	0.20

Representative cross-sections of samples under thermal aging at 800°C for 5000h are shown in Figure 5-48. Needle-like precipitates correspond to the δ-phase, while the bright small globular precipitates correspond to the σ-phase. The total precipitates fraction (δ+σ) in each sample was 12.1±1.2% for the wrought, 16.1±1.7% for LPBF, and 17.3±2.3% for DED; demonstrating that the higher the precipitates fraction, the shorter the fatigue life. However, the difference in the precipitates fraction in the LPBF and DED alloys is not substantial enough to explain the difference in their fatigue life. The main microstructural differences between them are in the size and distribution of the precipitates. The histograms below the micrographs in Figure 5-48 represent the area fraction of precipitates as a function of distance for a band of 5μm width demarked in the image. The wrought sample shows the smallest variation between the

peak and valleys, demonstrating a homogeneous (δ+σ) precipitates distribution. The LPBF sample exhibits an enrichment of precipitates area fraction along the grain boundaries. Intergranular precipitates are coarser than the intergranular ones, due very likely to the higher driving force for δ precipitation than in the bulk [176]. The DED samples show the highest heterogeneity of (δ+σ) precipitates distribution. The original highly segregated regions result in (δ+σ) precipitates clusters, while the original depleted region does not favor (δ+σ) precipitation, which is consistent with the ThermoCalc predictions.

The heterogeneities in chemical composition and (δ+σ) precipitates distribution are detrimental to the fatigue performance. On one hand, highly segregated regions will promote a bigger area of precipitates that embrittle the alloy and favor crack nucleation. While on the other hand, highly depleted regions are not strengthened by solution or precipitates, so that cracks can propagate easily. The initial composition variability impacts proportionality the degree of embrittlement in the segregated regions and the degree of strength loss in the depleted regions. Consequently, the fatigue life trend among the TA samples exposed at the same time, *i.e.*, wrought>>LPBF>DED, is explained by the heterogeneity of (δ+σ) precipitates distribution.

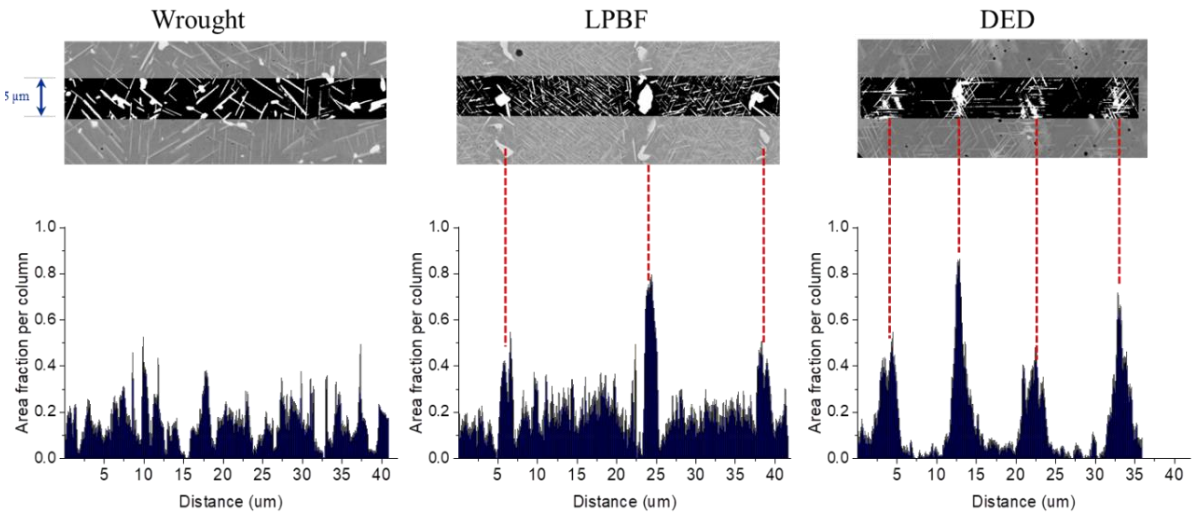

Figure 5-48. Micrographs of wrought, LPBF and DED after thermal ageing for 5000h. Histograms represent the area fraction of precipitates as a function of distance. Each column evaluates the precipitates fraction in 0.068 µm2 (5 µm width by 0.014 µm length). The bri The bright areas correspond to (δ+σ) precipitates dark areas correspond to the matrix.

5.4.4 Conclusions

This chapter assessed the influence of thermal- and oxidation-driven features on the uniaxial fatigue performance of Alloy 625 fabricated by LPBF, DED and wrought processes. The following conclusions are drawn from the results:

- Oxidation is more detrimental than thermal aging on the fatigue life of the AM samples, where the life reduction increases with increasing oxidation exposure time (refer to Figure 5-42). Oxidation induces interfacial defects (*i.e.*, free space formation) and subsurface voids that accelerate crack initiation. Prior to failure, the sample withstands abundant interfacial defects formation before subsurface voids coalesce and initiate crack formation. Interfacial voids originate from local decohesion of the oxide/alloy interface during cyclic loading. Subsurface voids

result from the interaction of internal oxidation, δ precipitate coarsening, and δ/matrix weakening.

- Neither the oxidation-driven features nor the heat-treatment evolution was detrimental to the wrought 625 under the conditions studied. The AM oxidized samples showed an acceleration of degradation during fatigue testing compared to the oxidized wrought (refer to Figure 5-45). Formation of interfacial defects in the AM samples was promoted by a convoluted scale/alloy interface and also the oxide/δ-precipitate/alloy interface, whereas grain-boundary precipitates enhanced the extent of internal oxidation promoting subsurface voids.
- The fatigue failure mechanism in thermally aged AM samples (both LPBF and DED) involves the fragmentation and coalescence of δ and σ subsurface precipitates, leading to crack development throughout the sample. The higher the segregation from AM processing, the greater the heterogeneity of the (δ+σ) precipitate distribution and the shorter the fatigue life (refer to Figure 5-48).

5.5 Fatigue Performance of Oxidized Alloy 625 at 950°C

5.5.1 Introduction

Alloy 625 oxidized at 950°C exhibits a chromia scale with delta precipitates in the alloy at the scale/alloy interface, and intergranular oxidation. Differences in the oxidation behavior at 950°C compared with 800°C for the same exposure times, based on sections 5.2 and 5.3, include the former developing a thicker and more convoluted chromia scale, delta precipitates embedded in the scale, deeper precipitates-free zone, and more extensive intergranular oxidation. Some of these features have been reported to have a negative influence on the fatigue life e.g., precipitates-free zone, intergranular oxidation depth [89], [92], and thicker oxide [91]–[93]. Since these oxidation-induced features are more pronounced at 950°C, together with the presence of other defects that vary depending on the manufacturing process, it is important to evaluate their effect on fatigue life.

5.5.2 Experimental Procedures

Uniaxial fatigue tests were conducted at room temperature on wrought, LPBF, and DED cylindrical test bars oxidized prior testing. The oxidation exposure times were 24h, 1000h, and 5000h at 950°C. The fatigue stress ratio was -1 (same tension load as compression), where the load followed a sinusoidal waveform at 33-35 Hz frequency. All experiments used a maximum stress level of 440 MPa, and the fatigue run-out condition was set to 10^7 cycles.

Fractographic analysis was performed after testing in each oxidized sample. Then, a cross-section of each tested bar was obtained and prepared metallographically, where their microstructure was characterized using BSE-SEM imaging.

5.5.3 Results and Discussion

The results of room temperature tests using thermal aged and oxidized test bars are shown in Figure 5-49. In the case of the oxidized samples, there is a correlation between a reduction in fatigue life and longer exposure. For example, the oxidized wrought, LPBF, and DED fatigue lives at 5000h were reduced by 91%, 70%, and 87%, respectively, relative to the fatigue lives after 1000h of oxidation. Additionally, it was consistent that the oxidized wrought sample had the longest mean fatigue life, and the oxidized DED sample had the shortest fatigue life for the three exposure times studied.

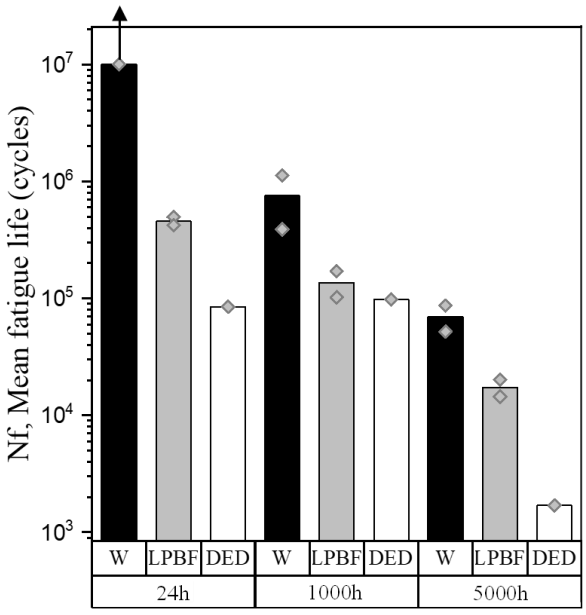

Figure 5-49. Mean fatigue life of the wrought (W), LPBF, and DED alloy 625 oxidized for 24h, 1000h, and 5000h at 950°C prior to testing.

Fractographic analysis is shown in Figure 5-50. The stages of fatigue are indicated: crack initiation, crack propagation, and final fracture. The oxidized wrought sample shows a single crack initiation site, while the LPBF sample presents two initiation sites, and the oxidized DED sample shows multiple initiation points. Crack initiation points start at the surface for all the studied conditions; therefore, it can be inferred that oxidation-induced changes play an important role in crack initiation. When analyzing the area ratio between the crack propagation region and the final failure region, the wrought test bars have a higher ratio, followed by the LPBF and DED samples. Differences in crack propagation stage length reflect differences in the bulk microstructure, e.g., precipitate compositions, sizes, and distributions.

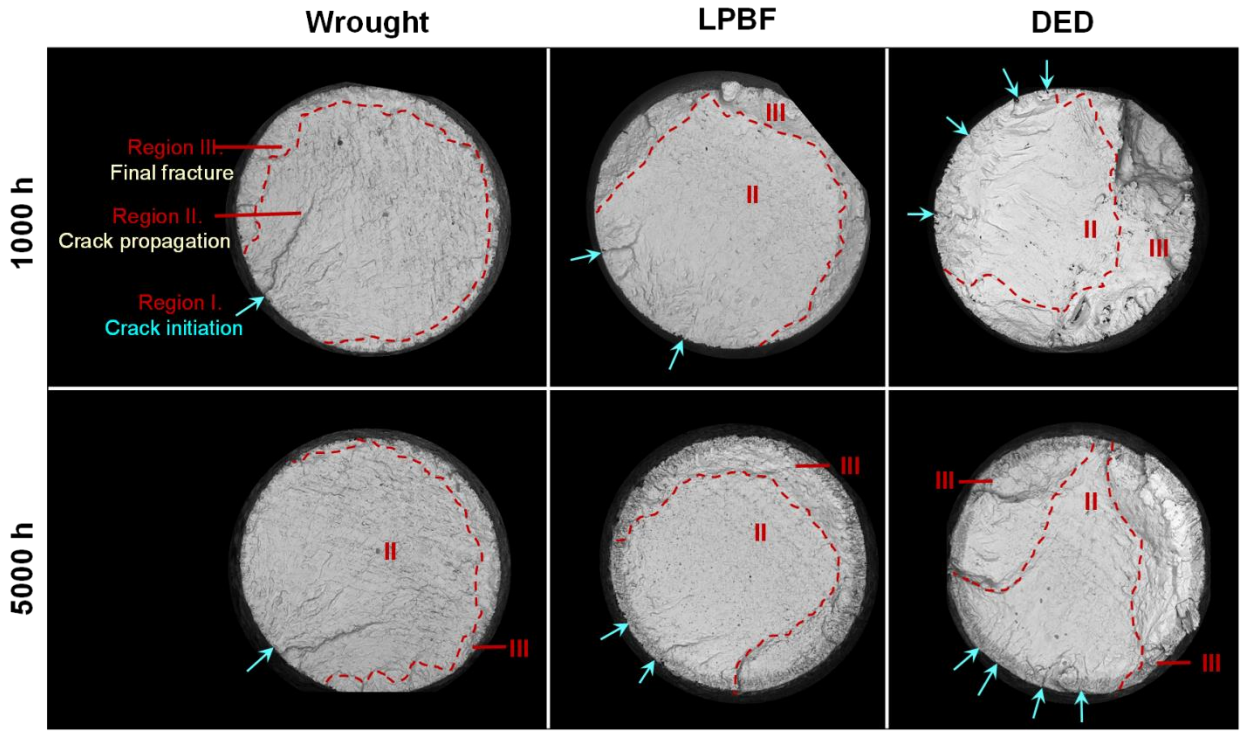

Figure 5-50. Fractographic BSE images of oxidized samples at 950°C for 1000 h and 5000 h. Crack initiation, crack propagation, and final fracture regions are identified and marked.

The microstructure of the oxidized samples was analyzed after fatigue testing and it is shown in Figure 5-51. This analysis offered valuable insight into the microstructural degradation and crack

initiation process during fatigue. An increase in scale damage and subsurface damage with time is observed, which explains the fatigue reduction with longer oxidation time. Such damage includes spallation, interfacial defects, and secondary cracks.

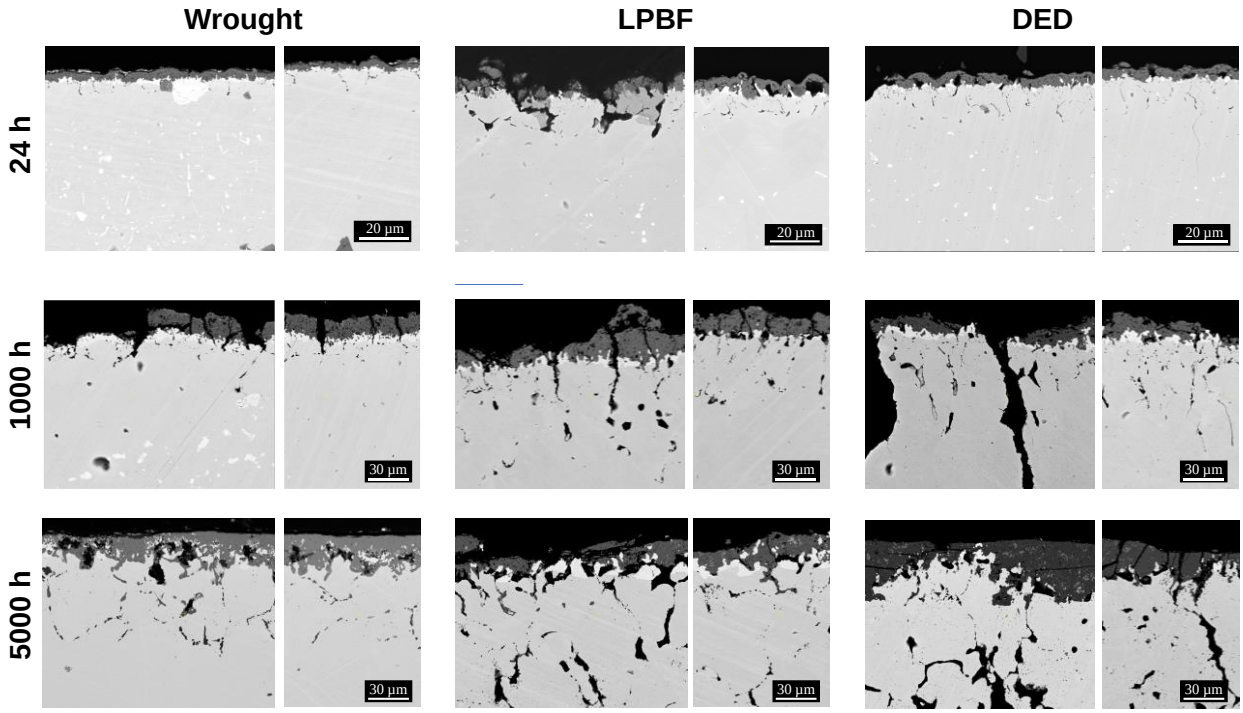

Figure 5-51. Cross-sectional BSE images of the oxidized test bars after testing. Each condition shows to pictures: the right one corresponds to the bigger cross-section area, or the lowest stress applied, and the left one is taken near to the failure zone.

5.5.3.1 Interfacial Defects and Spallation

LPBF and DED samples show interfacial defects, where the former had more defects than the latter. This could be attributed to the longer fatigue life of the LPBF sample, which endured more tension-compression cycles than the DED sample. Considering the same assumption, it is anticipated that the wrought sample will exhibit more defects than the LPBF and DED samples. However, the LPBF and DED samples had a weaker oxide/alloy interface due to the high sulfur content and the abundant voids. In addition, the LPBF sample experienced

more scale spallation compared to the DED sample. This indicates that the scale had accumulated a significant amount of strain that discrete interfacial defects were unable to relieve, ultimately resulting in buckling lateral growth and further detachment of the oxide [55]. The thicker chromia layer in the LPBF sample contributes to the elevated level of compressive stress in comparison to the DED sample.

5.5.3.2 Crack Nucleation in IGO:

Multiple cracks perpendicular to the load axis were observed in all samples, except for the sample that reached a run-out (i.e., wrought oxidized for 24h). The deepest cracks are associated with intergranular oxidation (IGO) and extend into the alloy further than the precipitates-free zone, where IGO acts as a notch. Cracks are able to grow easily via intergranular oxidation due to the incoherent interface, compressive stresses induced by the oxide formation, and the abundant voids in the AM samples. It will be informative to compare the toughness critical value (K_{IC}) of the different compositions. The alumina has a K_{IC} range of 0.4-2.0 MPa.$m^{1/2}$ [55], the chromia K_{IC} is 2.0 MPa.$m^{1/2}$ [55], and the alloy 625 K_{IC} is 7.1 MPa.$m^{1/2}$ [186]. Since alumina is the least resistant to cracking, this increases the susceptibility of IGO to nucleate cracks during fatigue.

In addition, it is important to note that the crack extending through the IGO may widen in the precipitates free zone due to the lower solution strengthening. Nb depletion in the subsurface due to the positive chemical interaction with Cr during oxidation causes a partial reduction of solution strengthening. Sudbrack et al. [92] reported that during high-temperature notch fatigue testing of oxidized Ni-based alloy ME3, the carbides precipitates-free zone resulted in a decrease in fatigue life. This effect may be more pronounced during high-temperature testing due to the potential for creep damage [90].

5.5.3.3 Oxide Nodules and Crack Initiation

An additional experiment was performed for a cast sample oxidized after 1000h, failing at 264 cycles. This value is two orders of magnitude smaller than the fatigue life of oxidized wrought, LPBF, and DED samples subjected to the same oxidation time. Further analysis of the microstructure revealed that secondary cracks consistently appeared near the oxide nodules formed in the cast sample, as depicted in Figure 5-52. The oxidized NbC and laves phase precipitates in the cast sample that are still attached proved to be a preferential site for crack initiation. There are several potential explanations for this, including stress concentration, lower K_{IC} when compared to chromia, and a porous structure making them more brittle. Stress concentration could occur due to the nodule geometry and thicker scale compared to the chromia scale.

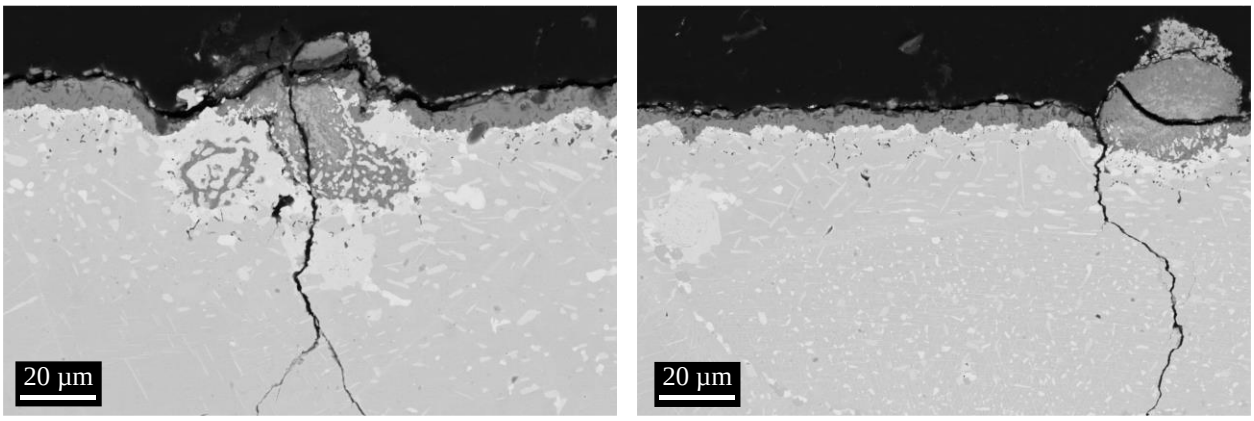

Figure 5-52. Cross-sectional images of oxidized cast sample after testing, showing secondary cracks. The cast was oxidized at 950°C for 1000h prior to the fatigue testing.

5.5.4 Conclusions

- As the oxidation time increases, the fatigue life of samples oxidized at 950°C decreases. In terms of fatigue performance, the wrought sample showed the best fatigue performance, followed by the LPBF and DED samples (refer to Figure 5-49).

- The fatigue life reduction is associated with damage in the scale and subsurface after fatigue testing, including interfacial defects, spallation, and secondary cracks that penetrated the alloy preferentially along intergranular oxidation (refer to Figure 5-51). The weaker nature of the intergranular oxidation and oxide/alloy interface in the LPBF and DED samples enhances the damage in their scale and subsurface relative to the wrought sample.

5.6 Mitigation Strategies: Effect of Solution Heat Treatment on Oxidation at High Temperatures of Alloy 625 Fabricated with Laser-Assisted Additive Manufacturing

5.6.1 Introduction

Previous sections have shown differences between oxidized AM samples and wrought that negatively impact their fatigue performance. These differences include enhanced intergranular oxidation, scale decohesion, and oxide transient products. Table 5-14 summarizes possible contributions from these variables and proposes potential mitigation strategies.

Table 5-14. Summary of oxidized features in AM samples that are involved in the fatigue crack initiation

Feature in AM oxidized samples	Contribution to the described feature	Potential mitigation strategies
Enhanced intergranular oxidation	Higher oxygen content contributes to greater voids formation than samples fabricated by conventional methods (wrought and cast).	Improving the oxygen atmosphere control during the AM process.
		Adding an oxygen-gettering element to the powder composition. In addition, it could result in oxide dispersion strengthening.
	Rougher surface finishing results in deeper IGO for the same sample kind.	Decrease the surface finishing roughness (finer SiC grit).
	Lower fraction of twinning boundaries (CSL-Σ3) increases the frequency of IGO [145]–[148].	Recrystallization during heat treatments promotes a higher fraction of twin boundaries in Ni-based alloys [85], [187]
	Lower Si content impedes the formation of a thin protective SiO_2 layer beneath the chromia that reduces IGO [12]	Si addition
	Higher alloy residual stresses increase the IGO fraction.	Stress relief heat treatments in the building parts, immediately post the

		manufacturing process [188].
Decohesion of the scale	Sulfur promotes decohesion of the scale [87], [189]	Desulfurization by hydrogen annealing before oxidation. A treatment with flowing H_2 gas will result in the formation of H_2S, removing the sulfur from the subsurface [189].
		Better control on sulfur content in the AM powder.
	Abundant (δ+σ)-precipitates formed beneath the chromia result in an additional interface in the system where vacancies can annihilate. Additionally, a more convoluted scale because of these precipitates increases residual stresses, resulting in scale buckling (local scale decohesion).	Homogenization heat treatment. Segregation dissolution will result in no preferential location for δ-phase nucleation, nor enhance δ-precipitates growth kinetics [190].
		AM process optimization to reduce cooling and heating rates. For example, heating substrate plate, remelt layer with lower volumetric energy density laser parameters, pulsed laser instead of continuous laser [191].
Additional transient products	Nb-Cr-Ti oxide nodules result from the oxidation of the interdendritic segregation in the coarse dendritic structures. These nodules delay the chromia establishment and increase the mass gain at the early stage of oxidation. Big nodules can also deplete the alloy of Nb and Mo, reducing the solution strengthening locally.	Homogenization heat treatment. Segregation dissolution will promote a continuous and exclusive formation of chromia scale.

This chapter will explore the benefits of solution heat treatment on the fatigue performance of AM oxidized samples. Initially, a heat treatment was designed per sample to

dissolve their respective interdendritic segregation and Laves precipitates. Afterwards, isothermal oxidation at 800°C and 950°C was evaluated for the different proposed heat treatments. Finally, an optimal heat treatment was selected per sample to evaluate its impact on the fatigue performance after oxidation for 1000h.

5.6.2 Experimental Procedures

5.6.2.1 Material Processing and Heat Treatments

Alloy 625 manufactured by three different processes was investigated: laser powder bed fusion (LPBF), direct energy deposition (DED), and wrought 625.

Heat treatments were performed in the LPBF and DED samples at 1150°C for 5 min, 30 min, and 60 min to provide different levels of segregation until homogenization. Prior to heat treatment, the samples were encapsulated in quartz tubes backfilled with argon. At the completion of heat treatment the encapsulated samples were quenched in water.

5.6.2.2 Oxidation Tests

Oxidation tests were performed on the LPBF and DED samples in as-built conditions and after the heat treatment previously mentioned. Coupons of approximate dimensions 10 x 10 x 2 mm^3 of each condition were cut using a high-speed water saw. Before oxidation, each sample was ground with P600 SiC paper (20 µm grit size) and then ultrasonically cleaned in ethanol. Oxidation tests were conducted in a horizontal open furnace at 800°C and 950°C for 1000h under a lab air atmosphere.

5.6.2.3 Microstructural Characterization

Microstructural characterization was performed on the cross-section of the as-built, heat-treated, and oxidized coupons. It was also performed on the oxidized test bars after fatigue testing. The metallographic preparation of the samples consisted of grinding using SiC papers with grit from P320 to P1200, then polishing using 2 µm alumina suspension and 0.25µm colloidal silica. The as-polished samples were examined using a scanning electron microscopy Apreo (ThermoFisher Scientific, Waltham, MA, USA) in backscattered electron mode (BSE). Additionally, chemical composition quantification before and after heat treatment was determined using electron probe microanalysis (EPMA) (JXA-8100, JEOL, Japan).

5.6.3 Results and Discussion

5.6.3.1 Effect of Solution Heat Treatment Time on Microstructure

Figure 5-53 shows the cross-sectional images of LPBF and DED samples in the as-built conditions and after heat treatment at 1150°C for 5 min, 30 min, and 60 min. The AM as-built microstructure consist of cellular-dendritic structures, with the DED sample having a coarser microstructure than the LPBF. The interdendritic regions of DED show occasional Laves phase precipitates, while the LPBF sample does not. After 5 min at 1150°C, the DED sample shows a partial dissolution of the interdendritic region and a decrease in the Laves phase fraction. After 30 min at 1150°C, the LPBF sample showed globular precipitates along the grain boundaries, whereas the DED sample started to show the same characteristics after 60 min at 1150°C. The cellular dendritic structure is not visible for the LPBF sample after 5 min at 1150°C, while the DED sample took 30 min at 1150°C to reach this point.

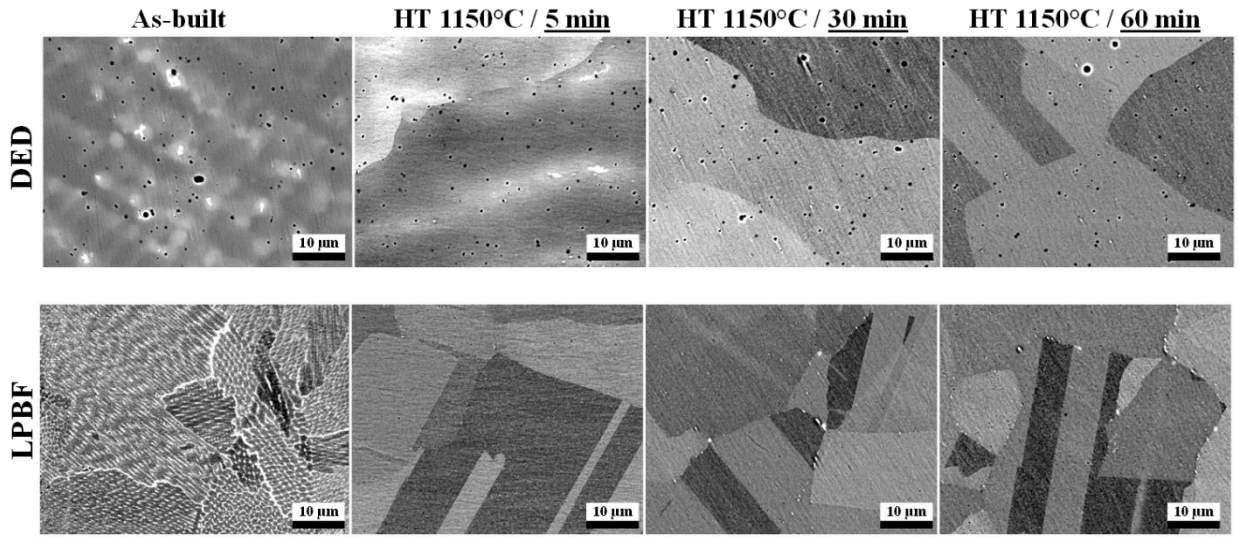

Figure 5-53. Microstructure of as-built LPBF and DED samples and heat treated at 1150°C for 5,30 and 60 min. Reprecipitation along grain boundaries is observed after complete solubilization of interdendritic regions.

Figure 5-54 shows the EPMA lines acquired for all conditions to measure the Nb and Mo composition evolution with the heat treatment time. The Nb and Mo profiles for the LPBF samples show complete dissolution after 5 min, whereas the DED took 30 min, and 60 min to homogenize the Mo and Nb composition, respectively. Despite the segregation ratio in concentration being higher for Nb than Mo in the DED sample, it homogenized faster . This can be explained by the fact that Mo has a lower diffusion coefficient in Ni compared to Nb [192].

Furthermore, the DED sample takes longer to dissolve the interdendritic segregation not only because of the higher segregation but also due to the Laves precipitates present in the DED sample. Laves phase dissolution constitutes the interfacial reaction aside from the diffusion of atoms in the matrix [193].

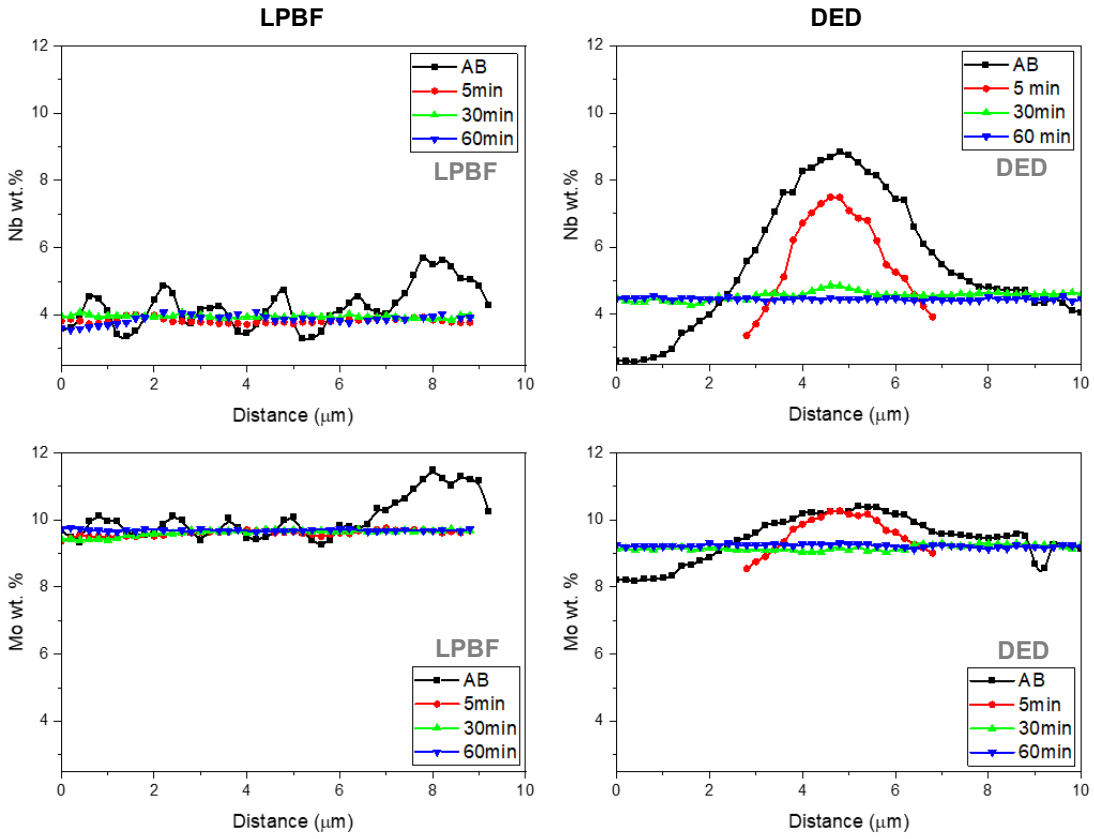

Figure 5-54. EPMA Mo (bottom) and Nb (top) compositional profiles for LPBF (right) and DED (left) samples at different heat treatment times.

The homogenization heat treatment also influences the character of the grain boundaries and the grain-size distribution. Figure 5-55 illustrates the EBSD maps of the as-built samples compared to the longer heat treatment for both samples, and Figure 5-56 and Table 5-15 summarize the grain-size evolution, and grain-boundary character evolution with heat-treatment time, respectively.

Dislocation energy from the rapid solidification during the additive processes act as a driving force of recrystallization during heat treatments, where a higher dislocation density is in the interdendritic region than the dendritic space [194]. Figure 5-55 shows that both samples experienced recrystallization reflected by the lamellar annealing twins. Coincide sit lattice (CSL) model to characterize grain boundaries where a finite fraction of lattice sites is coincident in the

two lattices. A grain boundary Σ1 represent complete coincidence or no boundary, and Σ3 represent twin boundaries with 60° of misorientation between lattices [195]. Characteristics of coherent twin boundaries (CSL $\Sigma 3^n$) include lower energy, lower mobility; improved materials properties such as creep, cracking, and corrosion resistance [145], [196]. The $\Sigma 3^n$ grain boundaries fraction in the LPBF sample increases from 2.4 % in the as-built condition up to 70.7%, and 77.6% after 5 min, and 60 min exposure, respectively. The DED sample shows recrystallization after 30 min at 1150°C, when the CSL fraction goes from 3.8% in the as-built condition up to 52%. After 60 min, the DED CSL fraction increases up to 73.7%.

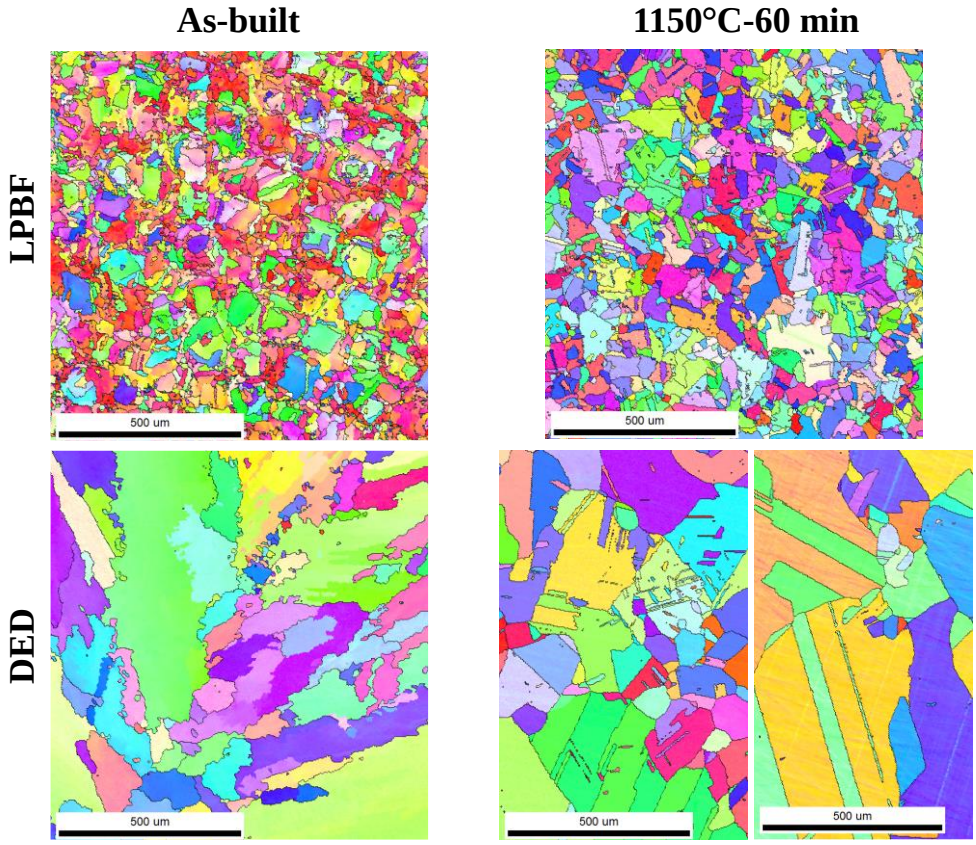

Figure 5-55. EBSD maps of wrought, LPBF and DED as-built and after 60min at 1150°C. LPBF and DED correspond to the horizontal plane (normal to the building direction).

Table 5-15. Grain boundaries character evolution with heat treatment time

Sample	Treated condition	Grain boundaries fraction		
		Σ3	Σ9	Σ27
LPBF	As-built	1.1%	1.0%	0.3%
	1150°C/5 min	65.1%	4.4%	1.3%
	1150°C/30 min	66.5%	4.8%	0.9%
	1150°C/60 min	70.2%	5.7%	1.7%
DED	As-built	2.0%	1.0%	0.8%
	1150°C/5 min	2.2%	0.3%	0.1%
	1150°C/30 min	48.5%	2.7%	0.8%
	1150°C/60 min	68.8%	4.0%	0.8%

Regarding the grain size, Figure 5-56 shows the grain-size distribution based on area fraction. The LPBF sample shows a slight growth with the exposure time. Potentially, the precipitates along grain boundaries act as pinning sites that thereby control the grain growth. Figure 5-56 shows that The DED sample shows a broader distribution, the difference is significant since the grain size axis is in log scale.

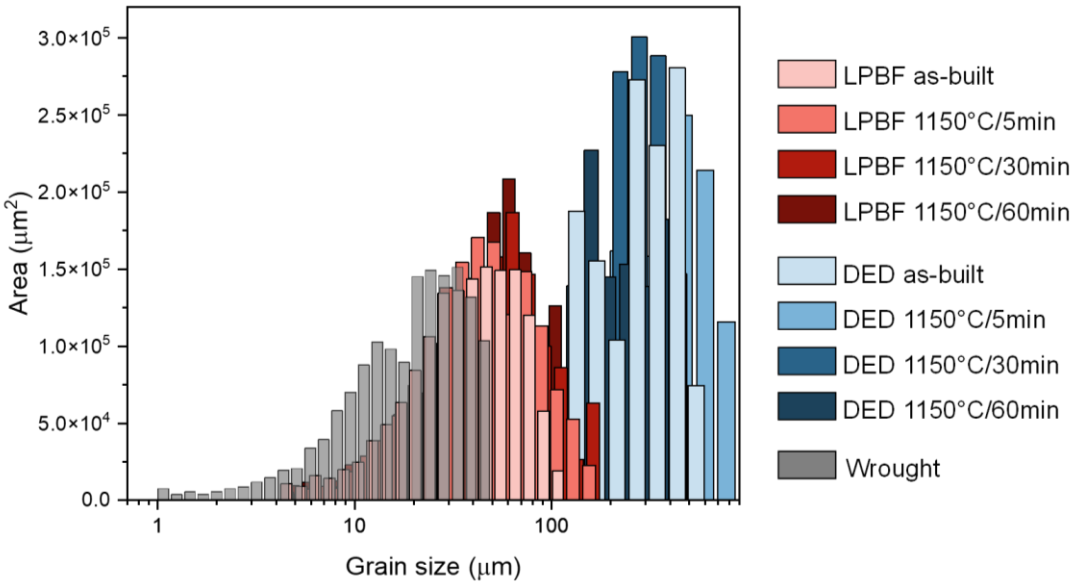

Figure 5-56. Grain size distribution evolution with heat treatment time

Initially, grains in the as-built samples were determined by the cellular-dendritic structures that shared the same orientation. In the as-built-condition, Ni-based alloys usually exhibit columnar grains at the bottom of the molten pool and smaller grains at edges and the top of the molten pool exhibit smaller grains. The overlapping between layers and between beads usually remelts the small grains. The partial remelting between layers, differences in laser pattern, a lower cooling rate, and laser spot size defocus during process contribute to a broader grain size distribution in the DED than LPBF sample.

Optimal heat treatment based on results must show complete dissolution of interdendritic segregation and a high amount of $\Sigma 3^n$ boundaries, The grain size barely changes with the time of heat treatments, thereby this variable is not considered. Additionally, the reprecipitation in the grain boundaries is not desirable since it decreases the elements that contribute to the solution strengthening. Therefore, 30 min and 60 min at 1150°C are the optimal heat treatments for the LPBF and DED samples, respectively.

5.6.3.2 Effect of Solution Heat Treatment on Oxidation

Oxidation kinetics were measured using a TGA for DED and LPBF samples in the as-built and optimal heat-treated condition, and the results are shown in Figure 5-57. As a reference, the oxidation kinetics of the wrought samples are included, and the error comes from acquiring kinetics for three samples per condition. The first observation is that the LPBF and DED heat-treated samples consistently show a lower mass gain and variability reduction (standard deviation) when comparing them relative to their respective as-built samples. This suggests that a more homogeneous microstructure is a possible contribution for this oxidation behavior improvement.

Figure 5-58 compares the oxidation rates under different conditions. At 800°C, the heat-treated DED sample shows a slower oxidation rate than the as-built sample, but it does not reach the wrought level. In the case of the LPBF sample, the heat-treated and as-built conditions are the same within the error margin. At 950°C, the heat-treated conditions show a slower oxidation rate compared to their corresponding as-built condition. In addition, there is no difference within the error among the heat-treated samples and the wrought.

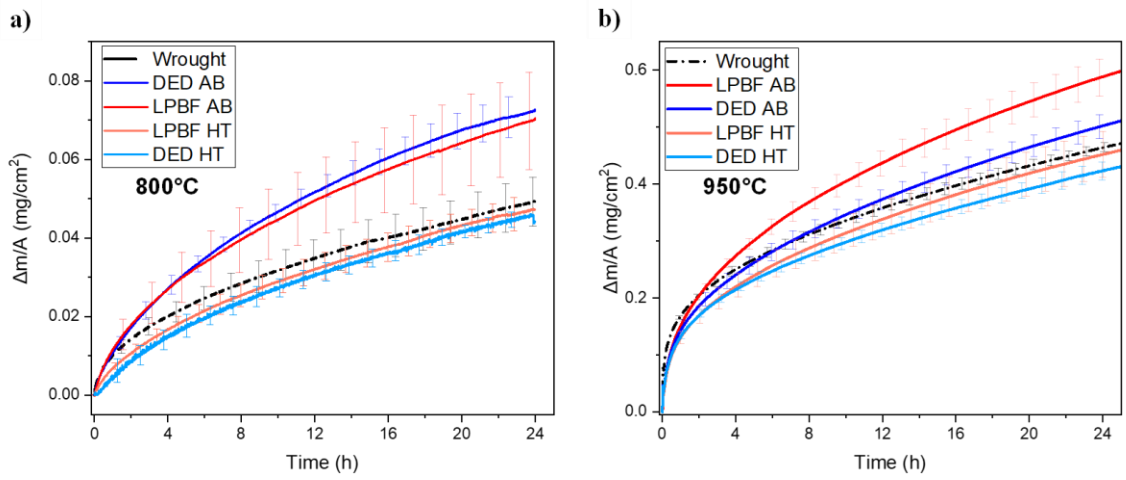

Figure 5-57. Oxidation kinetics of heat-treated samples compared with their respective as-built conditions at: a) 800°C, and b) 950°C.

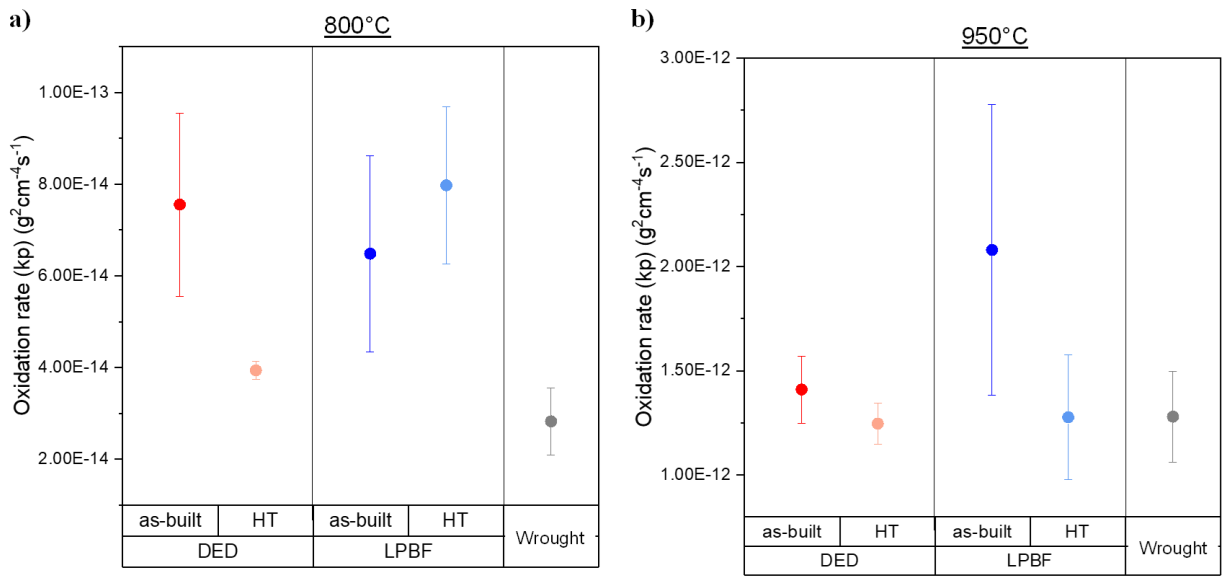

Figure 5-58. Parabolic rate constants of air oxidation for as-built and heat-treated conditions. a) 800°C and b) 950°C.

Figure 5-59 shows cross-sectional images of heat-treated samples after 1000h oxidation. At 800°C, samples show similar behavior to the one reported in section 5.2, they exhibit a continuous chromia scale formed with discrete (δ+σ)-precipitates beneath the chromia scale. One of the reported differences among LPBF and DED samples with wrought was the (δ+σ)-fraction beneath the chromia, where interdendritic regions were observed to have a higher concentration of these precipitates due to the positive impact of Nb segregation in the δ-phase nucleation driving force and growth kinetics. Figure 5-60 compares the (δ+σ)- phase fraction beneath the chromia scale on the as-built samples and for the different heat treatment conditions. In the case of the DED samples, there is a reduction in δ-phase fraction after 30 min, but any treatment shows a level as low as the wrought sample. In the case of LPBF samples, there is a δ-phase

fraction reduction after 5 min at 1150°C, reaching similar values to the wrought sample. The δ-phase fraction is kept in the same range after 30 min and 60 min at 1150°C. Reduction of subsurface precipitates is expected after homogenization heat treatments since there is no preferential location for nucleation or accelerated kinetics without Nb segregation.

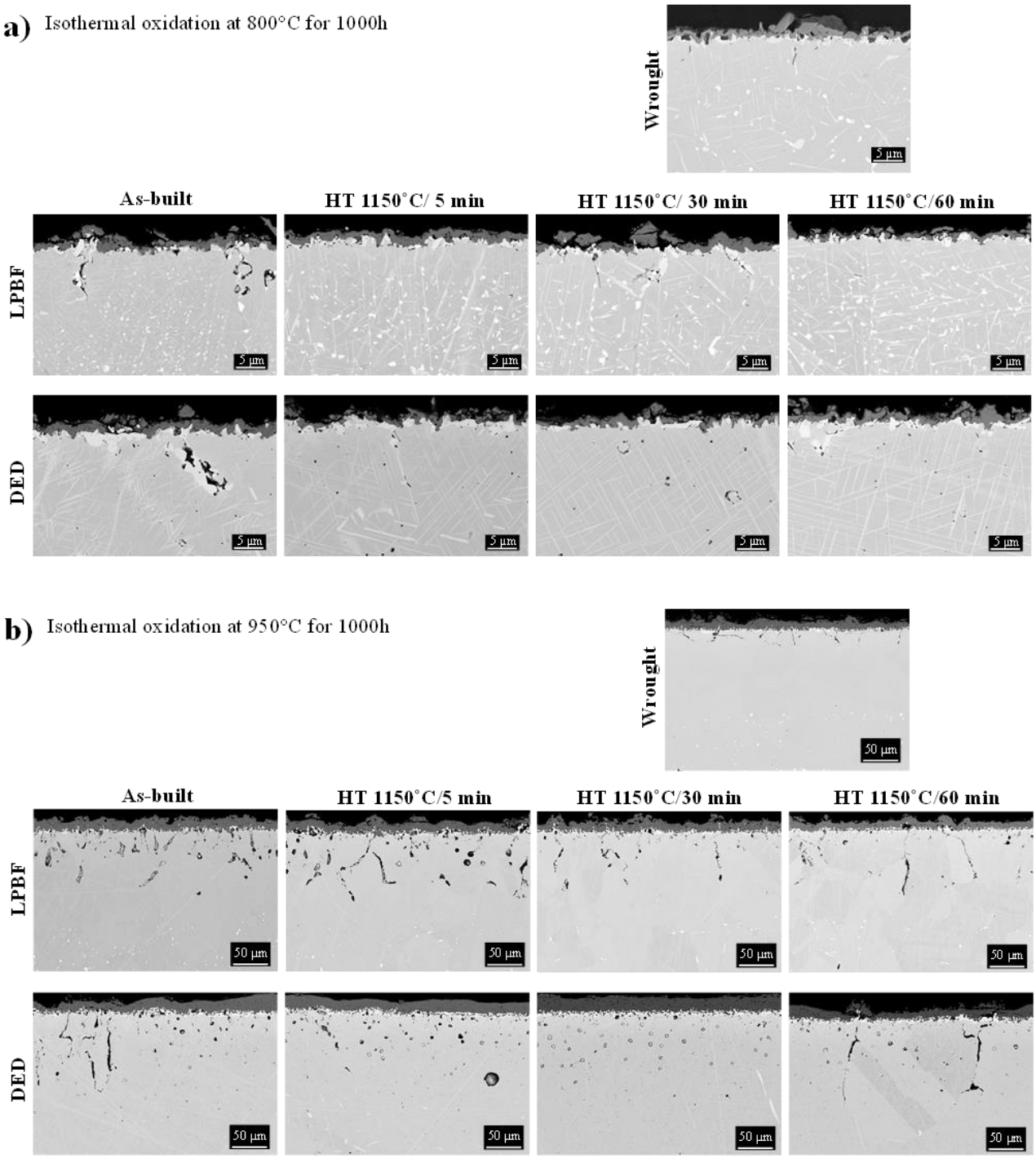

Figure 5-59. Cross-sectional BSE images of oxidized coupons for 1000h in the as-built conditions and after heat treatment. As a reference, the wrought oxidized in the same conditions is displayed. a) 800°C b) 950°C

At 950°C, the oxidation products are similar to the ones reported in section 5.3. All samples exhibit a continuous and slightly porous chromia scale. (δ+σ)-precipitates are observed beneath the chromia, and Al_2O_3 formed internally preferentially located along the alloy grain boundaries. Interestingly, there is no appreciable difference when comparing the intergranular oxidation (IGO) depth among the LPBF and DED as-built samples relative to their corresponding heat-treated ones.

Regarding the IGO frequency, Figure 5-61 illustrates the internal attack area fraction as a function of the heat-treated condition, where internal attack included internal oxidation, IGO, and Kirkendall voids. For the LPBF samples, the internal attack area fraction is lower after 30 min at 1150°C, and kept in the same range after 60 min at 1150°C. Whereas the DED sample exhibits a similar internal attack area in the as-built condition and after 5 min and 30 min at 1150°C, and there is an increase after 60 min at 1150°C.

On the one hand, the internal attack reduction is attributed in part to the increase of $\Sigma 3^n$ grain boundaries, and their higher resistance to show IGO compared to other random orientated grain boundaries. This contribution should be bigger in the LPBF sample than in the DED due to the significantly smaller grain size. On the other hand, the homogenization did not affect the higher oxygen concentration reported in the AM sample; thereby, there is still enough oxygen near the grain boundaries that result in IGO. This will be valid assuming that a potential reason for the $\Sigma 3^n$ is a lower permeability of oxygen. Additionally, the higher oxygen content in voids could also coarsen the Kirkendall voids.

Nonetheless, the impact of the IGO in the kinetics was described in section 5.3.3.1.3. Thereby, the reduction in the internal attack area fraction after an optimal heat treatment will explain the reduction in kinetics between the heat-treated samples and their respective as-built ones.

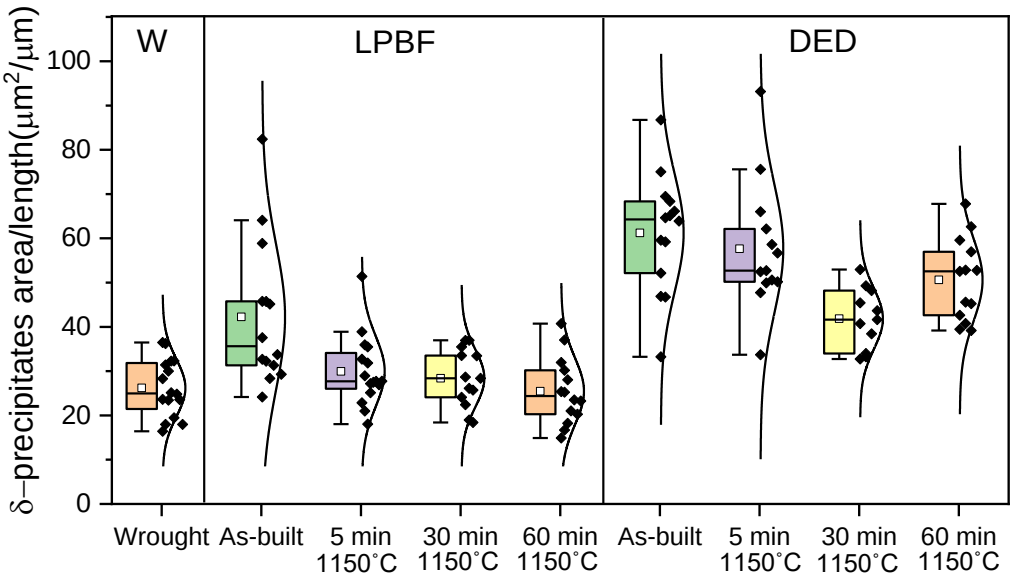

Figure 5-60. Evolution of the fraction of δ-precipitates beneath the chromia scale with heat treatment time.

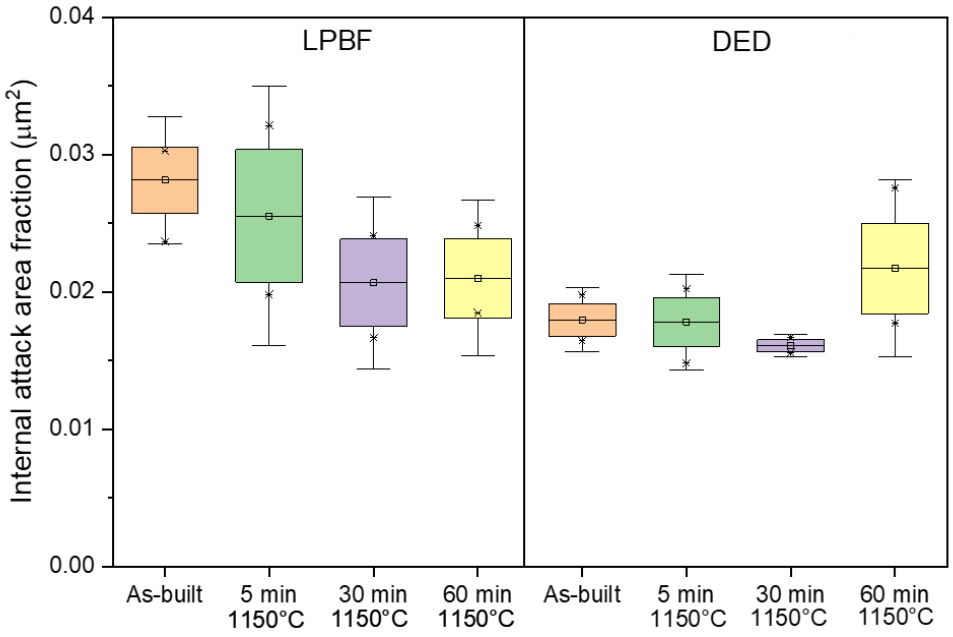

Figure 5-61. Internal attack fraction as a function of the heat treatment time. As-built and wrough values are included as a reference.

5.6.3.3 Effect of Optimal Solution Heat Treatment on Fatigue Performance of Oxidized Samples

To evaluate the mitigation level of the homogenization heat treatment, the fatigue of the oxidized heat-treated samples was assessed. Only the optimal heat treatment was evaluated. Figure 5-62 shows the mean fatigue life for the heat-treated samples compared to their corresponding as-built samples, and using the wrought alloy as a reference. At 800°C, both samples, DED and LPBF, show a slight improvement in the mean fatigue life after heat treatment. At 950°C, there is no difference between the heat-treated and the as-built sample for the LPBF. In the DED, the heat-treated sample has a shorter mean fatigue life than the as-built sample.

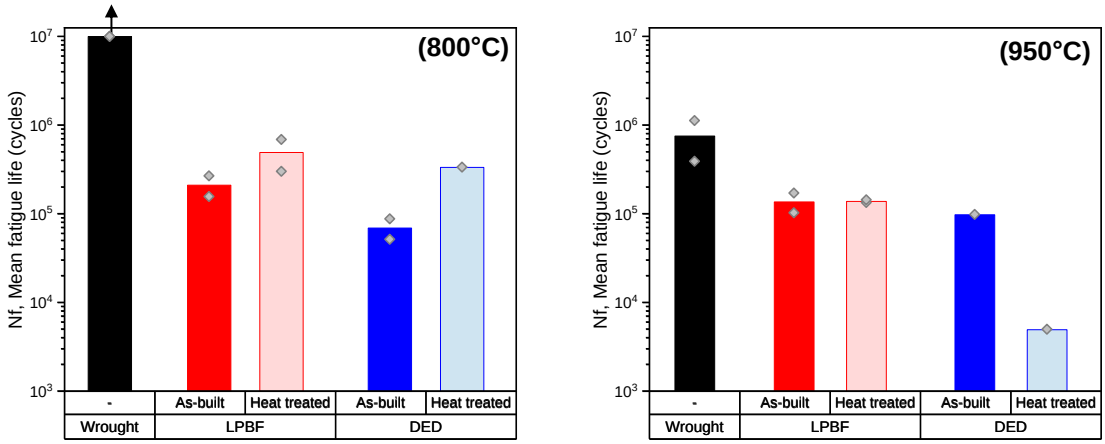

Figure 5-62. Mean room temperature fatigue life of wrought, LPBF and DED samples after oxidation for 1000h at 800°C at 950°

To understand mean fatigue life differences among heat treatment and as-built samples, it is important to analyze the microstructural degradation after the fatigue testing in the oxidized test bars. Figure 5-63 and Figure 5-64 illustrate the microstructure evolution of the oxidized test bars at 800°C and 950°C, respectively.

At 800°C, there is no appreciable difference in the degradation features between the heat-treated and as-built samples; all samples exhibit interfacial defects and subsurface voids described in section 5.4.3.4. However, interfacial defects and subsurface voids are less frequent in the heat-treated samples than in the as-built ones. This reinforces the observation that interfacial defects are associated with subsurface precipitates (see section 5.4.3.4.1). Homogenization treatments reduce the subsurface precipitates compared to the as-built sample. Therefore, if there are fewer and not concentrated regions of subsurface precipitates, fewer interfacial defects are expected. Regarding the subsurface voids, these are associated with the conglomeration of precipitates in the subsurface. Similar to the last point, the diffusive removal of segregated regions limits the conglomeration formations. Therefore, fewer subsurface voids are expected in the heat-treated samples.

At 950°C, all samples show spallation and secondary cracks associated with IGO. Section 5.5.3.2 showed that cracks nucleate in the IGO. This is attributed in part to the incoherence of the grain boundary, the tension stress due to expansion in the Al_2O_3 formation, and the fast propagation of a crack in a depleted region [91], [92]. In this case, reduction in the IGO frequency in the LPBF and DED samples did not compensate for the IGO depth effect. Enough cracks decreased the cross-section area tested in AM heat-treated samples, as they did in the as-built samples. Therefore, similar mean fatigue life is expected. Additionally, the significantly shorter fatigue life in the heat-treated DED sample shows differences in the crack propagation stage due to defects in the matrix.

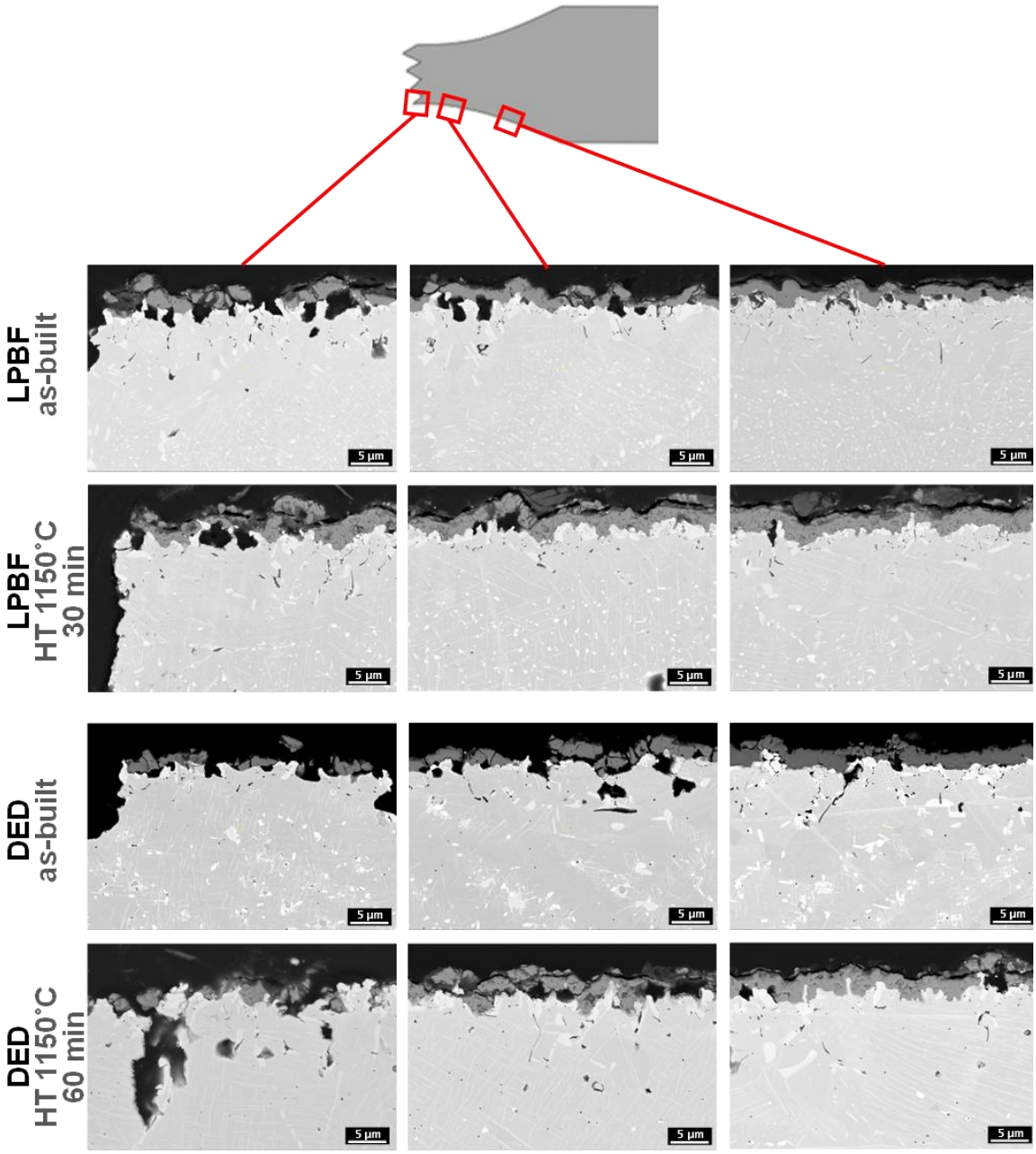

Figure 5-63. Cross-sectional BSE images of oxidized test bars (800°C/1000h) after fatigue testing, comparing as-built and optimal heat-treated conditions.

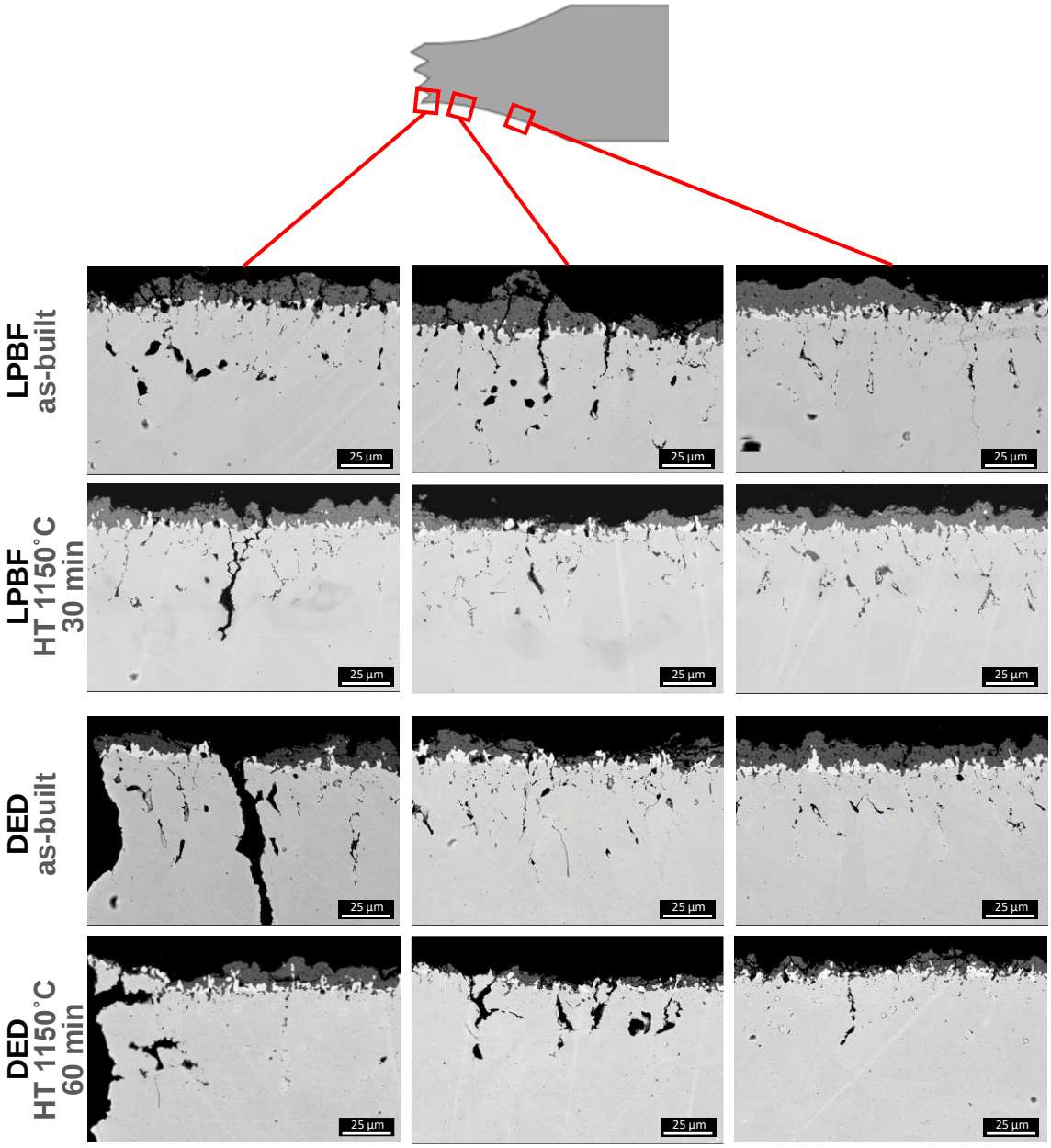

Figure 5-64. Cross-sectional BSE images of oxidized test bars (950°C/1000h) after fatigue testing, comparing as-built and optimal heat-treated conditions.

5.6.4 Conclusions

- Optimal homogenization heat treatment is 30 min and 60 min at 1150°C for the LPBF and DED samples, respectively. This heat-treatment assures complete dissolution of interdendritic segregation, increase of Σ3 grain boundaries, and avoids reprecipitation along the grain boundaries (refer to Figure 5-54 and Figure 5-55).
- Optimal heat treatments result in enhancement of oxidation kinetics at 950°C, where oxidation rates for samples heat-treated were comparable to that of the wrought alloy (refer to Figure 5-57). Since the contribution of IGO in kinetics at 950°C is significant, the oxidation rates reduction in the heat-treated samples is attributed in part to the good resistance of Σ3 grain boundaries to oxidize. However, the remaining IGO in the heat-treated sample shows similar depth compared to the corresponding as-built samples. The positive correlation of the IGO depth and the crack initiation impedes an improvement in the fatigue life for the heat-treated samples relative to the as-built samples.
- At 800°C, the oxidation rates were unaffected by the heat-treatment, indicating that the interdendritic segregation does not play an important role to the steady-state kinetics. However, the oxidation products distribution was affected by the heat treatment. A limited growth of subsurface precipitates due to the complete removal of the segregation was found in the heat-treated sample (refer to Figure 5-60). As a result, the interfacial defects and subsurface voids associated with precipitates were fewer than in the as-built test bars, in turn, enhancing slightly the mean fatigue life (refer to Figure 5-62).

6.0 Summary and Outlook

This study aimed to fill the gap of knowledge on the impact of oxidation at high temperatures on the mechanical fatigue of Alloy 625, with a particular focus placed on the role of the alloy manufacturing processes. The two laser-assisted additive manufacturing (AM) processes studied (laser powder bed fusion (LPBF) and direct energy deposition (DED)) exhibited accelerated degradation during oxidation at 800°C and 950°C compared to wrought and cast alloys. These differences detrimentally affected crack initiation during fatigue, resulting in early fatigue failure. The accelerated degradation during oxidation included poor interface bond scale/alloy, enhanced intergranular oxidation, more buckling of the chromia scale, and therefore more free space.

Therefore, laser-assisted additive manufactured Alloy 625 in the as-built condition is not recommended for high-temperature applications that involve mechanical loading. A homogenizing heat treatment may provide some improvement, but not close to reaching the fatigue strength of the wrought counterpart alloy. Further research is required to evaluate the effectiveness of different mitigation strategies to enhance its performance. Some mitigation strategies using the current AM parts include post-treatments as HIP and desulfurization by hydrogen annealing. Other strategies modifying the current AM processing conditions include decreasing the oxygen concentration in the atmosphere during the building, and optimizing the powder composition (e.g., decrease sulfur and oxygen content, increase silicon content). Still other directions could explore the effect of adjusting minor constituent contents (e.g., Si, Fe, Mn) on improving the properties on AM-built Alloy 625.

Appendix A - Quantitative Measurements of the Degradation State at the Failure Moment

Sample ID	Oxide products				Subsurface precipitates (δ-phase and σ-phase)				Oxide/alloy interfacial detachment					
	Max depth of internal oxidation [µm]		Oxide thickness [µm]		Precipitates size (ECD) [µm]			Precipitates AR		Detachment linear fraction [µm/ µm]		Non-planar interface index[2]		Defects area [µm^2]		
	Average	STD	Average	STD	Average	STD	Total sum[1]	Average	STD	Average	STD	Average	STD	Average	STD	Total sum[1]
Wrought 24h	1.10 ±	0.26	0.37 ±	0.09	0.29 ±	0.14	24.63	2.27 ±	0.98	0.13 ±	0.07	0.06 ±	0.02	0.17 ±	0.09	4.22
Wrought 300h	2.17 ±	0.48	1.09 ±	0.24	0.42 ±	0.18	43.19	2.60 ±	1.45	0.11 ±	0.04	0.05 ±	0.02	0.39 ±	0.43	16.12
Wrought 1000h	3.33 ±	0.90	1.56 ±	0.37	0.59 ±	0.37	84.94	2.53 ±	1.58	0.12 ±	0.03	0.06 ±	0.02	0.40 ±	0.50	16.12
LPBF 24h	1.67 ±	0.37	0.53 ±	0.13	0.29 ±	0.17	29.81	2.38 ±	1.04	0.34 ±	0.06	0.05 ±	0.04	0.32 ±	0.27	29.70
LPBF 300h	5.42 ±	1.19	1.37 ±	0.25	0.63 ±	0.42	112.78	2.55 ±	1.23	0.40 ±	0.05	0.11 ±	0.07	0.84 ±	1.18	143.97
LPBF 1000h	7.95 ±	2.04	1.95 ±	0.51	0.79 ±	0.55	146.65	2.55 ±	1.17	0.43 ±	0.09	0.14 ±	0.04	1.46 ±	1.84	193.21
DED 24h	1.61 ±	0.37	0.48 ±	0.11	0.30 ±	0.20	33.19	2.55 ±	1.33	0.41 ±	0.04	0.06 ±	0.05	0.21 ±	0.14	15.04
DED 300h	4.95 ±	0.99	1.46 ±	0.34	0.71 ±	0.51	116.88	2.96 ±	3.20	0.46 ±	0.07	0.14 ±	0.04	1.52 ±	1.67	218.59
DED 1000h	6.89 ±	1.82	2.27 ±	0.42	0.82 ±	0.67	174.83	2.88 ±	3.31	0.53 ±	0.09	0.21 ±	0.07	1.90 ±	2.29	239.61

[1] total summations calculated along 331.2 µm (8 micrographs at 5000x)

[2] $Non-planar\ interface\ index = \frac{Real\ oxide/alloy\ interface}{flat\ interface} - 1$; a zero value indicates that the interface is flat.

Bibliography

[1] S. Ford and S. Ford, “Additive manufacturing and sustainability : an exploratory study of the advantages and challenges advantages and challenges,” *Journal of Cleaner Production*, vol. 137, no. May, pp. 1573–1587, 2016, doi: 10.1016/j.jclepro.2016.04.150.

[2] B. Graybill, M. Li, D. Malawey, C. Ma, J. M. Alvarado-Orozco, and E. Martinez-Franco, “Additive manufacturing of nickel-based superalloys,” *ASME 2018 13th International Manufacturing Science and Engineering Conference, MSEC 2018*, vol. 1, no. June, 2018, doi: 10.1115/MSEC2018-6666.

[3] T. M. Pollock and S. Tin, “Nickel-based superalloys for advanced turbine engines: Chemistry, microstructure, and properties,” *Journal of Propulsion and Power*, vol. 22, no. 2, pp. 361–374, 2006, doi: 10.2514/1.18239.

[4] L. Kumar, R. Venkataramani, M. Sundararaman, P. Mukhopadhyay, and S. P. Garg, “Studies on the Oxidation Behavior of Inconel 625 Between 873 and 1523 K,” *Oxidation of Metals*, vol. 45, pp. 221–244, 1996.

[5] A. Chyrkin, P. Huczkowski, V. Shemet, L. Singheiser, and W. J. Quadakkers, “Sub-scale depletion and enrichment processes during high temperature oxidation of the nickel base alloy 625 in the temperature range 900-1000 °c,” *Oxidation of Metals*, vol. 75, no. 3–4, pp. 143–166, 2011, doi: 10.1007/s11085-010-9225-3.

[6] H. Buscail *et al.*, “Effects of water vapour on the oxidation of a nickel-base 625 alloy between 900 and 1,100 °C,” *Journal of Materials Science*, vol. 46, no. 18, pp. 5903–5915, 2011, doi: 10.1007/s10853-011-5544-2.

[7] U. Unnikrishnan and V. Yang, “A review of cooling technologies for high temperature rotating components in gas turbine,” *Propulsion and Power Research*, vol. 11, no. 3, pp. 293–310, 2022, doi: 10.1016/j.jppr.2022.07.001.

[8] C. U. Brown, G. Jacob, M. Stoudt, S. Moylan, J. Slotwinski, and A. Donmez, “Interlaboratory Study for Nickel Alloy 625 Made by Laser Powder Bed Fusion to Quantify Mechanical Property Variability,” *Journal of Materials Engineering and Performance*, vol. 25, no. 8, pp. 3390–3397, 2016, doi: 10.1007/s11665-016-2169-2.

[9] N. Ramenatte, A. Vernouillet, S. Mathieu, A. Vande Put, M. Vilasi, and D. Monceau, “A comparison of the high-temperature oxidation behaviour of conventional wrought and laser beam melted Inconel 625,” *Corrosion Science*, vol. 164, no. October 2019, p. 108347, 2020, doi: 10.1016/j.corsci.2019.108347.

[10] Q. Jia and D. Gu, “Selective laser melting additive manufacturing of Inconel 718 superalloy parts: Densification, microstructure and properties,” *Journal of Alloys and*

Compounds, vol. 585, 2014, doi: 10.1016/j.jallcom.2013.09.171.

[11] M. Romedenne, R. Pillai, M. Kirka, and S. Dryepondt, "High temperature air oxidation behavior of Hastelloy X processed by Electron Beam Melting (EBM) and Selective Laser Melting (SLM)," *Corrosion Science*, vol. 171, no. January, pp. 1–21, 2020, doi: 10.1016/j.corsci.2020.108647.

[12] A. Chyrkin, J. Nowak, W, and K. Stiller, "Intergranular oxidation of additively manufactured Ni-base alloy 625: The role of Si," *Corrosion Science*, vol. 219, no. 1, p. 111234, 2023.

[13] Q. Jia and D. Gu, "Selective laser melting additive manufactured Inconel 718 superalloy parts: High-temperature oxidation property and its mechanisms," *Optics and Laser Technology*, vol. 62, pp. 161–171, 2014, doi: 10.1016/j.optlastec.2014.03.008.

[14] T. Sanviemvongsak, D. Monceau, and B. Macquaire, "High temperature oxidation of IN 718 manufactured by laser beam melting and electron beam melting: Effect of surface topography," *Corrosion Science*, vol. 141, no. July, pp. 127–145, 2018, doi: 10.1016/j.corsci.2018.07.005.

[15] America Makes & ANSI Additive Manufacturing Standardization Collaborative (AMSC), "Standardization Roadmap for Additive Manufacturing," no. February, p. Public Draft, 2017.

[16] R. Reed, R. Perroy, and S. Careas, *The Superalloys, Fundamentals and Applications*, vol. 1. 2015.

[17] M. J. Donachie and S. J. Donachie, *Superalloys A Technical Guide*. 2002.

[18] H. L. Eiselstein and J. Gadbut, "Matrix-Stiffened Alloy (3160500)," 1964.

[19] H. L. Eiselstein and D. J. Tillack, "The Invention and Definition of Alloy 625," in *Superalloys 718, 625 and Various Derivatives*, 1991, pp. 1–14, doi: 10.7449/1991/superalloys_1991_1_14.

[20] S. Floreen, G. E. Fuchs, and W. J. Yang, "The Metallurgy of Alloy 625," in *Superalloys 718, 625 and Various Derivatives*, 1994, pp. 13–37, doi: 10.7449/1994/superalloys_1994_13_37.

[21] S. M. Corporation, "Inconel Alloy 625," *www.Specialmetals.com*, vol. 625, no. 2, pp. 1–28, 2013, doi: SMC-066.

[22] Y. Huang and T. G. Langdon, "The evolution of delta-phase in a superplastic Inconel 718 alloy," *Journal of Materials Science*, vol. 42, no. 2, pp. 421–427, 2007, doi: 10.1007/s10853-006-0483-z.

[23] H. Y. Zhang, S. H. Zhang, M. Cheng, and Z. X. Li, "Deformation characteristics of δ phase in the delta-processed Inconel 718 alloy," *Materials Characterization*, vol. 61, no.

1, pp. 49–53, 2010, doi: 10.1016/j.matchar.2009.10.003.

[24] F. P. Cone, “Observations on the development of delta phase in In718 alloy,” *Proceedings of the International Symposium on Superalloys and Various Derivatives*, vol. 1, pp. 323–332, 2001, doi: 10.7449/2001/superalloys_2001_323_332.

[25] C. Ruiz, A. Obabueki, and K. Gillespie, “Evaluation of the Microstructure and Mechanical Properties of Delta Processed Alloy 718,” *Superalloys*, pp. 33–42, 1992, doi: 10.7449/1992/superalloys_1992_33_42.

[26] J. F. Radavich and W. H. Couts, Jr., “Factors Affecting Delta Phase Precipitation and Growth at Hot Work Temperatures for Direct Aged Inco 718,” *Superalloys*, no. 317, pp. 497–507, 1984, doi: 10.7449/1984/superalloys_1984_497_507.

[27] M. Anderson, A. L. Thielin, F. Bridier, P. Bocher, and J. Savoie, “δ Phase precipitation in Inconel 718 and associated mechanical properties,” *Materials Science and Engineering A*, vol. 679, no. August 2016, pp. 48–55, 2017, doi: 10.1016/j.msea.2016.09.114.

[28] D. J.R., Ed., *ASM Specialty Handbook: Heat-Resistant Materials*. ASM Internacional, 1997.

[29] M. Sundararaman, P. Mukhopadhyay, and S. Banerjee, “Carbide Precipitation in Nickel Base Superalloys 718 and 625 and their Effect on Mechanical Properties,” *Superalloys 718, 625, 706 and Various Derivatives (1997)*, pp. 367–378, 1997, doi: 10.7449/1997/superalloys_1997_367_378.

[30] G. P. Sabol and R. Stickler, “Microstructure of Nickel-Based Superalloys,” vol. 11, 1969.

[31] S. T. Wlodek and R. D. Field, “The Effects of Long Time Exposure on Alloy 718,” *Superalloys 718, 625, 706 and Various Derivatives (1994)*, pp. 659–670, 1994, doi: 10.7449/1994/Superalloys_1994_659_670.

[32] M. J. Cieslak, T. J. Headley, T. Kollie, and A. D. Romig, “Melting and solidification study of Alloy 625,” *Metallurgical transactions. A, Physical metallurgy and materials science*, vol. 19 A, no. 9, pp. 2319–2331, 1988, doi: 10.1007/BF02645056.

[33] S. Kou, *Welding Metallurgy Second Edition*, vol. 822, no. 1–3. 2003.

[34] M. J. Cieslak, “The Solidification Behavior of an Alloy 625/718 Variant,” pp. 71–80, 1991, doi: 10.7449/1991/superalloys_1991_71_80.

[35] J. N. DUPONT, C. V. ROBINO, and A. R. MARDER, “Solidification and weldability of Nb-bearing superalloys,” *Welding journal*, vol. 77, no. 10, pp. 417s-431s, 1998, doi: 10.4319/lo.2013.58.2.0489.

[36] L. Wang, Y. Yao, J. Dong, and M. Zhang, “Effect of cooling rates on segregation and density variation in the mushy zone during solidification of superalloy inconel 718,” *Chemical Engineering Communications*, vol. 197, no. 12, pp. 1571–1585, 2010, doi:

10.1080/00986445.2010.493101.

[37] ASTM, “F2792 -12a Standard Terminology for Additive Manufacturing Technologies,” pp. 2–4, 2013, doi: 10.1520/F2792-12A.2.

[38] M. Despeisse and S. Ford, “The role of additive manufacturing in improving resource efficiency and sustainability,” *IFIP Advances in Information and Communication Technology*, vol. 460, pp. 129–136, 2015, doi: 10.1007/978-3-319-22759-7_15.

[39] G. A. Longhitano, M. A. Larosa, A. L. M. Jardini, C. A. de C. Zavaglia, and M. C. F. Ierardi, “Surface Finishes for Ti-6Al-4V Alloy Produced by Direct Metal Laser Sintering,” *Materials Research*, vol. 18, no. 4, pp. 838–842, 2015, doi: 10.1590/1516-1439.014415.

[40] Y. Huang *et al.*, “Rapid prediction of real-time thermal characteristics, solidification parameters and microstructure in laser directed energy deposition (powder-fed additive manufacturing),” *Journal of Materials Processing Technology*, vol. 274, no. July, p. 116286, 2019, doi: 10.1016/j.jmatprotec.2019.116286.

[41] A. Saboori, D. Gallo, S. Biamino, P. Fino, and M. Lombardi, “An overview of additive manufacturing of titanium components by directed energy deposition: Microstructure and mechanical properties,” *Applied Sciences (Switzerland)*, vol. 7, no. 9, 2017, doi: 10.3390/app7090883.

[42] L. L. Parimi, G. Ravi, D. Clark, and M. M. Attallah, “Microstructural and texture development in direct laser fabricated IN718,” *Materials Characterization*, vol. 89, pp. 102–111, 2014, doi: 10.1016/j.matchar.2013.12.012.

[43] A. J. Dunbar *et al.*, “Development of experimental method for in situ distortion and temperature measurements during the laser powder bed fusion additive manufacturing process ,” vol. 12, pp. 25–30, 2016.

[44] W. J. Sames, F. A. List, S. Pannala, R. R. Dehoff, and S. S. Babu, “The metallurgy and processing science of metal additive manufacturing,” *International Materials Reviews*, vol. 61, no. 5, 2016, doi: 10.1080/09506608.2015.1116649.

[45] V. Manvatkar, A. De, and T. Debroy, “Heat transfer and material flow during laser assisted multi-layer additive manufacturing,” *Journal of Applied Physics*, vol. 116, no. 12, 2014, doi: 10.1063/1.4896751.

[46] Y. Tian *et al.*, “Rationalization of microstructure heterogeneity in INCONEL 718 builds made by the direct laser additive manufacturing process,” *Metallurgical and Materials Transactions A: Physical Metallurgy and Materials Science*, vol. 45, no. 10, 2014, doi: 10.1007/s11661-014-2370-6.

[47] N. Birks, G. Meier, and F. Pettit, *Introduction to the High Temperature Oxidation of Metals*. Cambridge University Press, 1983.

[48] B. Gleeson, “High-Temperature Corrosion of Metallic Alloys and Coatings,” in *Materials Science and Technology Series*, 2000.

[49] S. Bradford, “Fundamental of Corrosion in Gases,” in *ASM Metals Handbook*, vol. 13, Ohio, 1987, pp. 122–173.

[50] M. Danielewski, “Kinetics of Gaseous Corrosion Processes, Corrosion: Fundamentals, Testing, and Protection,” in *ASM Metals Handbook*, vol. 13A, OH: ASM Internacional, 2003, pp. 97–105.

[51] L. Latu-Romain *et al.*, “Duplex n- and p-Type Chromia Grown on Pure Chromium: A Photoelectrochemical and Microscopic Study,” *Oxidation of Metals*, vol. 86, no. 5–6, pp. 497–509, 2016, doi: 10.1007/s11085-016-9648-6.

[52] C. Wagner, “Theoretical Analysis of the Diffusion Processes Determining the Oxidation Rate of Alloys,” *Journal of The Electrochemical Society*, vol. 99, no. 10, p. 369, 1952, doi: 10.1149/1.2779605.

[53] A. Atkinson, “Wagner theory and short circuit diffusion,” *Materials Science and Technology*, vol. 4, no. December, pp. 1046–1051, 1988, doi: 10.1179/mst.1988.4.12.1046.

[54] D. J. Young, *High Temperature Oxidation and Corrosion of Metals: Second Edition*, Second. Amsterdam: Elsevier, 2016.

[55] H. E. Evans, “Stress effects in high temperature oxidation of metals,” *International Materials Reviews*, vol. 40, no. 1, pp. 1–40, 1995, doi: 10.1179/imr.1995.40.1.1.

[56] F. N. Rhines and J. S. Wolf, “The Role of Oxide Microstructure and Growth Stresses in the High-Temperature Scaling of Nickel,” *Metallurgical Transactions*, vol. 1, no. June, pp. 1701–1710, 1970.

[57] D. R. Clarke, “The lateral growth strain accompanying the formation of a thermally grown oxide,” *Acta Materialia*, no. 51, pp. 1393–1407, 2003, doi: 10.1016/S1359-6454(02)00532-3.

[58] V. R. Howes and C. N. Richardson, “The initial stresses develop during temperature oxidation of Fe-Cr alloys,” *Corrosion Science*, vol. 9, pp. 385–394, 1969, doi: 10.1016/s0010-938x(69)80034-x.

[59] W. Przybilla and M. Schütze, “Role of Growth Stresses on the Structure of Oxide Scales on Nickel at 800 and 900°C,” *Oxidation of Metals*, vol. 58, no. August, pp. 103–145, 2002.

[60] S. Taniguchi, “Stresses Developed during the Oxidation Alloys,” *Transactions of the Iron and Steel Institute of Japan*, no. 25, 3, 1985.

[61] M. Schütze, “Stress effects in high temperature oxidation,” in *Shreir’s Corrosion*, B.

Cottis, M. Graham, R. Lindsay, S. Lyon, T. Richardson, D. Scantlebury, and H. Stott, Eds. Amsterdam: Elsevier, 2010, pp. 153–179.

[62] M. Schütze, M. Malessa, D. Renusch, P. F. Tortorelli, I. G. Wright, and R. B. Dooley, "Mechanical Properties and Adherence of Oxide Scales," *Materials Science Forum*, vol. 522–523, pp. 393–400, 2006, doi: 10.4028/www.scientific.net/msf.522-523.393.

[63] M. Schütze, "Modelling oxide scale fracture," *Materials at High Temperatures*, vol. 22, no. 1–2, pp. 147–154, 2005, doi: 10.1179/mht.2005.017.

[64] M. Schütze, P. F. Tortorelli, and I. G. Wright, "Development of a comprehensive oxide scale failure diagram," *Oxidation of Metals*, vol. 73, no. 3–4, pp. 389–418, 2010, doi: 10.1007/s11085-009-9185-7.

[65] G. C. Wood, I. G. Wright, T. Hodgkiess, and D. P. Whittle, "Comparison of the Oxidation of Fe-Cr, Ni-Cr and Co-Cr Alloys in Oxygen and Water Vapour," *Materials and Corrosion*, vol. 21, no. 11, pp. 900–910, 1970.

[66] R. Kane, "High-temperature gaseous corrosion," in *Corrosion: Fundamentals, Testing, and Protection. ASM Metals Handbook*, vol. 13A, ASM Internacional, 2003, p. 577.

[67] R. Rapp, "Kinetics, Microstructures and Mechanism of Internal Oxidation: Its Effect and Prevention in High Temperature Alloy Oxidation," *Corrosion*, vol. 21, no. 12, pp. 382–401, 1965, doi: 10.3323/jcorr1954.15.9_406.

[68] C. Wagner *et al.*, "Reaktionstypen bei der Oxydation von Legierungen," *Z. Elektrochem.*, vol. 63, pp. 772–782, 1959.

[69] R. Rapp, "The transition from internal to external oxidation and the formation of interruption bands in silver-indium alloys," *Acta Metallurgica*, vol. 9, no. 8, pp. 730–741, 1961.

[70] H. E. Evans, A. T. Donaldson, and T. C. Gilmour, "Mechanisms of breakaway oxidation and application to a chromia-forming steel," *Oxidation of Metals*, vol. 52, no. 5, pp. 379–402, 1999, doi: 10.1023/a:1018855914737.

[71] D. P. Whittle, "Spalling of protective oxide scales," *Oxidation of Metals*, vol. 4, no. 3, pp. 171–179, 1972, doi: 10.1007/BF00613091.

[72] K. A. Unocic and B. A. Pint, "Effect of environment on the high temperature oxidation behavior of 718 and 718plus," in *8th International Symposium on Superalloy 718 and derivatives*, 2014.

[73] E. N'dah, M. P. Hierro, K. Borrero, and F. J. Pérez, "Study of the cyclic oxidation resistance of superalloy IN-625: Lifetime predicted by COSP-modelling program," *Oxidation of Metals*, vol. 68, no. 1–2, pp. 9–21, 2007, doi: 10.1007/s11085-006-9048-4.

[74] S. Parizia *et al.*, "Effect of heat treatment on microstructure and oxidation properties of

Inconel 625 processed by LPBF," *Journal of Alloys and Compounds*, vol. 846, p. 156418, 2020, doi: 10.1016/j.jallcom.2020.156418.

[75] V. P. Deodeshmukh, "Long-term performance of high-temperature foil alloys in water vapor containing environment. Part II: Chromia vaporization behavior," *Oxidation of Metals*, vol. 79, no. 5–6, pp. 579–588, 2013, doi: 10.1007/s11085-012-9344-0.

[76] A. Chyrkin, "Oxidation-Induced Phase Transformations and Lifetime Limits of Chromia-Forming Nickel-Base Alloy 625," Rheinisch-Westfälischen Technischen Hochschule Aachen zur, 2011.

[77] T. Sanviemvongsak, D. Monceau, C. Desgranges, and B. Macquaire, "Intergranular oxidation of Ni-base alloy 718 with a focus on additive manufacturing," *Corrosion Science*, vol. 170, no. November 2019, p. 108684, 2020, doi: 10.1016/j.corsci.2020.108684.

[78] K. Wang, D. Du, G. Liu, Z. Pu, B. Chang, and J. Ju, "High-temperature oxidation behaviour of high chromium superalloys additively manufactured by conventional or extreme high-speed laser metal deposition," *Corrosion Science*, vol. 176, no. August, pp. 1–13, 2020, doi: 10.1016/j.corsci.2020.108922.

[79] M. R. Condruz, G. Matache, A. Paraschiv, and T. Badea, "High Temperature Oxidation Behavior of Selective Laser Melting Manufactured IN 625," *Metals*, vol. 10, p. 668, 2020, doi: doi.org/10.3390/met10050668.

[80] K. A. Unocic, L. M. Kolbus, R. R. Dehoff, S. N. Dryepondt, and B. A. Pint, "High-Temperature Performance of UNS N07718 Processed by Additive Manufacturing," in *NACE Corrosion*, 2014, p. 4478.

[81] W. J. Sames, F. A. List, S. Pannala, R. R. Dehoff, and S. S. Babu, "The metallurgy and processing science of metal additive manufacturing," *International Materials Reviews*, vol. 61, no. 5, pp. 315–360, 2016, doi: 10.1080/09506608.2015.1116649.

[82] L. Li *et al.*, "Influence of Building Direction on the Oxidation Behavior of Inconel 718 Alloy Fabricated by Additive Manufacture of Electron Beam Melting," *Materials*, vol. 11, p. 2549, 2018, doi: 10.3390/ma11122549.

[83] Y. Sun, L. Chen, L. Li, and X. Ren, "High-temperature oxidation behavior and mechanism of Inconel 625 super- alloy fabricated by selective laser melting," *Optics and Laser Technology*, vol. 132, no. April, p. 106509, 2020, doi: 10.1016/j.optlastec.2020.106509.

[84] Q. Jia and D. Gu, "Selective laser melting additive manufactured Inconel 718 superalloy parts: High-temperature oxidation property and its mechanisms," *Optics and Laser Technology*, vol. 62, pp. 161–171, 2014, doi: 10.1016/j.optlastec.2014.03.008.

[85] G. Marchese *et al.*, "The role of texturing and microstructure evolution on the tensile behavior of heat-treated Inconel 625 produced via laser powder bed fusion," *Materials*

Science & Engineering A, vol. 769, no. October 2019, p. 138500, 2020, doi: 10.1016/j.msea.2019.138500.

[86] D. Monceau and M. Vilasi, "High Temperature Oxidation of Additively Manufactured Structural Alloys," *Journal of Metals*, vol. 74, no. 4, pp. 1659–1667, 2022, doi: 10.1007/s11837-022-05198-z.

[87] T. Sanviemvongsak, D. Monceau, M. Madelain, C. Desgranges, J. Smialek, and B. Macquaire, "Cyclic oxidation of alloy 718 produced by additive manufacturing compared to a wrought-718 alloy," *Corrosion Science*, vol. 192, no. August, p. 109804, 2021, doi: 10.1016/j.corsci.2021.109804.

[88] G. Bertali, F. Scenini, and M. G. Burke, "The effect of residual stress on the Preferential Intergranular Oxidation of Alloy 600," *Corrosion Science*, vol. 111, pp. 494–507, 2016, doi: 10.1016/j.corsci.2016.05.022.

[89] M. Reger and L. Remy, "Fatigue Oxidation Interaction in IN 100 Superalloy," vol. 19, no. September, pp. 2259–2268, 1988.

[90] S. Cruchley *et al.*, "Effect of prior oxidation on high cycle fatigue performance of RR1000 and role of oxidation in fatigue crack initiation," *Materials at High Temperatures*, vol. 32, no. 1–2, pp. 68–73, 2015, doi: 10.1179/0960340914Z.00000000064.

[91] S. Cruchley, H. Y. Li, H. E. Evans, P. Bowen, D. J. Child, and M. C. Hardy, "The role of oxidation damage in fatigue crack initiation of an advanced Ni-based superalloy," *International Journal of Fatigue*, no. 81, pp. 265–274, 2015, doi: 10.1016/j.ijfatigue.2015.08.016.

[92] C. K. Sudbrack, S. L. Draper, T. T. Gorman, J. Telesman, T. P. Gabb, and D. R. Hull, "Oxidation and the Effects of High Temperature Exposures on Notched Fatigue Life of an Advanced Powder Metallurgy Disk Superalloy," in *Superalloys 2012*, 2012, pp. 863–872, doi: 10.1002/9781118516430.ch95.

[93] T. P. Gabb, J. Telesman, P. Kantzos, J. Smith, and P. Browning, "Effects of High Temperature Exposures on Fatigue Life of Disk Superalloys," in *Superalloys 2004*, 2004, pp. 269–274, doi: http://dx.doi.org/10.7449/2004/Superalloys_2004_269_274.

[94] G. de Leon Nope, G. Wang, J. M. Alvarado-Orozco, and B. Gleeson, "Role of Elemental Segregation on the Oxidation Behavior of Additively Manufactured Alloy 625," *JOM*, vol. 74, no. 4, pp. 1698–1706, 2022, doi: 10.1007/s11837-022-05200-8.

[95] J. N. Dupont, J. C. Lippold, and S. D. Kiser, *Welding Metallurgy and Weldability of Nickel-Base Alloys*, vol. 53, no. 9. New Jersey: John Wiley & Sons, 2009.

[96] B. Pieraggi, "Calculations of parabolic reaction rate constants," *Oxidation of Metals*, vol. 27, no. 3–4, pp. 177–185, 1987, doi: 10.1007/BF00667057.

[97] B. Pieraggi, "Defects and transport in oxides and oxide scales," *Shreir's Corrosion*, pp.

101–131, 2010, doi: 10.1016/B978-044452787-5.00009-3.

[98] D. Monceau and B. Pieraggi, “Determination of parabolic rate constants from a local analysis of mass-gain curves,” *Oxidation of Metals*, vol. 50, no. 5–6, pp. 477–493, 1998, doi: 10.1023/a:1018860909826.

[99] P. Berthod, C. Vébert, and L. Aranda, “Effect of dendritic orientation on the high temperature oxidation kinetic of tantalum-containing nickel-base alloys,” *Journal of Materials Science*, vol. 42, no. 1, pp. 352–362, 2007, doi: 10.1007/s10853-006-1033-4.

[100] A. K. Tyagi, K. Szot, A. Czyrska-Filemonowicz, D. Naumenko, and W. J. Quadakkers, “Significance of crystallographic grain orientation for oxide scale formation on FeCrAI ODS alloys studied by AFM and MCs+-SIMS,” *Materials at High Temperatures*, vol. 17, no. 1, pp. 159–163, 2000, doi: 10.1179/mht.2000.023.

[101] T. Connolley, P. A. S. Reed, and M. J. Starink, “Short crack initiation and growth at 600 °C in notched specimens of Inconel718,” *Materials Science and Engineering A*, vol. 340, no. 1–2, pp. 139–154, 2003, doi: 10.1016/S0921-5093(02)00169-7.

[102] P. Kofstad, *High Temperature Corrosion*. Elsevier Science Publishers LTD, 1988.

[103] R. A. Rapp, “The High Temperature Oxidation of Metals Forming Cation-Diffusing Scales,” *Metallurgical Transactions B*, vol. 15B, no. June, pp. 195–212, 1984.

[104] B. Chattopadhyay and G. C. Wood, “The transient oxidation of alloys,” *Oxidation of Metals*, vol. 2, no. 4, pp. 373–399, 1970, doi: 10.1007/BF00604477.

[105] A. N. Jinoop, C. P. Paul, and K. S. Bindra, “Laser-assisted directed energy deposition of nickel super alloys: A review,” *Proceedings of the Institution of Mechanical Engineers, Part L: Journal of Materials: Design and Applications*, vol. 233, no. 11, pp. 2376–2400, 2019, doi: 10.1177/1464420719852658.

[106] J. Nguejio, F. Szmytka, S. Hallais, A. Tanguy, S. Nardone, and M. Godino Martinez, “Comparison of microstructure features and mechanical properties for additive manufactured and wrought nickel alloys 625,” *Materials Science and Engineering: A*, vol. 764, no. July, p. 138214, 2019, doi: 10.1016/j.msea.2019.138214.

[107] A. Naoumidis, H. A. Schulze, W. Jungen, and P. Lersch, “Phase studies in the chromium-manganese-titanium oxide system at different oxygen partial pressures,” *Journal of the European Ceramic Society*, vol. 7, no. 1, pp. 55–63, 1991, doi: 10.1016/0955-2219(91)90054-4.

[108] A. Atkinson, M. R. Levy, S. Roche, and R. A. Rudkin, “Defect properties of Ti-doped Cr2O3,” *Solid State Ionics*, vol. 177, no. 19-25 SPEC. ISS., pp. 1767–1770, 2006, doi: 10.1016/j.ssi.2005.11.015.

[109] P. Berthod, F. Allègre, and E. Kretz, “Influence of Titanium on the High Temperature Oxidation and Chromia Volatilization of Ternary Ni–Cr–C Alloys,” *Oxidation of Metals*,

vol. 86, no. 5–6, pp. 581–595, 2016, doi: 10.1007/s11085-016-9656-6.

[110] S. Pedrazzini *et al.*, "Partitioning of Ti and Kinetic Growth Predictions on the Thermally Grown Chromia Scale of a Polycrystalline Nickel-Based Superalloy," *Metallurgical and Materials Transactions A: Physical Metallurgy and Materials Science*, vol. 50, no. 7, pp. 3024–3029, 2019, doi: 10.1007/s11661-019-05246-5.

[111] C. Issartel *et al.*, "Effects of titanium on a ferritic steel oxidation at 950°C," *Materials Science Forum*, vol. 461–464, no. I, pp. 69–76, 2004, doi: 10.4028/www.scientific.net/msf.461-464.69.

[112] S. Cruchley, H. E. Evans, M. P. Taylor, M. C. Hardy, and S. Stekovic, "Chromia layer growth on a Ni-based superalloy: Sub-parabolic kinetics and the role of titanium," *Corrosion Science*, vol. 75, pp. 58–66, 2013, doi: 10.1016/j.corsci.2013.05.016.

[113] B. Li, "Long-term cyclic oxidation behavior of wrought commercial alloys at high temperatures," Iowa State University, 2003.

[114] E. A. Gulbransen, K. F. Andrew, and F. A. Brassart, "Oxidation of Molybdenum 550° to 1700°C," *Journal of The Electrochemical Society*, vol. 110, no. 9, p. 952, 1963, doi: 10.1149/1.2425918.

[115] D. R. Schryer and J. L. Modisette, "An investigation of the effects of gaseous diffusion on the rate of oxidation of a metal forming a volatile oxide," *Planetary and Space Science*, vol. 3, no. C, pp. 31–37, 1961, doi: 10.1016/0032-0633(61)90221-5.

[116] K. R. Peters, D. P. Whittle, and J. Stringer, "Oxidation and hot corrosion of nickel-based alloys containing molybdenum," *Corrosion Science*, vol. 16, no. 11, 1976, doi: 10.1016/0010-938X(76)90010-X.

[117] D. A. Hughes and N. Hansen, "High angle boundaries formed by grain subdivision mechanisms," *Acta Materialia*, vol. 45, no. 9, pp. 3871–3886, 1997, doi: 10.1016/S1359-6454(97)00027-X.

[118] B. Tang, L. Jiang, R. Hu, and Q. Li, "Correlation between grain boundary misorientation and M23C 6 precipitation behaviors in a wrought Ni-based superalloy," *Materials Characterization*, vol. 78, pp. 144–150, 2013, doi: 10.1016/j.matchar.2013.02.006.

[119] G. Lindwall *et al.*, "Simulation of TTT Curves for Additively Manufactured Inconel 625," *Metallurgical and Materials Transactions A: Physical Metallurgy and Materials Science*, vol. 50, no. 1, pp. 457–467, 2019, doi: 10.1007/s11661-018-4959-7.

[120] M. R. Stoudt *et al.*, "The Influence of Annealing Temperature and Time on the Formation of δ-Phase in Additively-Manufactured Inconel 625," *Metallurgical and Materials Transactions A: Physical Metallurgy and Materials Science*, vol. 49, no. 7, pp. 3028–3037, 2018, doi: 10.1007/s11661-018-4643-y.

[121] V. Gunenthiram *et al.*, "Experimental analysis of spatter generation and melt-pool

behavior during the powder bed laser beam melting process," *Journal of Materials Processing Technology*, vol. 251, pp. 376–386, 2018, doi: 10.1016/j.jmatprotec.2017.08.012.

[122] S. G. K. Manikandan, D. Sivakumar, K. P. Rao, and M. Kamaraj, "Effect of weld cooling rate on Laves phase formation in Inconel 718 fusion zone," *Journal of Materials Processing Technology*, vol. 214, no. 2, pp. 358–364, 2014, doi: 10.1016/j.jmatprotec.2013.09.006.

[123] M. J. Sohrabi and H. Mirzadeh, "Interdi ff usion coe ffi cients of alloying elements in a typical Ni-based superalloy," vol. 169, no. August, p. 108875, 2019, doi: 10.1016/j.vacuum.2019.108875.

[124] A. M. de Sousa Malafaia, R. B. de Oliveira, L. Latu-Romain, Y. Wouters, and R. Baldan, "Isothermal oxidation of Inconel 625 superalloy at 800 and 1000 °C: Microstructure and oxide layer characterization," *Materials Characterization*, vol. 161, no. January, p. 110160, 2020, doi: 10.1016/j.matchar.2020.110160.

[125] Y. Xu, J. Lu, X. Yang, J. Yan, and W. Li, "Effect and role of alloyed Nb on the air oxidation behaviour of Ni-Cr-Fe alloys at 1000 °C," *Corrosion Science*, vol. 127, no. August, pp. 10–20, 2017, doi: 10.1016/j.corsci.2017.08.003.

[126] L. E. Shoemaker, "Alloys 625 and 725: Trends in properties and applications," *Proceedings of the International Symposium on Superalloys and Various Derivatives*, pp. 409–418, 2005, doi: 10.7449/2005/superalloys_2005_409_418.

[127] T. Sanviemvongsak, D. Monceau, C. Desgranges, and B. Macquaire, "Intergranular oxidation of Ni-base alloy 718 with a focus on additive manufacturing," *Corrosion Science*, vol. 170, no. November 2019, pp. 108684–108684, 2020, doi: 10.1016/j.corsci.2020.108684.

[128] A. Chyrkin *et al.*, "High-temperature oxidation behavior of additively manufactured IN625: Effect of microstructure and grain size," *Corrosion Science*, vol. 205, no. April, p. 110382, 2022, doi: 10.1016/j.corsci.2022.110382.

[129] D. M. England and A. V Virkar, "Oxidation Kinetics of Some Nickel-Based Superalloy Foils and Electronic Resistance of the Oxide Scale Formed in Air Part I," vol. 146, no. 9, pp. 3196–3202, 1999.

[130] K. A. Al-Hatab, M. A. Al-Bukhaiti, U. Krupp, and M. Kantehm, "Cyclic oxidation behavior of in 718 superalloy in air at high temperatures," *Oxidation of Metals*, vol. 75, no. 3–4, pp. 209–228, 2011, doi: 10.1007/s11085-010-9230-6.

[131] F. Rouillard, C. Cabet, K. Wolski, and M. Pijolat, "Oxide-layer formation and stability on a nickel-base alloy in impure helium at high temperature," *Oxidation of Metals*, vol. 68, no. 3–4, pp. 133–148, 2007, doi: 10.1007/s11085-007-9065-y.

[132] G. A. Greene and C. C. Finfrock, "Oxidation of inconel 718 in air at high temperatures,"

Oxidation of Metals, vol. 55, no. 5–6, pp. 505–521, 2001, doi: 10.1023/a:1010359815550.

[133] C. Örnek, "Additive manufacturing–a general corrosion perspective," *Corrosion Engineering Science and Technology*, vol. 53, no. 7, pp. 531–535, 2018, doi: 10.1080/1478422X.2018.1511327.

[134] G. Bi, C. N. Sun, H. chi Chen, F. L. Ng, and C. C. K. Ma, "Microstructure and tensile properties of superalloy IN100 fabricated by micro-laser aided additive manufacturing," *Materials and Design*, vol. 60, pp. 401–408, 2014, doi: 10.1016/j.matdes.2014.04.020.

[135] S. A. Khairallah, A. T. Anderson, A. Rubenchik, and W. E. King, "Laser powder-bed fusion additive manufacturing: Physics of complex melt flow and formation mechanisms of pores, spatter, and denudation zones," *Acta Materialia*, vol. 108, pp. 36–45, 2016, doi: 10.1016/j.actamat.2016.02.014.

[136] D. Wang *et al.*, "Mechanisms and characteristics of spatter generation in SLM processing and its effect on the properties," *Materials and Design*, vol. 117, pp. 121–130, 2017, doi: 10.1016/j.matdes.2016.12.060.

[137] E. A. Polman, T. Fransen, and P. J. Gellings, "The reactive element effect; Ionic processes of grain-boundary segregation and diffusion in chromium oxide scales," *Journal of Physics: Condensed Matter*, vol. 1, no. 28, pp. 4497–4510, 1989, doi: 10.1088/0953-8984/1/28/001.

[138] M. T. Lapington, D. J. Crudden, R. C. Reed, M. P. Moody, and P. A. J. Bagot, "Characterization of oxidation mechanisms in a family of polycrystalline chromia-forming nickel-base superalloys," *Acta Materialia*, vol. 206, p. 116626, 2021, doi: 10.1016/j.actamat.2021.116626.

[139] H. Jeong, S. H. Kim, W. S. Choi, and P. P. Choi, "Spallation resistance of oxide scales on Alloy 617 enhanced by boron addition," *Corrosion Science*, vol. 140, no. June, pp. 196–204, 2018, doi: 10.1016/j.corsci.2018.06.002.

[140] A. Vayyala *et al.*, "Effect of Nb Addition on Oxidation Mechanisms of High Cr Ferritic Steel in Ar–H2–H2O," *Oxidation of Metals*, vol. 92, no. 5–6, pp. 471–491, 2019, doi: 10.1007/s11085-019-09933-x.

[141] L. Latu-Romain *et al.*, "The Role of Oxygen Partial Pressure on the Nature of the Oxide Scale on a NiCr Model Alloy," *Oxidation of Metals*, vol. 88, no. 3–4, pp. 481–493, 2017, doi: 10.1007/s11085-016-9670-8.

[142] D. P. Whittle, Y. Shida, G. C. Wood, F. H. Stott, and B. D. Bastow, "Enhanced diffusion of oxygen during internal oxidation of nickel-base alloys," *Philosophical Magazine A: Physics of Condensed Matter, Structure, Defects and Mechanical Properties*, vol. 46, no. 6, pp. 931–949, 1982, doi: 10.1080/01418618208236942.

[143] Y. Shida, F. H. Stott, B. D. Bastow, D. P. Whittle, and G. C. Wood, "Development of preferential intergranular oxides in nickel-aluminum alloys at high temperatures,"

Oxidation of Metals, vol. 18, no. 3–4, pp. 93–113, 1982, doi: 10.1007/BF00662032.

[144] T. Watanabe, "Grain boundary engineering: Historical perspective and future prospects," *Journal of Materials Science*, vol. 46, no. 12, pp. 4095–4115, 2011, doi: 10.1007/s10853-011-5393-z.

[145] V. Y. Gertsman and S. M. Bruemmer, "Study of grain boundary character along intergranular stress corrosion crack paths in austenitic alloys," *Acta Materialia*, vol. 49, no. 9, pp. 1589–1598, 2001, doi: 10.1016/S1359-6454(01)00064-7.

[146] S. Yamaura, Y. Igarashi, S. Tsurekawa, and T. Watanabe, "Structure-dependent intergranular oxidation in Ni-Fe polycrystalline alloy," *Acta Materialia*, vol. 47, no. 4, pp. 1163–1174, 1999, doi: 10.1016/S1359-6454(99)00007-5.

[147] E. G. Wagenhuber, V. B. Trindade, and U. Krupp, "The role of oxygen-grain-boundary diffusion during intercrystalline oxidation and intergranular fatigue crack propagation in alloy 718," *Proceedings of the International Symposium on Superalloys and Various Derivatives*, pp. 591–600, 2005, doi: 10.7449/2005/superalloys_2005_591_600.

[148] V. B. Trindade, U. Krupp, P. E. G. Wagenhuber, Y. M. Virkar, and H. J. Christ, "Studying the role of the alloy-grain-boundary character during oxidation of Ni-base alloys by means of the electron back-scattered diffraction technique," *Materials at High Temperatures*, vol. 22, no. 3–4, pp. 207–212, 2005, doi: 10.1179/mht.2005.024.

[149] X. Y. Fang, H. Q. Li, M. Wang, C. Li, and Y. B. Guo, "Characterization of texture and grain boundary character distributions of selective laser melted Inconel 625 alloy," *Materials Characterization*, vol. 143, no. November 2017, pp. 182–190, 2018, doi: 10.1016/j.matchar.2018.02.008.

[150] M. T. Hasib, H. E. Ostergaard, Q. Liu, X. Li, and J. J. Kruzic, "Tensile and fatigue crack growth behavior of commercially pure titanium produced by laser powder bed fusion additive manufacturing," *Additive Manufacturing*, vol. 45, no. May, p. 102027, 2021, doi: 10.1016/j.addma.2021.102027.

[151] K. Dietrich, J. Diller, S. Dubiez-Le Goff, D. Bauer, P. Forêt, and G. Witt, "The influence of oxygen on the chemical composition and mechanical properties of Ti-6Al-4V during laser powder bed fusion (L-PBF)," *Additive Manufacturing*, vol. 32, no. July 2019, 2020, doi: 10.1016/j.addma.2019.100980.

[152] S.-K. Rittinghaus, V. R. Molina Ramirez, J. Zielinski, and U. Hecht, "Oxygen gain and aluminum loss during laser metal deposition of intermetallic TiAl," *Journal of Laser Applications*, vol. 31, no. 4, 2019, doi: 10.2351/1.5096974.

[153] K. P. Trumble and M. Rühle, "The thermodynamics of spinel interphase formation at diffusion-bonded Ni/Al2O3 interfaces," *Acta Metallurgica Et Materialia*, vol. 39, no. 8, pp. 1915–1924, 1991, doi: 10.1016/0956-7151(91)90160-3.

[154] P. S. Prevey, "X-Ray Diffraction Residual Stress Techniques," in *Materials*

Characterization, ASM Handbook, vol. 10, ASM, 1986, pp. 380–392.

[155] Q. Luo and A. H. Jones, "High-precision determination of residual stress of polycrystalline coatings using optimised XRD-sin2ψ technique," *Surface and Coatings Technology*, vol. 205, no. 5, pp. 1403–1408, 2010, doi: 10.1016/j.surfcoat.2010.07.108.

[156] C. Sarioglu, "Analysis of XRD stress measurement data of naturally grown oxide films Al2O3 and Cr2O3 based on existing Reuss, Voigt, and Hill models," *Surface Engineering*, vol. 18, no. 2, pp. 105–112, 2002, doi: 10.1179/026708402225002767.

[157] M. Guerain *et al.*, "Residual stress determination in oxide layers at different length scales combining Raman spectroscopy and X-ray diffraction: Application to chromia-forming metallic alloys," *Journal of Applied Physics*, vol. 122, no. 19, 2017, doi: 10.1063/1.4990146.

[158] P. Y. Hou and J. Stringer, "Room temperature strains in Cr2O3 scales formed at elevated temperatures on Ni-25wt%Cr and y- and Al-doped Ni-25wt%Cr," *Acta Metallurgica Et Materialia*, vol. 39, no. 5, pp. 841–849, 1991.

[159] K. P. Lillerud and P. Kofstad, "High Temperature Oxidation of Chromium.," *International Corrosion Conference Series*, vol. 127, no. 1, pp. 155–161, 1983.

[160] F. A. Golightly, F. H. Stott, and G. C. Wood, "The Relationship Between Oxide Grain Morphology and Growth Mechanisms for Fe-Cr-Al and Fe-Cr-Al-Y Alloys," *Journal of The Electrochemical Society*, vol. 126, no. 6, pp. 1035–1042, 1979, doi: 10.1149/1.2129170.

[161] T. Gheno, C. Desgranges, and L. Martinelli, "On the role of surface deformation in the oxidation of NiCr alloys at 340–600 °C," *Corrosion Science*, vol. 173, no. May, p. 108805, 2020, doi: 10.1016/j.corsci.2020.108805.

[162] W. J. Nowak, B. Wierzba, and J. Sieniawski, "Surface preparation effect on oxidation kinetics of Ni-base superalloy," *Journal of Physics: Conference Series*, vol. 936, no. 1, 2017, doi: 10.1088/1742-6596/936/1/012002.

[163] N. Sheng, K. Horke, A. Meyer, M. R. Gotterbarm, R. Rettig, and R. F. Singer, "Surface recrystallization and its effect on oxidation of superalloy C263," *Corrosion Science*, vol. 128, no. August, pp. 186–197, 2017, doi: 10.1016/j.corsci.2017.09.020.

[164] K. Chen *et al.*, "A high-resolution study of the different surface state effects on the corrosion behaviors of a ferritic steel and an austenitic steel in supercritical water," *Corrosion Science*, vol. 209, no. June, 2022, doi: 10.1016/j.corsci.2022.110757.

[165] C. Ostwald and H. J. Grabke, "Initial oxidation and chromium diffusion. I. Effects of surface working on 9-20% Cr steels," *Corrosion Science*, vol. 46, no. 5, pp. 1113–1127, 2004, doi: 10.1016/j.corsci.2003.09.004.

[166] S. Schroeder, S. Braun, U. Mueller, R. Sonntag, S. Jaeger, and J. P. Kretzer, "Particle

analysis of shape factors according to American Society for Testing and Materials," *Journal of Biomedical Materials Research - Part B Applied Biomaterials*, vol. 108, no. 1, pp. 225–233, 2020, doi: 10.1002/jbm.b.34382.

[167] C. Desgranges, F. Lequien, E. Aublant, M. Nastar, and D. Monceau, "Depletion and voids formation in the substrate during high temperature oxidation of Ni-Cr alloys," *Oxidation of Metals*, vol. 79, no. 1–2, pp. 93–105, 2013, doi: 10.1007/s11085-012-9328-0.

[168] Y. Oshida and H. W. Liu, "Grain Boundary Oxidation and an Analysis of the Effects of Pre-oxidation on Subsequent Fatigue Life," Syracuse, New York, 1986.

[169] R. Jiang, S. Everitt, N. Gao, K. Soady, J. W. Brooks, and P. A. S. Reed, "Influence of oxidation on fatigue crack initiation and propagation in turbine disc alloy N18," *INTERNATIONAL JOURNAL OF FATIGUE*, vol. 75, pp. 89–99, 2015, doi: 10.1016/j.ijfatigue.2015.02.007.

[170] F. H. Stott, "Methods of improving adherence," *Materials Science and Technology*, vol. 4, no. May, pp. 431–438, 1988, doi: 10.1179/mst.1988.4.5.431.

[171] H. E. Evans, "Spallation models and their relevance to steam- grown oxides," *Materials at High Temperatures*, vol. 3409, no. 22:1–2, pp. 155–156, 2014, doi: 10.1179/mht.2005.018.

[172] W. Christl, A. Rahmel, and M. Schütze, "Behavior of Oxide Scales on 2 . 25Cr-lMo Steel During Thermal Cycling . I. Scales Formed in Oxygen and Air," *Oxidation of Metals*, vol. 31, pp. 1–7, 1989.

[173] H. J. Grabke, D. Wiemer, and H. Viefhaus, "Segregation of sulfur during growth of oxide scales," *Applied Surface Science*, vol. 47, pp. 243–250, 1991.

[174] K. Son, M. E. Kassner, and K. A. Lee, "The Creep Behavior of Additively Manufactured Inconel 625," *Advanced Engineering Materials*, vol. 1900543, pp. 1–11, 2019, doi: 10.1002/adem.201900543.

[175] B. Pieraggi, R. A. Rapp, and J. P. Hirth, "Role of Interface Structure and Interfacial Defects in Oxide Scale Growth," *Oxidation of Metals*, vol. 44, pp. 63–79, 1995.

[176] S. Azadian, L. Wei, and R. Warren, "Delta phase precipitation in Inconel 718," vol. 53, pp. 7–16, 2004, doi: 10.1016/j.matchar.2004.07.004.

[177] D. J. Morrison and J. C. Moosbrugger, "Effects of grain size on cyclic plasticity and fatigue crack initiation in nickel," *International Journal of Fatigue*, vol. 19, no. Supp. No. 1, pp. 51–59, 1997, doi: 10.1016/s0142-1123(97)00034-0.

[178] F. L. Liang and C. Laird, "Control of intergranular fatigue cracking by slip homogeneity in copper I: Effect of grain size," *Materials Science and Engineering A*, vol. 117, no. C, pp. 95–102, 1989, doi: 10.1016/0921-5093(89)90090-7.

[179] S. Suresh, “Cyclic Deformation and Fatigue,” in *Materials Science and Engineering: A*, vol. 6, H. Muhrabi, Ed. VCH, Weinheim, Germany, 1993, pp. 509–563.

[180] A. Luft, “Microstructural processes of plastic instabilities in strengthened metals,” *Progress in Materials Science*, vol. 35, no. 2, pp. 97–204, 1991, doi: 10.1016/0079-6425(91)90002-B.

[181] D. Lambert, “Fatigue damage accumulation in nickel-base superalloys,” *Department of Engineering Materials*, no. August, 1994.

[182] Y. Murakami, “Chapter 6 - Effects of Nonmetallic Inclusions on Fatigue Strength,” in *Metal Fatigue: Effects of Small Defects and Nonmetallic Inclusions*, Elsevier Science Ltd, 2002, p. Elsevier Science Ltd,.

[183] C. Qiu, “NET-SHAPE HOT ISOSTATIC PRESSING OF A NICKEL-BASED POWDER SUPERALLOY,” University of Birmingham, 2010.

[184] A. de Bussac, “Prediction of the Competition Between Surface and Internal Fatigue Crack Initiation in Pm Alloys,” *Fatigue & Fracture of Engineering Materials & Structures*, vol. 17, no. 11, pp. 1319–1325, 1994, doi: 10.1111/j.1460-2695.1994.tb00219.x.

[185] J. A. Moore, D. Frankel, R. Prasannavenkatesan, A. G. Domel, G. B. Olson, and W. K. Liu, “A crystal plasticity-based study of the relationship between microstructure and ultra-high-cycle fatigue life in nickel titanium alloys,” *International Journal of Fatigue*, vol. 91, pp. 183–194, 2016, doi: 10.1016/j.ijfatigue.2016.06.006.

[186] Z. Chen, Z. Dong, C. Liu, Y. Dai, and C. He, “Characterization on Crack Initiation and Early Propagation Region of Nickel-Based Alloys in Very High Cycle Fatigue,” pp. 1–13, 2022.

[187] Y. Gao, Y. Ding, J. Chen, J. Xu, Y. Ma, and X. Wang, “Effect of twin boundaries on the microstructure and mechanical properties of Inconel 625 alloy,” *Materials Science and Engineering: A*, vol. 767, no. August, p. 138361, 2019, doi: 10.1016/j.msea.2019.138361.

[188] E. A. Lass *et al.*, “Formation of the Ni3Nb δ-Phase in Stress-Relieved Inconel 625 Produced via Laser Powder-Bed Fusion Additive Manufacturing,” *Metallurgical and Materials Transactions A: Physical Metallurgy and Materials Science*, vol. 48, no. 11. pp. 5547–5558, 2017, doi: 10.1007/s11661-017-4304-6.

[189] J. L. Smialek, D. T. Jayne, J. C. Schaeffer, and W. H. Murphy, “Effects of hydrogen annealing, sulfur segregation and diffusion on the cyclic oxidation resistance of superalloys: a review,” *Thin Solid Films*, vol. 253, no. 1–2, pp. 285–292, 1994, doi: 10.1016/0040-6090(94)90335-2.

[190] G. Marchese *et al.*, “Microstructural investigation of as-fabricated and heat- treated Inconel 625 and Inconel 718 fabricated by direct metal laser sintering : contribution of Politecnico di Torino and Istituto Italiano di Tecnologia (IIT) di Torino,” vol. 71, no. 4, pp. 273–278, 2016.

[191] S. Li *et al.*, “Melt-pool motion, temperature variation and dendritic morphology of Inconel 718 during pulsed- and continuous-wave laser additive manufacturing: A comparative study,” *Materials and Design*, vol. 119, pp. 351–360, 2017, doi: 10.1016/j.matdes.2017.01.065.

[192] M. S. A. Karunaratne and R. C. Reed, “Interdiffusion of niobium and molybdenum in nickel between 900 - 1300°C,” *Defect and Diffusion Forum*, vol. 237–240, no. PART 1, pp. 420–425, 2005, doi: 10.4028/www.scientific.net/ddf.237-240.420.

[193] F. J. Vermolen, C. Vuik, and S. van der Zwaag, “Particle dissolution and cross-diffusion in multi-component alloys,” *Materials Science and Engineering: A*, vol. 347, no. 1–2, pp. 265–279, 2003, doi: 10.1016/S0921-5093(02)00615-9.

[194] W. M. Tucho, P. Cuvillier, A. Sjolyst-Kverneland, and V. Hansen, “Microstructure and hardness studies of Inconel 718 manufactured by selective laser melting before and after solution heat treatment,” *Materials Science and Engineering A*, vol. 689, no. December 2016, pp. 220–232, 2017, doi: 10.1016/j.msea.2017.02.062.

[195] H. Pan, Y. He, and X. Zhang, “Interactions between Dislocations and Boundaries during Deformation,” 2021.

[196] G. S. Was, B. Alexandreanu, P. Andresen, and M. Kumar, “Role of Coincident Site Lattice Boundaries in Creep and Stress Corrosion Cracking,” *MRS Online Proceedings Library*, vol. 819, no. 21, pp. 1–5, 2004, doi: https://doi.org/10.1557/PROC-819-N2.1.